University of Manitoba

Optical Navigation Using Resident Space Objects

by

Matthew Driedger

A Thesis submitted to the Faculty of Graduate Studies of
The University of Manitoba
in partial fulfillment of the requirements of the degree of

DOCTOR OF PHILOSOPHY

Department of Mechanical Engineering
University of Manitoba
Winnipeg

Abstract

Estimators are critical to modern society and are present everywhere from automobile cruise control systems to satellite attitude determination and control. Ensuring that estimators produce reliable, trustworthy estimates is key to keeping users safe and systems functioning correctly. While many systems and metrics have been proposed to ensure estimator reliability, these come with disadvantages such as requiring time-consuming Monte Carlo simulations or encapsulating poorly performing estimators rather than addressing core issues. This dissertation examines the various factors that affect estimator reliability, specifically for Kalman Filter variants, and presents a new trustworthiness metric that quantifies a filter's reliability without requiring Monte Carlo simulations: the covariance trust ratio (CTR).

The reliability factors examined here include the type of Kalman filter used, whether a filter incorporates elements of the measurement source's state, the type of process noise covariance model used, and the type of measurement sources used. To examine how these factors affect a Kalman filter's reliability, this dissertation uses two existing methods from the literature, Normalized Estimate Error Squared (NEES) and Normalized Innovation Squared (NIS), in addition to the CTR.

The impact of these reliability factors on a Kalman filter's trustworthiness are demonstrated using a case study which explores how a spacecraft's orbital state can be estimated using relative angle and range measurements of Resident Space Objects (RSOs). This case study shows that the CTR is an effective method for quantifying an estimator's trustworthiness, highlights the effects of the various reliability factors studied here, and demonstrates that these factors can be quantitatively assessed to provide confidence in a filter's trustworthiness. In order for new estimation methods to become commercially viable, they must demonstrate their reliability and trustworthiness to potential users. The estimator reliability analysis and estimator trust quantification work presented in this dissertation

form an enabling technology that may aid in the more rapid adoption of state estimation techniques.

Acknowledgements

I would like to thank my advisor, Philip Ferguson, and my Defence Committee; Nariman Sepehri, Witold Kinsner, and Lauchie Scott, for their guidance and support throughout my doctorate. I would also like to thank the Natural Sciences and Engineering Research Council of Canada (NSERC) and Magellan Aerospace for supporting my research under IRCPJ 522151-17 as well as the University of Manitoba Faculty of Graduate Studies for supporting my research through the University of Manitoba Graduate Fellowship (UMGF).

Dedication

To my wife Abby, my parents Fred and Lori, and my friends. Thank you all for your support, love, and patience without which this would not have been possible.

"The entire universe has been neatly divided into things to (a) mate with, (b) eat, (c) run away from, and (d) rocks."

Terry Pratchett, *Equal Rites*, 1987

Generally, Kalman Filtering falls into the third category. However, this thesis attempts to tame the Kalman Filter and turn it into something that rocks.

Table of Contents

List of Tables

List of Figures

List Of Symbols

$\dot{A}_s$	scan area rate
A	continuous state transition model
A_{beam}	transmitted beam area
A_{CS}	cross sectional area
A_{det}	detector area
a	frame size
B	continuous control input model
$B(\theta_v, \theta_I)$	bidirectional reflection distribution function
B_k	discretized control input model
B_w	bandwidth
c	speed of light
D	diameter
$d_{M,k}$	Mahalanobis Distance
$\mathbb{E}$	expected value
E	relative error
e	residual
e_k	discretized estimate error
$F_\#$	lens focal number
F_N	noise figure
$F_x(t)$	gravitational force exerted in the x axis
$F_y(t)$	gravitational force exerted in the y axis
$F(\theta_{phase})$	shape-dependent function of phase angle
f	transmit frequency
$f(X_{k-1})$	discretized nonlinear state dynamics model
$\tilde{f}$	numerical approximation of a function
G	antenna gain
H	continuous linear observation model
H_k	discretized linear observation model
$h(X_{k-1})$	discretized nonlinear observation model
J	inertia
I	identity matrix
I_D	diffuse light flux

I_L	incoming light flux
I_o	optical incidence flux
I_{rx}	received light
I_{tx}	transmitted light
K	total number of timesteps
K_k	discrete Kalman gain
k	timestep
k_B	Boltzmann's constant
k_p	number of pixels
L	number of elements in the state vector
L_a	antenna length
M	magnitude
m	mass
m_t	minimum detectable visual magnitude
N	number of Monte Carlo simulations
N_{bg}	background illumination per pixel
N_D	dark current per pixel
N_R	read noise
N_s	received signal
$\hat{n}$	surface normal
n_X	number of state elements
n_z	number of measurement sources
$O(h^n)$	n^{th} higher order terms
P	state covariance estimate
P_k^{true}	true discrete state covariance
P_k	discrete state covariance estimate
P_R	central linearization point
P_{tx}	transmitted power
P_{rx}	power detected by a receiver
$P_{\hat{X}_k\hat{y}_k}$	UKF cross covariance
$P_{\hat{y}_k\hat{y}_k}$	UKF measurement covariance
$\mathcal{Q}$	observability matrix rank
Q	continuous process noise covariance
$Q_{adaptive}$	adaptive process noise covariance
Q_{fixed}	fixed process noise covariance
Q_k	discretized process noise covariance
Q_χ	χ^2 upper tail probability
R_c	continuous measurement noise covariance
R	relative position in a Cartesian reference frame
R_{com}	maximum communications range
R_k	discretized measurement noise covariance
R_{max}	maximum RSO range
R_{sun}	Sun-RSO vector
R_t	target SNR

R_X	autocorrelation function
r	position in a Cartesian reference frame
r_{beam}	transmitted beam radius
r_{det}	detector aperture radius
S_k	discretized measurement innovation covariance
SNR	signal to noise ratio
T	orbital period
T_I	internal noise temperature
T_N	noise temperature
T_S	surface temperature
t	time
Δt	time step
$\delta(\Delta t)$	dirac-delta function
t_e	exposure time
t_{search}	search time
U_u	EKF underweighting factor
u	continuous control input
u_k	discretized control input
V_{ri}	visual magnitude of a light source
V_{sun}	visual magnitude of the sun
v	continuous measurement noise
v_k	discretized measurement noise
W	continuous process noise covariance
W^c	second-order UKF weights
W^m	first-order UKF weights
W_a	antenna width
W_P	power spectral density
w	continuous process noise
w_{fixed}	fixed process noise
w_k	discretized process noise
X	continuous state
X_k	discretized state
X_k^{est}	discretized state estimate
X_k^{true}	discretized true state
x	observer's x axis position in a Cartesian reference frame
$\dot{x}$	observer's x axis velocity in a Cartesian reference frame
$\dot{x_{ri}}$	RSO i's x axis velocity in a Cartesian reference frame
x_{ri}	RSO i's x axis position in a Cartesian reference frame
Δx	relative x axis position in a Cartesian reference frame
$\mathcal{Y}$	UKF measurement Sigma points
y	observer's y axis position in a Cartesian reference frame
$\tilde{y}_k$	discretized measurement innovation

$\dot{y}$	observer's y axis velocity in a Cartesian reference frame
y_{ri}	RSO i's y axis position in a Cartesian reference frame
$\dot{y_{ri}}$	RSO i's y axis velocity in a Cartesian reference frame
Δy	relative y axis position in a Cartesian reference frame
z	continuous measurement
z_k	discretized measurement
α	UKF tuning parameter
α_d	beam divergence
α_u	EKF underweighting parameter
β	UKF tuning parameter
β_u	EKF underweighting parameter
γ_p	pixel size
γ_r	reflectivity
γ_v	optical cross section
$\gamma_{v,d}$	diffuse optical cross section
$\gamma_{v,s}$	specular optical cross section
ϵ	machine epsilon
$[\epsilon_1, \epsilon_2]$	two sided NEES probability region
$\epsilon_{\nu,k}$	NIS parameter
$\bar{\epsilon}_{\nu,k}$	average NIS statistic
$\bar{\epsilon}_{\nu av}$	time-average NIS statistic
$[\epsilon_{\nu 1}, \epsilon_{\nu 2}]$	two sided NIS probability region
ϵ_k	NEES parameter
$\bar{\epsilon}_k$	average NEES statistic
$\bar{\epsilon}_{av}$	time-average NEES statistic
η	covariance trust ratio
η_{av}	average covariance trust ratio
η_{median}	median covariance trust ratio
η_{min}	minimum fraction of transmitted light
η_q	mean quantum efficiency
η_R	ratio of transmitted to received light
η_{std}	covariance trust ratio standard deviation
θ	angle between a star tracker's bore axis and the line of sight vector between the observing spacecraft's inertial reference frame and the observed object
θ_{aspect}	aspect angle
θ_I	angle between the Sun-RSO vector and the RSO's surface normal
θ_{phase}	phase angle
θ_v	angle between the observer-RSO vector and the RSO's surface normal
$\dot{\theta}_s$	scan rate

κ	UKF tuning parameter
κ_A	matrix condition number
λ	UKF scaling parameter
λ_k	eigenvalue
$\lambda_{k,max}$	maximum eigenvalue
$\lambda_{k,min}$	minimum eigenvalue
μ	standard gravitational parameter
μ_{true}	moving mean estimate error
ξ	spectral amplitude
ρ	readout noise radius
ρ_a	antenna efficiency
ρ_d	diffuse reflectivity coefficient
σ	standard deviation
σ_c	radar cross section
σ_d	dark current
σ_{est}	estimated error standard deviation
σ_{true}	moving estimate error standard deviation
σ_v	along-track TLE error
σ_w	out-of-plane TLE error
τ	torque
τ_t	optical transmittance loss
Φ	discretized linear state transition model
Φ_*	RSO illumination
Φ_0	reference star stellar flux
ϕ	angle between an observer's body frame x axis and a Cartesian inertial frame x axis
$\dot{\phi}$	angular rate between an observer's body frame x axis and a Cartesian inertial frame x axis
χ_k	UKF Sigma points
χ^2	Chi-squared distribution
Ψ	nonlinearity metric
Ψ_A	angle measurement nonlinearity metric
Ψ_R	range measurement nonlinearity metric
$\dot{\Omega}_s$	solid angle scan rate
Ω_R	receiver aperture solid angle
Ω_e	solid angle search envelope
ω	slew rate

Chapter 1

Introduction

*"**sĭmŭlātĭo** , ōnis, f.,*

I.a falsely assumed appearance, a false show, feigning, shamming, pretence, feint, insincerity, deceit, hypocrisy, simulation, etc."

C. T. Lewis, and C. Short, *A Latin Dictionary.* Clarendon Press, 1879.

1.1 Motivation

State estimation is the process of predicting a system's current behaviour, typically using some combination of measurements, knowledge of the system's dynamics, and statistics. Estimators are ubiquitous to modern society and are used everywhere from cruise control [11] and battery state of charge estimation [12], to spacecraft navigation [13]. Underpinning these estimates are a myriad of assumed mathematical models including those describing how the system behaves, how measurements are obtained, how external disturbances affect the system, and how uncertainties can be statistically described. Further, in addition to uncertainties due to random variations such as measurement or process noises (known as aleatoric uncertainties), systems can also be subject to systematic uncertainties due to faulty assumptions or unknown information (collectively known as epistemic uncertainties) [14]. By necessity, state estimation uses a simplified model of reality consisting of many individual simplified models. These models must strike a careful balance between simulating real-world behaviour with sufficient accuracy to predict a system's behaviour but avoiding unnecessary complexity and computational effort. Striking this balance can be difficult and simulated estimator performance can be deceiving. However, if a developer fails to adequately model

the system, the estimator may produce erroneous state estimates and, depending on the severity of the estimator's error, the safety of reliant systems or users may suffer.

For an estimator to be applied to real-world applications, its estimates must be sufficiently accurate and the user must have some trust in the estimator's state predictions. In safety-critical tasks, accuracy on its own is insufficient; even if a filter has reached a precise steady-state estimate, operators may be reluctant to rely on these data if the estimator's trustworthiness cannot be otherwise validated. For example, operators may need to establish trust in a spacecraft's state estimate, whether using a video-feed or with secondary measurement sources, before docking with another spacecraft. Even for every-day tasks, measuring estimator trustworthiness can be highly beneficial. An example of this appears in mapping software such as Google Maps, which provides uncertainty bubbles surrounding location estimates based on the estimate's trustworthiness, as seen in Fig. 1.1. Trustworthiness can be established by using external methods such as redundancy [15] or monitoring software [10] to override poor estimates, or through experience using the estimator for prolonged periods. However, it would be better if the estimator itself was inherently trustworthy and if this trustworthiness could be quantified.

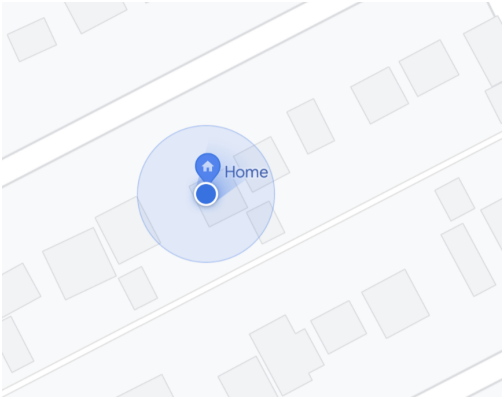

Fig. 1.1: Uncertainty bubble surrounding a position estimate in Google Maps.

There are existing reliability methods that use an estimator's intrinsic variables to determine an estimate's trustworthiness [16, 17, 18, 19]. Generally, these methods create a model of an estimator's performance and compare this model with an idealized value to create a ratio of the idealized value. Some reliability metrics, including Normalized Innovation Squared (NIS) [20], subjective logic tests [18], and residual tests [19] use the difference

between incoming measurements and the estimator's expected measurement values, known as the estimator's measurement innovation, to build covariance models of the estimator's performance. Other metrics such as Normalized Estimate Error Squared (NEES) [20] use truth data for building covariance models. Metrics developed for the Global Positioning System (GPS), such as Geometric Dilution of Precision (GDOP), compare a Jacobian of a GPS estimate's pseudorange matrix to the sum of the expected GPS error source standard deviations [17]. Despite their utility, existing reliability metrics are not perfect. Methods that use a filter's measurement innovation to measure performance, such as NIS [20], subjective logic tests [18], and residual tests [19] do not directly measure estimate reliability. Instead, these metrics measure the reliability of incoming measurements and how well a filter predicts these measurements. NEES and NIS require Monte Carlo simulations to build their statistical models, which can become cumbersome. Finally GDOP and similar position dilution of precision methods are limited to specific observer-target geometries.

While these assessment methods can help measure an estimator's performance, the choice of estimator is another key factor in ensuring a system is reliable. Some estimators, such as the Kalman Filter[1] and its variants, include state and measurement innovation covariance estimates in their calculations [21, 22, 23]. Even better, the Kalman Filter is an optimal filter, meaning that if the filter is used on a system with linear dynamics, linear measurements, and white noise sources[2], the filter's state covariance estimate exactly matches the true state covariance [21]. Extensions of the Kalman Filter, such as the Extended Kalman Filter (EKF) and the Unscented Kalman Filter (UKF), have been developed for systems that include nonlinear dynamics or nonlinear measurements. The EKF and UKF are nonlinear filters, in that they do not require linear dynamics or linear measurements, but retain the Kalman Filter's linear Kalman Gain. These nonlinear Kalman filters are not optimal, unless used on a linear system with white noise distributions. Despite their non-optimal natures, the covariance estimates of these Kalman filters can still be used to compare their performances to ideal

[1] In this dissertation, I refer to the original filter developed by Rudolf Kalman [21] as the "the Kalman Filter" and to the broader category of estimators based on this filter as "Kalman filters" or as "a Kalman filter."

[2] Note that there is a common belief that the Kalman Filter requires zero-mean Gaussian measurement and process noise distributions [24]. However, the Kalman Filter is optimal for any process and measurement noise distributions so long as they are white noises [24, 20].

values. Due to their inbuilt covariance estimates and the Kalman Filter's optimality, reliability methods are commonly used to assess the reliability of Kalman filters [18, 19, 20, 16, 25]. However, research into the factors that affect a Kalman filters' reliability are lacking.

This dissertation studies the various factors that can affect an estimator's trustworthiness, such as the estimator itself, the degree of nonlinearities present, how noise sources are modelled, and if elements of the measurement sources are included in the filter's dynamics model. By conducting this study, this dissertation aids researchers and engineers in developing estimators that are inherently more trustworthy, reducing implementation risks and improving system performances. Additionally, this dissertation explores a new method for quantifying an estimator's trustworthiness, without some of the limitations of previous metrics such as the use of Monte Carlo simulations. Specifically, the new covariance trust metric presented in this work improves on the previous NEES metric by removing its dependency on Monte Carlo simulations, which decreases the time it takes to develop and tune a Kalman filter. The trust factor analysis and new trust metric are evaluated using Resident Space Object (RSO) based navigation as a case study. The remainder of this chapter provides additional background on the case study, presents this dissertation's research hypotheses, reviews the research contributions made by this dissertation, and outlines of this dissertation's remaining structure.

1.2 Case Study

Spacecraft state estimation, including the estimation of position, velocity, orientation, and angular velocity, is critical to a wide range of space-missions, from Earth observation and telecommunications to interplanetary exploration [26, 27, 28]. These estimates allow a spacecraft to point cameras, antennas, solar arrays, and other components in their correct orientations; enable communications between the spacecraft and ground stations; and ensure that a myriad of other functions occur as intended. To perform these tasks, a given mission may utilize a variety of sensors and methods of state estimation including Global Navigation Satellite System (GNSS) receivers, ground-based tracking, and onboard sensors such as star trackers, sun sensors, moon sensors, earth limb sensors, and magnetometers. However,

each method has its drawbacks. GNSS-based estimation is generally limited to satellites in low orbits below GNSS constellations [29]. Ground-based tracking requires a series of ground stations which increase mission cost and complexity. Onboard sensors can provide information on a satellite's orientation or the direction of other bodies such as the sun or Earth, but most cannot provide absolute position information. Magnetometers can be used for attitude estimation and rough position estimation, but magnetometer-based position estimates may include large errors due to shifts in the Earth's magnetic field and cannot be performed around other planets and celestial bodies [30].

While most onboard sensors are limited to attitude and relative position solutions, star trackers have the potential to provide both position and attitude estimates. Traditionally, star trackers estimate a spacecraft's attitude by taking images of stars and comparing these images to an onboard star catalogue. Using this method, a star tracker can provide highly accurate attitude estimates, with errors of less than 1 arc-second [31]. However, star trackers detect other bodies including other spacecraft and orbital debris [32]. These sightings, analogous to those made by other wide field of view cameras, such as the one shown in Fig. 1.2, are currently filtered out as false matches by the star tracker's software. But RSO sightings have the potential to be used for navigation as well. As a case study for exploring estimator trustworthiness, this research explores how RSO detections by commercial star trackers can be used to improve a spacecraft's navigation (both attitude and orbital position) solution. Expanding the capabilities of star trackers can reduce the cadre of sensors required for a given mission; leading to decreases in spacecraft cost, shortening schedules, and reducing a spacecraft's dependence on ground based tracking.

One of the challenges in developing an RSO-based optical navigation method, and ensuring that the method is practical and commercially viable, is ensuring that estimates are reliable and can be trusted. This need for trustworthiness is especially acute in the space industry, where the Technology Readiness Levels (TRLs) of new technologies are rigorously tracked and few are willing to use low-TRL technologies. This driving need for reliability makes RSO-based optical navigation an excellent case study for exploring the factors that affect estimator reliability and how this reliability can be quantified.

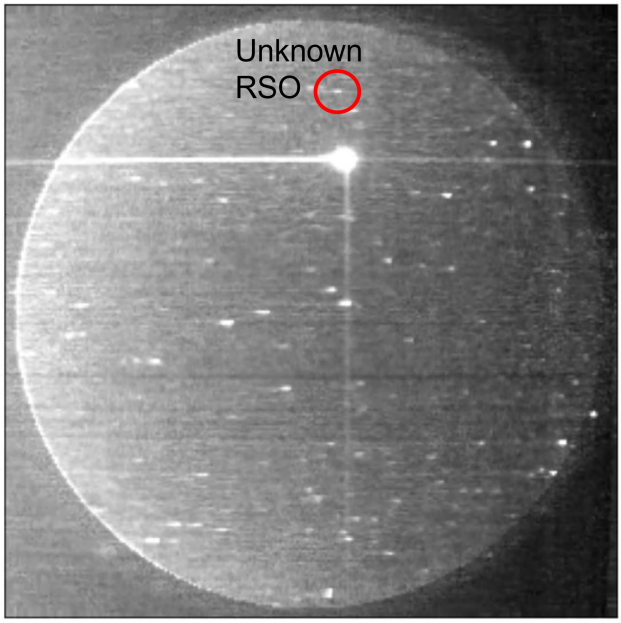

Fig. 1.2: Image containing an unknown resident space object taken by CASSIOPE's Fast Auroral Imager camera [9].

1.3 Hypotheses

This research explores the methods with which spacecraft, equipped with commercial star trackers, can estimate their state using RSO detections. To determine the viability of such a method, the following primary hypothesis is examined. This hypothesis forms the central research question in developing the RSO-based optical navigation system:

> **Hypothesis 1:** Estimator confidence can be determined and parameterized to characterize the reliability of a state estimate and reject or adapt the estimate as needed.

This primary hypothesis is supported by the following sub-hypothesis, which reinforces and explores the primary research question.

> **Hypothesis 1.1:** A state estimator's reliability is a function of a set number of quantifiable influencing-factors.

Additionally, the hypothesis for the RSO-based optical navigation case study explored in this research is as follows:

> **Hypothesis 2:** A spacecraft's state, including both attitude and position, can be estimated using RSO detections from a commercial star tracker.

1.4 Research Contributions

This dissertation makes several key contributions to the fields of estimation and space systems reliability, as well as to spacecraft state estimation. The contributions from this research are listed below:

Contribution 1: Developed a covariance trust metric which can quantitatively assess the reliability of a Kalman filter;

Contribution 2: Explored and quantified the effect of various factors that affect the performance and reliability of a Kalman filter;

Contribution 3: Developed an RSO-based optical navigation method that demonstrates that RSO-based optical navigation is feasible for an Earth-orbiting observing spacecraft detecting RSOs orbiting Earth. This feasibility is demonstrated using the above-mentioned covariance trust metric.

1.5 Dissertation Outline

This dissertation presents the results of a research program designed to study the feasibility of optical navigation using RSOs in Earth orbit for spacecraft state estimation, the factors that affect the trustworthiness of this navigation estimator, and how estimate trustworthiness can be quantified. Chapter 2 provides the background and a review of relevant literature to this study, while Ch. 3 and 4 examine the feasibility of estimating an observer's state using optical RSO measurements and range-based RSO measurements respectively. Chapter 5 uses the navigation methods presented in the previous chapters to explore the factors that affect estimator reliability and how an estimator's reliability can be quantified. Finally, Ch. 6 summarizes and discusses the results of this research, its contributions, and potential future research.

Chapter 2

Background and Literature Review

II

"Knowledge = power = energy = matter = mass; a good bookshop is just a genteel Black Hole that knows how to read."

Terry Pratchett, *Guards! Guards!*, 1989.

Chapter 2 provides a literature review and background information in several relevant areas to this dissertation's research into estimator reliability and RSO-based optical navigation. Section 2.1 provides background and literature related to my first hypothesis, including methods of measuring estimator reliability using the estimator's intrinsic parameters and methods of ensuring estimator reliability using extrinsic factors such as design heritage and software encapsulation. Section 2.2 provides a literature review for my second hypothesis, investigating if a spacecraft's state can be estimated using RSO detections. This section reviews various methods of spacecraft navigation using optical measurement sources. Afterwards, Sec. 2.3 provides background information relevant to this dissertation, including an overview of several estimators as well as the NEES and NIS reliability metrics. This is followed by a review of various optical and range-based sensors that can be used for RSO detection. The chapter concludes by summarizing how this dissertation relates to previous works.

2.1 Estimators and Estimator Reliability

This section discusses the various methods for assessing and ensuring estimator reliability present in the literature to help investigate Hypothesis 1 and Hypothesis 1.1:

> **Hypothesis 1** Estimator confidence can be determined and parameterized to characterize the reliability of a state estimate and reject or adapt the estimate as needed.
>
> **Hypothesis 1.1:** A state estimator's reliability is a function of a set number of quantifiable influencing-factors.

The section first provides a review of intrinsic reliability methods that use an estimator's internal variables to assess its performance. This is followed by a review of extrinsic reliability methods that are separate from the estimator itself.

2.1.1 Intrinsic Methods for Directly Evaluating Estimator Reliability

When developing and implementing an estimator, such as the Kalman filters presented in Sec. 2.3.1, the estimator's accuracy and reliability are both key. Accuracy is fairly straightforward to assess: it is the difference between the estimator's prediction and the true state. While more difficult to define, estimator reliability is often more important than accuracy, as passing unreliable state estimates to other systems or users can have disastrous consequences. As such, numerous methods have been developed to define and assess reliability, including methods which use an estimator's own intrinsic parameters and extrinsic methods that are independent from the system being evaluated. This subsection examines reliability methods that use these intrinsic parameters, while Sec. 2.1.2 examines reliability methods that use extrinsic such as technological maturity or software wrapping.

Evaluating a filter's performance directly can allow the filter to self-assess the reliability of its estimates [18], allow a designer to select estimator parameters for optimal performance [16], or directly detect anomalies rather than relying on external methods [19]. Fortunately, the Kalman Filter and related estimators include an intrinsic parameter that is very useful for reliability predictions: the state covariance estimate P_k. For an optimal filter, this covariance

is exact, meaning that P_k is directly related to the difference between the true state X_k^{true} and the filter's state estimate X_k^{est}:

$$P_k = \mathbb{E}\left[(X_k^{true} - X_k^{est})(X_k^{true} - X_k^{est})^T\right] \tag{2.1}$$

While Eq. 2.1 is only true for optimal filters, such as the Kalman Filter when estimating a system with linear dynamics, linear measurements, and white noises, this equation can still be used by reliability metrics to provide insight into the performance of even non-optimal filters.

There are several established methods in the literature for evaluating an estimator's reliability using the estimator variables themselves [33]. These metrics include the Mahalanobis Distance, Normalized Estimate Error Squared (NEES) and Normalized Innovation Squared (NIS) [34, 16, 18]. The Mahalanobis Distance describes the normalized distance between a state estimate X_k^{est} with an associated state covariance estimate P_k and the true state X_k^{true} with an associated covariance P^{true} as follows [34]:

$$d_{M,k}^2 = (X_k^{true} - X_k^{est})(P_k + P_k^{true})^{-1}(X_k^{true} - X_k^{est})^T \tag{2.2}$$

where P_k^{true} is often assumed to be zero for systems with known true states. In addition to filtering applications [35], the Mahalnobis Distance is a common metric used in Space Situational Awareness for covariance realism [36, 37].

NEES and NIS both build on the Mahalanobis Distance [38] by using a combination of Monte Carlo Simulations and χ^2 tests [20] to reduce stochastic variations while analyzing a filter's performance. NEES compares a filter's state covariance estimates to the filter's true state covariances. NEES provides a direct measure of a filter's optimality but, as NEES uses a system's true state in developing the NEES statistics, this metric is limited to verifying simulations or scenarios where high-accuracy truth data is available.

In contrast, NIS compares a filter's measurement innovation covariances to the filter's true measurement covariances and does not require truth data. However this disconnect means that, while NIS can provide insight into the quality of measurements and the filter's measurement model, NIS does not directly assess the optimality of a filter's state estimates.

Additionally, while NIS does not require truth data, NIS still requires Monte Carlo simulations, making NIS impractical to run outside of simulations [20]. Both NEES and NIS require Monte Carlo simulations to create sufficient data at each timestep to perform their χ^2 analyses. These simulations can make both NEES and NIS unwieldy to use, especially when testing multiple filter configurations or tuning parameters (such as this dissertation does in Ch. 5). While the Mahalanobis Distance does not require Monte Carlo simulations, the Mahalanobis Distance metric can vary due to process and measurement noises, which makes it more difficult to use in stochastic systems. To further complicate their use, the Mahalanobis Distance, NEES and NIS produce a single metric at each timestep. While this lack of granularity can make it difficult for a designer to determine how individual state elements are performing, these singular values can be used as cost functions. The lack of granularity and reliance on Monte Carlo simulations motivated me to develop the covariance trust metric presented in Ch. 5 of this dissertation.

In addition to their utility in assessing filter reliability, both NEES and NIS can be used to quantify filter performance for optimization purposes. Chen *et al.* used NEES [16] and NIS [25] to evaluate the performance of an Unscented Kalman Filter (UKF). While this dissertation focuses on ensuring reliability, their focus was on using NEES and NIS as cost functions for a Bayesian Optimizer. They used this optimizer to tune the UKF tuning parameters of a line-following robot [16] and an aero-robotic Skycrane landing system [25].

Similar to this dissertation, Gibbs investigated the reliability of Kalman filters [19] . However, while this dissertation focuses on quantifying the reliability of the filter's state estimates, Gibbs focused on the reliability of the filter's measurements, developing three tests to detect observation outliers and filter inconsistencies caused by modelling errors, non-white measurement noises, and improperly sized measurement noises [19]. Griebel *et al.* also developed a method for evaluating Kalman filters using the filter's measurements [18]. Griebel *et al.* used subjective logic to compare the statistical distributions of measurements and measurement innovations to a Kalman filter's statistical assumptions. Using this method, Griebel *et al.* were able to assess a Kalman filter's online performance [18].

Gamse *et al.* proposed a methodology for ensuring a Kalman filter's reliability using several existing assessment methods, including controllability, observability, the state transition

matrix determinant, and the square roots of the state covariance estimate [33]. I explored several factors that Gamse *et al.* do not examine while investigating Hypothesis 1.1, including the effects of filter variants, estimating elements of the measurement-source state in the filter, how the process noise is modelled, and measurement linearity.

2.1.2 Extrinsic Methods for Ensuring Estimator Reliability

This section examines extrinsic methods for determining an estimator's reliability. Unlike intrinsic reliability methods, these extrinsic methods are not dependent on the estimator or the estimator's intrinsic parameters like covariance or measurement innovation. Instead, these extrinsic reliability methods examine factors such as the estimator's level of technological development [1] or establish mechanisms and procedures to identify when the estimator produces poor results and to intercede before these poor estimates are used [10].

There are various methods for ensuring an estimator produces outputs that are robust to external factors and will not harm their parent systems. These methods are especially important in the space industry, which is highly reluctant to use any technology that does not have significant flight heritage, due to the extreme costs associated with spacecraft development [39]. In the 1970s, NASA defined the Technology Readiness Level (TRL) method [1] for assessing the maturity of a given technology, including software and physical hardware from the component to spacecraft level. The current NASA TRL scale, shown in Table 2.1, allows managers and technology users to assess the risks associated with incorporating a given technology in their prospective mission. NASA typically requires a TRL of at least 6 before a technology can be integrated into a systems engineering process [1]. The RSO-based navigation case study presented in this dissertation is an example of a technology which is low on the TRL scale. Presently, this case study is somewhere between TRL 2 and 3. Demonstrating the reliability of this method, and those like it, is critical for the method to be advanced further up the TRL scale towards an eventual implementation on an actual system.

Software containing complex functionality or being of uncertain origin, such as the RSO-navigation method presented in later chapters, is referred to as SOUP: "Software Of Unknown Pedigree," or "Software Of Uncertain Provenance" [40]. In safety-related or high-reliability

Table 2.1: NASA Technology Readiness Level (TRL) definitions [1].

TRL Level	Description
1	"Basic principles observed and reported"
2	"Technology concept and/or application formulated"
3	"Analytical and experimental critical function and/or characteristic proof-of-concept"
4	"Component and/or breadboard validation in laboratory environment"
5	"Component and/or breadboard validation in relevant environment"
6	"System/subsystem model or prototype demonstration in a relevant environment (ground or space)"
7	"System prototype demonstration in a target/space environment"
8	"Actual system completed and 'flight qualified' through test and demonstration (ground or flight)"
9	"Actual system 'flight proven' through successful mission operations"

applications, where the software development processes, methodologies, and safety-related properties are paramount, ensuring the reliability of SOUP is critical. However, it remains difficult to fully verify complex functions such as stochastic nonlinear filtering applications using traditional test methods, which inhibit their use in mission-critical space systems [41]. Several methods have been developed to ensure that this type of software is reliable in the healthcare and unmanned aviation industries [40, 42, 43].

Many methods of increasing the reliability of SOUP are programmatic in nature; authors such as Cook *et al.* and Oliveira *et al.* have proposed managerial frameworks including planning, code reviews, training, and documentation [42, 43]. However, these methods cannot anticipate all potential software failure modes for complex functions, which necessitates monitoring software to encapsulate their code. Such encapsulation, also referred to as wrapper software, isolates the high-risk function from the rest of the system to ensure that unreliable outputs are caught before being propagated. NASA has recommended wrappers as one method of risk mitigation, but has not provided specific standards on their use [44].

Fortunately, ASTM (formerly known as the American Society for Testing and Materials) has developed a standard for safely using SOUP in safety-critical roles: *ASTM F3269-17: Standard Practice for Methods to Safely Bound Flight Behavior of Unmanned Aircraft Systems Containing Complex Functions* [10]. This standard proposes pairing high-risk software with a

monitoring watchdog and a recovery control function. In this setup, as seen in Fig. 2.1, the non-pedigreed complex function works in parallel to one or more recovery control functions to carry out the same task. These recovery control functions perform the same tasks as the complex function but are well understood, heavily tested, and are less risky than the complex function. However, the increased reliability of the recovery control functions come at the cost of reduced capabilities, poorer performance, or lower accuracy (hence the desire to use the complex function). The safety monitor observes the system's state and, if the complex function exceeds preset limits, the safety monitor commands the run-time assurance architecture (RTA) switch to send the recovery control function output to the user. This system allows the complex SOUP function to be utilized, while greatly reducing the risk of a failure being passed on to other systems.

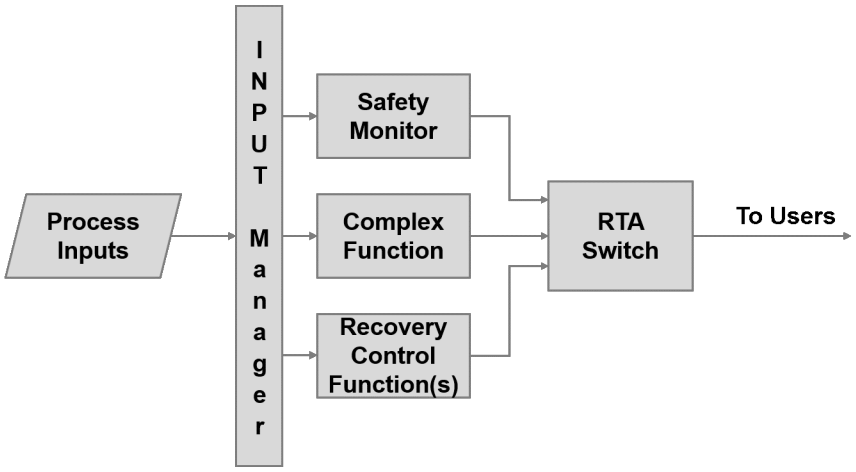

Fig. 2.1: Functional components of a system running an ASTM F3269-17 run-time assurance architecture [10].

By implementing similar safety monitoring methods, space systems can more readily adopt complex functions, such as nonlinear estimators, without adding undue risks to a project. However, safety monitoring methods like ASTM F3269-17 require methods of measuring the reliability of an estimate that an RTA switch can use to select between the complex function and recovery control functions. Applications such as RTA switching are an excellent example where intrinsic and extrinsic reliability methods can be paired to produce better, more reliable estimators [45].

2.1.3 Relation to Hypothesis 1

This subsection briefly summarizes the relationship between the literature described in Sec. 2.1 and Hypotheses 1 and 1.1.

Hypothesis 1 There are existing methods to determine and parameterize the reliability of a state estimate. However these methods have weaknesses that can be improved upon. Geometric reliability methods such as GDOP [17] are excellent for highly characterized systems such as GPS but cannot be generalized for broader estimation applications. Metrics that use an estimator's measurement innovation, such as NIS [20], subjective logic [18], and residual tests [19], can provide insight into the quality of measurements, detect measurement outliers, and identify issues with a filter's measurement model. However, these measurement innovation-based metrics do not directly assess the optimality of a filter's state estimates or state covariance estimates. Methods that do directly evaluate the state covariance estimates, namely NEES, require access to truth data. Additionally, NEES, NIS, and related methods require Monte Carlo simulations which can be time consuming, especially when testing multiple filter configurations and model parameters. This dissertation built on previous reliability assessment metrics by developing a new reliability metric which can be used to evaluate an estimator's state covariance estimate without requiring Monte Carlo simulations. By removing the need for Monte Carlo simulations, researchers and engineers can test filters more quickly, enabling more rapid testing, or more thorough testing in the same time-span as the existing NEES test.

Hypothesis 1.1 There has not been much systematic research into the factors that affect an estimator's reliability. Gamse *et al.* [33] explored several parameters, including controllability, observability, the state transition matrix determinant, and the square roots of the state covariance estimate. This dissertation builds on Gamse *et al.*'s work by examining additional factors including the effects of filter variants, estimating elements of the measurement-source's state in the filter, how the process noise is modelled, and measurement linearity.

2.2 Spacecraft Navigation Using RSO Detections

Optical navigation refers to methods of using images of celestial bodies such as planets, moons, and other landmarks to determine a spacecraft's orbital position. This section discusses the various optical navigation methods for spacecraft present in the literature to help investigate Hypothesis 2:

> **Hypothesis 2:** A spacecraft's state, including both attitude and position, can be estimated using RSO detections from a commercial star tracker.

Various forms of optical navigation have been used or proposed for many interplanetary [46, 47], lunar [48, 49, 50], and other [51, 52] exploratory missions since the Apollo program. Other work [13, 53] has examined optical navigation techniques for rendezvous and docking applications, where the observing spacecraft is in close proximity to an observed-object. Optical navigation techniques have used various sensors, including custom designs such as VISNAV [53], the mid-range optical state estimation camera proposed by Alfonso *et al.* [54], or the Apollo space sextant [50]. Dual-purpose science cameras such as those on Voyager 2 [46] and New Horizons [51], as well as wide field of view star trackers [47], have also been used or proposed for navigation as well. Enright *et al.* [47] investigated using detections of Mars and its moons to estimate the trajectory of a spacecraft performing an Earth-Mars transfer.

Optical navigation is typically used for spacecraft outside of Earth orbit. However, Hu *et al.* [55] explored the feasibility of using optical navigation for orbital estimation in Low Earth Orbit (LEO): examining how an observing spacecraft could use optical sightings of a reference satellite in geostationary orbit to estimate the observer's state using a batched least-squares estimator. While Hu *et al.* [55] bring credence to the concept of RSO-based navigation techniques, they did not examine potential imaging sensors, observations of multiple objects or objects outside of Geostationary Earth Orbit (GEO), or the numerical sensitivities associated with navigating using objects at varying distances. My own research [56, 57] has filled these gaps in Hu's previous work and has investigated various other factors affecting the feasibility of RSO-based optical navigation, including observability, measurement precision, and RSO brightness. This research will be described in detail in the following chapter.

2.2.1 Relation to Hypothesis 2

As explored in Sec. 2.2, optical navigation methods are an active field of research. While much of this research focuses on close proximity navigation [13, 53, 54] some researchers such as Enright *et al.* [3] and Hu *et al.* [55] have explored optical navigation using navigational targets at greater distances. Hu *et al.* specifically examined using GEO spacecraft as navigational targets. However, Hu *et al.* did not examine the various factors that will affect the feasibility of RSO-based optical navigation. This dissertation builds on Hu's work by examining various factors affecting the feasibility of using RSOs as navigational targets, including measurement observability, measurement precision, tracking errors, and RSO brightness.

2.3 Background

This section provides a brief overview of several topics relevant to this dissertation, including the Kalman Filter [21], Extended Kalman Filter (EKF) [22], and Unscented Kalman Filter (UKF) [23] as well as a review of the NEES and NIS reliability assessment metrics [20]. Afterwards, this section provides background information on various optical and range-based sensors that can be used for RSO detection.

2.3.1 Estimators

The Kalman Filter [21] and its variants are a widely used set of estimation methods, used across industries [11, 12, 13] to predict a system's state using measurements and knowledge of the system's dynamics. The following paragraphs provide an overview of the discretized versions of the Kalman Filter, Extended Kalman Filter, and Unscented Kalman Filter. Note that continuous versions of these filters have been developed [58, 59, 60] but, for brevity, these variants are not presented here.

The Kalman Filter The Kalman Filter is used to predict the current state X_k of a linear system using linear measurements z_k at each timestep k such that

$$X_k = \Phi X_{k-1} + B_k u_k + w_k \tag{2.3}$$

where Φ is the system's discretized state transition model, B_k is the discretized control input model, u_k is the control input, and w_k is the process noise. The system's measurements are made such that

$$z_k = H_k X_k + v_k \tag{2.4}$$

where H_k is the observation model and v_k is the measurement noise.

The discrete Kalman Filter is typically separated into an *a priori* or predictive phase and an *a posteriori* or update phase. During the *a priori* phase, the filter estimates the system's state $\hat{X}_{k|k-1}$ and state estimate covariance $\hat{P}_{k|k-1}$ at the current timestep k. These estimates are calculated using the *a posteriori* state estimate $\hat{X}_{k-1|k-1}$ and state covariance estimate $P_{k-1|k-1}$ from the previous timestep $k-1$ and propagated forward in time using the known state dynamics of Eq. 2.3 [21]:

$$\hat{X}_{k|k-1} = \Phi \hat{X}_{k-1|k-1} + B_k u_k \tag{2.5}$$

and

$$\hat{P}_{k|k-1} = \Phi P_{k-1|k-1} \Phi^T + Q_k \tag{2.6}$$

where $Q_k = \mathbb{E}[w_k w_k^T]$ is the process noise covariance.

Next, during the *a posteriori* phase, the filter incorporates measurement knowledge into its estimate. First, the filter calculates the measurement innovation $\tilde{y}_k$: the difference between the measurement z_k and the filter's prediction of the expected measurement [21].

$$\tilde{y}_k = z_k - H_k \hat{X}_{k|k-1} \tag{2.7}$$

The filter then calculates the measurement innovation covariance [21]:

$$S_k = H_k \hat{P}_{k|k-1} H_k^T + R_k \tag{2.8}$$

which is used to find the Kalman gain K_k [21]:

$$K_k = \hat{P}_{k|k-1} H_k^T S_k^{-1} \tag{2.9}$$

where $R_k = \mathbb{E}[v_k v_k^T]$ is the measurement noise covariance. The filter then updates the state estimate $X_{k|k}$ and state covariance estimate $P_{k|k}$ using the Kalman gain and the filter's *a priori* predictions [21]:

$$X_{k|k} = \hat{X}_{k|k-1} + K_k \tilde{y}_k \tag{2.10}$$

and

$$P_{k|k} = (I - K_k H_k)\hat{P}_{k|k-1} \tag{2.11}$$

If the process noise w_k and measurement noise v_k are white noises, and if the state and measurement dynamics are truly linear, per Eq. 2.3, then the Kalman Filter will be an optimal filter. This optimality means that the Kalman Filter's predicted state estimate covariance should be the actual covariance of the estimator error [21].

Extended Kalman Filter The Extended Kalman Filter [22] is a nonlinear extension of the Kalman Filter[1], designed to allow the filter to estimate the states of systems with nonlinear state or measurement dynamics. For these systems, the state X_k dynamics can be expressed as:

$$X_k = f(X_{k-1}, u_k) + w_k \tag{2.12}$$

where the current state X_k is some function f of the state at the previous timestep X_{k-1} and control input u_k plus the process noise w_k. Similarly, the measurement dynamics are expressed as:

$$z_k = h(X_k) + v_k \tag{2.13}$$

where the current measurement z_k is some function h of the system's state X_k plus the measurement noise v_k. The EKF uses the same equations as the Kalman Filter, shown previously in Eq. 2.5-2.11. However, the EKF uses linear approximations of the state transition matrix Φ and the observation model H_k using the following Jacobians [22]:

[1]Nonlinear in the sense that the EKF does not require linear state or measurement dynamics. The EKF retains the Kalman Filter's linear Kalman Gain function.

$$\Phi = \left.\frac{\partial f}{\partial X}\right|_{(\hat{X}_{k-1|k-1}, u_k)} \tag{2.14}$$

and

$$H_k = \left.\frac{\partial h}{\partial X}\right|_{\hat{X}_{k|k-1}} \tag{2.15}$$

Note that if the EKF is used with nonlinear state and measurement dynamics, it is not an optimal filter [8]. This non-optimality means that the filter's state covariance estimate is not an exact match to the true state covariance. The extent of this mismatch will vary, depending on how nonlinear the state and measurement dynamics are and how non-white the process and measurement noises are. Additionally, the timestep size will also affect the degree of non-optimality. As the timestep size approaches zero, so will the difference between the true dynamics and their Jacobian-based approximations and the filter will approach an optimal solution.

Unscented Kalman Filter The Unscented Kalman Filter [23] is another extension of the Kalman Filter for nonlinear systems[2]. Like the EKF, the UKF is used to estimate the states of systems with nonlinear dynamics or nonlinear measurements, as previously described in Eq. 2.12 and 2.13. However, unlike the EKF, the UKF does not linearize any part of the system and is better suited to highly nonlinear models [61]. Instead of linearizing the system, the UKF propagates a set of sample points, known as sigma points, and derives new mean and covariance estimates from these propagated sigma points [62].

To use the UKF, the user first calculates the following weights [62]:

$$W_0^m = \lambda/(L+\lambda) \tag{2.16}$$

$$W_0^c = \lambda/(L+\lambda) + (1-\alpha^2+\beta) \tag{2.17}$$

$$W_i^m = W_i^c = (2(L+\lambda))^{-1} \tag{2.18}$$

[2]As with the EKF, the UKF is a nonlinear filter, as the UKF does not require linear state or measurement dynamics. However, the UKF also retains the Kalman Filter's linear Kalman Gain function.

for $i = 0,...2L$, where L is the number of elements in the state vector X, $\lambda = \alpha^2(L + \kappa) - L$, and α, β, and κ are the UKF tuning parameters. The α and κ parameters control the spread of the sigma points around the mean sigma value while β controls the sigma point distribution. Wan and van der Merwe recommend $10^{-5} \leq \alpha \leq 1$, $\kappa = 0$, and, for Gaussian distributions, $\beta = 2$ [62].

The sigma points χ_{k-1} are calculated using L, λ, the previous state estimate $\hat{X}_{k-1}$, and the previous state covariance estimate P_{k-1} [62]:

$$\chi_{k-1} = \begin{bmatrix} \hat{X}_{k-1} & \hat{X}_{k-1} \pm \sqrt{(L+\lambda)P_{k-1}} \end{bmatrix} \tag{2.19}$$

The sigma points are then propagated forward to the current timestep using the state transition function f [62]:

$$\chi_{k|k-1} = f(\chi_{k-1}) \tag{2.20}$$

and the mean *a priori* state estimate $\hat{X}_k^-$ is calculated as [62]:

$$\hat{X}_k^- = \sum_{n=0}^{2L} W_i^m \chi_{i,k|k-1} \tag{2.21}$$

The mean *a priori* state estimate $\hat{X}_k^-$, propagated sigma points $\chi_{k|k-1}$, and the process noise covariance Q_k are then used to calculate the *a priori* state covariance estimate [62]:

$$P_k^- = \sum_{n=0}^{2L} W_i^c \left[\chi_{i,k|k-1} - \hat{X}_k^-\right]\left[\chi_{i,k|k-1} - \hat{X}_k^-\right]^T + Q_k \tag{2.22}$$

The measurement sigma points $\mathcal{Y}_{k|k-1}$ are then calculated as [62]:

$$\mathcal{Y}_{k|k-1} = h(\chi_{k|k-1}) \tag{2.23}$$

Using the measurement sigma points and the measurement noise covariance R_k, the measurement sigma mean $\hat{y}_k^-$ and measurement covariance $P_{\hat{y}_k\hat{y}_k}$ are calculated as [62]:

$$\hat{y}_k^- = \sum_{n=0}^{2L} W_i^m \mathcal{Y}_{i,k|k-1} \tag{2.24}$$

and

$$P_{\hat{y}_k\hat{y}_k} = \sum_{n=0}^{2L} W_i^c \Big[\mathcal{Y}_{i,k|k-1} - \hat{y}_k^-\Big]\Big[\mathcal{Y}_{i,k|k-1} - \hat{y}_k^-\Big]^T + R_k \tag{2.25}$$

The cross covariance $P_{\hat{X}_k\hat{y}_k}$ is calculated as [62]:

$$P_{\hat{X}_k\hat{y}_k} = \sum_{n=0}^{2L} W_i^c \Big[\chi_{i,k|k-1} - \hat{X}_k^-\Big]\Big[\mathcal{Y}_{i,k|k-1} - \hat{y}_k^-\Big]^T \tag{2.26}$$

and then used to derive the Kalman gain K_k [62]:

$$K_k = P_{\hat{X}_k\hat{y}_k} P_{\hat{y}_k\hat{y}_k}^{-1} \tag{2.27}$$

Finally, the Kalman gain K_k and measurements y_k are used to update the state estimate $\hat{X}_k$ and the state covariance estimate P_k [62]:

$$\hat{X}_k = \hat{X}_k^- + K_k(y_k - \hat{y}_k^-) \tag{2.28}$$

and

$$P_k = P_k^- - K_k P_{\hat{y}_k\hat{y}_k} K_k^T \tag{2.29}$$

While the UKF does not use the same linearizations as the EKF, the UKF is not an optimal filter and so the filter's state covariance estimate is not an exact match to the true state covariance. The UKF's non-optimality, and its performance compared to the EKF, will vary depending on the state and measurement dynamics, timestep size, and the statistical distributions of noises. I examine how these factors affect the performance of both the EKF and UKF in Ch. 5.

2.3.2 NEES and NIS

NEES and NIS are used later in this dissertation to compare against the new trust evaluation method presented in Ch. 5, because they are considered to be the classical estimator reliability assessment methods [18]. The Mahalanobis Distance metric is not used, as it is very similar to NEES but is calculated using data from a single timestep, which makes the Mahalanobis Distance significantly more variable than NEES.

Both NEES and NIS function by running N independent Monte Carlo simulations of an estimator, including the underlying dynamics and measurement models. Using these simulations, three sets of test statistics are created: one for each timestep of each individual Monte Carlo simulation, the average Monte Carlo statistic for each timestep, and an 'average of averages' statistic across all Monte Carlo simulations and all timesteps. These statistics are then compared to expected two sided probability regions to determine if the results fall within their expected bounds.

NEES compares a filter's state covariance estimate P_k with the estimate error e_k between the estimated state X_k^{est} and true state X_k^{true} at every timestep k.

$$e_k \triangleq X_k^{true} - X_k^{est} \tag{2.30}$$

Note that NEES can only be conducted when the system's true state X^{true} is known. This generally restricts NEES to assessing simulation performances and laboratory tests where high-fidelity truth data is available [16]. Using the estimate error and state covariance estimate, the NEES parameter ϵ_k^i is calculated for each Monte Carlo instance i at each timestep k as [20]:

$$\epsilon_k^i = e_{k,i}^T P_{k,i}^{-1} e_{k,i} \tag{2.31}$$

where $e_{k,i}$ and $P_{k,i}$ are the estimate error and state covariance estimate at timestep k for Monte Carlo Simulation i. For a single Monte Carlo simulation, ϵ_k^i is equivalent to the Mahalanobis Distance. NIS compares a filter's measurement innovation covariance S_k with the filter's measurement innovation $\tilde{y}_k$: the difference between the measurements z_k and the filter's predicted measurements $H\hat{X}_k$.

$$\tilde{y}_k = z_k - H\hat{X}_k \tag{2.32}$$

As NIS does not rely on the true state, NIS can be performed on estimators implemented in the real world. However, NIS still requires Monte Carlo simulations or multiple parallel filter implementations, which can make the method difficult to implement outside of a laboratory

environment. The NIS parameter $\epsilon^i_{\nu,k}$ is calculated for each Monte Carlo instance i at each timestep k as [20]:

$$\epsilon^i_{\nu,k} = \tilde{y}^T_{k,i} S^{-1}_{k,i} \tilde{y}_{k,i} \tag{2.33}$$

where $\tilde{y}_{k,i}$ and $S_{k,i}$ are the measurement innovation and measurement innovation covariance at timestep k for Monte Carlo Simulation i.

For an ideal system, in which P_k and S_k perfectly model the state and measurement uncertainties respectively (*i.e.* $P_k = e_k e_k^T$ and $S_k = \tilde{y}_k \tilde{y}_k^T$), ϵ^i_k and $\epsilon^i_{\nu,k}$ will be equal to the number of state elements n_X and the number of measurement sources n_z respectively [20]. However, due to random variability in noise sources, individual ϵ^i_k and $\epsilon^i_{\nu,k}$ values may vary significantly from these ideal values.

For a non-optimal system, the state covariance estimate will not be equal to the true state estimate covariance (*i.e.* $P_k \neq e_k e_k^T$) and so the NEES statistic ϵ^i_k will not be equal to the number of state elements n_X. Similarly, the NIS statistic $\epsilon^i_{\nu,k}$ will not be equal to the number of state elements n_z. If the estimator is overly conservative and produces a state covariance estimate P_k that is greater than the optimal value, the NEES statistic will be less than n_X. Conversely, if the estimator is overly-optimistic and produces a state covariance estimate P_k that is less than than the optimal value, the NEES statistic will be greater than n_X. The same relationship generally applies to the measurement innovation covariance S and the NIS statistic. However, because NIS uses measurements and the measurement innovation to generate its test statistic, rather than measuring P_k and e_k directly, NIS is better suited to detecting nonlinear measurement dynamics or non-white measurement noises [18, 19].

As previously mentioned, individual NIS and NEES statistics will naturally vary from their ideal values due to random Gaussian noise, even for optimally behaving filters. As such, Monte Carlo simulations are key for both NEES and NIS to account for the variability in individual ϵ^i_k and $\epsilon^i_{\nu,k}$ values. By simulating both the underlying dynamic system and the filter N times, the average NEES statistic $\bar{\epsilon}_{\nu,k}$ can be calculated for each timestep k [20]:

$$\bar{\epsilon}_k = \frac{1}{N} \sum_{n=1}^{N} \epsilon^i_k \tag{2.34}$$

where ϵ_k^i is the NEES value for the ith Monte Carlo run. If only a single Monte Carlo run is performed, the average NEES statistic is equivalent to the Mahalanobis Distance. These average NEES statistics are necessary to account for random variability in individual NEES statistics. While an individual ϵ_k^i may deviate from its optimal value of n_X, if P_k is optimal and if each element of e_k is independent and Gaussian-distributed, $\bar{\epsilon}_k$ will be equal to the number of state elements n_X times the number of Monte Carlo simulations N (*i.e.* $\mathbb{E}(\bar{\epsilon}_k) = Nn_X$).

Similarly, the average NIS values $\bar{\epsilon}_{\nu,k}$ for each timestep k are calculated as [20]:

$$\bar{\epsilon}_{\nu,k} = \frac{1}{N}\sum_{n=1}^{N} \epsilon_{\nu,k}^i \tag{2.35}$$

as with $\bar{\epsilon}_k$, for an optimally behaving filter, $\bar{\epsilon}_{\nu,k}$ will be equal to the number of measurement sources n_z times the number of Monte Carlo simulations N (*i.e.* $\mathbb{E}(\bar{\epsilon}_{\nu,k}) = Nn_z$).

Once $\bar{\epsilon}_k$ and $\bar{\epsilon}_{\nu,k}$ have been calculated, they can be compared with two sided NEES and NIS probability regions to determine if the filter's results are near-optimal. The two sided NEES probability region $[\epsilon_1, \epsilon_2]$ is the region in which $1 - Q_\chi$ of all of the NEES estimates $\bar{\epsilon}_k$ should lie (*i.e.* $P(\bar{\epsilon}_k \in [\epsilon_1, \epsilon_2]) = 1 - Q_\chi$), assuming that each of the Nn_X degrees of freedom are independent Gaussian-distributed variables. This probability region can be calculated using the following χ^2 probabilities [20]:

$$\epsilon_1 = \frac{1}{N}\chi^2_{Nn_X}\left(\frac{Q_\chi}{2}\right) \tag{2.36}$$

$$\epsilon_2 = \frac{1}{N}\chi^2_{Nn_X}\left(1 - \frac{Q_\chi}{2}\right) \tag{2.37}$$

where $\chi^2_{Nn_X}(b)$ is a chi-square distribution with the subscript Nn_X denoting the degrees of freedom and the variables within the brackets describing the distribution's tail probability. n_X is the number of state elements, N is the number of Monte Carlo simulations, and Q_χ is the upper tail probability (the likelihood that the distribution is greater than the expectation). Note that the degrees of freedom for conducting χ^2 tests on individual ϵ_k^i statistics is n_X, while the degrees of freedom for conducting χ^2 tests on the time-average NEES statistic $\bar{\epsilon}_{av}$ is NKn_X where K is the total number of timesteps.

Similarly, the two sided NIS probability region $[\epsilon_{\nu 1}, \epsilon_{\nu 2}]$ is the region in which $1 - Q_\chi$ of all NIS estimates $\bar{\epsilon}_{\nu,k}$ should lie (*i.e.* $P(\bar{\epsilon}_{\nu,k} \in [\epsilon_{\nu 1}, \epsilon_{\nu 2}]) = 1 - Q_\chi$), again assuming that each of the Nn_z degrees of freedom are independent Gaussian-distributed variables. This region can be calculated using the following χ^2 probabilities [20]:

$$\epsilon_{\nu 1} = \frac{1}{N}\chi^2_{Nn_z}\left(\frac{Q_\chi}{2}\right) \tag{2.38}$$

$$\epsilon_{\nu 2} = \frac{1}{N}\chi^2_{Nn_z}\left(1 - \frac{Q_\chi}{2}\right) \tag{2.39}$$

where n_z is the number of measurement sources. As with the NEES χ^2 tests, the degrees of freedom for conducting χ^2 tests on individual $\epsilon^i_{\nu,k}$ statistics is n_z, while the degrees of freedom for conducting χ^2 tests on the time-average NIS statistic $\bar{\epsilon}_{\nu av}$ is NKn_z where K is the total number of timesteps.

To evaluate a filter's overall performance across all timesteps, the average NEES value $\bar{\epsilon}_{av}$ and the average NIS value $\bar{\epsilon}_{\nu av}$ can be calculated over the total number of timesteps K:

$$\bar{\epsilon}_{av} = \frac{1}{K}\sum_{i=1}^{K}\bar{\epsilon}_i \tag{2.40}$$

and

$$\bar{\epsilon}_{\nu av} = \frac{1}{K}\sum_{i=1}^{K}\bar{\epsilon}_{\nu,i} \tag{2.41}$$

However, care should be taken when interpreting the average NEES and NIS values as, if either statistic is non-stationary over the simulation, an average NEES or NIS statistic can misrepresent an estimator's behaviour.

While NEES and NIS are effective methods of measuring a filter's trust, these methods have several drawbacks. Both metrics rely on Monte Carlo simulations for creating sufficiently large datasets for analysis [20]. These Monte Carlo simulations can become burdensome, especially if a designer wishes to evaluate multiple filter configurations. Additionally, both metrics provide the user with a single metric at each timestep. This singular value can be beneficial if the metric is being used as a cost function [16]. However, their lack of granularity makes it difficult for a designer to determine how individual state elements are performing.

Additionally, NEES requires knowledge of the true state which limits its use to only evaluation and simulation applications. This is not the case for NIS, but the need for Monte Carlo simulations makes using NIS impractical to run outside of simulations [20].

2.3.3 Navigation Sensors

Spacecraft use a variety of different attitude determination sensors to estimate orbital position, attitude, and attitude rates. Table 2.2 summarizes the most common navigation sensors, the data they provide, and their estimation errors. Typically, no single sensor can fully satisfy a spacecraft's attitude determination needs and so a combination of sensors is used. This section provides a background on various methods of spacecraft navigation using optical and range-based sensors for spacecraft navigation and RSO-detection, including star trackers, global navigation satellite systems, Radar, laser rangefinders, Light Detection and Ranging (LIDAR) devices, and laser communication terminals.

2.3.3.1 Star Trackers

Star trackers are traditionally used to estimate a spacecraft's attitude. These sensors consist of several hardware subsystems, typically separated into two segments: the camera head unit (CHU) and the data processing unit (DPU). The CHU can be further segmented into the lens assembly, imaging sensor, and baffle. These sensors estimate a spacecraft's attitude by focusing star light through the lens assembly onto the imaging sensor to form a digital image. The baffle reduces image blooming from stray light sources such as the sun or moon. The DPU processes this image, filtering out background noise, stray light, and radiation effects. Stars with a brightness below a certain level, referred to as a cut-off visual magnitude [72], are also removed from the image. These stars are removed because using dim stars decreases accuracy, requires more memory, increases the number of false star matches, and makes the star tracker more susceptible to noise [73]. After the DPU processes the image, the positions of remaining potential guide stars are centroided and correlated to the star tracker's onboard star catalogue [74].

During star correlation, difficulties may arise due to false positives caused by RSOs, hot

Table 2.2: Spacecraft navigation sensor summaries.

Sensor	Data Provided	Error	Notes
Magnetometer	Position and attitude	Angle: 5 degrees (3σ) [63] Angular Rate: 0.003 deg/s (3σ) [63] Position: 4-8 km [30]	Functional only near planets/bodies with a magnetic field. Estimates require a stable, well mapped magnetic field.
Star Tracker	Attitude only	5 Arcseconds (RMS) [64, 65]	
Sun Sensor	Attitude only	0.1 degrees (RMS) [64, 66]	Functional only in sunlight.
Earth Limb Sensor	Attitude only	0.25 degrees [64]	Functional only when facing the Earth, in Earth orbit.
GPS	Position and Attitude	1.5 m (1σ) [67]	Susceptible to jamming spoofing attacks[68, 69]
Ground Based Laser Range Finding	Position only	$<$ 1 cm (RMS) [70]	Requires substantial ground-based infrastructure.
Ground Based Optical Range Finding	Position only	1 km [71]	Dependent on the satellite's optical properties, orbit, and size.

spots on the imaging sensor, or uncatalogued stars. Similarly, false negatives may be caused by obstructed stars in the sensor's star field image [75]. As such, star matching algorithms must compensate for these factors to reliably match star field images to the star catalogue. As the RSO population increases, star trackers have been forced to implement increasingly sophisticated RSO rejection algorithms. These algorithms attempt to identify and actively reject non-star images prior to forwarding the starfield image to the guide star catalogue correlator for identification [74]. Recent research by York University and Magellan Aerospace [76] has made progress towards using these RSO identification algorithms for detecting and cataloguing RSOs.

An accurate RSO catalogue, maintained through a combination of space and ground-based assets, is key to preventing in-orbit collisions with spacecraft. In addition to custom-designed optical and radio-frequency (RF) sensors, several authors have proposed utilizing satellite

star-trackers to serve as RSO detectors in addition to state estimators [76, 77, 78]. Using these sensors, various tracking algorithms are used to estimate the RSOs' orbits and log them into databases [79, 80]. However, these same sensors and methods could be used in reverse to estimate the observer's position based on identifying previously characterized RSOs. Other researchers, such as Enright *et al.* [3] have proposed using star trackers for optical navigation as well: examining how star tracker detections of Mars and its moons can be used to estimate a spacecraft's position during a hyperbolic Mars-approach.

2.3.3.2 Global Navigation Satellite Systems

Global Navigation Satellite Systems (GNSS), such as the Global Positioning System (GPS), Galileo, and the Global Navigation Satellite System (GLONASS), have been developed to provide accurate positional data for users. These systems consist of satellite constellations, with each constituent satellite broadcasting a unique signal which details the satellite's orbital data and the signal's time of transmission. Using these signals from multiple satellites, a receiver calculates its own position by determining the time of flight for each signal.

While GNSS was originally developed for terrestrial applications, signals from GNSS networks such as GPS can be received by spacecraft in LEO. Many LEO satellites include GPS receivers as a part of their attitude and orbit determination systems [81, 67]. Such GPS-equipped satellites can estimate their orbital positions to accuracies of 1.5 m [67]. However, GNSS signals are susceptible to malicious jamming and spoofing attempts, which may result in signal outages over affected regions [68, 69].

2.3.3.3 Radar

Radar can be used to detect objects and estimate their cross sections, as well as their relative distance and velocity from the observer, by transmitting radio frequency pulses and detecting any signals reflected by objects in the radar's field of view. Radar has been used for target position estimation since its inception [82, 83], and numerous ground-based [84, 85] as well as space-based [86] observatories have used radar to track space-based objects.

Space-based radar is not commonly used for RSO detection. However, radar and Synthetic Aperture Radar (SAR) are widely used onboard satellites, such as the Radarsat Constellation

Mission [4], to provide high resolution Earth observation images for various scientific, commercial, and military applications. These SAR images are constructed by moving a SAR antenna over a target. Another variant, Inverse Synthetic Aperture Radar (ISAR) works by moving an object in front of a stationary antenna. ISAR applications include RSO tracking using ground-based observers [87]. Researchers have proposed using Earth Observation SAR data to identify and track RSOs [88].

2.3.3.4 Laser Rangefinders and LIDAR Devices

Laser rangefinders and LIDAR devices transmit focused light beams and receive the reflected signals in order to determine the range between the laser-emitter and reflecting object using time of flight methods. While both laser rangefinders and LIDAR devices use this same principle, LIDAR devices include a method (typically mechanical) to scan an area with the laser beam to build a multi-dimensional image [89]. Conversely, laser rangefinders only measure the distance between the rangefinder and the reflecting object.

High-power ground-based laser rangefinders can detect retroreflector-equipped spacecraft at ranges of up to 36000 km [90]. Objects that are not equipped with retroreflectors, such as defunct satellites and rocket bodies, can be detected to distances of up to 3000 km when using these high-power ground-based lasers [90].

Nayak and Udrea [91] explored methods of using spacecraft-mounted laser rangefinders and LIDAR systems to build three-dimensional images of RSOs. Using a $144 \times 86 \times 287$ m elliptical asteroid, a 5 m cubic RSO, and a $5 \times 5 \times 10$ m RSO as candidate targets, Nayak and Udrea investigated the feasibility of mapping each object using observing spacecraft. The researchers were able to produce three-dimensional images of these objects at ranges of 750 m and 250 m for the asteroid and RSOs respectively [91] with predicted estimate errors of less than 1 m. This study used a laser rangefinder with a 3 km maximum range and a Jenoptik scanning LIDAR unit with a 5 km maximum range [91, 92].

While LIDAR devices can scan large areas to sub-meter accuracies [91], these devices typically require complex moving parts to function. These moving parts are a concern for space missions, as they can fail due to the harsh environment and inability to perform maintenance. However, Pollini [89] has demonstrated the use of flash imaging LIDAR devices

for detecting RSOs [89] in space. Unlike conventional LIDAR units, flash imaging LIDAR does not require moving parts and can image their surroundings. The device that Pollini investigated is capable of imaging its surroundings to ranges of up to 1.1 km [89]. This limited range makes Pollini's flash imaging LIDAR device more suitable for applications where an imaging spacecraft is closer to its target, such as rendezvous and docking operations. However, as a technology, flash imaging LIDAR could become an effective RSO-ranging method.

2.3.3.5 Laser Communication Terminals

Laser communication terminals emit and receive focused beams of light that are encoded with communications signals. These devices are becoming a promising means of spacecraft communication, due to their lower mass, greater security, higher data rates, and reduced power consumption when compared to traditional RF devices [93, 94]. Some laser communication terminals, designed to communicate between geostationary and LEO spacecraft, have communications ranges of 45000 km [93]. While laser communication terminals are not designed to act as object-ranging sensors, research has shown that these devices could be used to sense RSOs as a secondary capability [95, 88].

This dissertation examines the feasibility of using several of these sensors for RSO-based navigation. The use of star trackers is examined in Ch. 3 while the use of Radar, laser rangefinders, LIDAR devices, and laser communications terminals are examined in Ch. 4.

2.4 Dissertation Research and Related Works

This section summarizes how the research presented in this dissertation relates to previous works by other researchers. Table 2.3 summarizes how this dissertation relates to the work of other estimator-reliability research while Table 2.4 summarizes how this dissertation relates to other optical navigation research.

Table 2.3: Comparison between other estimator reliability research and this dissertation.

	Chen *et al.* [16, 25]	**Griebel et al.[18]**	**Gibbs[19]**	**Gamse[33]**	**This Dissertation**
Kalman Filter Parameters Assessed	state estimate, measurement estimate, covariances	measurement, measurement covariance	measurement, measurement covariance	state estimate, measurement estimate, covariances	state estimate and state estimate covariance
Developed Tests?	No, but used existing tests	Yes, for measurement reliability	Yes, for measurement anomalies	No, but showed methods of using existing tests systematically to assess filter performance	Yes, for state estimate and state estimate covariance reliability
Investigated Factors Affecting Reliability?	No	Yes, for measurement reliability	No	Numeric factors only	Yes, for state estimate and state estimate covariance reliability

Table 2.4: Comparison between other optical navigation research and this dissertation.

	Enright *et al.*[47]	**Hu *et al.*[55]**	**Clemens[76, 32]**	**This Dissertation**
Optical Navigation	Yes, during Earth-Mars planetary transfer	Yes, spacecraft state estimation using GEO object	No	Yes, spacecraft state estimation in LEO
Measurement Source	Mars, Mars' Moons	GEO Satellite	RSOs	RSOs
Sensor	Star Tracker	Not specified	Star Tracker	Star Tracker

2.4.1 Chapter Summary and Dissertation Structure

This chapter has reviewed the literature, background information, and context necessary for this dissertation's research into estimator reliability and RSO-based optical navigation. The literature review included examining methods for evaluating the reliability of an estimator, existing optical navigation techniques for estimating an observing spacecraft's orbital state, an overview of several Kalman filters, and a review of the optical and range-based sensors available for spacecraft navigation. Chapter 3 uses the information presented in Ch. 2 to assess the feasibility of Research Hypothesis 2, investigating if a spacecraft's state, including both attitude and position, can be estimated using RSO detections from a commercial star tracker. Similarly, Ch. 4 examines the feasibility of using various existing sensors for estimating an observing spacecraft's orbital state using range measurements. Lastly, Ch. 5 uses the estimator reliability research presented in this chapter to assess Hypothesis 1 by examining the factors that affect the reliability of the Kalman filters presented in Chapters 3 and 4.

Chapter 3

Optical Navigation Using Resident Space Objects

III

"With the sextant he made obeisance to the sun-god, he consulted ancient tomes and tables of magic characters, muttered prayers in a strange tongue that sounded like Indexerrorparallaxrefraction, made cabalistic signs on paper, added and carried one, and then, on a piece of holy script called the Grail – I mean, the Chart – he placed his finger on a certain space conspicuous for its blankness and said, "Here we are." When we looked at the blank space and asked, "And where is that?" he answered in the cipher-code of the higher priesthood, "31 -15 – 47 north, 133 – 5 – 30 west." And we said, "Oh," and felt mighty small."

Jack London, *The Cruise of the Snark*, 1911.

3.1 Introduction

This chapter forms a feasibility study assessing Research Hypothesis 2, investigating if a spacecraft's state, including both attitude and position, can be estimated using RSO detections from a commercial star tracker. The following section, 3.2, presents the simplified two-dimensional geometry and measurement model used for this study. Afterwards, Sec. 3.3 explores various error sources and limitations of this system, including numerical precision, TLE/propagator accuracy, and RSO observability. Sec. 3.4 describes the design and simulation results of an EKF and an UKF used to predict the spacecraft's state using the models presented in Sec. 3.2. Sec. 3.5 discusses the results of these simulations and Sec.

3.6 provides the chapter's summary.

The contents of this chapter have been published in Driedger, Matthew, Rososhansky, Michael and Ferguson, Philip, "Unscented Kalman filter based method for spacecraft navigation using resident space objects," *Aerospace Systems*, vol. 3, pp. 197-205, 2020 as well as in Driedger, Matthew and Ferguson, Philip, "Feasibility Study of an Orbital Navigation Filter Using Resident Space Object Observations," *Journal of Guidance, Control, and Dynamics*, vol. 44, no. 3, pp. 622-628, 2021. Reproduced with permission from Springer Nature and the American Institute of Aeronautics and Astronautics respectively.

3.2 Problem Formulation

To assess Research Hypothesis 2, I used a simplified two-dimensional model of an observing satellite detecting various objects, representing RSOs and stars, with a goal of estimating its pointing orientation and inertial position. As discussed in Ch. 2, star trackers are normally used for only attitude (pointing) estimation. However, a star tracker observing nearby space objects may be capable of estimating its position as well.

The observing spacecraft measures the relative angle θ between its camera's bore axis and the line of sight vector from the observing spacecraft's internal reference frame and the observed object. The measurement angle θ is analogous to what we would obtain from a star tracker. However, for simplicity, I have assumed that this angle has been derived from the position of a centroided image on an imaging plane already. Using these measurements, the observing spacecraft attempts to estimate its position, attitude, and rates. The geometry of this observer-object relationship is shown in Fig. 3.1.

The observer has a position of $r = [x, y]^T$ in an Earth-centric inertial Cartesian coordinate system and a pointing angle ϕ between its body frame and inertial frame x axes. The observer uses a star tracker to measure the relative angle θ between the star tracker's bore axis and the line of sight vector between the observing spacecraft's inertial reference frame and the observed object. I assume that the observing spacecraft knows the position of the observed objects

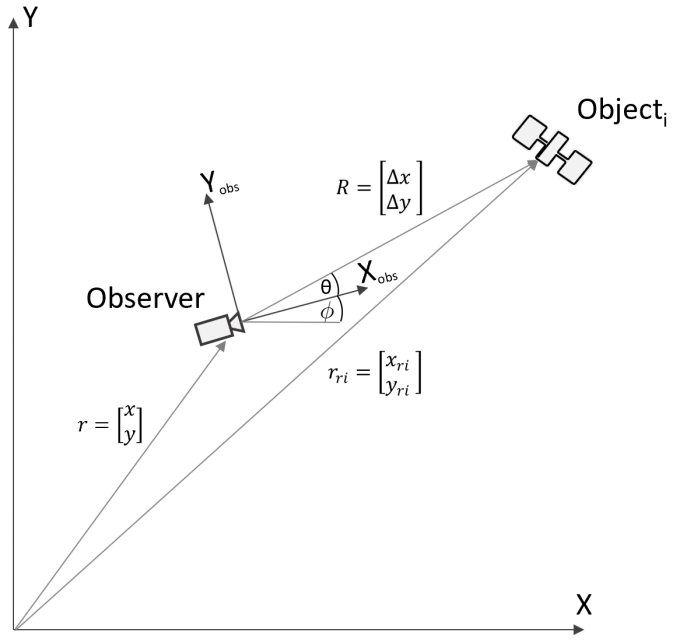

Fig. 3.1: An observing spacecraft (Observer) with a camera measuring the angle θ between the camera's bore axis and the line of sight vector $[\Delta x,\, \Delta y]^T$ between the observing spacecraft's internal reference frame and an external observed Object i.

to a certain accuracy (discussed later in Sec. 3.3), by accessing a database of observable objects. The global position of each observed object i is $r_{ri} = [x_{ri}, y_{ri}]^T$ while $R = [\Delta x, \Delta y]^T$ denotes the relative position between the object and observer. The relationship between the measured angle θ and observer-object geometry from Fig. 3.1 can be expressed as:

$$\tan(\theta + \phi) = \frac{\Delta y}{\Delta x} = \frac{y_{ri} - y}{x_{ri} - x} \tag{3.1}$$

This can be rearranged as a function of the observed object and the observer's positions:

$$\theta = \tan^{-1}\left[\frac{y_{ri} - y}{x_{ri} - x}\right] - \phi \tag{3.2}$$

Equation 3.2 is nonlinear, which means that the Kalman Filter cannot use this equation to estimate the observer's state. As discussed in Ch. 2, there are extensions to the Kalman Filter, including the Extended Kalman Filter and Unscented Kalman Filter, which can use angular measurement equations such as Eq. 3.2. However, these extensions are not optimal

filters and so their state covariance estimates may not be an accurate representation of the actual state covariance.

The feasibility study presented in this chapter does not examine the effects of measurement nonlinearities on estimator trust. Instead, this chapter focuses on error sources and limitations of using angle-based RSO measurements for state estimation, including numerical measurement precision, TLE/propagator accuracy, and RSO observability. While the feasibility study presented in this chapter does not explore estimator reliability, this feasibility study confirms that RSO-based optical navigation is a potentially viable method which is worthy of further scrutiny. As such, Ch. 5 uses RSO-based optical navigation as a case study to explore the trustworthiness of estimators using nonlinear measurements such as the one shown in Eq. 3.2.

For this feasibility study, I have chosen to use two translational dimensions and one rotational dimension. These simplifications keep the filter and underlying model clear and understandable, while demonstrating the fundamental feasibility of RSO-based optical navigation. Despite the reduced dimensionality presented here, this feasibility study provides critical insights into the specific challenges of an RSO-based optical navigation method.

3.3 Observability Analysis

To assess the feasibility of estimating a spacecraft's orbital state using RSO detections from a commercial star tracker, this section explores several factors affecting this system's measurement observability. These factors include instantaneous measurement observability, numerical precision as a function of RSO-observer range, TLE/propagator accuracy, and RSO brightness. The following subsections explore each of these factors in turn.

3.3.1 Measurement Observability and H Invertibility

It is well-understood in the field of estimation that instantaneous measurement observability can be described by the invertibility of $H^T H$ [96]. To explore the measurement observability of a combined position and attitude estimator, I first examined a reduced state vector X, comprised of the observing spacecraft's x position and ϕ attitude, and the associated

linearized observation matrix H using a collection of RSO and star measurements. I derived H, using one star measurement and one RSO measurement, as:

$$H = \begin{bmatrix} \frac{\partial \theta_i}{\partial x} & \frac{\partial \theta_i}{\partial \phi} \end{bmatrix} = \begin{bmatrix} a_{star} & -1 \\ a_{ri} & -1 \end{bmatrix} \tag{3.3}$$

where, for subscript $j = ri$ and $j = star$ for the RSO and star observation respectively:

$$a_j = \frac{y_j - y}{x_j^2 + y_j^2 + x^2 + y^2 - 2x_j x - 2y_j y} \tag{3.4}$$

Noting that $|r_j|^2 = x_j^2 + y_j^2$ and $|r|^2 = x^2 + y^2$ and dividing the numerator and denominator by $|r_j|^2$:

$$a_j = \frac{\frac{y_j}{|r_j|^2} - \frac{y}{|r_j|^2}}{1 + \frac{|r|^2}{|r_j|^2} - 2\frac{x_j x}{|r_j|^2} - 2\frac{y_j y}{|r_j|^2}} \tag{3.5}$$

Note that the value of a_j varies depending on the units used for position. However, this variability can be negated by normalizing the distances using the observer's distance magnitude, r, as follows:

$$a_j = \frac{\frac{y_j/r}{|r_j/r|^2} - \frac{y/r}{|r_j/r|^2}}{1 + \frac{1}{|r_j/r|^2} - 2\frac{x_j x}{r^2|r_j/r|^2} - 2\frac{y_j y}{r^2|r_j/r|^2}} \tag{3.6}$$

When the observed object is a star, the observer-object distance $\left|r_j\right|^2 = |r_{star}|^2 \approx \infty$ and it becomes immediately apparent that a_{star} approaches zero. However, for RSOs at some nearby distance from the observer ($y_{ri} \neq y$), a_{ri} is non-zero. This demonstrates that observations of very distant objects such as stars do not provide observer position information and that a kinematic position estimate requires observations of objects closer than infinity. Using this information, we can approximate a_{star} in Eq. 3.3 as zero:

$$H = \begin{bmatrix} \frac{\partial \theta_i}{\partial x} & \frac{\partial \theta_i}{\partial \phi} \end{bmatrix} = \begin{bmatrix} a_{star} & -1 \\ a_{ri} & -1 \end{bmatrix} \approx \begin{bmatrix} 0 & -1 \\ a_{ri} & -1 \end{bmatrix} \tag{3.7}$$

The instantaneous observability of our measurements can be described by the invertibility of $H^T H$. For our observation matrix, this is:

$$H^T H = \begin{bmatrix} a_{ri}^2 & -a_{ri} \\ -a_{ri} & 2 \end{bmatrix}$$

By inspection, the above matrix is invertible for any non-zero a_{ri} of a reasonable magnitude. This range where $H^T H$ is invertible, and thus measurements are observable, is explored in the following subsection.

3.3.2 Measurement Precision and RSO Distance

As discussed previously, when RSOs are at a sufficiently far distance from the observer, a_{ri} will also approach zero. The relative numerical error in computing the inverse of $H^T H$ also increases as the RSO is moved further away until this error dominates the calculation. This matrix inversion error is related to the unitless ratio between the maximum and minimum singular values of the matrix, known as the matrix's condition number. For a positive definite matrix such as $H^T H$, the singular values are the matrix's eigenvalues λ_k and the matrix's condition number κ_A can be expressed as:

$$\kappa_A = \frac{\lambda_{k,max}}{\lambda_{k,min}} = \frac{\frac{1}{2}(a_{ri}^2 + 2 + \sqrt{a_{ri}^4 + 4})}{\frac{1}{2}(a_{ri}^2 + 2 - \sqrt{a_{ri}^4 + 4})} \tag{3.8}$$

Using κ_A, the relative error E of $(H^T H)^T$ is [97]:

$$E = \frac{||(H^T H)^T - \tilde{f}||}{||(H^T H)^T||} \leq \kappa_A e \tag{3.9}$$

Where $\tilde{f}$ is the numerical approximation of $(H^T H)^T$. The residual e in each element of $(H^T H)^T$ can be approximated as the machine epsilon ϵ: the smallest floating point number that a computer can store. As I performed this analysis in Matlab, the default double precision machine epsilon is 2.22x10^{-16} [98]. However, many space-grade processors [99] are limited to single precision floating point machine epsilons of 1.19x10^{-7} [98].

To examine how inversion accuracy varies with RSO-observer distance, I developed a simplified system of two observed objects: one representing a star and a second representing

an RSO. I placed the star 100 light years from the observer, an effectively infinite distance, while I placed the RSO 1 m away from the observer. I normalized these distances by dividing them by r and varied the RSO's position to be increasingly far from the observer. Using equations (3.8) and (3.9), I tracked the relative error of $(H^T H)^T$ for both single and double precision machine epsilons. Figure 3.2 shows that the relative inversion error has a global minimum when the RSO's position is approximately 4,500 km away from the observer. When a double precision ϵ is used, this error remains below 1% for distances under 2.3×10^{10} km and only exceeds 100% at 2.2×10^{11} km. However, the inversion error is much greater when a single precision ϵ is used and exceeds 100% at distances under 23 km and over 9.8×10^{5} km.

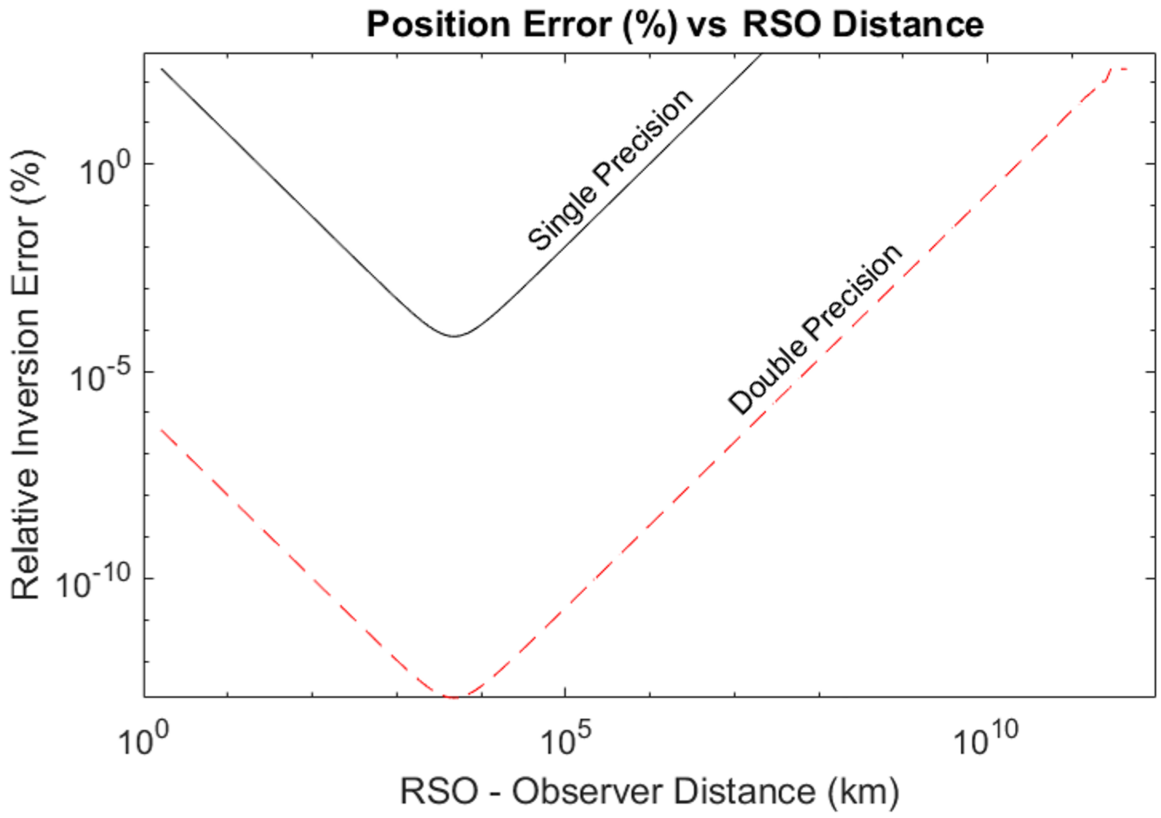

Fig. 3.2: Relative inversion error vs RSO-observer distance for single and double precision machine epsilons ϵ.

This analysis suggests using measurements from both near and far objects allows for sufficient position and attitude observability, as long as the observer can detect the objects. This is true for both single and double precision floating point-capable processors. However,

a double precision capable processor will avoid inversion issues for extremely close and far objects.

3.3.3 Measurement Precision and RSO Propagation Uncertainty

The proposed navigation strategy I presented earlier in this chapter requires knowledge of RSO positions. Space researchers and military organizations, such as US Space Surveillance Network (SSN), measure and track orbital parameters of most RSOs larger than 5-10 cm in diameter, with the SSN tracking, correlating, and cataloguing approximately 23,000 such objects [100]. Of these, approximately 24% are satellites, 18% are rocket bodies, and the remaining 58% consist of orbital debris [101].

The orbits of trackable RSOs are published by the United States Space Force as Two-Line Element sets (TLEs), which consist of several orbital parameters including the RSO's identifier, epoch, six orbital elements, and a B* term which describes the object's ballistic coefficient. Using an RSO's TLE, its orbit can be propagated using methods such as the Simplified General Perturbations 4 (SGP4) model. However, TLE-derived orbit propagations contain errors, especially due to factors such as variable atmospheric drag [102]. Perturbation-based uncertainties have been mitigated to some extent by the SGP4-XP (eXtended Perturbations) model, which builds on SGP4 by incorporating improved gravitational, solar radiation, and atmospheric drag models amongst other improvements [103]. While SGP4-XP provides improved propagation errors compared to SGP4 [104], TLEs for LEO objects are updated several times per day whereas those in higher orbits are updated several times per week to account for the increased uncertainty of objects in lower orbits [105].

For an RSO-based optical navigation method be viable, an observing spacecraft will need to propagate the orbits of a number of reference RSOs and have periodic TLE updates for these objects to correct for propagation errors. As such, selecting reference RSOs in stable orbits is key to minimizing propagation errors. Over a thirty-day observation period, Riesing and Cahoy [105] found that CubeSats in sub-400 km orbits can experience mean in-track position errors of 4.52 km, even with multiple TLE updates per day. This error is highest in sub-300 km orbits where it can exceed 25 km within a single day [102]. Fortunately, propagation error decreases with increasing altitude and Wang *et al.* [102] found that, over a

three-month observation period, spacecraft in low-eccentricity orbits between 900 and 1000 km had average single-day in-track position errors of approximately 200 m. As propagation errors in LEO are primarily caused by atmospheric drag, RSOs in lower orbits will need more frequent TLE updates and have larger propagation errors. This suggests that RSOs in higher altitudes will work better as navigation aids for RSO-based optical navigation.

3.3.4 Measurement Precision and RSO Brightness

For an optical detector such as a star tracker to see an RSO, sunlight must be reflected off of the RSO towards the detector. The intensity of this reflected light is referred to as the RSO's apparent visual magnitude. Apparent visual magnitude V_{ri} is a function of the magnitude of the light source (*i.e.*, the sun, $V_{sun} = -26.5$ near the Earth), the distance $R = \sqrt{\Delta x^2 + \Delta y^2}$ between the RSO and the detector, and the RSO's optical cross section (OCS) γ_v.

$$\gamma_v = A_{CS}\gamma_r F(\theta_{phase}) \tag{3.10}$$

The OCS describes how effectively the RSO is able to reflect light and is a function of the RSO's cross sectional area A_{CS}, reflectivity γ_r, and a shape-dependent function $F(\theta_{phase})$ which varies with the phase angle θ_{phase} between the RSO-observer vector R and the RSO-sun vector [2]. This sun-RSO-observer geometry is shown in Fig. 3.3. An RSO's OCS can be expressed by the following equation [2]:

$$\gamma_v = R^2 10^{-0.4(V_{ri} - V_{sun})} \tag{3.11}$$

To determine the maximum distance at which a commercial star tracker can detect RSOs, I calculated the mean OCS of several spacecraft using their mean apparent visual magnitudes taken from ground-based observations over a one year time-span by Gasdia [2]. Gasdia took these values, summarized in Table 3.1, from a single fixed observatory over multiple orbits at various phase angles. As a result, the mean values presented here are representative for these spacecraft. However, depending on the phase angle at the time of measurement, these satellites may appear significantly brighter or dimmer. Ground-based visual magnitude measurements are slightly dimmer than what an on-orbit detector could measure, as discussed

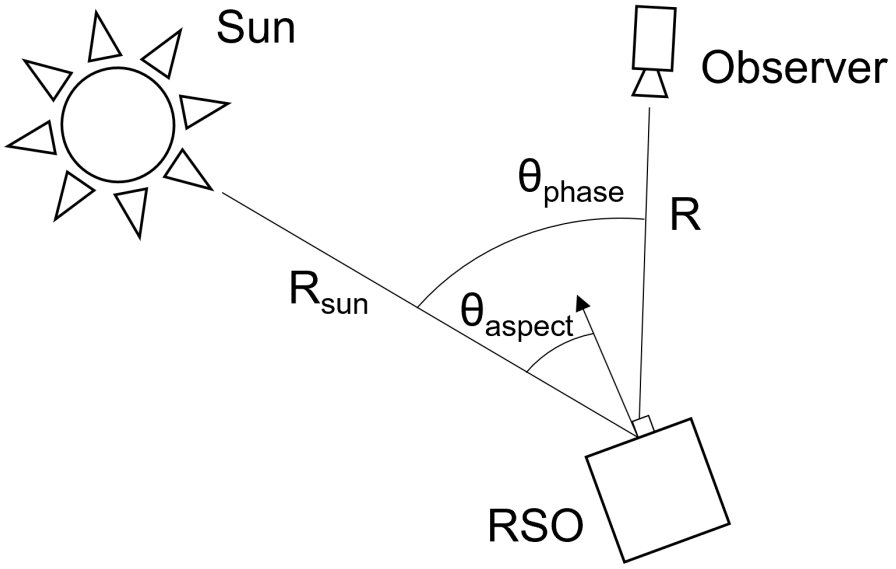

Fig. 3.3: Geometry between the Sun, an RSO, and an Observer.

Table 3.1: Parameters for several spacecraft calculated using ground-based observations. Note that the size of DMSP-5D2 F12 is unknown [2].

Spacecraft	Length (m)	Orbit (km)	Mean Apparent Visual Magnitude	Mean OCS (γ_v) (m^2/sr)
DMSP-5D2 F7	9.3	835	7	0.0278
DMSP-5D2 F12	Unknown	800	5	0.1608
OPAL	0.42	750	8	0.00892
SpinSat	0.56 (diameter)	345	9	0.00075

by Gow *et al.* [106], but are within one visual magnitude of on-orbit measurements for the same radar cross section. As such, the mean apparent visual magnitudes and mean OCS values presented in Table 3.1 are conservative compared to what an orbital observer would see.

To establish the RSO-observer ranges at which RSOs can be reliably detected, I rearranged Eq. (3.11) as a function of apparent visual magnitude:

$$V_{ri} = -2.5 \log_{10} \frac{\gamma_v}{R^2} + V_{sun} \tag{3.12}$$

As discussed in Ch. 2, star trackers use visual magnitude thresholds to remove objects

below a threshold brightness from images [73]. The limiting magnitudes for other star trackers, as well as other star tracker parameters, are shown in Table 3.2.

Table 3.2: Specifications for various commercial star trackers. Note that unknown specifications are denoted by a dashed line.

Star Tracker	**Cross Boresight Accuracy (arc-sec)**	**Boresight Accuracy (arc-sec)**	**Limiting Magnitude**	**Field of View (deg)**
Ball Aerospace HAST [107, 32]	0.03	–	5.5	9.47
Jena Optronik APS [32, 108]	1	8	6	20
Blue Canyon NST [109]	6	40	7.5	10 × 12
Sinclair Interplanetary ST-16 [65, 110]	7	70	5.75	15
Moscow Experimental Design Bureau 'Mars' AD-1 [31]	15	–	5-6	18

However, star trackers have the capacity to detect dimmer objects than what the star tracker's cut-off magnitude would otherwise allow. If a dim RSO is detected with a sufficiently large signal to noise ratio (SNR), it will reliably appear above the background noise. The relationship between SNR and the received signal is [111]:

$$SNR = \frac{N_s t_e}{\sqrt{N_s t_e + k_p(N_{bg} t_e + N_D t_e + N_R^2)}} \tag{3.13}$$

where N_s is the received signal, t_e is the exposure time, k_p is the number of pixels under consideration for the SNR calculation, N_{bg} is the total number of photons of background illumination per pixel, N_D is the dark current per pixel, and N_R is the read noise. Using the quadratic equation, this can be re-arranged to find N_s

$$N_s = \frac{SNR^2 + \sqrt{SNR^4 + 4k_p(N_{bg} t_e + N_D t_e + N_R^2)}}{2t_e} \tag{3.14}$$

Following [31], I modelled the received signal from an RSO as

$$N_s = \frac{\pi}{4}\eta_q \tau_t D^2 \Phi_* \tag{3.15}$$

where η_q is the star tracker's quantum efficiency, τ_t is the optical transmittance loss, D is the star tracker's lens diameter, and Φ_* is the RSO's illumination. I modelled the RSO's visual magnitude m_t as [31]

$$m_t = -\frac{5}{2}\log_{10}\left(\frac{\Phi_*}{\Phi_0}\right) \tag{3.16}$$

where Phi_0 is the stellar flux from a reference star. Rearranging Eq. 3.16, this becomes

$$\Phi_* = \Phi_0 10^{-0.4 m_t} \tag{3.17}$$

Lastly, I modelled the number of pixels illuminated by an RSO moving a linear distance d across the star tracker sensor as

$$k = \pi\rho^2 + 2\rho d = \pi\rho^2 + \frac{2 f_s \tan(\omega t_e)}{\gamma_p} \tag{3.18}$$

where ρ is the star tracker's point spread function radius, f_s is the star tracker's focal length, ω is the relative angular rate between the star tracker and RSO, and γ_p is the star tracker's pixel length. I combined Eq. 3.14, 3.14,3.17, and 3.18, to find the limiting visual magnitude

$$m_t = -\frac{5}{2}\log_{10}\left(2\frac{SNR^2 + \sqrt{SNR^4 + 4(\pi\rho^2 + \frac{2 f_s \tan(\omega t_e)}{\gamma_p})(N_{bg} t_e + N_D t_e + N_R^2)}}{\pi \eta_q \tau_t D^2 t_e \Phi_0}\right) \tag{3.19}$$

As these parameters are highly dependent on the star tracker used, a general performance increase beyond the stated limiting magnitude cannot be given. However, using values for "star tracker design 1" in [3] and a SNR threshold of 8 as suggested by [72], an illustrative performance increase can be shown. Using Eq. 3.19, I recalculated the limiting visual magnitude with the values summarized in Table 3.3.

Table 3.3: Star tracker parameters used to calculate the limiting visual magnitude for the "star tracker 1" design described in [3]. Values are from [3] unless otherwise noted.

Parameter	**Value**
Signal to noise ratio (SNR)	8 [72]
Point spread function radius (ρ)	3 pixels
Focal length (f_s)	1.44 mm
Relative angular rate (ω)	1 deg/s
Exposure time (t_e)	0.1 s
Pixel length (γ_p)	2.2 μm
Background illumination per pixel (S_{bg})	21 mV arcsec^{-1} [112]
Dark Current (N_D)	25 e-pixel^{-1}s^{-1} [113]
Read Noise (N_R)	2.6 e-RMS [113]
Quantum efficiency (η_q)	0.5
Optical transmittance loss (τ_t)	0.9 [32]
Lens diameter (D)	12 mm
Reference star stellar flux (Φ_0)	1.8×10^{10} photons m^{-2}s^{-1} [114]

I converted the background illumination, based on the maximum zodiacal light, from mV arcsec^{-1} to units of photons s^{-1}m^{-2}sr^{-1} using the following equation [32]

$$L_b = 5.6 \times 10^{10} 10^{-0.4 S_{bg}} \left(\frac{180}{\pi}\right) 3600^2 \tag{3.20}$$

and then calculated the resulting background photons as [32]

$$N_{bg} = \frac{\pi}{4} \eta_q \tau_t t_e L_b D^2 (f_s/\gamma_p)^2 \tag{3.21}$$

Using these values, the expected limiting visual magnitude for the star tracker is 7.7. If the background illumination is increased to 15 mV, the expected sunlit Earth shine 10 degrees from the Earth limb [112], and the relative angular rate is increased to 10 deg/s, the limiting magnitude becomes 7.1. These limiting magnitudes are noticeably higher than the star tracker's stated 5.75 mV detection limit [3] and show that a commercial star tracker can likely detect RSOs at greater distances than what their published visual magnitude thresholds would suggest. This difference is likely due to considerations other than the limiting visual magnitude itself, such as additional computational requirements from larger star catalogues, increased false-positives caused by the inclusion of low-brightness stars, and higher centroiding errors in low-brightness stars. While these results show that star trackers

can detect RSOs at greater distances than what their stated limiting magnitudes would suggest, it must be stressed that the performance increase gained by using an SNR cut-off approach may vary significantly between star trackers.

Using Eq. (3.12), I plotted the mean visual magnitude for each RSO in Table 3.1 as a function of mean OCS and observer-satellite distances from 100 km to 10^4 km. I overlaid these plots, seen in Fig. 3.4, with the limiting visual magnitudes of "star tracker design 1" [3], including both the cut-off magnitude and the theoretical SNR-based cut-off threshold. These two thresholds illustrate how a star tracker's RSO-detection capabilities could be improved if the star tracker's cut-off magnitude was not used. The MOST Space Telescope [31, 115], a 15 cm diameter Maksutov optical telescope, is included as well to illustrate the capabilities of a larger, more sensitive optical camera. Note that MOST does not use a visual magnitude cut-off and the visual magnitude limit shown represents the upper limit of the MOST telescope's detection capabilities [116].

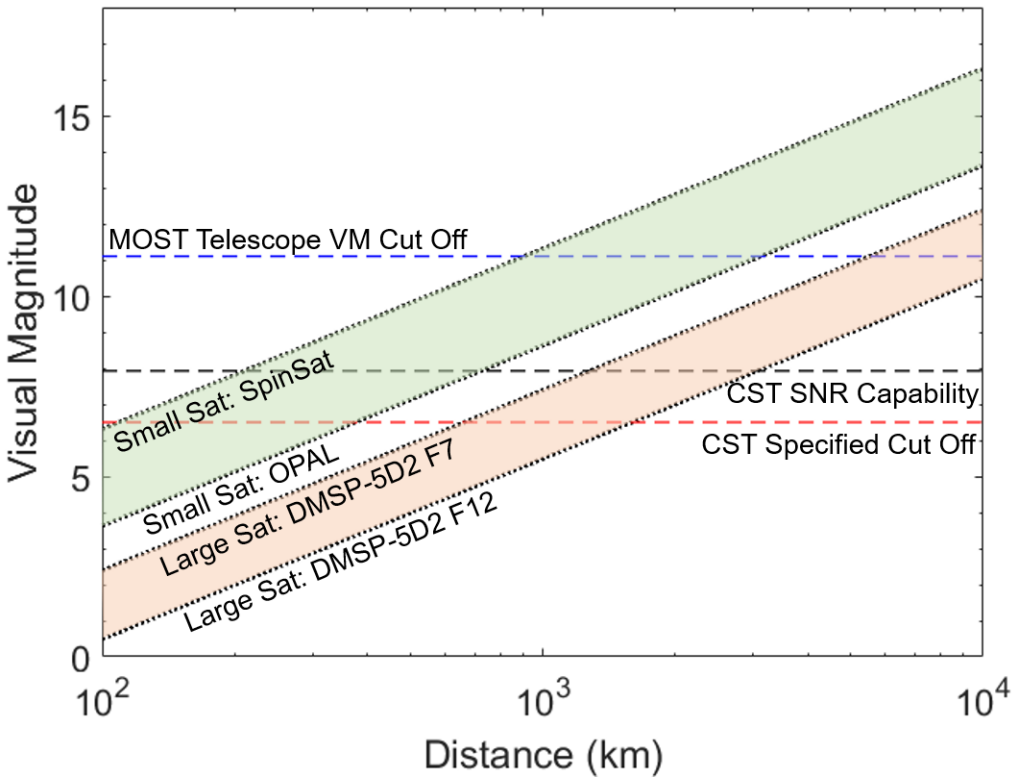

Fig. 3.4: Apparent Visual Magnitude (VM) vs object-observer distance for various RSOs. Limiting VMs are shown for the MOST Space Telescope and a CubeSat star tracker (CST) using its visual magnitude cut-off and its theoretical SNR-based detection limit.

While the apparent visual magnitudes presented in Fig. 3.4 may vary considerably depending on the RSO's aspect and phase angles, the mean apparent visual magnitudes presented here provide a guide to how each RSO can be from an observer while being sufficiently visible. Figure 3.4 shows that a CubeSat-type star tracker is theoretically capable of regularly detecting larger spacecraft to distances up to 1000 km while the MOST space telescope could detect spacecraft at distances beyond 3000 km. However, small satellites may become undetectable to a commercial star tracker at distances of 200 km even when the star tracker is pushed to its SNR cut-off.

The RSO detectability analysis presented here provides an upper bounds on the expected RSO detectability range for a commercial star tracker. However, this analysis neglected streaking effects due to the angular rate at which RSOs move across the star tracker's field of view. Unless the star tracker sensor's pixels are large enough to fully contain the detected RSO for the full image exposure period, some of the light received by the sensor from the RSO will fall on neighbouring pixels and result in the RSO appearing to be dimmer than what was shown in this analysis. This trailing loss error will be a function of the relative rotation between the star tracker and RSO. Examining the effect of relative RSO angular rates on detectability is beyond the scope of this dissertation but an RSO's SNR, and therefore its maximum detectable range, will be inversely proportional to the RSO's relative angular rate. Such trailing loss errors will be non-negligible, especially for LEO RSOs. As such, caution should be taken when applying Eq. 3.19 to RSOs with relative angular rates with respect to a star tracker.

From this analysis, it is clear that a star tracker's ability to optically detect RSOs is one of the key limiting factors that will determine if RSO-based optical navigation is feasible. Comparatively, the limits imposed by numerical computation are minor. However, given the sheer quantity of RSOs in orbit —over 23,000 objects larger than 5-10 cm [100]— these detection range limitations should not be severe enough to make RSO-based optical navigation unfeasible.

3.4 State Estimation using Optical Measurements

This section describes the simulations that I performed to evaluate Hypothesis 2, using the simplified model presented in 3.2. Subsection 3.4.1 describes the navigation environment that I developed to test estimator performances. This environment includes simplified dynamics and measurement models of an observing spacecraft viewing various quantities of stars and RSOs on a two-dimensional plane. Using this environment, I implemented and tested an EKF and UKF to estimate the observing spacecraft's state using star and RSO measurements, presented in Subsections 3.4.2 and 3.4.3 respectively.

3.4.1 Navigation Scenario

I developed a simplified two-dimensional model, consisting of an observing satellite measuring the relative angle between itself and several other bodies. I made some of these other bodies, representing RSOs, move in circular orbits while I placed others, representing stars, at fixed positions. The observing spacecraft's state vector $X = [x \quad y \quad \dot{x} \quad \dot{y} \quad \phi \quad \dot{\phi}]^T$ included the observer's position and velocity in x and y as well as its attitude ϕ and angular rate $\dot{\phi}$. I based the measurement model on Eq. (3.2) and the geometry shown in Fig. 3.1:

$$\begin{aligned} z(t) &= h[X(t)] + v(t) \\ &= \tan^{-1}\left[\frac{y_{ri} - y(t)}{x_{ri} - x(t)}\right] - \phi(t) + v(t) \end{aligned} \tag{3.22}$$

where v is an additive Gaussian white noise and $z(t)$ are the measurements. I simulated the observing spacecraft moving in a circular orbit, using Cartesian coordinates in an Earth-centric inertial reference frame. This resulted in the following continuous linear system of equations:

$$\dot{X}(t) = AX(t) + B[u(t) + w(t)] \tag{3.23}$$

where $w(t)$ is process noise, A is the continuous state transition model:

$$A = \begin{bmatrix} 0 & 0 & 1 & 0 & 0 & 0 \\ 0 & 0 & 0 & 1 & 0 & 0 \\ 0 & 0 & 0 & 0 & 0 & 0 \\ 0 & 0 & 0 & 0 & 0 & 0 \\ 0 & 0 & 0 & 0 & 0 & 1 \\ 0 & 0 & 0 & 0 & 0 & 0 \end{bmatrix} \tag{3.24}$$

B is the continuous control input model with observing spacecraft's inertia J:

$$B = \begin{bmatrix} 0 & 0 & 0 \\ 0 & 0 & 0 \\ 1/m & 0 & 0 \\ 0 & 1/m & 0 \\ 0 & 0 & 0 \\ 0 & 0 & 1/J \end{bmatrix} \tag{3.25}$$

and $u(t)$ is the force and torque exerted on the spacecraft:

$$u(t) = \begin{bmatrix} F_x(t) & F_y(t) & \tau(t) \end{bmatrix}^T \tag{3.26}$$

where $F_x(t)$ and $F_y(t)$ are the gravitational forces exerted in the x and y axes. I applied these forces as a special perturbation using Cowell's method[1]:

$$F_x(t) = -\frac{\mu m}{r^{3/2}} x(t) \tag{3.27}$$

$$F_y(t) = -\frac{\mu m}{r^{3/2}} y(t) \tag{3.28}$$

where μ is the Earth's standard gravitational parameter, r is the observer's orbital radius, and m is the observing spacecraft's mass. For this analysis, I used a fixed value for r to linearize the state dynamics. This approximation introduces an error when calculating the EKF's state transition Jacobian but, as discussed in Sec. 3.5, this approximation did not significantly affect the filter's performance.

[1]Multiplied by the observing spacecraft's mass to cancel out the mass term in Eq

Additionally, I applied an arbitrary sinusoidal torque τ on the observing spacecraft with a magnitude M of 5 µNm and $n = 1$ oscillations per orbit.

$$\tau(t) = M \cos\left(\frac{2\pi n}{T} t\right) \tag{3.29}$$

I calculated the process noise Q_k using the Q evaluation process described by van Loan [117]. Since I modelled the continuous process noise w as a Gaussian white noise with a standard deviation, the continuous process noise covariance W is equal to:

$$W = \mathbb{E}[ww^T] \tag{3.30}$$

I calculated the discretized measurement noise covariance matrix R_k from the measurement noise v_k as:

$$R_k = \mathbb{E}[v_k {v_k}^T] \tag{3.31}$$

I propagated the observing spacecraft's state vector using a 4^{th} order Runge Kutta integrator. I chose to use 1 s time steps t to be slightly greater than the Sinclair Interplanetary star tracker's 0.5 s maximum update rate [65], to account for other computational steps. I based the mass m and inertia J of the observing spacecraft, 84 kg and 2.8 kgm^2 respectively, off of a small spacecraft such as Sputnik [118]. I applied the process noise w as a Gaussian white noise with a standard deviation of one percent of the gravitational force and applied torque. These noise standard deviations equated to 7.3 N and 0.05 µNm respectively. Note that the actual process noises that a spacecraft will experience are unlikely to be zero-mean white noises. I chose to use Gaussian white process noise models because Kalman filters require white noises for optimal estimates and I wished to examine other reliability factors. I also propagated the near objects, representing RSOs, in circular orbits using the same 4^{th} order Runge Kutta integrator and 1 s time steps as the observing spacecraft. I placed the far objects, representing stars, at fixed locations. To represent the cross-boresight accuracy of a commercially available nanosatellite star tracker, I applied a Gaussian white measurement noise v with a standard deviation of 5 arc-seconds to the measurements [65].

3.4.2 EKF for Optical Navigation Using RSO Measurements

To determine if an RSO-based optical navigation method can effectively estimate a spacecraft's position and attitude, I developed an EKF based on the methods described in Sec. 2.3.1. I chose to use an EKF as this filter is commonly used for nonlinear attitude and position estimation [48, 47, 119] and my measurement function, shown in Eq. 3.22, is highly nonlinear.

I fed the sample measurements, as well as the RSO positions, generated using the measurement and dynamic models presented in Sec. 3.4.1, to the EKF to estimate the observing spacecraft's state at each time step. When assessing the filter's performance, I used convergence criteria based on [8]. Namely:

1) Estimation errors should not increase to an apparently infinite value;

2) Estimation errors should approach an unbiased value with a mean of approximately zero.

Based on Gelb's [8] definitions of divergence, estimators that fail the first convergence criteria are said to exhibit *true divergence* while those that fail the second criteria exhibit *apparent divergence*.

Unfortunately, because of the highly nonlinear measurement equation, the filter exhibited true divergence. Because of this, I had to supplement the EKF's process noise model for the filter to converge. I increased the process noise matrix Q along its diagonal elements by adding 0.1 times an identity matrix to Q. This increased process noise artificially increased the filter's covariance estimate, preventing the covariance from becoming so low that measurements no longer had any effect on the estimate. This phenomenon is commonly referred to as "falling asleep" in the estimation community and occurs if, at steady-state, the state covariance estimate's time-derivative becomes zero [8]. With an artificially increased Q, the filter was better-able to handle the highly nonlinear measurement relation and converged for most of the tested scenarios.

I first evaluated the EKF's performance using several scenarios to determine its feasibility when observing various quantities of stars and RSOs. Initial scenarios included using only stars, using a combination of stars and RSOs, and only RSOs. The purpose of these tests was to evaluate the basic performance of the EKF and I did not include the observability

constraints analyzed in Sec. 3.3. I examined these observability factors in Sec. 3.4.2.1.

All tests used 1 second time steps with the observing spacecraft in a 400 km circular orbit and an initial estimate error of [500 km 500 km 1 km/s 1 km/s 0.52 rad 0.017 rad/s]^T. When RSO observations were included, I modelled the RSOs in equally-spaced 1000 km circular orbits at 45°, 135°, 225°, and 315°counter-clockwise from the x-axis. I modelled the stars at fixed effectively infinite equally-spaced distances (100 light years) at 0°, 90°, 180°, and 270°counter-clockwise from the x-axis.

In order for both the EKF and UKF to converge, the initial state estimate must be sufficiently close to the true initial state. Based on a preliminary convergence study, the EKF was able to converge for initial state estimate errors of less than [2,750 km 2,750 km 10 km/s 10 km/s 0.52 rad 0.017 rad/s]^T, albeit with a longer convergence time than for the initial estimate error used in this study. The UKF was able to converge for a larger maximum initial estimate error of [4,000 km 4,000 km 10 km/s 10 km/s 0.52 rad 0.017 rad/s]^T, again with longer convergence times than when using the values used in this study. Both of these initial maximum estimate errors are well within the range of a TLE propagated using SGP4, even if the TLE is several days old [102]. A spacecraft operator should be capable of uploading an initial state estimate within these maximum error bounds, either based on a spacecraft's planned insertion orbit or by uploading a TLE-derived state estimate to the spacecraft after launch. As such, these maximum initial estimate error values support the overall feasibility of RSO-based optical navigation.

To assess the performance of each scenario, I examined both the estimate errors and the square roots of each of the diagonal elements of the filter's covariance matrix P. As discussed in Sec. 2.1.1, these diagonal estimates correspond to the filter's estimate of each state's variance and form the predicted standard deviations σ of each element. These variances would perfectly match the actual error variance of an optimal filter, such as the Kalman Filter, if given linear measurements, linear dynamics and white process and measurement noises. While the EKF examined here is not an optimal filter, examining how well the filter's predicted standard deviations bound the estimate errors provides insight into the filter's reliability.

Test 1: Infinitely Far Objects and Position Estimation I performed the first test to verify that the model functioned as expected when observing only four infinitely far objects. As expected, based on the observability analysis, the filter was incapable of convergent position estimates and exhibited true divergence but, the filter's predicted position error standard deviations σ bounded the position error. However, the filter quickly converged on an attitude estimate with errors of approximately 3×10^{-6} radians as seen in Fig. 3.5 (a) and (b). Due to the artificially increased process noise covariance Q, the filter's predicted angle error standard deviation was considerably larger than the actual angular error. While conservative, this meant that the filter considerably over-estimated the actual angle estimate error. This test confirmed that star measurements alone are insufficient to estimate an observer's position.

Test 2: Position and Attitude Estimation with Both Infinitely Far and Near Objects Next, I added four equally spaced RSOs in 1,000 km circular orbits. Using this combination of RSOs and stars, the filter quickly converged on a full state estimate with a position error of approximately 20 m and an average attitude error of approximately 7×10^{-7} radians, as seen in Fig. 3.5 (c) and (d). Again, the filter's predicted angle error standard deviation was considerably larger than the actual angular error, due to the artificially increased Q. The filter's predicted position error standard deviations over-estimated the actual estimate errors, but not to as great of an extent as the predicted angle error standard deviation. As seen in Fig. 3.5 (d), the predicted x-position error standard deviation responded dynamically with the x-position error.

The periodic pattern seen in the filter's predicted position standard deviation was caused by the relative positions of the stars and RSOs with respect to the observer and the effect that these relative geometries had on the filter's measurement Jacobian H_k:

$$H_k = \frac{\partial z_k}{\partial X} = \begin{bmatrix} \frac{y_{s1}-y}{x^2+y^2-2xx_{s1}-2yy_{s1}+x_{s1}^2+y_{s1}^2} & -\frac{x_{s1}-x}{x^2+y^2-2xx_{s1}-2yy_{s1}+x_{s1}^2+y_{s1}^2} & 0 & 0 & -1 & 0 \\ \frac{y_{s2}-y}{x^2+y^2-2xx_{s2}-2yy_{s2}+x_{s2}^2+y_{s2}^2} & -\frac{x_{s2}-x}{x^2+y^2-2xx_{s2}-2yy_{s2}+x_{s2}^2+y_{s2}^2} & 0 & 0 & -1 & 0 \\ \frac{y_{s3}-y}{x^2+y^2-2xx_{s3}-2yy_{s3}+x_{s3}^2+y_{s3}^2} & -\frac{x_{s3}-x}{x^2+y^2-2xx_{s3}-2yy_{s3}+x_{s3}^2+y_{s3}^2} & 0 & 0 & -1 & 0 \\ \frac{y_{s4}-y}{x^2+y^2-2xx_{s4}-2yy_{s4}+x_{s4}^2+y_{s4}^2} & -\frac{x_{s4}-x}{x^2+y^2-2xx_{s4}-2yy_{s4}+x_{s4}^2+y_{s4}^2} & 0 & 0 & -1 & 0 \\ \frac{y_{r1}-y}{x^2+y^2-2xx_{r1}-2yy_{r1}+x_{r1}^2+y_{r1}^2} & -\frac{x_{r1}-x}{x^2+y^2-2xx_{r1}-2yy_{r1}+x_{r1}^2+y_{r1}^2} & 0 & 0 & -1 & 0 \\ \frac{y_{r2}-y}{x^2+y^2-2xx_{r2}-2yy_{r2}+x_{r2}^2+y_{r2}^2} & -\frac{x_{r2}-x}{x^2+y^2-2xx_{r2}-2yy_{r2}+x_{r2}^2+y_{r2}^2} & 0 & 0 & -1 & 0 \\ \frac{y_{r3}-y}{x^2+y^2-2xx_{r3}-2yy_{r3}+x_{r3}^2+y_{r3}^2} & -\frac{x_{r3}-x}{x^2+y^2-2xx_{r3}-2yy_{r3}+x_{r3}^2+y_{r3}^2} & 0 & 0 & -1 & 0 \\ \frac{y_{r4}-y}{x^2+y^2-2xx_{r4}-2yy_{r4}+x_{r4}^2+y_{r4}^2} & -\frac{x_{r4}-x}{x^2+y^2-2xx_{r4}-2yy_{r4}+x_{r4}^2+y_{r4}^2} & 0 & 0 & -1 & 0 \end{bmatrix} \tag{3.32}$$

where x_{si} and y_{si} are the i^{th} star's Cartesian position and x_{ri} and y_{ri} are the i^{th} RSO's Cartesian position. Through visual inspection, it is apparent that as the observer's x or y position approaches a star or RSO's x or y position, elements of H_k will approach zero. Similarly, when the difference between the observer's position and the observed object reach their maximum extent, elements of H_k will also reach their maximum extents. The peaks in the filter's predicted position standard deviation seen in Fig. 3.5 (d) occur when elements of H_k approach zero. Similarly, the valleys in the filter's predicted position standard deviation occur when elements of H_k approach their maximum values. This covariance phasing effect occurs in subsequent tests as well.

Test 3: Position and Attitude Estimation with Only Near Objects To determine how well my RSO-based optical navigation filter functioned using RSO observations alone, I removed the stars from the model. Figure 3.5 (e) and (f) show that the position estimate converged to an error of approximately 50 m, similar to the previous test, while the attitude estimate converged to an error of 4×10^{-5} radians. The filter's predicted standard deviations bounded the estimate errors similarly to the previous test but were proportional to Test 3's estimate errors.

3.4.2.1 EKF Simulation Results With Observability Constraints

While Tests 2 and 3 were able to converge on state estimates, these tests did not incorporate the observability constraints analyzed in Sec. 3.3. Of these constraints, the two which will

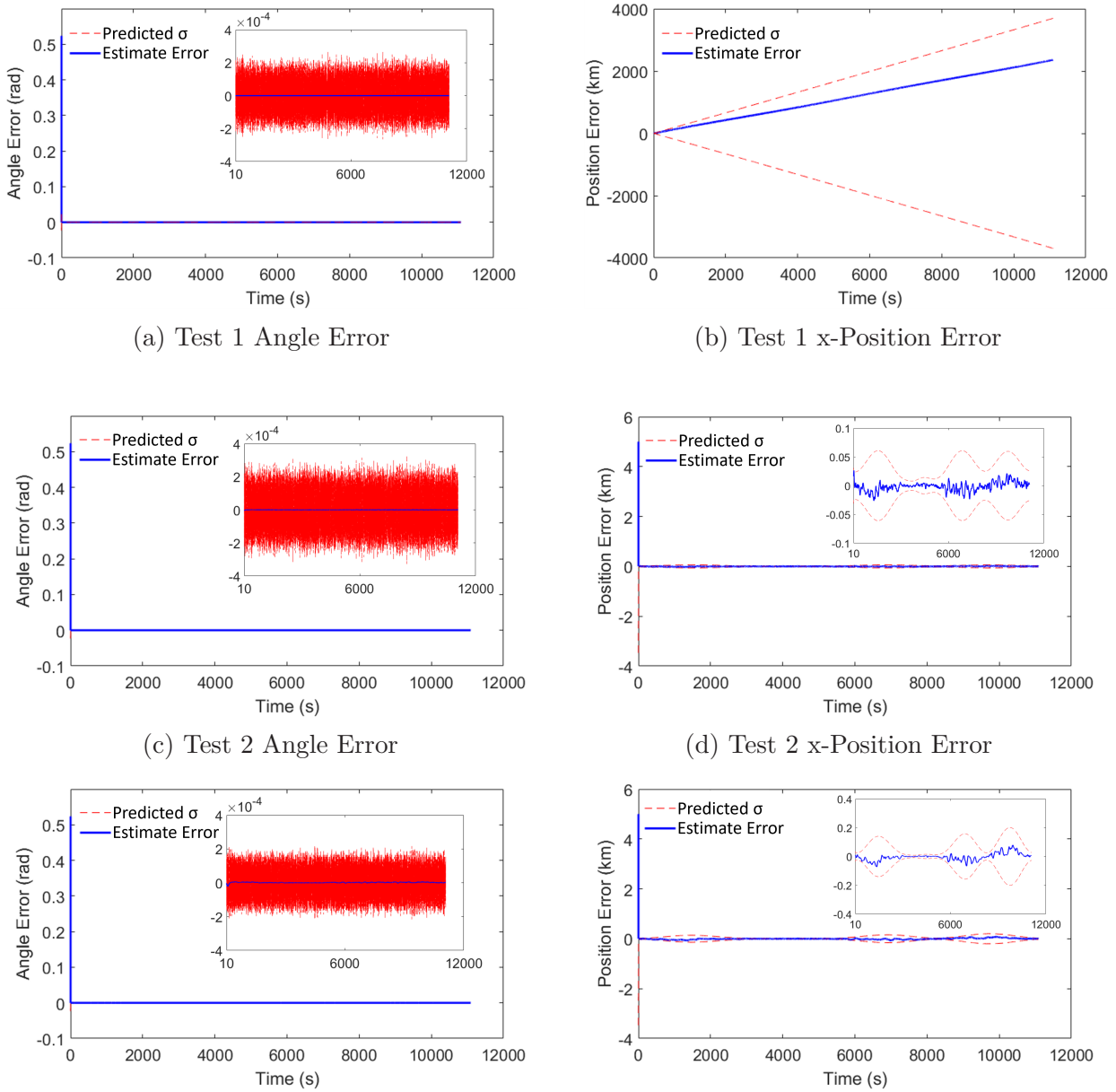

(a) Test 1 Angle Error

(b) Test 1 x-Position Error

(c) Test 2 Angle Error

(d) Test 2 x-Position Error

(e) Test 3 Angle Error

(f) Test 3 x-Position Error

Fig. 3.5: Extended Kalman Filter x-Position and angular position errors with associated predicted error standard deviations σ for observation tests 1-3. Test 1 estimated the observer's position using infinitely far objects. Test 2 estimated the observer's position and attitude using both infinitely far and nearby objects. Test 3 estimated the observer's position and attitude using only nearby objects.

have the largest impact on an RSO-based optical estimator are TLE/propagator error and RSO brightness.

Discrepancies between where an observing spacecraft believes an RSO is, from the

observer's on-board TLE propagator, and the true measured position of the RSO will introduce errors into the estimation filter. To represent this error, I propagated two versions of each RSO which represent the true and perceived RSO positions. The "true" RSO propagation model, used to calculate observer measurements, included a constant 5.64×10^{-6} m/s^2 deceleration to represent dynamics that were not captured by a propagator. This deceleration roughly modelled the single-day in-track propagation error of 200 m for an RSO in a 1000 km circular orbit [102]. I used the position of the second "perceived" RSO propagation model for y_{ri} and y_{ri} in Eq. (3.22) while running the filter. This RSO model did not include deceleration, but I initialized the perceived RSOs with a random Gaussian in-track position error with a mean of zero and standard deviation of 5 km. As star positions are known to a high accuracy, I modelled the objects in this simulation representing stars as fixed objects and did not include decelerations or position errors.

The second key constraint introduced in the following simulation is an RSO detection range and field of view. Under this constraint, I took measurements when the true position of an RSO was within 3,000 km of the observing spacecraft, based on the detection limit of a CubeSat-class star tracker using the SNR detection limit described in Sec. 3.3.4. I chose to use a 315° field of view, representing multiple cooperating star trackers, to provide the EKF with sufficient measurements without drastically increasing the number of simulated RSOs. I limited the field of view to 315°, rather than 360°, due to angle wrapping issues as estimates approached a full rotation. I centred the restricted field of view on the observing spacecraft's x axis. Additionally, to represent the cross-boresight accuracy of a commercially available nanosatellite star tracker, I discretized sample measurements to 5 arc-seconds and then applied a Gaussian white measurement noise v with a standard deviation of 5 arc-seconds [65].

Using these new constraints, I simulated the EKF again under similar conditions to the previous tests, using a combination of star and RSO measurements and only RSO measurements. As I have already established that the filter cannot estimate position with only stars, I did not repeat the star-only test. I used thirty-six equally spaced RSOs in 1,000 km circular orbits to ensure that the observing spacecraft could detect some of these objects at any given time. When used, I placed eight equally-spaced RSOs 100 light years away from

the orbit centre.

Test 4: Position and Attitude Estimation with Both Infinitely Far and Near Objects Using these more rigorous constraints, the observing spacecraft detected between two and eight stars and LEO objects at any time, with a mean of six detected objects. The filter converged on a position estimate with a cyclic position error, with peaks of 5 km. The filter's estimated x-position error standard deviation was considerably smaller than the actual estimate error, as the filter did not model TLE-error. The filter's attitude estimate had an apparent divergence, with an approximate 1×10^{-4} radian bias and an average attitude error of approximately 2×10^{-4} radians, as seen in Fig. 3.6 (a) and (b). While the filter's predicted estimate error covariance was of an appropriate magnitude, it could not account for the estimate bias and so the angle estimate error was unbounded. The significant error spikes seen in the EKF's position estimate error occurred when stars, which were not subject to TLE errors, left the EKF's field of view. This occurred because the filter did not include a TLE-error model, and the RSO and star measurement sources were processed with the same 5 arc-second measurement error. While the EKF's estimate errors remained bounded during the simulation, the filter's estimate errors increased over larger time scales as the simulated TLE propagation error grew.

Test 5: Position and Attitude Estimation with Only Near Objects I then removed the stars from the model. Using only RSOs, the filter observed between one and five RSOs with a median of three over the simulation. Figure 3.6 (c) and (d) show that the position estimate converged to a cyclical error similar to the previous test with peaks of approximately 5 km. The attitude estimate had a slow true divergence, and the attitude error grew from 6.8×10^{-4} radians after 100 seconds to 7.0×10^{-4} radians after two orbits (11,000 seconds). As with Test 4, while the filter's position estimate errors were bounded for the simulated timescales, these errors would increase over larger time scales as the simulated TLE propagation error grew. As this test did not include star measurements, it did not experience the same error spikes as the previous test. The angle and position covariance estimates were very similar to the previous test.

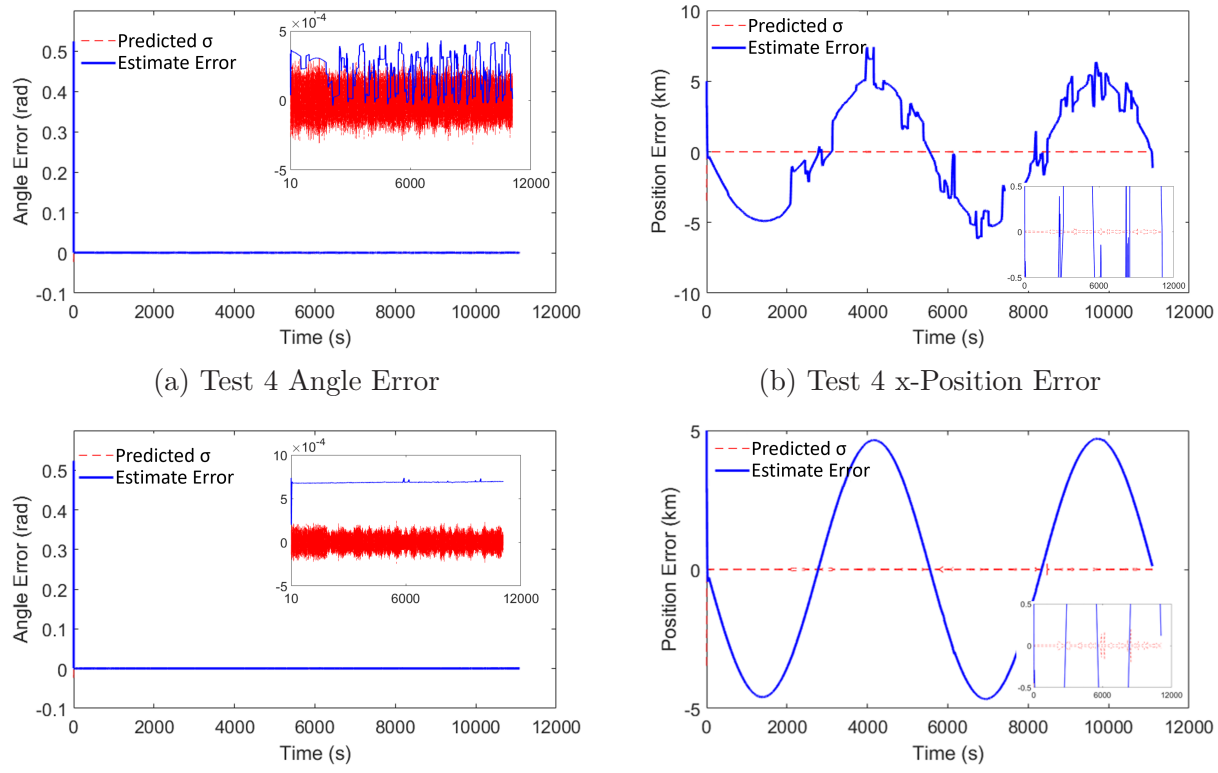

(a) Test 4 Angle Error

(b) Test 4 x-Position Error

(c) Test 5 Angle Error

(d) Test 5 x-Position Error

Fig. 3.6: Extended Kalman Filter x-Position and angular position errors with associated predicted error standard deviations σ when observing RSOs and stars and only RSOs with observability constraints including limited detection ranges, limited fields of view, and 5 km errors between the perceived and true RSO positions.

3.4.3 UKF for Optical Navigation Using RSO Measurements

Establishing trust in a new method is critical to enable adoption and commercialization in the space industry. While the results of the EKF were promising, the EKF required the process noise covariance to be artificially increased. This alteration was arbitrary and may make users question the estimator's overall reliability. As such, I repeated the previous tests using an Unscented Kalman Filter (UKF). Unlike the EKF, the UKF does not linearise the dynamics or measurements and is therefore better-suited to highly nonlinear models such as my measurement function [23, 61].

Aside from not artificially increasing the process noise covariance or requiring any linearization, the UKF used the same model parameters as the previous EKF, including

the same observing spacecraft dynamics model, measurement equation, RSO model, time step size, 4^{th} Order Runge Kutta integrator, and initial estimate error. I set the UKF tuning parameters α, β, and κ to 1.639×10^{-5}, 0, and 2 respectively. I selected the β, and κ parameters based on Wan's [11] recommended values while I selected α based on manual filter tuning.

I tested the UKF's performance using the same test conditions as the EKF tests, summarized in Fig. 3.7 and 3.8. Figure 3.7 shows the UKF's performance when measuring only star-like objects, a mix of star-like and RSO-like objects, and with only RSO-like objects without considering TLE-errors or a maximum detection range. As with the EKF, the UKF was unable to provide a convergent position estimate when measuring only stars, with both position and velocity exhibiting true divergence. The UKF's angular position estimate was approximately the same as the EKF, with errors of approximately 4×10^{-6} radians. When observing both stars and RSOs, the UKF converged to a position error of approximately 50 m and an attitude estimate error of approximately 6×10^{-6} radians. These estimates are slightly worse than the EKF under similar conditions. The UKF was also less accurate when only RSOs were observed, with positional errors of approximately 200 m and attitude errors of 2×10^{-5} radians. For all three tests, the predicted standard deviations σ bounded the state estimate errors much more closely than the EKF did. This indicates that the UKF was more capable of accurately predicting the state estimate covariance than the EKF.

Figure 3.8 shows the UKF's performance when I included TLE errors and a maximum detection range, using the same simulated conditions as the EKF. Figure 3.8 (a) and (b) show the filter's performance when detecting both stars and RSOs. The UKF's estimate errors were very similar to the EKF's errors and, as with the EKF, the UKF experienced error spikes when stars and RSOs entered and left the filter's field of view. Figure 3.8 (c) and (d) show the UKF's performance when detecting only RSOs. The UKF's position estimate error experienced the same cyclical error as the EKF, however the UKF's attitude estimate error converged, unlike the EKF's attitude estimate. As with the EKF, the UKF's estimated error standard deviations were unable to bound the filter's estimate errors, because the TLE error was not included in the filter's measurement model. The UKF's estimated angle error standard deviations were noticeably smaller than the EKFs, because the EKF's estimated

angle error standard deviations were artificially increased by increasing the EKF's process noise covariance Q.

Despite its larger estimate errors, the UKF did not require changes to its process noise covariance Q to converge. This lack of covariance augmentation means that the UKF is a more reliable estimator in this application.

3.5 Discussion

The EKF and UKF tests presented in Sec. 3.4 support my hypothesis that RSO-based optical navigation is possible for an observing spacecraft in Earth-orbit observing other objects that are also orbiting the Earth. Figures 3.5 (c) to (f) show that the EKF can converge for all state elements using RSO observations. However, as shown by the first test and predicted by the observability analysis, the EKF cannot converge on position estimates using only star measurements. The second test, which used both star and RSO measurements, converged to a full state estimate, including a more accurate attitude estimate. The third test, using only RSO measurements, had converged to a similar position error to the second test. These results should be expected as the RSO measurements contained both position and attitude information while the star measurements contained only attitude information. The EKF's predicted error standard deviations bounded the estimate errors in these first three tests, however this bounding –and the filter's convergence in general– required artificially increasing Q. Figure 3.7 shows that the UKF converged on full state estimates without artificially increasing the process noise covariance. Additionally, the UKF's estimate errors were bounded by the filter's estimated error standard deviations more closely than for the EKF. This indicates that the UKF was better-able to estimate the state error covariance P. As such, the UKF is an inherently more trustworthy filter in this application as it converged using only knowledge of its measurement and process noises.

When I applied the constraints introduced in Sec. 3.3 to the EKF and UKF, their steady-state errors increased significantly. The cyclical position errors shown in Fig. 3.6 and 3.8 were caused by the difference between the "true" and assumed RSO positions and their error-peaks matched the difference between these two RSO models. Due to the unmodelled

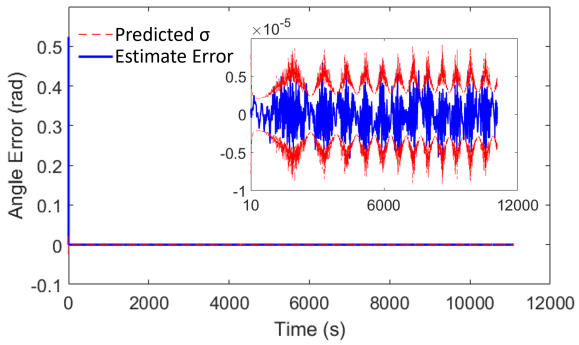

(a) Test 1 Angle Error

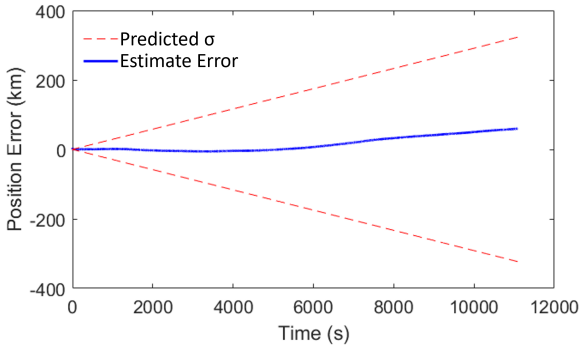

(b) Test 1 x-Position Error

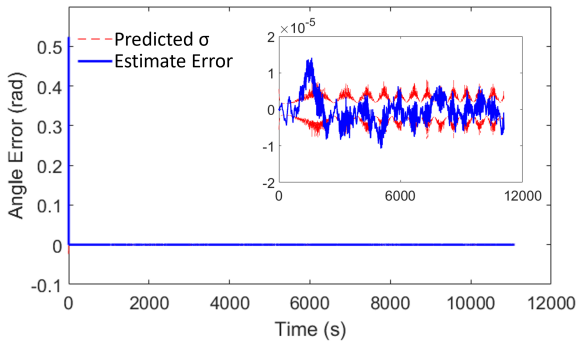

(c) Test 2 Angle Error

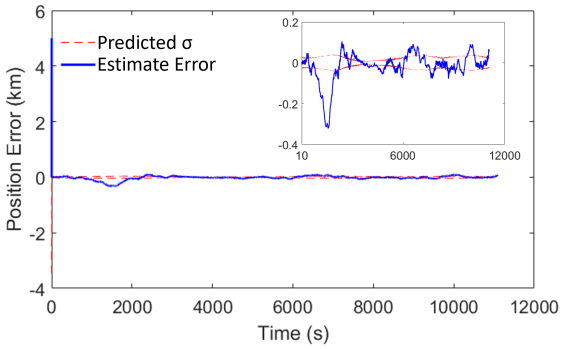

(d) Test 2 x-Position Error

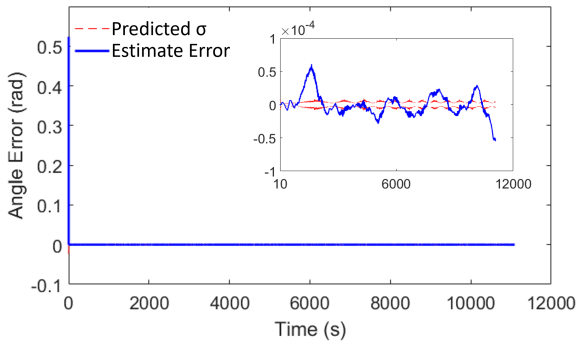

(e) Test 3 Angle Error

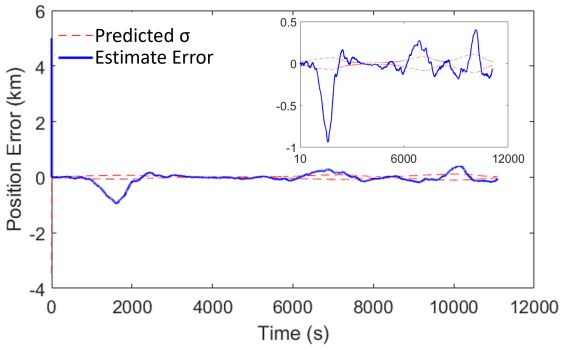

(f) Test 3 x-Position Error

Fig. 3.7: Unscented Kalman Filter x-Position and angular position errors with associated predicted error standard deviations σ for several observation conditions. Test 1 estimated the observer's position using infinitely far objects. Test 2 estimated the observer's position and attitude using both infinitely far and nearby objects. Test 3 estimated the observer's position and attitude using only nearby objects.

measurement errors included in these tests, both the EKF and UKF severely underestimated the state error covariance P. The $H^T H$ inversion error was negligible at the detection ranges used in this simulation. When I removed the RSO position error, as seen in Fig. 3.5 and 3.7

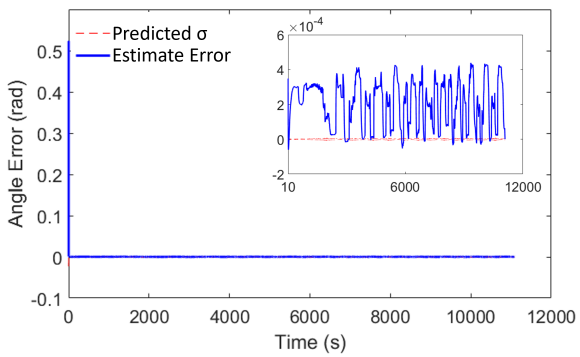

(a) Test 8 Angle Error

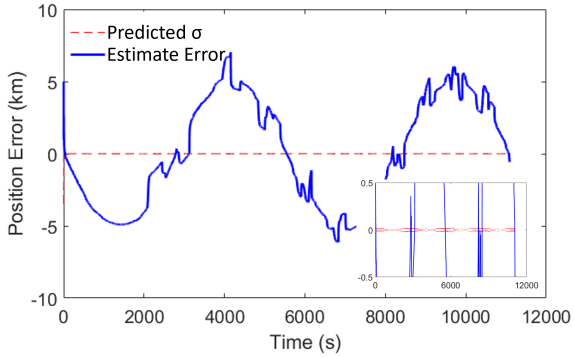

(b) Test 8 x-Position Error

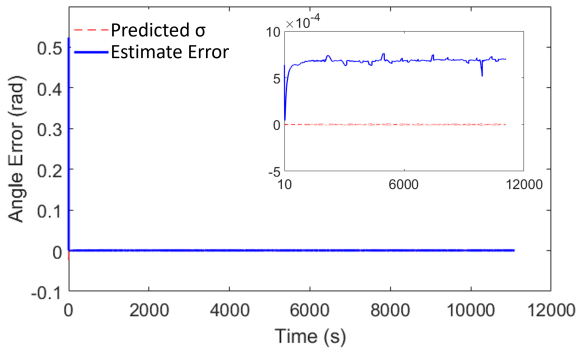

(c) Test 9 Angle Error

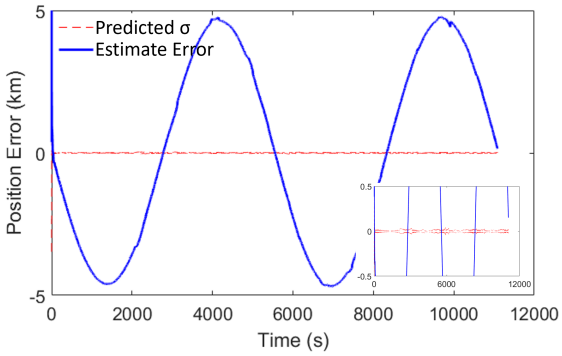

(d) Test 9 x-Position Error

Fig. 3.8: Unscented Kalman Filter x-Position and angular position errors with associated predicted error standard deviations σ when observing RSOs and stars and only RSOs with observability constraints including limited detection ranges, limited fields of view, and 5 km errors between the perceived and true RSO positions.

the both filters performed substantially better.

This chapter used a simplified dynamics model, in which the observer's orbital radius was assumed to be constant. However, this approximation does not appear to have caused a significant impact on either the EKF or UKF's performance. The fixed radius approximation is removed in Ch. 5 and both filters had comparable performances to the results shown in this chapter.

3.6 Chapter Summary

This chapter has explored the feasibility of an RSO-based Optical Navigation filter by first examining the practical limitations of this method and then modelling such a system using

two variations of the Kalman Filter. The two filters presented here, an Extended Kalman Filter (EKF) and an Unscented Kalman Filter (UKF), both achieve promising results, as demonstrated by their ability to converge on navigation solutions. Of these two filters, the UKF performed the best because it converged without artificially increasing the process noise covariance and was able to closely bound the state estimate errors using the filter's predicted error standard deviations.

The analysis presented in this chapter lends credence to Hypothesis 2, that an RSO-based state estimator is feasible and can converge on full state estimates. The errors between the true and expected RSO positions and the detection threshold of the star tracker used are the likely limiting factors for this method. While the model presented here has several simplifications, including reduced dimensionality, the simulations demonstrate that convergent state estimates are possible within a fraction of an observer's orbit while observing relatively few RSOs.

While this chapter demonstrated that RSO-based optical navigation is possible, this method's nonlinear measurement model affected the trustworthiness of both the EKF and UKF. As such, Ch. 4 investigates the feasibility and trustworthiness of a less nonlinear[2] measurement model: RSO-based navigation using range measurements. I hypothesized that using less nonlinear measurements would reduce EKF's linearization error and improve the filter's trustworthiness. As a part of a larger trust-factor study, Ch. 5 compares the trustworthiness of these two navigation methods. Additionally, Ch. 5 investigates two ways to improve the quality of my simulation model and reduce estimate errors, thereby improving the performance of an RSO-based optical navigator:

1) Implementing a more detailed orbital propagator.

2) Augmenting the filter to also estimate the reference RSO states and include RSO position error in the filter's measurement error model.

While other simplifications can be removed in future work, they are unlikely to change the overall feasibility of this navigation technique. Expanding the orbital model to a full six degree-of-freedom system and including elliptical orbits would add complexity to the

[2]See Sec. 5.3.1.2 for a formal examination of measurement linearity.

dynamics and measurement equations but would not fundamentally change the observability of the filter.

Chapter 4

Range-based Navigation Using Resident Space Objects

"So I go out every night with a homemade sextant and sight Deneb. It's kind of silly if you think about it. I'm in my space suit on Mars and I'm navigating with sixteenth-century tools."

Andy Weir, *The Martian*, 2011.

IV

4.1 Introduction

Estimating an observing spacecraft's orbital state using range-based RSO measurements presents an alternative to the angle-based RSO measurements explored in Ch. 3. While the UKF and EKF were both able to converge using angle-based RSO measurements in the previous chapter (albeit with an artificially increased process noise covariance model for the EKF), both filters underestimated the state estimate error covariances. I hypothesized that these under-estimates were due to the highly nonlinear measurements used in Ch. 3. As such, this chapter examines how well the EKF and UKF perform when using range measurements, which are less nonlinear[1] than the previous angle measurements.

This chapter first examines the feasibility of using various existing sensors for estimating an observing spacecraft's orbital state using range measurements. Section 4.2 explores the feasibility of various sensors for RSO detection, including radar, LIDAR, laser range finders, and optical communication terminals. Section 4.3 uses the results of these sensor-investigations

[1]See Sec. 5.3.1.2 for a formal examination of measurement linearity.

to develop a Kalman filter for estimating an observing spacecraft's orbital state using RSO measurements. Finally, Sec. 4.4 summarizes this chapter.

The contents of this chapter have been published in Driedger, Matthew and Asgari, Aref and Ferguson, Philip, "Feasibility of Gathering Resident Space Object Range Measurements Using In-Orbit Observers," in *IEEE Journal of Radio Frequency Identification*, vol. 6, pp. 250-257, 2022 © 2022 IEEE [88].

4.2 RSO Ranging Methods

This section explores the feasibility of using various range-based sensors to measure the distance between an observing spacecraft and RSOs. These sensors include radar, laser communication devices, laser rangefinders, and LIDAR devices. All of these devices rely on transmitting and receiving a signal and are subject to inverse-square laws. Because of this, only a small portion of the transmitted signal will be detected by the receiver, and the maximum ranges of these devices are significantly shorter than the optical methods discussed in Ch. 3.

4.2.1 Radar Ranging Methods

This section explores the maximum feasible range at which existing Earth observation SAR antennas can detect RSOs by examining how the antenna's Signal to Noise Ratio (SNR) varies as a function of range and the RSO's radar cross section. I performed this analysis using the SAR parameters for the RCM spacecraft, shown in Table 4.1, and the radar cross sections of various RSOs, shown in Table 4.2.

The RCM SAR antenna's SNR was calculated for each RSO using the following equation [120]:

$$SNR = \frac{P_{tx} G^2 c^2 \sigma_c}{(4\pi)^3 f^2 R^4 k_B T_N B_w F_N} \tag{4.1}$$

Table 4.1: SAR parameters for the Radar Constellation Mission (RCM) spacecraft [4, 5]. The transmitted power was estimated using the spacecraft's peak power usage from [4].

Parameter	**Value**
Antenna length (L_a)	6.75 m
Antenna width (W_a)	1.38 m
Transmit frequency (f)	5.405 GHz
Antenna bandwidth (B_w)	100 MHz
Transmitted power (P_{tx})	1 kW
Antenna type	Active phased array

where P_{tx} is the antenna's transmitted power, G is the antenna's gain, c is the speed of light, σ_c is the radar cross section of the detected object, f is the antenna's transmitted frequency, R is the distance between the observer's antenna and detected object, k_B is Boltzmann's constant, T_N is the antenna noise temperature, B_w is the antenna's bandwidth, and F_N is the antenna's noise figure. The antenna gain G was calculated as [121]:

$$G = \frac{4\pi L_a W_a f^2 \rho_a}{c^2} \tag{4.2}$$

where L_a is the antenna's length, W_a is the antenna's width, and ρ_a is the antenna efficiency. To determine the maximum possible range at which a radar device can detect an RSO, I assumed an ideal ρ_a value of unity. The antenna's noise figure F_N was calculated as [120]:

$$F_N = \frac{T_S + T_I}{T_S} = \frac{T_N}{T_S} \tag{4.3}$$

where T_S is the antenna's surface temperature, T_I is the antenna's internal noise temperature, and the antenna noise temperature T_N is the sum of T_S and T_I. I assumed that the antenna's surface temperature was 290 K and its internal noise temperature was 700 K, based on discussions with SAR specialists at Magellan Aerospace. The resulting antenna noise temperature T_N was 990 K.

Using Eq. 4.1, 4.2 and 4.3, I calculated SNR as a function of observer-target range for each of the radar cross sections in Table 4.2. Figure 4.1 shows these SNR-range relationships.

It is likely overly-optimistic to assume that range data can be extracted from SAR images with SNR-values of unity. However, this SNR-value provides a convenient limit for determining the maximum possible detection range at which an RSO can be detected by a

Table 4.2: Radar cross sections σ_c for various resident space objects [6].

RSO	**Radar Cross Section σ_c [m^2]**
Delta 2nd stage break-up debris	0.0025
Able-Star upper stage break-up debris	0.035
Delta upper stage	0.30
Cosmos 546	3.44

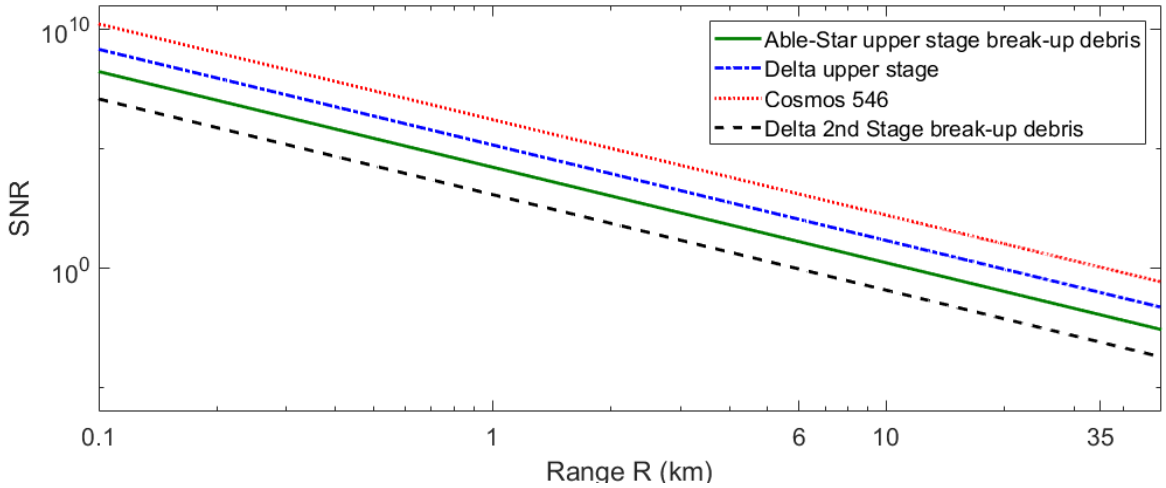

Fig. 4.1: Signal to Noise Ratio (SNR) vs observer-target range for several Resident Space Objects (RSOs) as detected by a Synthetic Aperture Radar (SAR) antenna with parameters based on the Radar Constellation Mission (RCM) spacecraft.

SAR antenna. If range data can be extracted to an SNR-value of 1, then in ideal scenarios the maximum detectable range for small debris like the Delta rocket 2nd stage debris shown in Table 4.2 is approximately 6 km, while larger RSOs like Cosmos 546 can be detected to distances of 35 km.

While radar's maximum RSO-detection range appears to be great enough for RSO-based range navigation methods, it is important to consider the pointing and power requirements of such as system. SAR systems use a substantial amount of power. For example, the RCM satellites have average power consumptions of 220 W, but their peak power consumptions are 1600 W while operating their SAR payloads [4]. These peak consumption rates are primarily caused by their SAR antennas [4]. Additionally, SAR spacecraft are typically designed for Earth observation missions and, like RCM, have fixed solar arrays [4]. Combined, this means that a spacecraft attempting to observe RSOs would likely have to point its solar arrays away from the sun while consuming significant amounts of power. This would put the

spacecraft in a negative power mode, which would quickly drain its batteries. Due to these factors, an observing spacecraft attempting to use a SAR payload for RSO-detection as a secondary capacity would be restricted to detecting objects between itself and the spacecraft's ground-targets. Taking into account the idealized nature of my range analysis, and the additional on-board image processing requirements that such a system would require, radar is not a feasible method for RSO-based navigation methods.

4.2.2 Laser Communication, Laser Rangefinders, and LIDAR

Laser communications devices are used to communicate between LEO and GEO spacecraft as well as between spacecraft and ground stations [94]. Because laser communications devices use concentrated laser-beams with small beam divergences, these devices weigh less, use less power, provide greater security, and communicate at higher data rates when compared with traditional RF transceivers [94, 93]. Due to these advantages, laser communications have been proposed for satellite constellations and mega constellations such as Starlink and Kuiper [94]. To ensure interoperability between laser communications devices, the Consultative Committee for Space Data Systems (CCSDS) is developing standards for optical communications [122].

Some laser communications devices, designed for communicating between LEO and GEO, have ranges greater than 45000 km [93]. These ranges greatly exceed those of laser rangefinders and LIDAR units. Space-based rangefinders such as the one studied by Nayak and Udrea [91] have ranges of up to 3 km, while LIDAR units studied by Moebius *et al.* [92] and Pollini *et al.* [89] have ranges of 5 km and 1.1 km respectively. The commercially-available Jena Optronik RVS 3000 LIDAR has a slightly greater 10 km detection range. Even high-power ground-based laser rangefinders are limited to ranges of 3000 km when imaging RSOs without retroreflectors [90]. The greater ranges of laser communications devices are largely because the laser communications receiver is located on the targeted device and laser communications devices do not rely on reflecting a signal from their target. Conversely, laser rangefinders and LIDAR units rely on a small portion of their transmitted signal striking a target and a fraction of this reflected signal being reflected back to the laser rangefinder or LIDAR unit's receiver.

Despite these limitations, the sheer quantity of proposed satellites equipped with laser

Table 4.3: Parameters for the LCTv2.2 laser communications device [7].

Parameter	Value
Detector Aperture Radius (r_{det})	0.0675 m
Maximum Communications Range (R_{com})	45000 km
Beam Divergence α_d	7.2 μrad

communications devices (12000 for Starlink and 3236 for Kuiper Systems [94]) and their maximum ranges make laser communication devices worthy of further analysis. As such, I performed a feasibility study to determine their likely maximum range if they were adapted to act as laser rangefinders, in addition to their primary communications role.

Laser communication devices are not designed to receive reflected signals and may require hardware or software modifications to act as such. I chose to leave analyzing the feasibility of these modifications up to future researchers. Instead, I examined the maximum detection range at which a laser communications device could detect a target, assuming that these hardware challenges could be resolved without affecting the laser communication device's performance. As previously mentioned, the maximum range for this device, if acting as a rangefinder, will be limited by the strength of the return signal reflected by the targeted RSO. Reflected signal strength is highly dependent on the target's surface properties and the angles between the transmitter, target surface, and receiver. Depending on the target's surface, light may be reflected specularly, diffusely, or some combination of the two. Diffuse reflectivity occurs when light is scattered at many angles from a surface and is a function of the surface's diffuse reflectivity. Meanwhile, specular reflectivity is the mirror-like reflection of light and is a function of the surface's specular reflectivity coefficient [123].

To determine the maximum feasible detection range for a laser communications device, I first used the minimum fraction of transmitted light that is received by laser communications device to determine the device's maximum range. I then used this ratio to determine the maximum detectable range for a specularly reflective disc, a diffuse flat disc, and a combined diffusely/specularly reflective sphere. For this study, I used the specifications of the LCTv2.2 laser communications device, summarized in Table 4.3 [7].

Maximum Range Analysis The first step in this analysis was to determine the minimum fraction of light transmitted by a laser communications device to the light received by

the device. If a laser communications device with a beam divergence α_d [rad] is aimed towards another laser communications device with a communications aperture r_{det} [m] at the transmitting device's maximum communication range R_{com} [m], as shown in Fig. 4.2, the transmitted beam's area A_{beam} [m^2] at R_{com} [m] will be:

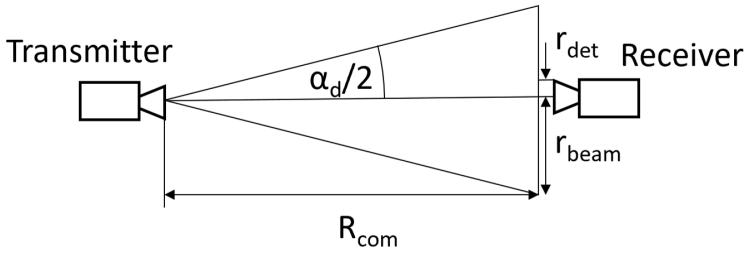

Fig. 4.2: Geometry for an optical transmitter with a beam divergence α_d and a receiver, with a receiving aperture radius r_{det} some distance R_{com} away.

$$A_{beam} = \pi r_{beam}^2 = \pi[R_{com}\tan(\alpha_d/2)]^2 \tag{4.4}$$

while the receiving device's detector area A_{det} [m^2] is:

$$A_{det} = \pi r_{det}^2 \tag{4.5}$$

Using these two areas, and assuming $A_{det} < A_{beam}$ at R_{com}, the minimum fraction of transmitted light required to detect a transmitted signal is η_{min}:

$$\eta_{min} = \frac{A_{det}}{A_{beam}} = \frac{r_{det}^2}{[R_{com}\tan(\alpha_d/2)]^2} = \frac{r_{det}^2}{R_{com}^2\tan(\alpha_d/2)^2} \tag{4.6}$$

Using the LCTv2.2's parameters, shown in Table 4.3, η_{min} for this laser communications device is 5.5×10^{-7}. While Eq. 4.6 examines a one-way transmission scenario, η_{min} represents the threshold of received-to-transmitted power for any transmitted signal. Assuming that a set of laser communications terminals have identical transmission and receiver hardware and that the receiver does not include polarization filters, η_{min} also represents the minimum threshold of received-to-transmitted power for reflected signals. In this study, I leveraged this relationship to determine the maximum range at which a laser communications terminal could detect a signal which was reflected from an RSO.

The power detected by a receiver P_{rx} [W] from light reflected from an RSO is a function of the RSO's optical cross section γ_v [m^2/sr], the optical incidence of light travelling towards the RSO I_o [W/m^2], and the solid angle of the receiver's aperture Ω_R [sr] at the RSO-observer range R [m] [124, 125]:

$$P_{rx} = \gamma_v I_o \Omega_R \tag{4.7}$$

where Ω_R is:

$$\Omega_R = \frac{A_{det}}{R^2} \tag{4.8}$$

Combining Eq. 4.7 and Eq. 4.8, and dividing both sides by the transmitted signal power P_{tx} [W], the ratio of received to transmitted power for a signal to be transmitted from a source and reflected by an RSO is:

$$\frac{P_{rx}}{P_{tx}} = \frac{\gamma_v I_o A_{det}}{R^2 P_{tx}} \tag{4.9}$$

A laser communication terminal's transmitted optical incidence I_o is a function of the transmitted signal power P_{tx} and the beam area A_{beam} at the RSO-observer range R such that:

$$I_o = \frac{P_{tx}}{A_{beam}} \tag{4.10}$$

Combining Eq. 4.9 and Eq. 4.10, and noting that $P_{rx}/P_{tx} \geq \eta_{min}$, the ratio of the returned signal from the RSO and the transmitted signal must be greater or equal to η_{min}:

$$\eta_{min} \leq \frac{P_{rx}}{P_{tx}} = \frac{\gamma_v A_{det}}{R^2 A_{beam}} = \frac{\gamma_v r_{det}^2}{R^4 \tan^2(\alpha_d/2)} \tag{4.11}$$

At the maximum RSO range R_{max}, this will become:

$$\eta_{min} = \frac{\gamma_v r_{det}^2}{R_{max}^4 \tan^2(\alpha_d/2)} \tag{4.12}$$

and, solving for R_{max}:

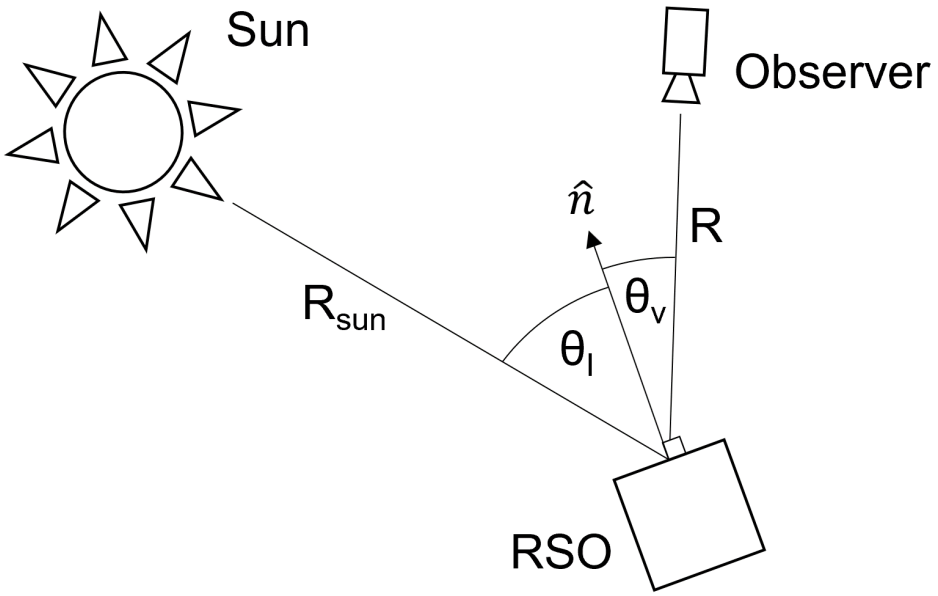

Fig. 4.3: Geometry between the Sun, RSO surface, and observer.

$$R_{max} = \left(\frac{\gamma_v r_{det}^2}{\eta_{min} \tan^2(\alpha_d/2)}\right)^{1/4} \tag{4.13}$$

Combining Eq. 4.6 and 4.13, the maximum RSO range R_{max} is:

$$R_{max} = \left(\frac{\gamma_v r_{det}^2}{\frac{r_{det}^2}{R_{com}^2 \tan(\alpha_d/2)^2} \tan^2(\alpha_d/2)}\right)^{1/4} = \left(\gamma_v R_{com}^2\right)^{1/4} \tag{4.14}$$

Using Eq. 4.14, I calculated the maximum detectable range of a given RSO with a known optical cross section γ_v. For a flat plate, γ_v is [124]

$$\gamma_v = A_{rso} B(\theta_v, \theta_I) \cos(\theta_v) \cos(\theta_I) \tag{4.15}$$

where $B(\theta_v, \theta_I)$ is the RSO's the bidirectional reflection distribution function. $B(\theta_v, \theta_I)$ is a function of the reflecting object's material properties and is highly dependent on the angles θ_v and θ_I. Where θ_v is the angle between the observer-RSO vector R and the RSO's surface normal $\hat{n}$ and θ_I is the angle between the Sun-RSO vector R_{sun} and the RSO's surface normal $\hat{n}$, shown in Fig. 4.3 [124]. Figure 4.3 is similar to Fig. 3.3, however Fig. 4.3 includes θ_v whereas Fig. 3.3 includes the phase angle θ_{phase} which is the sum of θ_v and θ_I.

$B(\theta_v, \theta_I)$ is at its maximum value, known as the glint angle, when θ_v, θ_I, and the surface normal are in the same plane and the two angles are equal and opposite to each other. The $B(\theta_v, \theta_I)$ value for objects that are highly specularly reflective will decrease rapidly if either angle changes. At this glint angle, a specularly reflective object can be viewed from very large distances [126].

Maximum Detectable Range of a Flat Disc I examined the maximum detectable range for a 0.5 m radius specularly reflective flat aluminzed Kapton disc. I chose aluminized Kapton because it is used in the outer layer of Multi-Layer Insulation (MLI), which is a common spacecraft material with a high specular reflectivity. I calculated γ_v using Eq. 4.15 and used this value to find the maximum expected detectable range for this disc using $B(\theta_v, \theta_I)$ values for aluminized Kapton at $B(0^o, 0^o)$ and $B(4^o, 0^o)$ from [127] as well as the LCTv2.2's maximum one-way communications range of 45000 km [7]. When θ_v and θ_I were aligned at the 0^o glint angle, the maximum detectable range was 35.8 km. However, when I rotated θ_v 4^o away from the RSO's surface normal, this maximum range dropped to 1.9 km. This drastic range reduction shows that the detectable range for specularly reflective RSOs is highly dependent on θ_v and θ_I. If either angle is varied by a few degrees, the RSO can become undetectable.

Unlike specular reflectivity, diffuse reflectivity is not affected by θ_v. As such, I investigated the maximum detectable range for a diffuse flat disc. Using a Lambertian diffuse reflectance model [128], light I_D is reflected evenly by a surface and is a function of the incoming light's intensity I_L [lux], the surface's diffuse reflectivity coefficient ρ_d, and the angle θ_I between the incoming light and object's surface normal:

$$I_D = I_L \rho_d \cos(\theta_I) \tag{4.16}$$

I modelled the light reflected by this diffuse disc as emanating equally in a half-sphere of radius R from a point source to determine the amount of light I_{rx} received by a detector with an aperture radius r_{det}:

$$I_{rx} = I_D \frac{r_{det}^2}{2R^2} = \frac{I_L \rho_d r_{det}^2 \cos(\theta_I)}{2R^2} \tag{4.17}$$

The amount of light incident I_L to a r_{rso} radius disc can be expressed as a fraction of the total light transmitted by a laser communications device I_{tx}:

$$I_L = \frac{A_{rso} I_{tx}}{A_{beam}} = \frac{r_{rso}^2 I_{tx}}{R^2 \tan^2(\alpha_d/2)} \tag{4.18}$$

Combining Eq. 4.17 and 4.18, and dividing both sides by I_{tx}, I expressed the returned light as a ratio η_R of the light transmitted I_{tx} to light received I_{rx}:

$$\eta_R = \frac{I_{rx}}{I_{tx}} = \frac{\rho_d r_{rso}^2 r_{det}^2 \cos(\theta_I)}{R^4 \tan^2(\alpha_d/2)} \tag{4.19}$$

Rearranging Eq. 4.19, I found the maximum RSO-observer range R_{max}, at the minimum η_{min} ratio:

$$R_{max} = \left(\frac{\rho_d r_{rso}^2 r_{det}^2 \cos(\theta_I)}{\eta_{min} \tan^2(\alpha_d/2)} \right)^{1/4} \tag{4.20}$$

I then combined Eq. 4.6 and 4.20:

$$\begin{aligned} R_{max} &= \left(\frac{\rho_d r_{rso}^2 r_{det}^2 \cos(\theta_I)}{\frac{r_{det}^2}{R_{com}^2 \tan(\alpha_d/2)^2} \tan^2(\alpha_d/2)} \right)^{1/4} \\ &= \left(\rho_d r_{rso}^2 \cos(\theta_I) R_{com}^2 \right)^{1/4} \end{aligned} \tag{4.21}$$

Solving Eq. 4.21 for the previous 0.5 m radius flat circular aluminized Kapton disc, assuming a diffuse reflectivity ρ_d of 0.07 [127], and an angle θ_I of zero, the maximum detectable range for the LCTv2.2 [7] is approximately 1.5 km. This is shorter than the disc's maximum specular range, but can be detected over a range of angles θ_I. The maximum detectable diffuse range remains above 1 km for θ_I angles greater than $\pi/4$.

Maximum Detectable Range of a Sphere This range analysis assumed that the disc's surface was perfectly flat. However, aluminized Kapton, and especially MLI, often has a multifaceted, "crinkly" appearance. An object covered by such a material will scatter light unevenly and, while each facet has a smaller surface area, there is a greater probability that some facets will be oriented with their glint angles facing an observer. If the number of facets increases, the probability that a portion of these facets is oriented at the glint angle increases,

but the size of each facet decreases. As the number of facets approaches infinity, each facet will become infinitesimally small, the object's reflective properties will approach those of a sphere. Using this approximation, I performed a second set of diffuse and specular reflectivity analyses using this spherical assumption.

A specularly reflective sphere's specular optical cross section $\gamma_{v,s}$ can be expressed as [123]:

$$\gamma_{v,s} = \frac{\rho_s r_{rso}^2}{4} \tag{4.22}$$

while a diffusely reflective sphere's diffuse optical cross section $\gamma_{v,d}$ is [123]:

$$\gamma_{v,d} = \frac{2\rho_d r_{rso}^2}{3\pi}[\sin(\theta_{phase}) + (\pi - \theta_{phase})\cos(\theta_{phase})] \tag{4.23}$$

For a phase angle of zero, this simplifies to:

$$\gamma_{v,d} = \frac{2\rho_d r_{rso}^2}{3} \tag{4.24}$$

These two models can be combined as:

$$\gamma_v = r_{rso}^2\left(\frac{2\rho_d}{3} + \frac{\rho_s}{4}\right) \tag{4.25}$$

I solved Eq. 4.13 for each of these optical cross sections, using a 0.5 m radius MLI-covered object with a ρ_s and ρ_d of 0.92 and 0.07 respectively [127]. The maximum specularly reflective range was 2.5 km, the maximum diffusely reflected range was 1.7 km, and the combined specular-diffuse range was 2.6 km. While these ranges were all greater than that of a diffusely reflective disc, an MLI-covered surface will likely not reach this spherical-limit[2]. If the surface has fewer facets, and if these facets have biased surface normals, the RSO's reflective properties will lie somewhere between the properties of a sphere and a flat plate. However, based on my theoretical maximum detectable range of between 1.0 km and 2.6 km, the LCTv2.2 laser communications device would have a comparable range to the Jenoptik scanning LIDAR unit [92] used by Nayak and Udrea in their study [91].

[2]Reflectivity testing of MLI sheets is an interesting area for future research, however quantifying the number, size, and orientation of surface facets would be challenging.

This analysis assumed that the transmitted and reflected signals were in the visual spectrum. However, as noted by [129], materials such as MLI, solar arrays, and aluminum can have reflectivities which are two to ten times higher at a wavelength of 1100 nm. Many laser communications terminals[94] and laser rangefinders[91, 130] operate in the infrared region and could achieve detection ranges which are higher than those presented here.

Search Time Analysis Using the 2.6 km maximum detection range, I calculated the search time required to find an RSO using the mean TLE catalogue errors from [131]. Assuming a laser communications device is searching for an object at a predicted range R,the scan rate $\dot{\Omega}_s$ in str/s will be:

$$\dot{\Omega}_s = \frac{\dot{A}_s}{R^2} = \frac{2R\tan(\alpha_d/2)R\tan(\dot{\theta}_s)}{R^2} = 2\tan(\alpha_d/2)\tan(\dot{\theta}_s) \tag{4.26}$$

Where $\dot{A}_s$ is the scan area rate at the RSO-observer range R, α_d is the laser beam's divergence, and $\dot{\theta}_s$ is the scan rate. Using the LCTv2.2's 7.2 μrad beam width, the 2.6 km combined specular-diffuse range, and a scan rate of 3^o/s based on [132], the expected scan rate is 3.8×10^{-7} str/s. Using the elliptical area A formed by the average along-track σ_v and out-of-plane σ_w TLE errors, I calculated the 1-σ search envelope Ω_e in steradians as:

$$\Omega_e = \frac{A}{R^2} = \frac{\pi\sigma_v\sigma_w}{R^2} \tag{4.27}$$

using the average average along-track TLE error of 0.471 km and the average out-of-plane TLE error of 0.126 km for LEO objects from [131], as well as my calculated 2.6 km combined specular-diffuse range, the resulting search envelope was 0.0325 str. Finally, I calculated the required search time t_{search} as:

$$t_{search} = \frac{\Omega_e}{\dot{\Omega}_s} \tag{4.28}$$

Using Eq. 4.28, it would take 8.6×10^4 s or approximately 23.9 hours to search the 0.0325 str 1-σ search envelope. Using a laser communications device for RSO ranging is unfeasible based on the results of this search-time analysis, the detection range analysis, and the challenges in adapting a laser communication terminal's hardware to function as a laser rangefinder.

4.2.2.1 RSO Ranging Summary

Based on the maximum expected range for each of the RSO ranging methods presented in this section, summarized in Table 4.4, LIDAR devices are the most promising with a maximum range of 10 km.

Table 4.4: Expected RSO detection ranges for various ranging methods.

RSO Ranging Method	**Expected Range**
SAR	6 - 35 km
Laser Rangefinders [91]	3 km
Flash LIDAR [89]	5 km
LIDAR [130]	10 km

The detection distances for these ranging methods are considerably shorter than the optical detection method presented in Ch. 3. As such, it is important to establish if enough RSOs will come close enough to an observing spacecraft for the observing spacecraft to use RSO-ranging measurements for position and attitude estimation. Research into conjunction event frequency by Richardson-Little *et al.* [133] for the RSO constellation and by Klinkrad [134] for the European Remote-Sensing Satellite (ERS) constellation can provide some insight. Both of these satellite constellations are located in sun synchronous orbits, with ERS at 782 km altitudes and RCM at 592 km. Richardson-Little *et al.* found that approximately 847 objects between 5-10 cm in diameter will come within 1.5 km of each RCM satellite over its 7.33 year lifetime [133], or approximately 9.6 conjunction events per month. Meanwhile, Klinkrad determined that, over a 14 month period starting in 1996, the two satellites in the ERS constellation experienced 2323 and 2273 potential conjunction events with objects of various sizes within 25 $\times$ 10 $\times$ 10 km collision reference ellipsoids, centred on each spacecraft [134], or 5.5 and 5.4 conjunction events per day. Based on the frequency of these conjunction events, navigation using RSO-ranging data will be difficult. However, the number of RSOs orbiting the Earth are increasing significantly [100]. While the further growth of the RSO population endangers our continued use of space, this growth may also make spacecraft navigation using RSO-ranging measurements feasible in the near future.

4.3 State Estimation Analysis

To determine how effectively range-based RSO measurements can be used to estimate RSO positions, I implemented an EKF and a UKF using the same dynamics models as previously described in Ch. 3 Sec. 3.4.1.[3] The observing spacecraft's state vector $X = [x \;\; y \;\; \dot{x} \;\; \dot{y} \;\; \phi \;\; \dot{\phi}]^T$ was the same as in Ch. 3 and included the observer's position and velocity in x and y as well as its attitude ϕ and angular rate $\dot{\phi}$. I propagated the observer's state using Eq. 3.27 through 3.30. Again, I placed the observing spacecraft in a 400 km circular orbit, starting at 0° from the x-axis, with a mass m of 84 kg, and an inertia J of 2.8 kgm^2. I applied the same zero-mean Gaussian process noises of one percent of the gravitational force (7.3 N) and applied torque (0.05 μNm). I propagated the observer's state using a fourth order Runge Kutta integrator with the same 1 s timesteps as Ch. 3. As with the previous EKF implementation in Ch. 3, I had to increase the EKF's process noise covariance Q for the EKF to converge. As such, I also tested a UKF's performance in this navigation scenario.

The measurement function was:

$$z(t) = h[X(t)] + v(t) = \sqrt{[x(t) - x_{ri}(t)]^2 + [y(t) - y_{ri}(t)]^2} + v(t) \tag{4.29}$$

As in Sec. 3.4.1, h is the measurement function, $X(t)$ is the observer's state at time t, and $z(t)$ are the measurements. $x_{ri}(t)$ and $y_{ri}(t)$ are RSO i's position at time t. I modelled the measurement noise $v(t)$ as a zero-mean additive Gaussian white noise, with a standard deviation of 10 m, based on the Jena Optronik RVS 3000 LIDAR [130]. Equation 4.29 does not contain any information about the observing spacecraft's attitude, so neither the EKF nor UKF would be able to converge on accurate ϕ or $\dot{\phi}$ estimates. As such, I did not attempt to estimate the observing spacecraft's attitude ϕ or angular acceleration $\dot{\phi}$.

Using this observer model, I tested the performance of the EKF and UKF using the same initial position and velocity estimate errors as Ch. 3: [500 km 500 km 1 km/s 1 km/s]^T. These tests used the same TLE errors as in Ch. 3. as well as a 10 km maximum detection range and 40° field of view field of view based on the Jena Optronik RVS 3000's specifications [130]. To

[3]This included the fixed observer orbital radius assumption when calculating the orbital perturbations. Both the EKF and UKF had comparable performances to the results shown in this chapter when this approximation was removed in Ch. 5.

account for this maximum range, I modelled 3 RSOs in various altitudes and starting angles, summarized in Table 4.5, to ensure that some RSOs would be visible periodically during the simulation. These three conjunction events, occurring within a 2.33 hour window, is higher than what previous researchers predicted for the RCM [133] and ERS [134] constellations, but could be possible as the number of RSOs increase in LEO over time. Based on these conditions, as shown in Fig. 4.4, two RSOs were initially observable. There were no RSOs visible between approximately 3100 s and 5000 s as well as between 9000 s and 11000 s. As with Ch. 3, I assessed each filter's performance by examining the filter's estimate error and the square root of the diagonal elements of the filter's covariance matrix. These square roots correspond to the filter's predicted estimate error standard deviation.

Table 4.5: RSO starting orbital radii and angles from the x axis.

RSO Number	**Initial Altitude (km)**	**Initial Angle from the x Axis (°)**
1	401	0
2	390	-1
3	395	0

Figure 4.5 shows the x position and attitude estimate errors for both the EKF and UKF. The position estimates, shown in Fig. 4.5, initially converged. However, when no RSOs were visible between 3100 s and 5000 s as well as between 9000 s and 11000 s, both filters began to diverge until RSO measurements became available. As in Ch. 3, both filters significantly underestimated their state estimate covariances due to the unmodelled TLE error. However, when no measurements were available, the covariance estimates increased accordingly. These tests confirm that both filters can converge on position estimates when including TLE errors, a 10 km maximum detection range, and a 40° field of view if sufficient RSOs are visible. These tests assumed that there were 3 RSOs in close proximity to the observing spacecraft with sufficient reflectivity to be detectable. Assuming these conditions are met, RSO-navigation using range measurements is possible.

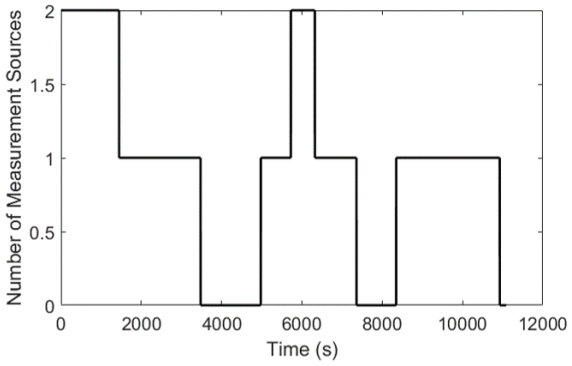

(a) Total Number of Detected RSOs over Time

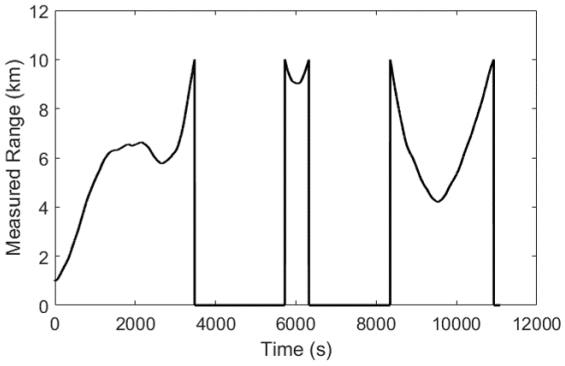

(b) Measurement Source 1 over Time

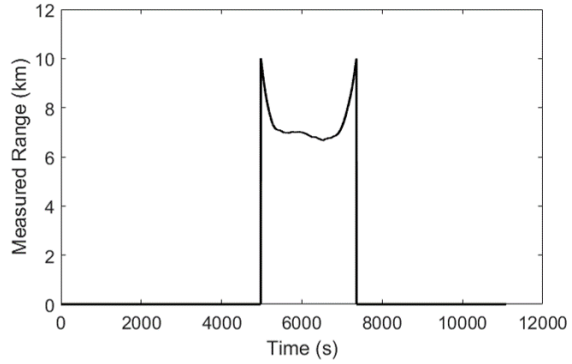

(c) Measurement Source 2 over Time

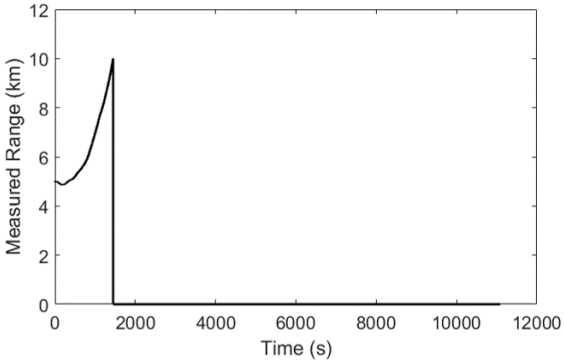

(d) Measurement Source 3 over Time

Fig. 4.4: Total number of detected RSOs and individual measurement values over time.

4.4 Chapter Summary

This chapter examined the feasibility of using several different classes of sensors, including laser communication terminals, laser rangefinders, Light Detection and Ranging devices (LIDARs), and synthetic aperture radars (SARs). Based on this analysis, LIDAR devices are the most promising sensors to use as range-based sensors for RSO-based navigation. Conversely, laser communications terminals are not feasible for RSO ranging. It may be possible to use SAR for RSO-based navigation, however SAR payloads use large amounts of power and typically have restrictive pointing requirements. These constraints would limit SAR-equipped spacecraft to observing RSOs that pass between itself and the spacecraft's typical observation target.

Using parameters from the most promising ranging sensor, a LIDAR device, I adapted the RSO navigation simulation from Ch. 3 to use range measurements and proceeded to test the performance of an EKF and a UKF when subjected to a combination of TLE errors and

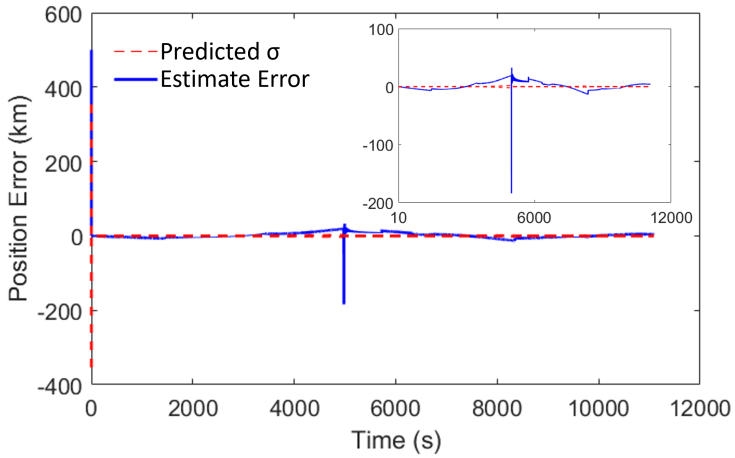

(a) Test 5 EKF x Position Error and σ

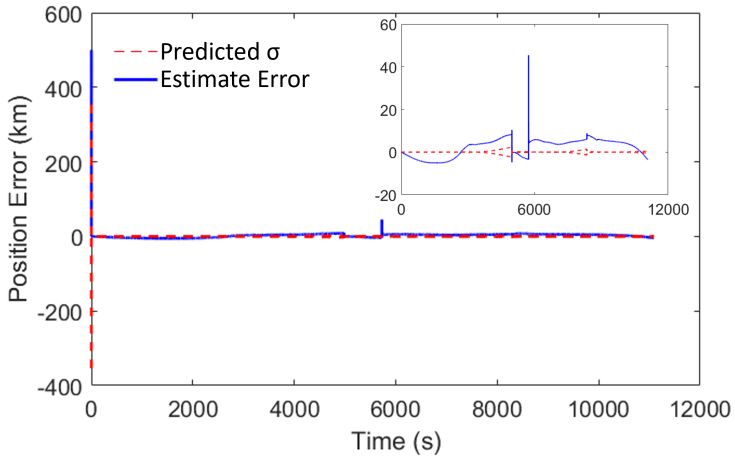

(b) Test 6 UKF x Position Error and σ

Fig. 4.5: Extended Kalman Filter (EKF) and Unscented Kalman Filter (UKF) Resident Space Object (RSO) x position errors, and the corresponding square roots σ of each filter's covariance estimate, when estimating an observing spacecraft's orbital state with TLE errors and measurement restrictions.

measurement constraints. The EKF and UKF were both capable of estimating the observing spacecraft's position and velocity. However, as in Ch. 3, I had to artificially increase the EKF's process noise covariance for the filter to converge. Additionally, neither filter was able to accurately predict their true estimate errors using the square roots of their state covariance estimates due to the TLE error included in the measurement model. The effect of this covariance error mismodelling provides additional evidence for Hypothesis 1.1, that a state estimator's reliability is a function of a set number of quantifiable influencing-factors, and that unmodelled measurement errors are one such factor. Chapter 5 explores how including

the reference RSO states and RSO position errors in the filter's state and dynamics models affects the filter's trustworthiness.

Based on the analyses performed in this chapter, it may be possible for a spacecraft, using RSO range measurements, to estimate its orbital position and velocity in the near future. The primary limiting factors for this method are the maximum detection range of the ranging sensor and the number of RSOs entering this detection range. Based on the work of [133] and [134], there are likely not enough conjunction events for an observing sensor to receive sufficient measurements at present. However, as the number of RSOs increases over time [100], this method will become more viable. Additionally, this chapter assumed that each detected RSO could be matched to an object with a known orbit. Object identification was not within the scope of my research, but future research into object identification methods are necessary for the feasibility of this method.

Chapter 5 builds on the results of Ch. 3 and 4 to explore in detail how measurement nonlinearity, among other factors, affect an estimator's trustworthiness.

Chapter 5

Filter Reliability

"Don't trust the cannibal just 'cos he's usin' a knife and fork!"

Terry Pratchett, *Carpe Jugulum*, 1998.

This chapter examines methods of ensuring the reliability of the Kalman filters previously presented in Ch. 3 and 4. To explore how researchers can better-quantify filter reliability, Sec. 5.1 examines the various trustworthiness factors that affect reliability. Section 5.2 then explores metrics that can be used to quantify a filter's reliability, including a metric that I made [57]. Section 5.3 applies these metrics to quantitatively explore how the trustworthiness factors introduced in Sec. 5.1 affect the overall performance of a Kalman filter by conducting a series of Monte Carlo simulations for each permutation of trustworthiness factors. Section 5.3.1 introduces the trustworthiness factors to be tested, as well as my hypotheses for each trustworthiness factor's performance. Section 5.3.2 presents the test methodology for conducting these Monte Carlo simulations and Sec. 5.3.3 presents and discusses the test results. Finally, Sec. 5.4 provides a summary for this chapter.

The contents of this chapter contains research that has been published in the following articles: [135], [45] and [136].

V

5.1 Factors that Affect Filter Reliability

In Sec. 2.1.1, I broadly described the performance of a Kalman filter using three metrics: accuracy, precision, and trustworthiness. Accuracy and precision are traditional performance metrics, with accuracy describing the presence and magnitude of any estimate biases, which cause a filter's mean estimate error to become non-zero, and precision describing the magnitude

of a filter's estimate error standard deviation [137]. Finally, I have defined the third metric, trustworthiness, as how well the filter's state covariance models the estimate error [57].

Assuming that a Kalman filter is properly constructed, that the measurements and dynamics are linear, and that all noise sources are white noises, the filter's estimate error should be unbiased and exhibit a variance reflected by the diagonal elements of the filter's covariance estimate [8, 138]. The presence of any biases can indicate that the filter may have been constructed incorrectly or that the underlying dynamics contain non-ideal noises. Additionally, biases can cause issues with any associated control systems or give operators an inaccurate depiction of the system being estimated.

Issues with a filter's precision are less severe, as long as the filter meets any associated estimation requirements. The magnitude of a filter's estimate error at steady state should be a function of the magnitude of the process and measurement noise covariances [8, 138]. If the filter's precision must be improved, a designer can use less noisy sensors, reduce process noise sources, or refine their dynamics model to explicitly include more noise sources.

Quantifying and interpreting a filter's trustworthiness is more challenging than quantifying the filter's accuracy or precision. It is possible for a filter to converge to a precise solution with a predicted estimate error covariance that is significantly different from the true estimate error covariance. If the estimated covariance is undersized, the filter is underestimating the variability within the system. Similarly, if the estimated covariance is oversized, it is overestimating the system's variability. Ensuring that the filter presents an accurate representation of the underlying system is key to establishing the filter's reliability and to enabling the filter's use in complex systems. This need for reliability is especially true for space applications [39]. In this chapter, I explore how the following factors affect filter trustworthiness.

Filter Variant Various versions of the Kalman Filter such as the EKF and UKF, referred to in this chapter as the filter variant, use different approaches to nonlinearities. The filter's ability to accurately model nonlinear state and measurement dynamics will affect the filter's trustworthiness. Any differences between the filter's approximation and the true measurement and/or state dynamics, such as linearization errors, will introduce unmodelled errors into the

system.

Measurement State Element Model Measurement sources may experience dynamics that, if neglected, can introduce unmodelled uncertainty into a system. However, if the filter estimates both the desired state and aspects of the measurement source's dynamics, the filter should capture more of these unknowns and therefore improve estimator confidence.

Process Noise Covariance Model A filter which more accurately models process noise, and includes more sources of process error such as linearization and integration errors, should perform better and have more trustworthy results than a filter with a less accurate process noise model.

Measurement Linearity and Observability A filter which uses more linear measurement sources should experience less severe linearization errors and should therefore be more trustworthy. However, the estimated state must be fully observable for the filter to fully converge for all state elements. If a filter's measurements are insufficient for full observability, and if the unobservable state elements are not stable (and therefore not detectable), the filter will diverge [139]. In these situations, if the filter is sufficiently nonlinear or if the initial state estimate is too far from the true state, it is possible for the state to change more rapidly than what is assumed in the filter's dynamics model. In the absence of measurements for the unobservable state elements, their corresponding estimate errors will become unbounded by the state covariance estimate and result in poor trustworthiness.

5.2 Measuring Filter Reliability

Quantitative metrics are essential for comparing the trustworthiness factors described in 5.1, in order to determine how these factors affect a filter's trustworthiness. To evaluate these factors, I used three such metrics: Normalized Estimate Error Squared (NEES) [20], Normalized Innovation Squared (NIS) [20], and Covariance Trust Ratio (CTR) [57]. NEES and NIS are established metrics from the literature, previously described in Ch. 2.3.2, and both use Monte Carlo simulations to accumulate sufficiently large datasets to analyze an

estimator's performance. Conversely, CTR is a metric that I devised which uses data framing to perform a statistical analysis of a filter's error and covariance estimates. Section 5.2.1 presents the CTR metric while Sec. 5.2.2 demonstrates its use on the simulations previously conducted in Ch. 3. The CTR metric, as well as NEES and NIS, are used in Sec. 5.3.3 to evaluate the reliability for each Trustworthiness Factor Combination (TFC) described in 5.1.

Note that in addition to these quantitative metrics, a method for qualitatively evaluating the reliability of an optimal filter is to observe the proportion of state estimate errors that are bounded by the square roots of each of the diagonal elements of the filter's covariance matrix P [33]. These diagonal estimates form the filter's estimate of each state's variance and therefore the square roots of these values form the predicted standard deviations of each element σ_{est}. These variances should perfectly match the actual error variance for an optimal filter, such as a classic Kalman Filter, using linear measurements, and linear dynamics as well as white process and measurement noise estimates that match the true process and measurement noises. For these optimal conditions, 68% of the state estimate errors should be bounded by the filter's predicted variances. However, nonlinear extensions of the Kalman Filter, including both the EKF and UKF, may not accurately represent the real error variance.[1] By observing how well the filter's predicted estimate error standard deviations bound the filter's state estimate errors, the observer can evaluate the filter's performance. While qualitative, this method is still useful to illustrate filter performance for the reader and can form the basis for quantitative assessment methods. In fact, both the NEES and CTR metrics quantitatively evaluate how well a filter's covariance estimate bounds its estimate errors.

5.2.1 Covariance Trust Assessment Method for Kalman Filters

As an alternative to NEES and NIS, I developed the CTR $\eta^j(k,a)$ in [57] for quantifying the estimator trust for each state element j at each timestep k for a moving frame a. As with NEES and NIS, the CTR is related to the Mahalanobis Distance [34]. However, while

[1] This is especially true for the EKF presented in Ch. 3, as it was unable to accurately estimate the error variance without artificially increasing the process noise. The UKF was able to better capture the error variance, but it still provided non-optimal estimates.

the Mahalanobis Distance metric is calculated using data from a single timestep, the CTR uses windowed average estimate error means and standard deviations to reduce the CTR's variability.

$$\eta^j(k,a) = \frac{|\mu^j_{true}(k,a) + \sigma^j_{true}(k,a)|}{\sigma^j_{est}(k)} \tag{5.1}$$

where the moving mean estimate error $\mu^j_{true}(k,a)$ is defined as

$$\mu^j_{true}(k,a) = \frac{1}{a+1} \sum_{i=k-a/2}^{k+a/2} e^j(i) \tag{5.2}$$

and the moving standard deviation of the filter's estimate error $\sigma^j_{true}(k,a)$ is defined as

$$\sigma^j_{true}(k,a) = \sqrt{\frac{1}{a+1} \sum_{i=k-a/2}^{k+a/2} \left[e^j(i) - \mu^j_{true}(k)\right]^2} \tag{5.3}$$

The CTR $\eta^j(k,a)$ compares the square root of the diagonal elements of the filter's state covariance P (*i.e.* the filter's estimated error standard deviation σ^j_{est} for each state element) with the moving mean estimate error $\mu^j_{true}(k,a)$ and moving standard deviation of the filter's estimate error $\sigma^j_{true}(k,a)$ for each timestep k and state element j. These truth statistics are calculated using a moving frame of $a+1$ timesteps, centred on the current timestep k, and the filter's estimate error $e(k)$ [57].

For an optimal filter, such as the Kalman Filter estimating a system with linear dynamics, linear measurements, white process noises, and white measurement noises, the estimated error standard deviations σ^j_{est} will match the true error standard deviations $\sigma^j_{true}(k,a)$ and the mean estimate errors $\mu^j_{true}(k,a)$ will be zero. This will result in CTR values of unity. It is desirable for a non-optimal filter to have CTR values that are as close to unity as possible, however CTR values above and below zero provide some insight into the filter's performance. CTR values $\eta^j(k,a)$ greater than unity indicate that the filter is under-estimating its state covariance P while values less than unity mean the filter is over-estimating P.

Increasing the size of a decreases the CTR's variability if the frame is stationary –*i.e.* that the estimate error statistics remain constant over this sampled span on both sides of the current timestep. While estimate errors *should* become stationary if the estimate

error converges, this is not always the case for non-optimal filters. As such, I explored dynamically varying the frame size at each timestep using a series of stationarity tests. This dynamic frame sizing maximized the stationary frame over which the CTR was calculated and reduced the CTR's variability between simulations. Based on this stationarity study, described in Appendix B, using a variable frame size a provides a marginally more repeatable CTR than using a fixed frame size. However, determining the optimal variable frame size at each timestep is too numerically costly for practical use. As such, I used a fixed frame size throughout my research.

I used five variations of the CTR metric to evaluate filter performance: as a time-dependent function, as a cumulative distribution function, as a probability density function, the state-element average, and the overall average. The time-dependent function, as shown in Fig. 5.1, shows $\eta^j(k, a)$ for each timestep k. This formulation is useful for determining how an estimator's trustworthiness varies with time.

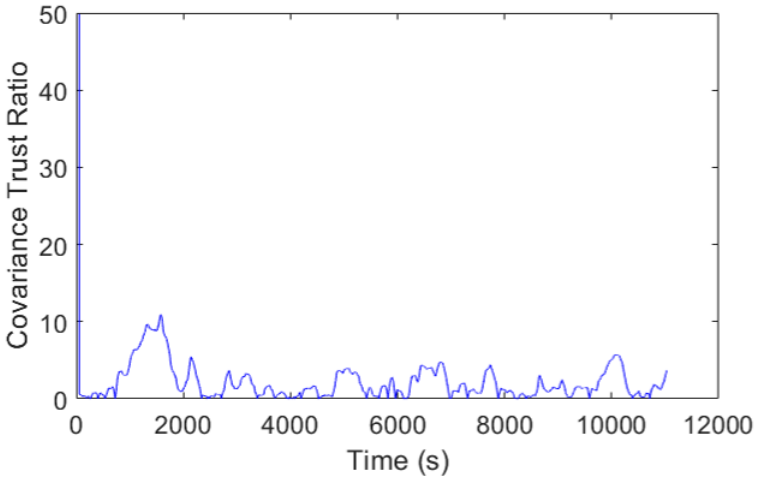

Fig. 5.1: Example of the Covariance Trust Ratio (CTR) as a time-dependent function. Note that the fluctuations seen in the CTR are due to measurement Jacobian phasing effects, as described in Sec. 3.4.2

Similarly, the cumulative distribution function shows the percentage of the CTR that is below a given value. This formulation, shown in Fig. 5.2, is useful for determining the CTR threshold $\eta_t(a)$, the percentile at which the CTR is at or below unity. The cumulative distribution function is also useful for visualizing how the ratio's tails are distributed.

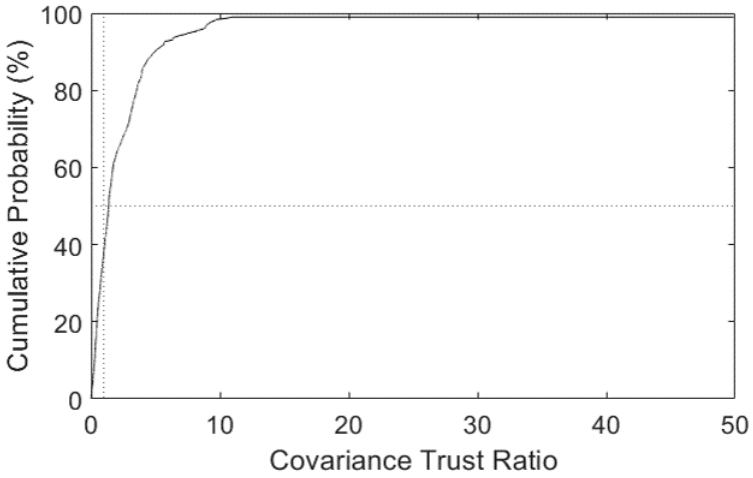

Fig. 5.2: Example of the Covariance Trust Ratio (CTR) as a cumulative distribution function.

In addition to the cumulative distribution function, it is also useful to the CTR as a probability density function. This formulation, shown in 5.3, shows the probabilities of individual binned CTR values.

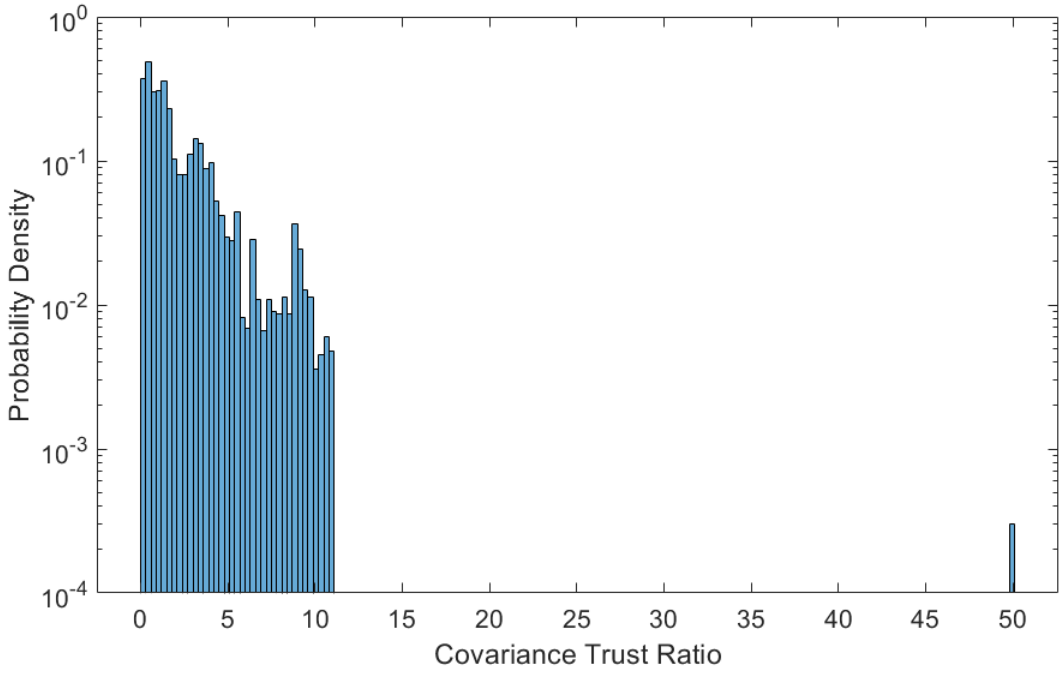

Fig. 5.3: Example of the Covariance Trust Ratio (CTR) as a probability density function.

Typically, I use linear-linear probability density function plots. However, this CTR example contained a large anomalous value at the first timestep which can only be seen

when the y axis uses a logarithmic scale. Figures 5.1 and 5.2 also show this anomalous value at the first timestep and at a 100% cumulative probability respectively. This anomalous value occurs because the filter used to generate these results had a very large initial estimate error at the first timestep. This initial estimate error was unrepresentative of the filter's performance and biased $\eta^j(1,a)$. Due to this bias, I recommend that other researchers do not include $\eta^j(1,a)$ when calculating the average CTR metrics $\eta^j_{av}(a)$ and $\eta_{av}(a)$.

The average CTR $\eta^j_{av}(a)$ for each state element j over the total number of timesteps K, excluding the first timestep, is calculated as [57]

$$\eta^j_{av}(a) = \frac{1}{K-1}\sum_{i=2}^{K}\eta^j(i,a) \tag{5.4}$$

The average CTR $\eta^j_{av}(a)$ for each state element are useful for comparing the relative trustworthiness of different state elements and identifying specific state elements which are performing poorly. Finally the average CTR for all j state elements $\eta_{av}(a)$ is calculated as [57]

$$\eta_{av}(a) = \frac{1}{n_x}\sum_{j=1}^{n_x}\eta^j_{av}(a) \tag{5.5}$$

In addition to its utility in measuring filter trustworthiness, the average CTR is useful for comparing the performance of various filters and as a cost function for various optimizers. See Appendix B for an optimization application example.

5.2.2 Covariance Trust Ratio Implementation and Simulation

To demonstrate the utility of the CTR, I compared the performance of the UKF and EKF estimators presented in Ch. 3 when conducting Test 3: estimating an observer's state using angle measurements from nearby objects while neglecting observability constraints on order to examine each filter's reliability over an extended period. The CTR was applied using a centred frame size a of 300 samples, chosen by first setting a to an arbitrarily large number and then progressively reducing a until η^j_k changed by less than 2% of the previous simulation's values. The CTR was first calculated after 151 timesteps when a centred frame of size a was possible and to exclude the initial filter estimate. Note that the initial filter estimate at the first

timestep was excluded, as previously discussed in Sec. 5.2.1, to eliminate the bias caused by the filter's initial state estimate. The EKF was simulated with and without augmenting its process noise covariance Q (discussed in Ch. 3) to quantitatively assess how increasing Q affected its performance as well.

Figures 5.4, 5.5, and 5.6 show the CTR $\eta^j(k,a)$ probability density functions and cumulative distribution functions for the EKF without augmented Q while Fig. 5.7, 5.8, and 5.9 show the CTR $\eta^j(k,a)$ probability density functions and cumulative distribution functions for the EKF with augmented Q. Similarly, Fig. 5.10, 5.11, and 5.12 show the CTR $\eta^j(k,a)$ probability density functions and cumulative distribution functions for the UKF. Tables 5.1, 5.2, and 5.3 present the CTR thresholds $\eta_t(a)$, average CTRs $\eta^j_{av}(a)$, median CTRs $\eta^j(k,a)$, and CTR standard deviations for the EKF without Q augmentation, the EKF with Q augmentation, and for the UKF respectively.

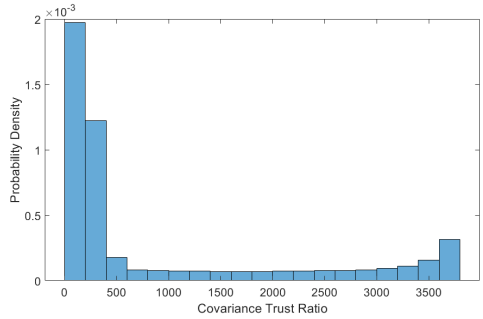

(a) X position CTR PDF

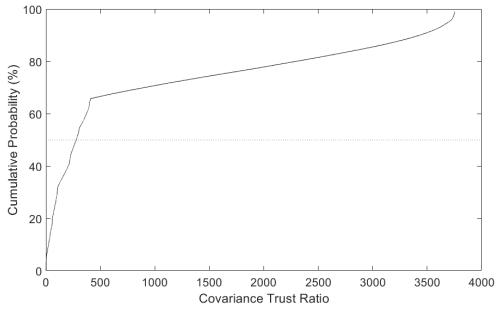

(b) X position CTR CDF

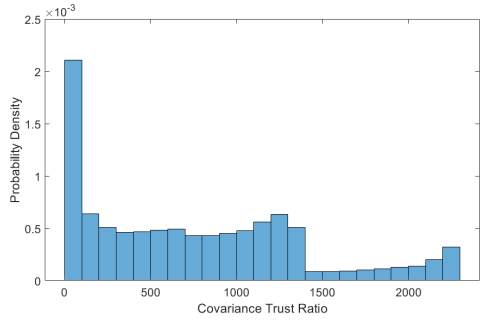

(c) Y position CTR PDF

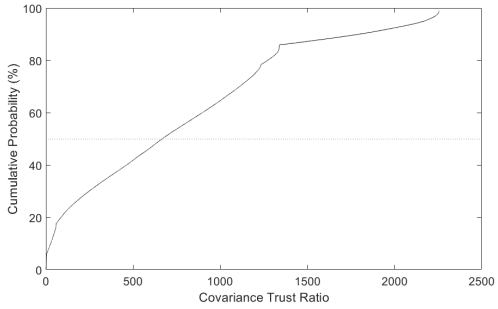

(d) Y position CTR CDF

Fig. 5.4: CTR $\eta_{k,a}^{j}$ PDFs and CDFs for EKF position estimates without augmented Q.

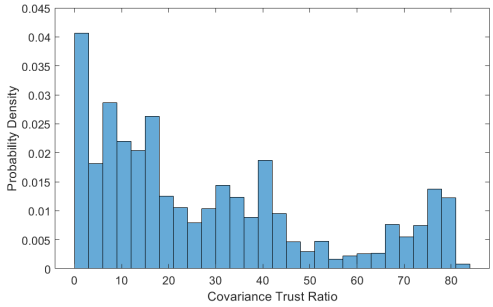

(a) X velocity CTR PDF

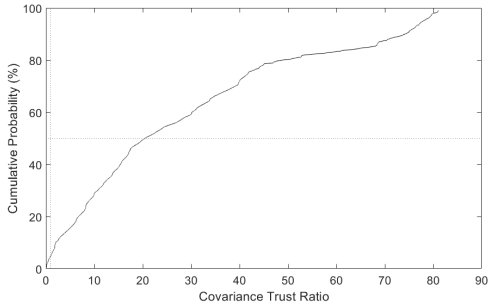

(b) X velocity CTR CDF

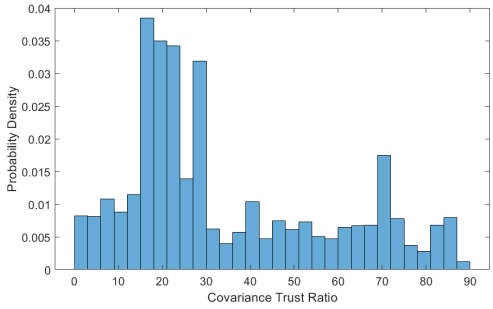

(c) Y velocity CTR PDF

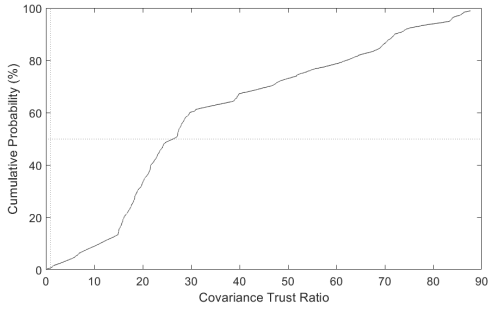

(d) Y velocity CTR CDF

Fig. 5.5: CTR $\eta_{k,a}^{j}$ PDFs and CDFs for EKF velocity estimates without augmented Q.

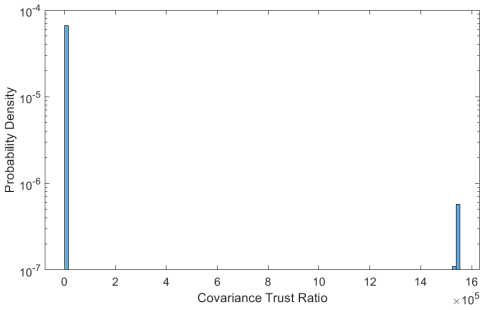

(a) Angular position CTR PDF

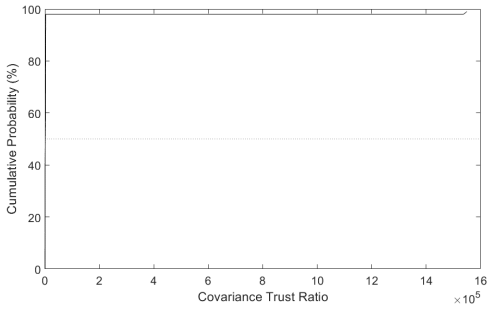

(b) Angular position CTR CDF

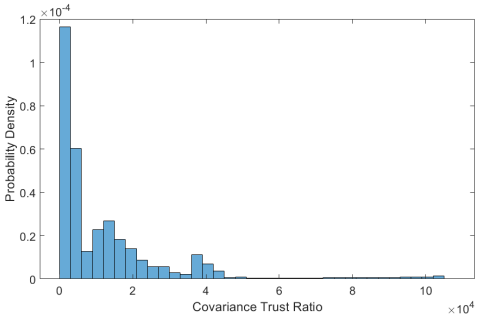

(c) Angular velocity CTR PDF

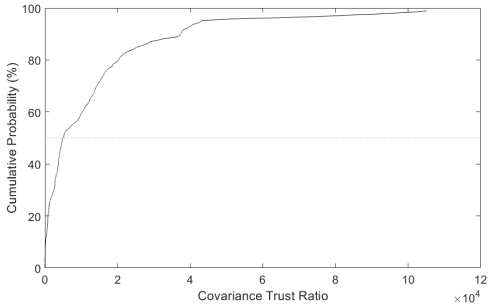

(d) Angular velocity CTR CDF

Fig. 5.6: CTR $\eta_{k,a}^{j}$ PDFs and CDFs for EKF angle state estimates without augmented Q.

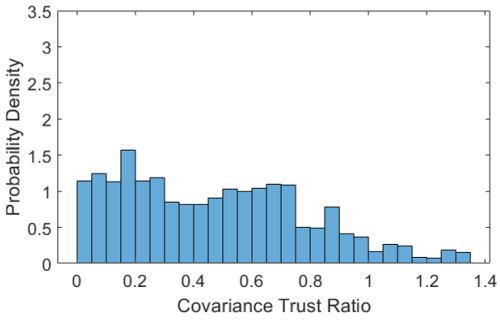

(a) X position CTR PDF

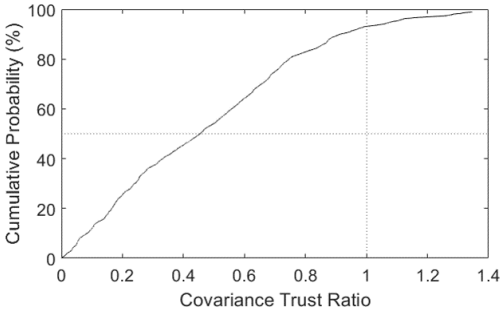

(b) X position CTR CDF

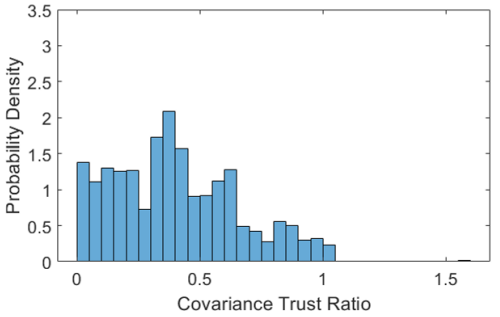

(c) Y position CTR PDF

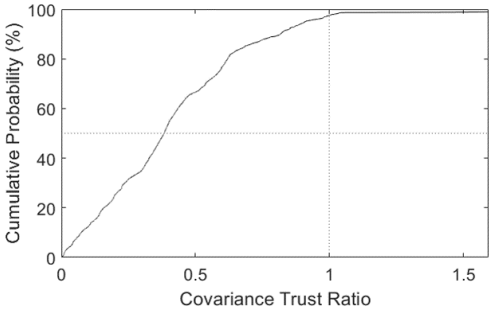

(d) Y position CTR CDF

Fig. 5.7: CTR $\eta_{k,a}^{j}$ PDFs and CDFs for EKF position estimates with augmented Q.

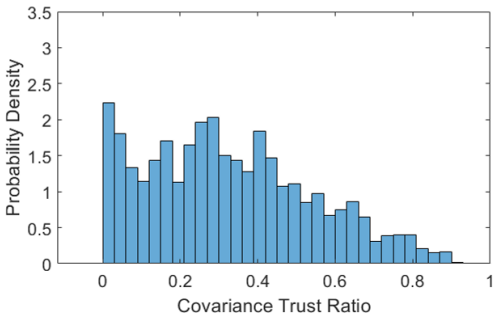

(a) X velocity CTR PDF

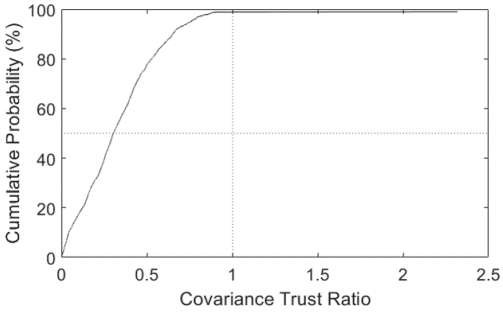

(b) X velocity CTR CDF

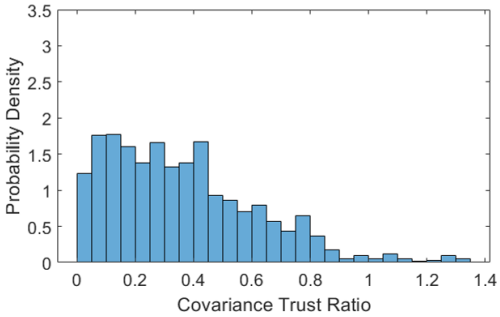

(c) Y velocity CTR PDF

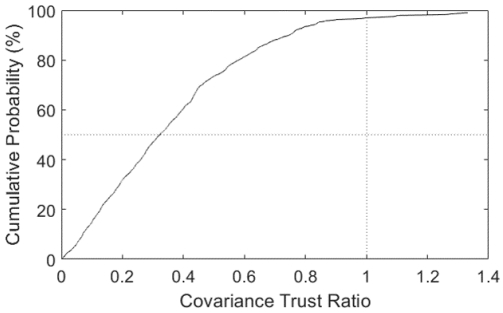

(d) Y velocity CTR CDF

Fig. 5.8: CTR $\eta_{k,a}^{j}$ PDFs and CDFs for EKF velocity estimates with augmented Q.

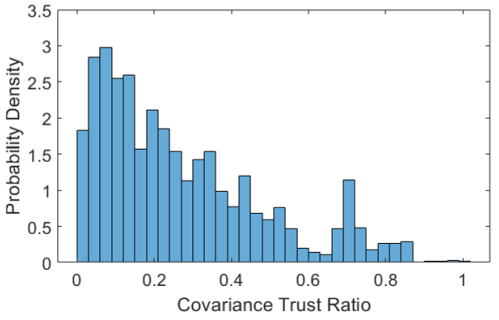

(a) Angular position CTR PDF

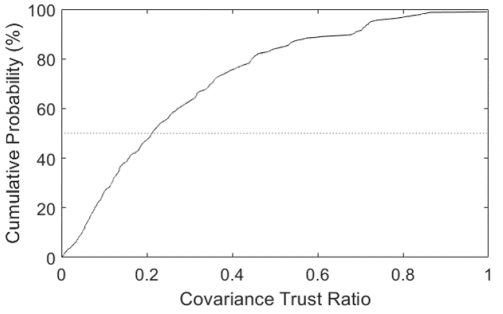

(b) Angular position CTR CDF

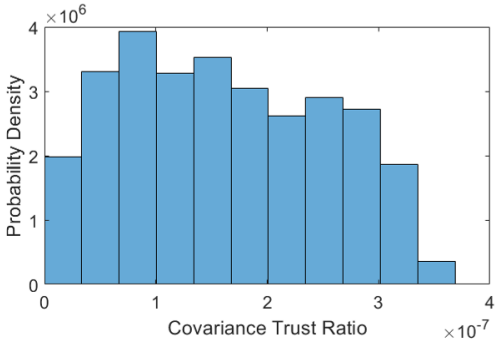

(c) Angular velocity CTR PDF

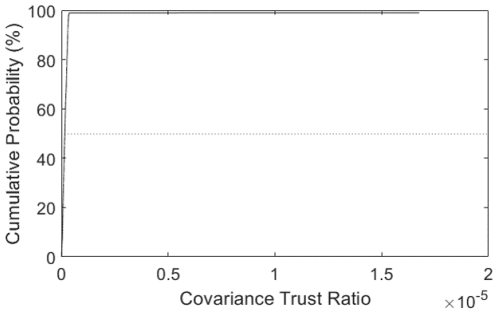

(d) Angular velocity CTR CDF

Fig. 5.9: CTR $\eta_{k,a}^{j}$ PDFs and CDFs for EKF angle state estimates with augmented Q.

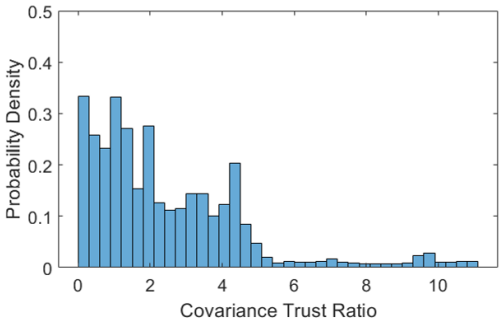

(a) X position CTR PDF

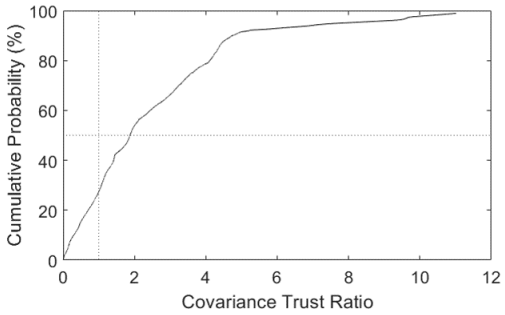

(b) X position CTR CDF

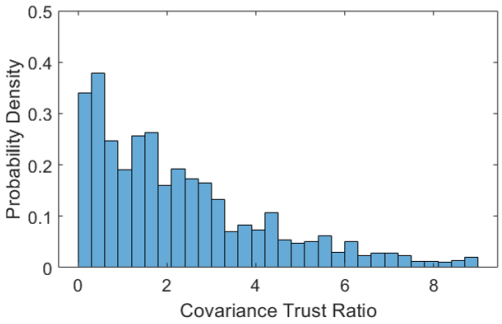

(c) Y position CTR PDF

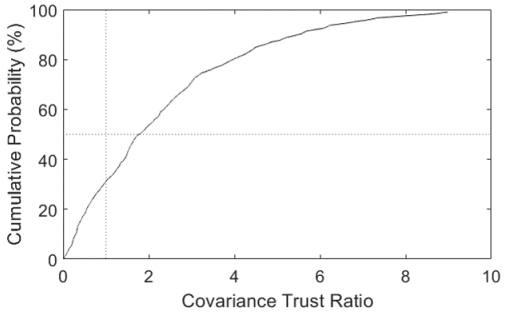

(d) Y position CTR CDF

Fig. 5.10: CTR $\eta_{k,a}^{j}$ PDFs and CDFs for UKF position estimates.

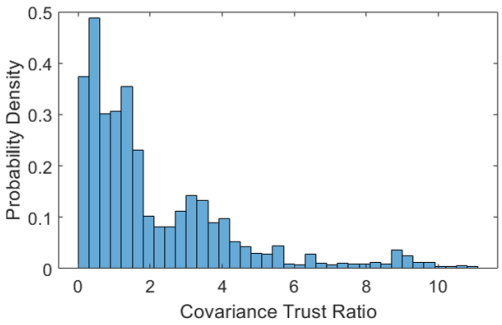

(a) X velocity CTR PDF

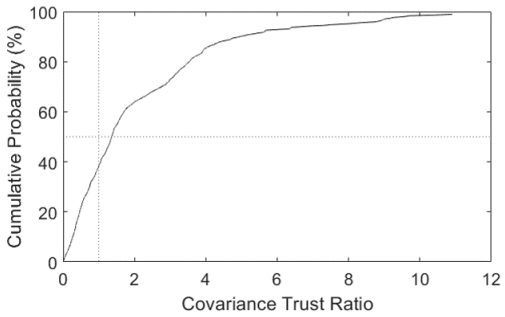

(b) X velocity CTR CDF

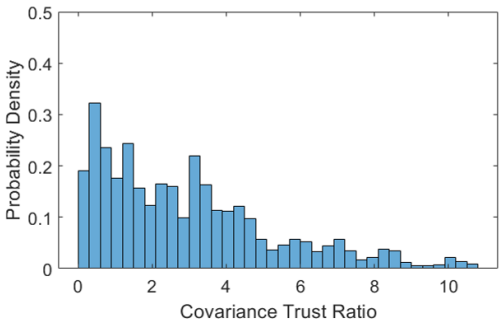

(c) Y velocity CTR PDF

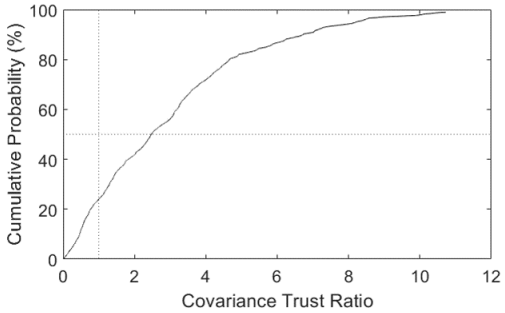

(d) Y velocity CTR CDF

Fig. 5.11: CTR $\eta_{k,a}^{j}$ PDFs and CDFs for UKF velocity estimates.

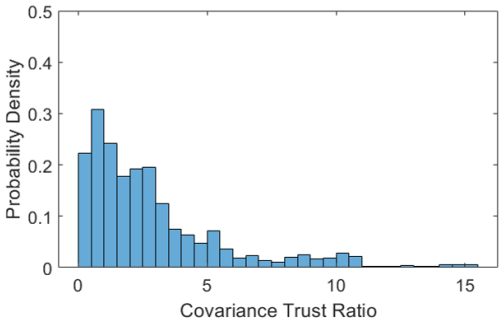

(a) Angular position CTR PDF

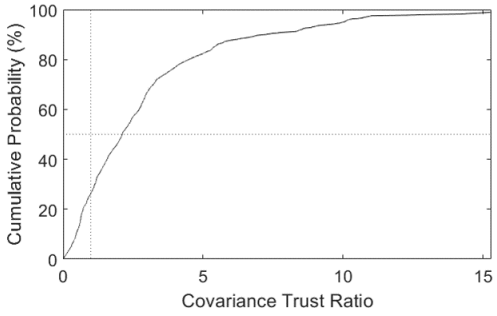

(b) Angular position CTR CDF

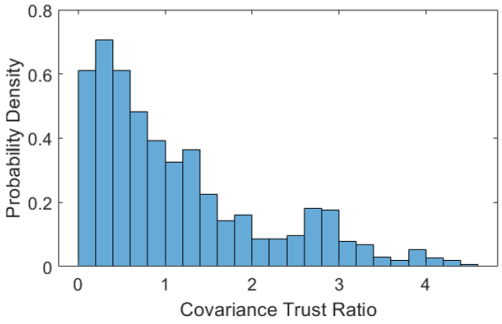

(c) Angular velocity CTR PDF

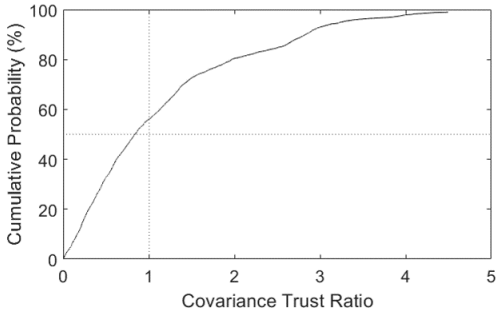

(d) Angular velocity CTR CDF

Fig. 5.12: CTR $\eta^j_{k,a}$ PDFs and CDFs for UKF angle state estimates.

Table 5.1: Covariance Trust Ratio (CTR) results for the Extended Kalman Filter (EKF) without augmented process noise covariance Q.

State Element	$\eta_t(a)$ [%]	$\eta^j_{av}(k)$	$\eta^j_{median}(k)$	$\eta^j_{std}(k)$
x Position	1.6	923.4	273.7	1245
y Position	1.2	751.5	657.0	635.8
x Velocity	4.8	28.4	20.1	24.3
y Velocity	0.7	34.5	25.8	23.2
Angular Position	0.3	1.72×10^4	1331	1.55×10^5
Angular Velocity	0.3	1.25×10^4	4782	1.76×10^4

Table 5.2: Covariance Trust Ratio (CTR) results for the Extended Kalman Filter (EKF) with augmented process noise covariance Q. *Note: all angular position and angular velocity CTRs were below unity.

State Element	$\eta_t(a)$ [%]	$\eta^j_{av}(k)$	$\eta^j_{median}(k)$	$\eta^j_{std}(k)$
x Position	93.2	0.5	0.4	0.3
y Position	97.7	0.4	0.4	0.3
x Velocity	98.9	0.3	0.3	0.2
y Velocity	97.0	0.4	0.3	0.3
Angular Position	NA*	0.3	0.2	0.2
Angular Velocity	NA*	1.67×10^{-7}	1.59×10^{-7}	2.58×10^{-7}

Table 5.3: Covariance Trust Ratio (CTR) results for the Unscented Kalman Filter (UKF).

State Element	$\eta_t(a)$ [%]	$\eta^j_{av}(k)$	$\eta^j_{median}(k)$	$\eta^j_{std}(k)$
x Position	27.9	2.4	1.9	2.2
y Position	31.0	2.3	1.7	2.0
x Velocity	37.8	2.1	1.3	2.1
y Velocity	24.0	3.0	2.5	2.4
Angular Position	26.2	2.9	2.1	2.8
Angular Velocity	56.2	1.1	0.8	1.0

As shown by Tables 5.1, 5.2, and 5.3, the EKF performed very poorly when it was used without an augmented Q. Figures 5.4 to 5.6 show that without augmenting Q, the EKF has CTR distributions with large right-sided tails. These distributions indicate that while a majority of CTRs may fall within a given range, there are a significant number of outliers that often reach values that are several orders of magnitude above the ideal value of unity. While the difference between $eta^j_{av}(k)$ and η^j_{median} in Table 5.1 alludes to this uneven CTR distribution, the CDF and PDF CTR plots show the CTR distribution explicitly. Figures 5.7 to 5.9 show that when the EKF's Q is augmented, the CTR distribution tails become much smaller and the outliers remain within three times the optimal value of unity.

The EKF performed better than the UKF for all state estimates except for angular velocity when the EKF's Q was augmented. As seen in Fig. 5.10 to 5.12, the UKF CTR distributions had larger tails and higher outlier CTR values than the EKF, when the EKF's Q was augmented. The EKF's better performance was to be expected, as the EKF's Q was specifically tuned to improve the filter's state covariance estimates. However, the angular velocity results illustrate how augmenting Q can cause a filter's covariance estimates to become overly conservative if the Q augmentation is inappropriately large for a given state element.

These quantitative results reaffirm the results presented in Ch. 3, confirming that the UKF performed better than the EKF when the EKF's process noise covariance was not artificially increased. The CTR results show that the EKF with Q augmentation modelled the state covariance more accurately than the UKF. However, the UKF was able to converge to a similar, if slightly worse, state covariance model without artificially increasing Q.

5.3 Analysis of the Factors that Affect Filter Reliability

This section explores how the various trustworthiness factors introduced in Sec. 5.1 affect a filter's reliability by running a series of tests using various combinations of these trustworthiness factors. I used the metrics described in Sec. 5.2 to compare the results of these Trustworthiness Factor Combinations (TFCs) to each other. Subsection 5.3.1 describes each filter variation that was tested, Subsection 5.3.1.5 presents the test hypotheses, Subsection 5.3.2 presents the test methodology, and finally Subsection 5.3.3 presents and discusses the results of these tests.

5.3.1 Filter Formulations and Trustworthiness Factors to be Tested

This subsection introduces each trustworthiness factor that I tested. These factors included two Kalman filter variants, estimating only the observer's state or the observer and measurement states, three measurement types, and three process noise covariance models. Each of these trustworthiness factors is described in detail in this section and I present my hypotheses for how each trustworthiness factor would affect a filter's trustworthiness.

For the sake of brevity, many of the hypotheses presented in this section describe the expected trustworthiness results when using one trustworthiness factor as 'better' or 'worse' than other trustworthiness factors. In this context, 'better' refers to average CTR values that are nearer to unity, indicating that the filter's covariance estimates are more similar to those expected from an optimal estimator. Conversely, 'worse' refers to average CTR values that are further from unity, indicating that the filter's covariance estimates are less similar to those expected from an optimal estimator.

5.3.1.1 Filter Variant

To explore how filter linearization affects reliability, I used two extensions of the Kalman Filter: the Extended Kalman Filter (EKF)[8] and the Unscented Kalman Filter (UKF)[62]. The EKF linearizes both the state dynamics and measurement functions whereas the UKF does not use any linearization and preserves any nonlinearities present in the system.

Filter Variant Hypothesis: The UKF will have a better trustworthiness than the EKF, as the UKF is able to model nonlinear state and measurement dynamics while the EKF linearizes the state and measurement dynamics.

5.3.1.2 Measurement Model

To test how measurement linearity and observability affect filter trust, I used three measurement models $z_i(X)$ for each measurement-source i to estimate a system's state $X = [x\ y\ \dot{x}\ \dot{y}\ \phi\ \dot{\phi}\ x_{ri}\ y_{ri}\ \dot{x}_{ri}\ \dot{y}_{ri}]^T$. Where x and y are the observer's position in the Earth Centred Inertial (ECI) Cartesian reference frame, $\dot{x}$ and $\dot{y}$ are the observer's velocity in the ECI frame, ϕ is the angle between the observer's body frame and inertial frame x axes, $\dot{\phi}$ is the angular velocity of the observer's body frame with respect to the inertial frame x axes, x_{ri} and y_{ri} are the ith RSO's coordinates in the ECI frame, and $\dot{x}_{ri}$ and $\dot{y}_{ri}$ are the ith RSO's velocity in the ECI frame. Note that while X includes state elements for both an RSO and an observer in order to present and examine the measurement functions, some of the filter formulations that I examined only estimated the observer's state.

The first model (Range) measures the range $R_i(X)$ between the observer and each RSO i in a two dimensional Cartesian coordinate system

$$z_i(X) = R_i(X) = \sqrt{(x - x_{ri})^2 + (y - y_{ri})^2} \tag{5.6}$$

The second measurement model (Angle) measures the angle $\theta_i(X)$ between the observer-RSO vector and the observer's x-axis in the ECI frame.

$$z_i(X) = \theta_i(X) = \tan^{-1}\left[\frac{y_{ri} - y}{x_{ri} - x}\right] - \phi \tag{5.7}$$

The third measurement model (Angle and Range) uses both measurement types for each measurement source.

$$z_i(X) = \begin{bmatrix} R_i(X) \\ \theta_i(X) \end{bmatrix} \tag{5.8}$$

While both Eq. 5.6 and 5.7 are nonlinear, Eq. 5.7 is significantly more nonlinear than Eq. 5.6 as shown in Fig. 5.13, which plots the RSO-observer distance in the x and y axes vs the resulting measurements. Note that ϕ was set to zero for angle measurements.

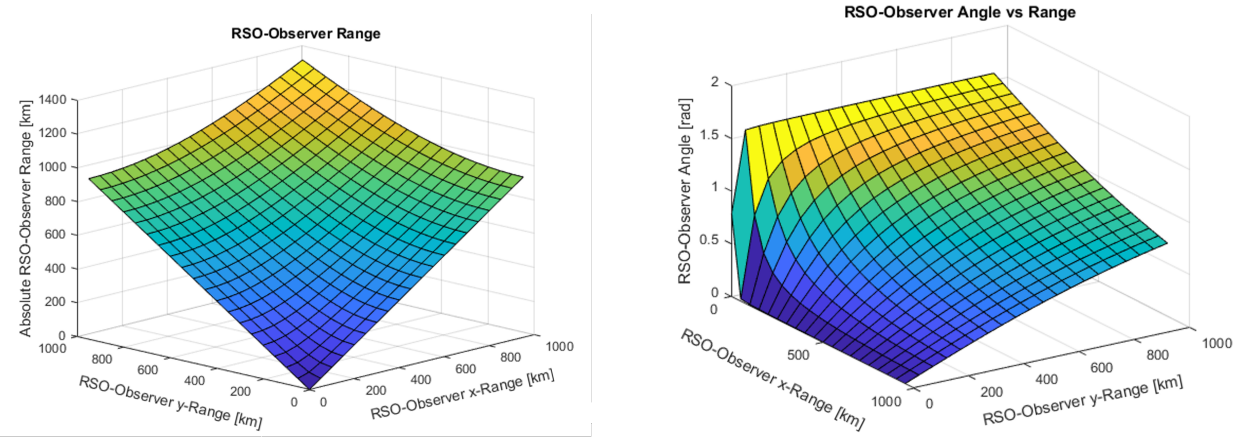

(a) Absolute RSO-Observer range (b) RSO-Observer angle

Fig. 5.13: Measurement functions as a function of x-axis and y-axis ranges.

I quantified the degree of nonlinearity for Eq. 4.29 and 5.7 by comparing each measurement model to their linearized forms using a linearization metric, calculating these metrics for a set of RSO-observer geometries, and then determining the statistical properties of these nonlinearity metrics.

I first constructed the linearized range measurement $\hat{R}_i(X)$ around a central point P_R as

$$\hat{R}_i(X) = R_i(P_R) + H_{k,R}(X - P_R) \tag{5.9}$$

where $H_{k,R}$ is the range measurement observation matrix

$$H_{k,R} = \frac{\partial R_i}{\partial X} = \begin{bmatrix} \frac{x-x_{ri}}{R_i} & \frac{x-y_{ri}}{R_i} & 0 & 0 & 0 & 0 & -\frac{x-x_{ri}}{R_i} & -\frac{y-y_{ri}}{R_i} & 0 & 0 \end{bmatrix} \tag{5.10}$$

Similarly, I constructed the linearized angle measurement $\hat{\theta}_i(X)$ around a central point P_A as

$$\hat{\theta}_i(X) = R_i(P_A) + H_{k,A}(X - P_A) \tag{5.11}$$

where $H_{k,A}$ is the angle measurement observation matrix

$$H_{k,A} = \frac{\partial \theta_i}{\partial X} = \begin{bmatrix} \frac{y_{ri}-y}{C_1} & -\frac{x_{ri}-x}{C_1} & 0 & 0 & 0 & 0 & -\frac{y_{ri}-y}{C_1} & \frac{x_{ri}-x}{C_1} & 1 & 0 \end{bmatrix} \tag{5.12}$$

where

$$C_1 = x^2 + y^2 - 2xx_{ri} - 2yy_{ri} + x_{ri}^2 + y_{ri}^2 \tag{5.13}$$

To quantify the linearization errors for Eq. 5.6 and 5.9, I used the following nonlinearity metrics $\Psi_R(X)$ and $\Psi_A(X)$. These nonlinearity metrics are based on the metric proposed by [140]. However, I chose not to take the infimum or supremum of the nonlinearity ratio in order to examine the ratio's distribution as a function of the system's state X. The first of these, $\Psi_R(X)$, quantified the range measurement nonlinearity

$$\Psi_R(X) = \frac{|\hat{R}_i(X) - R_i(X)|}{|R_i(X)|} \tag{5.14}$$

while $\Psi_A(X)$ quantified the angular measurement nonlinearity.

$$\Psi_A(X) = \frac{|\hat{\theta}_i(X) - \theta_i(X)|}{|\theta_i(X)|} \tag{5.15}$$

I linearized each equation about its origin, to represent the EKF's linearization point, as well as each function's optimal linearization point, to represent the best possible linearization for each measurement function. These optimal linearization points minimized each function's average linearization error for a given region of interest and allowed a fair nonlinearity comparison of the two functions. However, Eq. 5.7 is symmetric about its origin and has a global Optimal Central Linearization Point (OCLP) $P_A = [0\ 0\ 0\ 0\ 0\ 0\ 0\ 0\ 0\ 0]^T$ which corresponds to $\hat{\theta}_i X = 0\ \forall X$. While this linearization point technically minimizes the average linearization error for all possible RSO and observer states, the resulting linearized function approximates all measurements as equal to zero and is not a practical solution. Note that this does not affect the viability of using angle measurements in the EKF, as the EKF uses the nonlinear angle measurement equation rather than $H_{k,A}X$ to calculate its measurement innovation. To avoid this origin symmetry issue when calculating the angle measurement's nonlinearity metric, I elected to compare each equation's nonlinearity for RSO-observer distances between 0.01 km and 1000 km.

Equation 5.6's global OCLP P_R is equal to $[0\ 0\ 0\ 0\ 0\ 0\ 0\ 0\ 0\ 0]^T$. Unlike Eq. 5.7, this linearization point is truly optimal and minimizes the average linearization error for all possible RSO and observer states. Using P_R, I calculated the range measurement equation's linearized and nonlinearized solutions by placing the observer at its body frame origin, varying an RSO's position in the observer body frame from 0.01 km to 1000 km in both x and y axes, and calculating the resulting measurements using Eq. 5.6 and 5.9. Using these measurements, I then calculated the nonlinearity metric $\Psi_R(X)$.

Similarly, I calculated $\Psi_A(X)$ for the same RSO-observer geometries using Eq. 5.15 with the observer's angular position ϕ set to zero for all measurements. However, while Eq. 5.7 has a (trivial) global OCLP P_A at the coordinate system origin, the equation does not have a clear locally optimal P_A for the region between 0.01 km and 1000 km. To find an approximate OCLP, I used the *bayesopt* Bayesian optimization function included in the MATLAB Statistics and Machine Learning Toolbox[141]. I used the average Ψ_A value for the RSO-observer distance range as the objective function for this Bayesian optimizer, with the RSO position elements of P_A as the function input, and used default *bayesopt* settings. Based on this optimization study, the approximate OCLP for this set of RSO-observer ranges was $P_A = [0\ 0\ 0\ 0\ 0\ 0\ 78.9\ 0\ 0\ 0]^T$. I then calculated Eq. 5.7's nonlinearity metric Ψ_A using the same procedure that I used for $\Psi_R(X)$ for the optimized central linearization point as well as for the origin, to represent the EKF's linearization point.

I found the means, medians, and standard deviations for $\Psi_R(X)$ and $\Psi_A(X)$ as calculated for RSO-observer distances between 0.01 km and 1000 km in 10 km increments. These results, summarized in Table 5.4, show that the range measurements can be effectively linearized across the RSO-observer distances examined –with error statistics approximately equal to MATLAB's default double precision machine epsilon [98]– whereas angle measurements have significant linearization errors when linearized at the local OCLP. When linearized at the global OCLP, which the EKF uses, the angle measurements have a uniform linearization error metric of unity. This uniform metric is caused by Eq. 5.7's symmetry which corresponds to $\hat{\theta}_i X = 0\ \forall X$. As previously noted, the EKF does not approximate $h_\theta(X)$ as $\hat{\theta}_i X$ in its governing equations and so linearizing Eq. 5.7 at its global OCLP does not affect the viability of using angle measurements with the EKF.

In fact, the range measurement's linearized solution is equivalent to its linearized form. This can be seen by expanding Eq. 5.9. As Eq. 5.9's central linearization point P_R is at the coordinate system origin, the equation can be expressed as

$$\hat{R}_i(X) = H_{k,R}X = \begin{bmatrix} \frac{x-x_{ri}}{R_i} \\ \frac{y-y_{ri}}{R_i} \\ 0 \\ 0 \\ 0 \\ 0 \\ -\frac{x-x_{ri}}{R_i} \\ -\frac{y-y_{ri}}{R_i} \\ 0 \\ 0 \end{bmatrix} X \tag{5.16}$$

$$= \frac{x-x_{ri}}{R_i}x + \frac{y-y_{ri}}{R_i}x + -\frac{x-x_{ri}}{R_i}x_{ri} + -\frac{y-y_{ri}}{R_i}y_{ri}$$

$$= \frac{1}{R_i}\Big(x^2 - x_{ri}x + y^2 - y_{ri}y - xx_{ri} + x_{ri}^2 - yy_{ri} + y_{ri}^2\Big)$$

$$= \frac{1}{R_i}\Big((x-x_{ri})^2 + (y-y_{ri})^2\Big) = \frac{R_i^2}{R_i} = R_i$$

Linearizing the range measurement changes the equation's format, but does not change its output and does not introduce linearization errors. These range measurements are still nonlinear. However, range measurements are not subject to linearization error and, as shown in Table 5.4, are demonstrably less nonlinear than angle measurements.

Table 5.4: Linearization metric results for angle and range measurements.

	Range Measurement at Global OCLP	**Angle Measurement at Local OCLP**	**Angle Measurement at Global OCLP**
Mean Ψ	9×10^{-17}	6.12	1
Median Ψ	1×10^{-16}	0.914	1
Ψ Standard Deviation	9×10^{-17}	497	$8e\times10^{-17}$

In addition to linearity, the observability of a measurement source must also be considered. Observability describes how well the state can be inferred from the knowledge contained in its measurements. While determining the observability of nonlinear systems can be difficult [142], it is clear by inspection that Eq. 5.6 contains no angular information. As such, angular position and angular velocity will be unobservable if only Eq. 5.6 is used.

Measurement Linearity and Observability Hypothesis: Equation 5.6 is more linear than Eq. 5.7 but contains no angular information. As such, filters relying on only range measurements will have better position and velocity trusts than filters with only angular measurements but these range only filters will have divergent angular positions and angular velocities. As such, the overall trustworthiness of a filter with only range measurements should be significantly worse than the other two options. A filter with only angle measurements should have slightly worse position and velocity trusts, but much better (convergent) angular position and angular velocity trusts. As such, an angle only filter should have better overall trustworthiness than a range only filter. Finally, a filter with both range and angular velocity measurements should have the best trustworthiness for all state elements.

5.3.1.3 Including Measurement States in the Estimated State

To examine how estimating measurement source dynamics affects estimator reliability, I used the simulation environment described in Ch. 2 with an updated dynamics model that uses Cowell's method [143], without the fixed orbital radius approximation used in previous chapters, and a fourth-order Runge Kutta integrator. The overall test methodology is described in Sec. 5.3.2. Using this environment, in which an observer estimates its orbital state using measurements from orbital RSOs, I implemented two Kalman filter variants. One estimates only the observer's state (Observer Only) while the second (Observer and RSOs) estimates both the observer's orbital state and the orbital states of each RSO measurement-source.

Measurement State Element Model Hypothesis: A filter which includes elements of the measurement-source's dynamics will have better average CTR values than an estimator

which does not include elements of the measurement-source state in the state array.

5.3.1.4 Process Noise Covariance Model

To explore how process noise covariance affects a filter's trust, I examined three cases, all based on van Loan's process noise covariance discretization method [117]. The first (van Loan) implemented van Loan's process noise covariance discretization method[117] without modification, the second adds a constant value to the process noise covariance model which I refer to as the 'Fixed Bump,' and the third adds an integration error model which I refer to as the 'Adaptive Bump.'

van Loan's Method Using van Loan's process noise discretization method [117], I first formed a $2n \times 2n$ matrix C

$$C = \left[\begin{array}{c:c} -A & BW_PB^T \\ \hdashline 0 & A^T \end{array}\right] \cdot \Delta t \tag{5.17}$$

where n is the dimension of the state matrix, A is the continuous state transition model, B is the continuous control input model, Δt is the time step, and W_P is the power spectral density of the process noise. From [59][2], the power spectral density W for a stationary random process, *i.e.* white noise, is equal to the white noise's spectral amplitude ξ

$$W_P = \xi \tag{5.18}$$

and the white noise's autocorrelation function $R_X(\Delta t)$ is related to the power spectral density as follows

$$R_X(\Delta t) = \xi\delta(\Delta t) \tag{5.19}$$

where $\delta(\Delta t)$ is the dirac-delta function. For a Gaussian random process [59][3]

$$R_X(\Delta t) = \mathbb{E}[X(t)X(t+\Delta t)] \tag{5.20}$$

[2] p.p 75
[3] p.p 65

and for a stationary Gaussian random process, $R_X(0) = \mathbb{E}[ww^T] = Q$. Using $R_X(0) = Q = \xi\delta(\Delta t)$, and approximating $\delta t(\Delta t)$ as $\frac{1}{\Delta t}$, this becomes

$$Q = \frac{\xi}{\Delta t} \tag{5.21}$$

and can be rearranged to

$$W_P = \xi = Q\Delta t \tag{5.22}$$

Next, following van Loan's method [117], I calculated the matrix exponent of C as

$$D = e^C = \begin{bmatrix} \ddots & \Phi^{-1}Q_k \\ 0 & \Phi^T \end{bmatrix} \tag{5.23}$$

and found the discretized state transition matrix Φ by transposing the lower-right partition of D. I then calculated the discretized process noise covariance Q_k by multiplying the upper-right partition of D by Φ. Note that the upper-left partition of D is inconsequential for this analysis.

Fixed Bump While van Loan's method provides an accurate model of a system's discretized process noise covariance, Q_k may be insufficient to prevent EKF divergences. If Q_k contains null diagonal elements, the corresponding steady state values in the state covariance P_k and the Kalman gain K_k will become zero as well [8].[4] This can be seen by examining the Riccati equation for the state covariance $_k$ [8]

$$\dot{P}_k = \Phi P_k + P_k\Phi^T - P_k H_k^T R_k^{-1} H_k P_k + B_k Q_k B_k^T \tag{5.24}$$

where H_k is the discretized observation model and R_k is the discretized measurement noise covariance. At steady state, where $\dot{P}_k = 0$, Eq. 5.24 becomes the algebraic Riccati equation [8]

$$\Phi P_k + P_k\Phi^T - P_k H_k^T R_k^{-1} H_k P_k = -B_k Q_k B_k^T \tag{5.25}$$

[4] p.p 279–280

As described by [8], if elements of $B_k Q_k B_k^T$ are null, the corresponding steady state elements of P_k will also become null. Equations 2.8 and 2.9 show that the Kalman gain K_k is a function of P_k, H_k, and R_k. Depending on how H_k maps measurements to state elements, null P_k elements may result in null K_k elements. If this occurs, the null K_k elements will cause the filter to lose its ability to respond to new measurements [8], as can be seen by examining the EKF's *a posteriori* state update (Eq. 2.10), and new state elements will become a function of only the filter's *a priori* state estimates. This phenomenon, in which a filter becomes incapable of responding to new measurements, is commonly referred to as "falling asleep." If a filter becomes incapable of responding to measurements, the filter may diverge.

Adding a fictitious 'fixed' process noise w_{fixed} to a filter's discretized process noise model w_k, and a corresponding fictitious 'fixed' process noise covariance Q_{fixed} to Q_k, is a common technique for improving the performance of a filter that is diverging or falling asleep [8]. Using this method, a designer adds some arbitrary values to the process noise model

$$w_{total} = w_k + w_{fixed} \tag{5.26}$$

which results in an increased process noise covariance.

$$Q_{total} = \mathbb{E}[w_{total} w_{total}^T] = \mathbb{E}[w_k w_k^T] + \mathbb{E}[w_{fixed} w_{fixed}^T] = Q_k + Q_{fixed} \tag{5.27}$$

While simple, the choice of Q_{fixed} values is largely heuristic and dependant on the designer's experience [8]. Tuning Q_{fixed} can take a significant amount of time and, if oversized, can reduce the filter's ability to react to new measurements and thereby reduce the filter's trustworthiness.

Note that as described by [144], the UKF in its most common form does not have a discrete time algebraic Riccati equation as it is based on a different nonlinear estimation principle. As such, the mechanism described in this section, by which the Kalman Filter and EKF can fall asleep, is not applicable to the UKF. No mention of this phenomenon affecting the UKF was found in the literature and the UKF presented in Ch. 3 did not fall asleep under conditions which caused the EKF to do so. However, it is possible that the UKF may

still be affected by this phenomenon under certain conditions. A formal proof demonstrating whether the UKF can fall asleep is outside the scope of this thesis but this chapter will assess if increasing the UKF's process noise covariance improves the filter's trust.

Adaptive Bump While the Kalman Filter and its variants account for unknown variations in the state's dynamics and measurements, there are other unknowns that these filters do not account for. One of these unknowns is integration error. I explored how including an integration error model –which I refer to as an 'Adaptive Bump'– in the process noise covariance affects the overall system's performance.

I chose to use the *step doubling* method [145] for approximating the upper bounds of the Taylor Series truncation error as the basis for this Adaptive Bump. As described by [146], this method involves performing three fourth-order Runge Kutta operations: one to propagate the state X from the current timestep X_k to the desired timestep X_{k+1} while the other two Runge Kutta operations use two half-steps to first propagate X from X_k to $X_{k+1/2}$ and then from $X_{k+1/2}$ to X_{k+1}. The resulting difference in X_{k+1} values is approximately equal to the upper bound of the Taylor series truncation error [146].

Press and Teukolsky demonstrate the Step Doubling method in [146]. They consider some function $y(t)$ which they wish to integrate from some time k to a timestep $k+2h$ using two approximate solutions: y_1 which uses a timestep of size $2h$

$$y(k+2h) = y_1 + (2h)^5\phi + O(h^6) + ... \tag{5.28}$$

and y_2 which uses two timesteps of size h.

$$y(k+2h) = y_2 + 2(h)^5\phi + O(h^6) + ... \tag{5.29}$$

If y_1 and y_2 are both fourth-order functions (like the fourth-order Runge Kutta), h^5 is the next-highest order term. Press and Teukolsky assume ϕ remains constant over the step, and is some number with an order of magnitude of $y^5(k)/5!$ [146].

The difference Δ between Eq. 5.28 and 5.29 is

$$\Delta = y_2 - y_1 \tag{5.30}$$

and, ignoring h^6 order terms and higher, $y(k+2h)$ is

$$y(k+2h) = y_2 + \frac{\Delta}{15} + O(h^6) + ... \tag{5.31}$$

Equation 5.31 shows that the 5^{th} order terms in $y(k+2h)$ can be expressed as $\Delta/15$. This still does not fully represent the integration error but does bound it to the next highest order, *i.e.*

$$O(h^5) \approx Q_{adaptive} = \frac{\Delta}{15} = \frac{y_2 - y_1}{15} \tag{5.32}$$

Using Eq. 5.32, I modelled the 5^{th} order integration error covariance, my so-called 'Adaptive Bump' $Q_{adaptive}$, at each timestep as

$$Q_{adaptive} = \frac{1}{225}[\Delta\Delta^T] \tag{5.33}$$

and added this integration error covariance to the discretized process noise covariance estimate Q_k, calculated using [117]. Together, this forms a more holistic process noise covariance model Q_{total}.

$$Q_{total} = Q_k + Q_{adaptive} \tag{5.34}$$

This method is far from perfect as it only models a generic 5^{th} order integration error. Manually calculating the 5^{th} order Taylor series expansion would provide a more accurate bound and require less computation time while running the filter, as it would not need to run two versions of the Fourth Order Runge Kutta method. However, calculating the Taylor series expansion requires manual calculations by the user and must be re-calculated for each dynamics model. Using the step doubling method as a basis for calculating $Q_{adaptive}$ provides an adequate generic integration error model that is applicable across systems and can be used to test if a custom-tailored integration error model is worthwhile.

Process Noise Covariance Model Hypothesis: A Kalman filter variant which uses only van Loan's method of discretizing the process noise covariance will slightly under-estimate the true process noise present in the system and, if null Q_k elements exist, the filter may

diverge. As such, filters using only the van Loan method will generally under-estimate P and have the worst trusts of the three options I have described.

Adding a 'Fixed Bump' to van Loan's method should usually over-compensate for noise in the system and overestimate P, resulting in the most conservative trustworthiness. Conversely, adding an 'Adaptive Bump' to van Loan's method should still under-estimate P but will be much closer to the true P value than either of the other methods. As such, filters using the 'Adaptive Bump' should have the best trustworthiness.

5.3.1.5 Test Hypotheses Summary

The following list summarizes and enumerates the trust-comparison hypotheses that I tested.

Hypothesis 1.2.1: Filters using the UKF will have better trusts (*i.e.* closer to unity) than those using the EKF.

Hypothesis 1.2.2: Filters estimating both the observer's state and the RSO state elements will have better trusts (*i.e.* closer to unity) than those estimating only the observer's state.

Hypothesis 1.2.3a: Filters with range measurements will have more conservative (*i.e.* lower-valued) position and velocity state element trusts. These filters will have divergent (*i.e.* very high-valued) angular position and angular velocity state elements which will cause non-conservative (*i.e.* high-valued) overall trusts.

Hypothesis 1.2.3b: Filters with angle measurements will have more conservative (*i.e.* lower-valued) angle and angular velocity trusts, slightly less conservative position and velocity trusts, and better overall trusts (*i.e* nearer to unity) than the range only filters.

Hypothesis 1.2.3c: Filters using both range and angle measurements will have the best overall trusts (*i.e* nearer to unity) compared to angle only and range only filters.

Hypothesis 1.2.4a: Filters using only van Loan's discretized process noise covariance model will slightly under-model the covariance and have the least conservative (*i.e.* highest) trusts.

Hypothesis 1.2.4b: Filters adding the "Fixed Bump" will grossly over-model covariance and have the most conservative trusts (*i.e.* lowest).

Hypothesis 1.2.4c: Filters adding the "Adaptive Bump" will most accurately model covariance and have the best trusts (*i.e.* closest to unity).

Hypothesis 1.2.5a: The UKF estimating both the observer and RSO states, using both range and angle measurements, and using the "Adaptive Bump" process noise covariance model will have the best average CTR (*i.e.* closest to unity).

Hypothesis 1.2.5b: The EKF estimating only the observer state, using only range measurements, and using the van Loan process noise covariance model will have the worst average CTR (*i.e.* highest valued).

5.3.2 Test Methodology

To compare the results of each TFC, I ran a Monte Carlo simulation with 96 runs for each permutation of trustworthiness factors to determine the statistical distributions of each filter's estimate error, calculate each TFC's NEES and NIS values, and determine each TFC's average CTR values. The test methodology for this analysis is summarized in Fig.5.14.

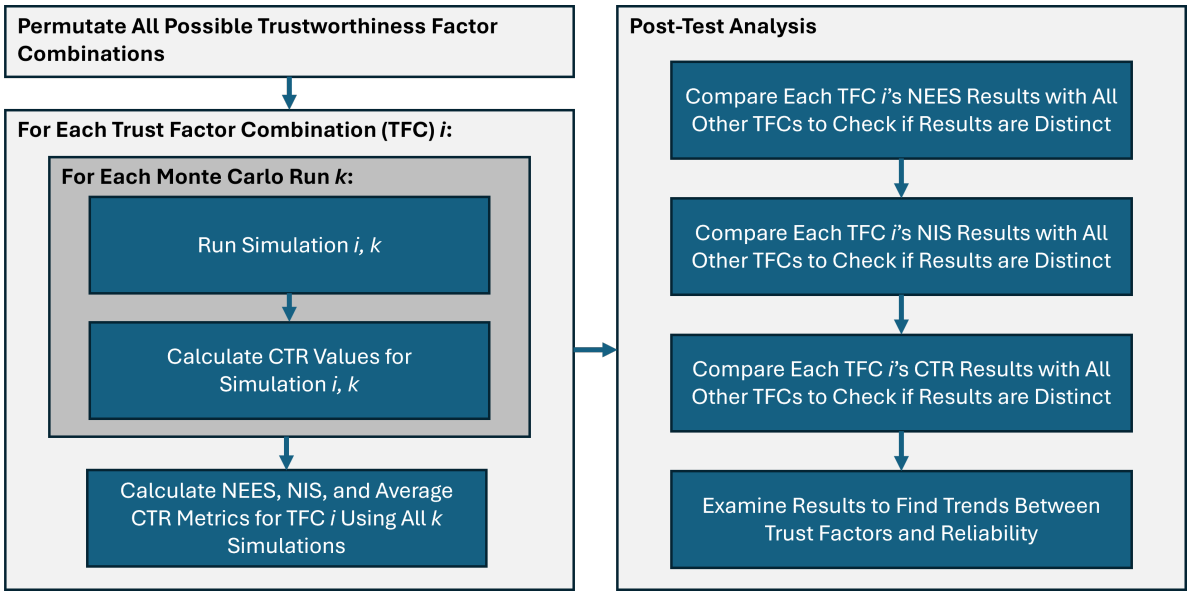

Fig. 5.14: Trustworthiness evaluation methodology.

Based on manual testing, this number of Monte Carlo runs provided consistent results while also efficiently using the simulation computer's 16 core processor. For the full set of TFCs, see Tables 5.5 and 5.6. Note that, in order to compare the relative performance of

TFCs estimating only the observing spacecraft's state elements, I examined two sub-cases. The first sub-case assumed that these TFCs had perfect knowledge of the RSO positions while the second sub-case included an error between each RSO's assumed and true positions. The last column of Table 5.5 denotes the TFCs that had perfect knowledge of the RSO positions. This column is repeated in Table 5.6 for consistency, however the TFCs in Table 5.6 all estimated the RSO states and used these state estimates when forming their measurement innovations.

Table 5.5: Tested Trustworthiness Factor Combinations (TFCs) estimating only observer state elements.

Test Case	**Filter Variant**	**Measurement Type(s)**	**Process Noise Covariance Model**	**Perfect RSO Position Knowledge**
1a	EKF	Angle	van Loan	Yes
2a	EKF	Range	van Loan	Yes
3a	EKF	Angle & Range	van Loan	Yes
4a	EKF	Angle	Fixed Bump	Yes
5a	EKF	Range	Fixed Bump	Yes
6a	EKF	Angle & Range	Fixed Bump	Yes
7a	EKF	Angle	Adaptive Bump	Yes
8a	EKF	Range	Adaptive Bump	Yes
9a	EKF	Angle & Range	Adaptive Bump	Yes
10a	UKF	Angle	van Loan	Yes
11a	UKF	Range	van Loan	Yes
12a	UKF	Angle & Range	van Loan	Yes
13a	UKF	Angle	Fixed Bump	Yes
14a	UKF	Range	Fixed Bump	Yes
15a	UKF	Angle & Range	Fixed Bump	Yes
16a	UKF	Angle	Adaptive Bump	Yes
17a	UKF	Range	Adaptive Bump	Yes
18a	UKF	Angle & Range	Adaptive Bump	Yes
1b	EKF	Angle	van Loan	No
2b	EKF	Range	van Loan	No
3b	EKF	Angle & Range	van Loan	No
4b	EKF	Angle	Fixed Bump	No
5b	EKF	Range	Fixed Bump	No
6b	EKF	Angle & Range	Fixed Bump	No
7b	EKF	Angle	Adaptive Bump	No
8b	EKF	Range	Adaptive Bump	No
9b	EKF	Angle & Range	Adaptive Bump	No
10b	UKF	Angle	van Loan	No
11b	UKF	Range	van Loan	No
12b	UKF	Angle & Range	van Loan	No
13b	UKF	Angle	Fixed Bump	No
14b	UKF	Range	Fixed Bump	No
15b	UKF	Angle & Range	Fixed Bump	No
16b	UKF	Angle	Adaptive Bump	No
17b	UKF	Range	Adaptive Bump	No
18b	UKF	Angle & Range	Adaptive Bump	No

Table 5.6: Tested Trustworthiness Factor Combinations (TFCs) estimating both observer and RSO state elements.

Test Case	**Filter Variant**	**Measurement Type(s)**	**Process Noise Covariance Model**	**Perfect RSO Position Knowledge**
19	EKF	Angle	van Loan	NA
20	EKF	Range	van Loan	NA
21	EKF	Angle & Range	van Loan	NA
22	EKF	Angle	Fixed Bump	NA
23	EKF	Range	Fixed Bump	NA
24	EKF	Angle & Range	Fixed Bump	NA
25	EKF	Angle	Adaptive Bump	NA
26	EKF	Range	Adaptive Bump	NA
27	EKF	Angle & Range	Adaptive Bump	NA
28	UKF	Angle	van Loan	NA
29	UKF	Range	van Loan	NA
30	UKF	Angle & Range	van Loan	NA
31	UKF	Angle	Fixed Bump	NA
32	UKF	Range	Fixed Bump	NA
33	UKF	Angle & Range	Fixed Bump	NA
34	UKF	Angle	Adaptive Bump	NA
35	UKF	Range	Adaptive Bump	NA
36	UKF	Angle & Range	Adaptive Bump	NA

Simulation Parameters For each Monte Carlo run, I simulated both the system's dynamics and the desired filter. Each filter ran for two observer orbits at 1 s timesteps for a total run-time of approximately 11000 timesteps. Based on manual testing, I found that two orbits were sufficient to determine if a filter's estimate error remained bounded by the square root of its state covariance estimate and if the filter's estimate error would increase over time. Hardware and data-storage limitations prevented me from running these tests at smaller timesteps, but manual testing showed that smaller timesteps did not have a significant impact on filter performance.

For all tests, the observing spacecraft was placed in a 400 km altitude circular orbit, the initial estimate error e_0 was set to $e_0 = [100\ km\ 110\ km\ 1.1\ km/s\ 1\ km/s\ 30\ deg\ 5\ deg/s]^T$, and the initial P estimate was set to $P = [e_0 e_0^T]$. As in Ch. 3, I set the observing spacecraft's mass and inertia to 84 kg and 2.8 kg^2, based on Sputnik's mechanical properties [118]. I applied a sinusoidal angular acceleration to the observer with an arbitrary amplitude of 0.5 mNm, which I selected to be approximately five times the system's angular acceleration process noise, and a period of 46.2 minutes (equal to half of the observer's orbital period). I modelled four RSOs in 1000 km altitude circular orbits at 0°, 30°, 150°, and 270°counterclockwise from the x-axis. When the RSO states were estimated, the same initial position and velocity estimate errors as the observer were applied to the RSOs and the initial P estimate was again set to $P = [e_0 e_0^T]$.

The orbital state dynamics were modelled using Cowell's method [143] and integrated using a fourth-order Runge Kutta integrator, without the fixed orbital radius approximation used in Ch. 3 and Ch 4. A zero-mean Gaussian white acceleration noise with a standard deviation of 1.13×10^{-4} m/s^2 was applied to the observer and measurement sources, based on the sum of the solar pressure and drag forces for a spacecraft in a 1,000 km altitude orbit with a drag coefficient C_d of 2, a reflectivity of 1, and an area of 0.62 m^2, multiplied by a safety factor of 10. Additionally, a zero-mean Gaussian white angular acceleration noise with a standard deviation of 1.74×10^{-4} rad/s^2, equal to the applied angular acceleration amplitude, was applied to the observer. This angular acceleration noise was selected to model a coarse pointing attitude. When used, the 'Fixed Bump' Q_{fixed} was set to a diagonal matrix with diagonal elements $\text{diag}(Q_{fixed}) = [1\times10^{-8}\ 1.2\times10^{-8}\ 1.2\times10^{-12}\ 1\times10^{-12}\ 9\times10^{-10}\ 2.5\times10^{-11}]$.

These Q_{fixed} values were selected based on trial and error so that the EKF, when estimating only the observer's state, would produce state covariance estimates which visually appeared to consistently bound its state estimate errors.

When angle measurements were used, a zero-mean Gaussian white measurement noise with a standard deviation of 5 arc-seconds was applied to mimic the accuracy of a commercially available star tracker [65]. Similarly, when range measurements were used, a zero-mean Gaussian white measurement noise with an arbitrary standard deviation of 10 m was applied to all range measurements. This range measurement error standard deviation is ten times the measurement standard deviation of a commercially available terrestrial laser rangefinder [147] and is sufficiently close to an actual laser rangefinder's performance for the purposes of this study.

For trust factor combinations that only estimated the observing spacecraft's state and did not assume perfect RSO position knowledge, I modelled the error between each RSO's assumed and true positions by propagating two versions of each RSO. The first true RSO state was modelled as previously described and used to generate measurements. The second assumed RSO state was modelled with an initial along-track orbit offset and used to calculate the filter's expected measurements. The along-track orbit offset was modelled as a random Gaussian error with a mean of zero and a standard deviation of 5 km, to approximate the accuracy of a TLE estimate [105]. I chose to propagate the RSO orbits rather than calculating them explicitly to ensure that there was no mismatch between the true dynamics and the dynamics models used by the UKF and EKF, when the RSO states are estimated. While I could have calculated the true RSO orbits to increase simulation speeds, I chose to use the same dynamics model for the assumed and true RSO states to reduce the chances of an implementation error.

As noted by [148], the EKF is known to underestimate state covariances during its initial settling period, especially when the initial estimate error is large. To compensate for this, I implemented Lear's Method for measurement underweighting as described in [148] for trust factor combinations using the EKF. Lear's Method adds the following underweighting factor U_u to the EKF's measurement equation (Eq. 2.8) [148]

$$S = H_k \hat{P}_{k|k-1} H_k^T + R_k + U_u \tag{5.35}$$

where U_u is a percentage of the *a priori* estimation error covariance defined using the underweighting parameters α_u and β_u as [148]

$$U_u = \begin{cases} \beta_u H_k \hat{P}_{k|k-1} H_k^T, & \text{if } \sqrt{\text{trace}\hat{P}_{k|k-1}} > \alpha_u \\ 0, & \text{otherwise} \end{cases} \tag{5.36}$$

When measurement underweighting was used, I used the same underweighting α_u of 1000 and β_u of 0.2 as used in [148].

Similarly, the UKF is known to produce non-positive definite (non-PD) covariance estimates which cause the UKF to fail [60]. These non-PD estimates caused the lower triangular Cholesky factorization, used to calculate the sigma points in Eq. 2.19, to fail when calculating the matrix square root. To avoid non-PD UKF covariance estimates, I used Symmetric Cholesky Factors as described by [149] to calculate the matrix square root. While more complex than other Cholesky factorization methods, the Symmetric Cholesky Factors were less susceptible to non-PD solutions and produced more stable results.

I calculated the average CTR, NEES, and NIS performance metrics for each Monte Carlo run. The average CTR was calculated using a frame size of 111 timesteps, based on the results of a Bayesian optimizer. I used Welch's t-test [150] to compare the TFCs with each other to confirm if the differences in these performance metrics results were statistically significant. I chose to use Welch's t-test because it is robust against non-normality and it does not require each distribution to have equal variance [151]. When comparing TFCs, I used three separate Welch's t-tests: one to test if the two TFCs had equal means, one to test if the first mean was greater than the second, and one to test if the first mean was less than the second. I used a significance level of 5% for all tests. Note that I chose not to use the Mahalanobis Distance for this analysis, as the NEES metric is equivalent to the average Mahalanobis Distance over all 96 Monte Carlo simulations.

5.3.3 Test Results and Discussion

This section presents and discusses the average CTR, NEES, and NIS results for each of the TFCs discussed in Sec. 5.3.1. Section 5.3.3.1 presents the average CTR, NEES, and NIS results while Sec. 5.3.3.2 discusses and relates these results to my previously stated hypotheses.

5.3.3.1 Test Results

This section presents the trust factor test results. I first show how the initial settling period affects the results and discuss which filters converged before presenting the average CTR, NEES, and NIS results for each TFC. Lastly, I note how non-PD covariance estimates in previous UKF implementations affected the trust metrics.

Initial Settling Effects and Convergence I implemented measurement underweighting [148] in order to reduce the magnitude of the initial settling periods. While measurement underweighting reduced the magnitude of the initial settling periods, during which the EKF's state covariance estimates were significantly under-estimated, the EKF-based TFCs still had noticeable initial settling periods. Figure 5.15 shows an example of this settling as it affected Test Case 1a. These settling periods were due to the large initial estimate errors used in this study. As noted by [148], the EKF is known to underestimate state covariances during its initial settling period, especially when the initial estimate error is large. These initial underestimated state covariances were reflected in all three reliability metrics. The initial values were substantial and biased the average CTR, NEES, and NIS values. To account for these initial settling periods, this section presents the average CTR, NEES, and NIS results for the full simulation period as well as for a truncated period beginning 500 seconds after the start of the simulation. This 500 second delay ensured that all TFCs were no longer effected by initial settling effects.

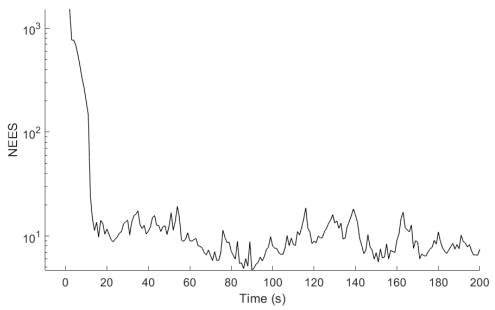

(a) NEES values

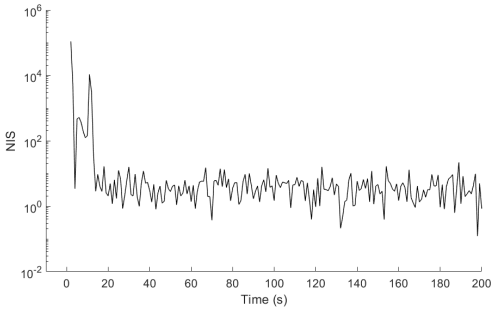

(b) NIS values

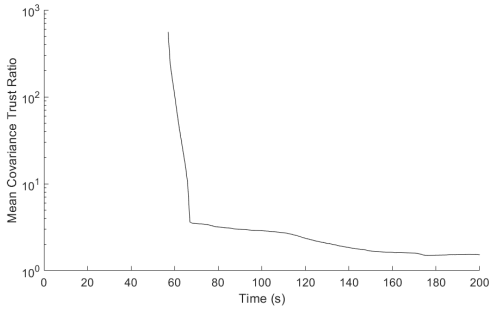

(c) average CTR values

Fig. 5.15: Initial NEES, NIS, and average CTR settling periods for Monte Carlo run 1 of TFC Test Case 1a: filters using the EKF to estimate the observer's state using angle measurements and the van Loan process noise covariance model with perfect knowledge of RSO positions.

Filter Convergence While estimator trust is the primary focus of my analysis, knowing which TFCs converged or failed to converge provides useful context with which to frame my results. Tables 5.7, 5.8, and 5.9 summarize the convergence results for each TFC. For the observed period, many combinations had state estimate errors that decreased from the initial estimate error and then appeared to move as random Brownian motion. While they remained bounded, these errors did not decrease to a limit or to a cyclic pattern. Using Gelb's [8] definitions of divergence, TFCs that experienced this behaviour did not experience true divergence. However, it is hard to say if these filters experienced apparent divergence as their estimate errors did approach unbiased values. However, these values were not particularly close to zero (orders of magnitude above the process noise covariance) and, while they remained bounded, the errors did not continue to converge after reaching this random motion phase. Based on this behaviour, I listed the combinations which experienced this behaviour as likely convergent.

To see if this behaviour was stable over longer durations, I simulated a single instance of each TFC for 10 orbits. The convergence results presented in Tables 5.7-5.9 remained consistent over this extended simulation period. However, without a clear pattern, this apparent convergence is not guaranteed to continue over longer durations. Further, TFCs that estimated only the observer's state elements and were not provided with perfect knowledge of RSO positions are subject to increasingly large measurement innovation errors as the RSOs drifted further from their expected positions. While not observed during the simulated period, these TFCs will eventually diverge as the measurement innovation error increases. Additionally, there is some uncertainty regarding the long-term stability of the TFCs that did not have full observability. See Sec. 5.3.3.2 for further discussion regarding observability and convergence.

Table 5.7: Convergence results for TFCs estimating only observer state elements, with perfect knowledge of RSO positions.

Test Case	**Estimator**	**Measurement Type(s)**	**Process Noise Covariance Model**	**Convergence**
1a	EKF	Angle	van Loan	All state elements converged
2a	EKF	Range	van Loan	Pos./vel. state elements converged
3a	EKF	Angle and Range	van Loan	All state elements converged
4a	EKF	Angle	Fixed Bump	All state elements converged
5a	EKF	Range	Fixed Bump	Pos./vel. state elements converged
6a	EKF	Angle and Range	Fixed Bump	All state elements converged
7a	EKF	Angle	Adaptive Bump	All state elements converged
8a	EKF	Range	Adaptive Bump	Pos./vel. state elements converged
9a	EKF	Angle and Range	Adaptive Bump	All state elements converged
10a	UKF	Angle	van Loan	All state elements converged
11a	UKF	Range	van Loan	Pos./vel. state elements converged
12a	UKF	Angle and Range	van Loan	All state elements converged
13a	UKF	Angle	Fixed Bump	All state elements converged
14a	UKF	Range	Fixed Bump	Pos./vel. state elements converged
15a	UKF	Angle and Range	Fixed Bump	All state elements converged
16a	UKF	Angle	Adaptive Bump	All state elements converged
17a	UKF	Range	Adaptive Bump	Pos./vel. state elements converged
18a	UKF	Angle and Range	Adaptive Bump	All state elements converged

Table 5.8: Convergence results for TFCs estimating only observer state elements, without perfect knowledge of RSO positions. Note that 'likely converged' indicates that a TFC appears to have converged, based on Gelb's [8] divergence criteria, but that there is some uncertainty regarding this convergence.

Test Case	**Estimator**	**Measurement Type(s)**	**Process Noise Covariance Model**	**Convergence**
1b	EKF	Angle	van Loan	All state elements likely converged
2b	EKF	Range	van Loan	Pos./vel. state elements likely converged
3b	EKF	Angle and Range	van Loan	All state elements likely converged
4b	EKF	Angle	Fixed Bump	All state elements likely converged
5b	EKF	Range	Fixed Bump	Pos./vel. state elements likely converged
6b	EKF	Angle and Range	Fixed Bump	All state elements likely converged
7b	EKF	Angle	Adaptive Bump	All state elements likely converged
8b	EKF	Range	Adaptive Bump	Pos./vel. state elements likely converged
9b	EKF	Angle and Range	Adaptive Bump	All state elements likely converged
10b	UKF	Angle	van Loan	All state elements likely converged
11b	UKF	Range	van Loan	Pos./vel. state elements likely converged
12b	UKF	Angle and Range	van Loan	All state elements likely converged
13b	UKF	Angle	Fixed Bump	All state elements likely converged
14b	UKF	Range	Fixed Bump	Pos./vel. state elements likely converged
15b	UKF	Angle and Range	Fixed Bump	All state elements likely converged
16b	UKF	Angle	Adaptive Bump	All state elements likely converged
17B	UKF	Range	Adaptive Bump	Pos./vel. state elements likely converged
18b	UKF	Angle and Range	Adaptive Bump	All state elements likely converged

Table 5.9: Convergence results for TFCs estimating both observer and RSO state elements. Note that 'likely converged' indicates that a TFC appears to have converged, based on Gelb's [8] divergence criteria, but that there is some uncertainty regarding this convergence.

Test Case	**Estimator**	**Measurement Type(s)**	**Process Noise Covariance Model**	**Convergence**
19	EKF	Angle	van Loan	All state elements likely converged
20	EKF	Range	van Loan	Pos./vel. state elements likely converged
21	EKF	Angle and Range	van Loan	All state elements converged
22	EKF	Angle	Fixed Bump	All state elements diverged
23	EKF	Range	Fixed Bump	All state elements diverged
24	EKF	Angle and Range	Fixed Bump	All state elements diverged
25	EKF	Angle	Adaptive Bump	All state elements likely converged
26	EKF	Range	Adaptive Bump	Pos./vel. state elements likely converged
27	EKF	Angle and Range	Adaptive Bump	All state elements converged
28	UKF	Angle	van Loan	All state elements converged
29	UKF	Range	van Loan	Pos./vel. state elements converged
30	UKF	Angle and Range	van Loan	All state elements converged
31	UKF	Angle	Fixed Bump	All state elements diverged
32	UKF	Range	Fixed Bump	All state elements diverged
33	UKF	Angle and Range	Fixed Bump	All state elements diverged
34	UKF	Angle	Adaptive Bump	All state elements likely converged
35	UKF	Range	Adaptive Bump	Pos./vel. state elements likely converged
36	UKF	Angle and Range	Adaptive Bump	All state elements likely converged

Filter Reliability Results To provide insight into each TFC's performance, after the initial convergence period, the summary result tables presented in this section include both the mean and median reliability metrics for the whole simulated period as well as for a limited frame beginning 500 s after the start of the simulation. This sample frame starts after all filters completed their initial settling periods.

The trustworthiness factor analysis results are summarized in Tables 5.10, 5.11 and 5.12 with the mean CTRs plotted for each TFC in Fig. 5.16 and 5.17. These figures include the results for observer-only TFCs (TFCs estimating only observer state elements) for scenarios in which they had perfect knowledge of RSO positions as well as scenarios which included RSO position errors. While the observer-only TFCs that included RSO position errors are far more realistic, I chose to also present the results for observer-only TFCs with perfect RSO position knowledge as well, in order to provide an idealized benchmark with which to compare the TFCs that estimated both the observer and RSO state elements. As will be discussed in Sec. 5.3.3.2, many TFCs which estimated both the observer and RSO state elements did not have full observability ranks whereas the equivalent observer-only TFCs had proportionally higher or full observability ranks. As seen in Fig. 5.17, the results for the observer-only TFCs which included RSO positions errors differ from the equivalent TFCs that estimated both RSO and observer state elements by orders of magnitude. These results demonstrate the importance of adequately capturing a system's uncertainties but, due to the magnitude of the unmodelled measurement errors in the observer-only TFCs, cannot provide insight into the effects of observability on estimator trust.

Figures 5.18, 5.19, 5.20 and 5.21 provide representative probability distribution functions and cumulative distribution functions. See Appendix C for probability distribution functions and cumulative distribution functions for each TFC.

Table 5.10: Covariance Trust Ratios (CTRs) for TFCs estimating only observer state elements, with perfect knowledge of RSO positions.

Test Case	**Estimator**	**Measurement Type(s)**	**Process Noise Covariance Model**	**Full Mean CTR**	**Full Median CTR**	**Framed Mean CTR**	**Framed Median CTR**
1a	EKF	Angle	van Loan	1.132	0.984	1.007	0.978
2a	EKF	Range	van Loan	0.932	0.695	0.722	0.688
3a	EKF	Angle and Range	van Loan	1.277	1.041	1.076	1.032
4a	EKF	Angle	Fixed Bump	0.868	0.739	0.777	0.737
5a	EKF	Range	Fixed Bump	0.411	0.374	0.377	0.374
6a	EKF	Angle and Range	Fixed Bump	0.785	0.723	0.731	0.723
7a	EKF	Angle	Adaptive Bump	1.168	1.026	1.045	1.022
8a	EKF	Range	Adaptive Bump	0.925	0.691	0.715	0.685
9a	EKF	Angle and Range	Adaptive Bump	1.269	1.042	1.065	1.032
10a	UKF	Angle	van Loan	0.870	0.842	0.865	0.837
11a	UKF	Range	van Loan	0.958	0.704	0.826	0.695
12a	UKF	Angle and Range	van Loan	1.023	0.970	0.988	0.963
13a	UKF	Angle	Fixed Bump	0.779	0.746	0.776	0.743
14a	UKF	Range	Fixed Bump	0.612	0.531	0.540	0.527
15a	UKF	Angle and Range	Fixed Bump	0.815	0.800	0.804	0.797
16a	UKF	Angle	Adaptive Bump	0.865	0.839	0.862	0.836
17a	UKF	Range	Adaptive Bump	0.808	0.701	0.737	0.692
18a	UKF	Angle and Range	Adaptive Bump	1.030	0.971	0.990	0.964

Table 5.11: Covariance Trust Ratio (CTR) results for TFCs estimating only observer state elements, without perfect knowledge of RSO positions.

Test Case	**Estimator**	**Measurement Type(s)**	**Process Noise Covariance Model**	**Full Mean CTR**	**Full Median CTR**	**Framed Mean CTR**	**Framed Median CTR**
1b	EKF	Angle	van Loan	742.7	682.0	700.9	676.3
2b	EKF	Range	van Loan	1.769e+03	1.765e+03	1.772e+03	1.772e+03
3b	EKF	Angle and Range	van Loan	2.549e+03	2.640e+03	2.612e+03	2.668e+03
4b	EKF	Angle	Fixed Bump	145.4	151.3	144.6	152.4
5b	EKF	Range	Fixed Bump	217.4	213.7	216.5	213.4
6b	EKF	Angle and Range	Fixed Bump	388.0	396.6	393.8	399.5
7b	EKF	Angle	Adaptive Bump	816.0	755.5	773.6	750.6
8b	EKF	Range	Adaptive Bump	1.632e+03	1.619e+03	1.629e+03	1.623e+03
9b	EKF	Angle and Range	Adaptive Bump	2.353e+03	2.442e+03	2.412e+03	2.468e+03
10b	UKF	Angle	van Loan	158.1	166.9	158.9	168.7
11b	UKF	Range	van Loan	329.5	315.0	330.5	316.0
12b	UKF	Angle and Range	van Loan	351.9	334.6	356.2	337.8
13b	UKF	Angle	Fixed Bump	77.98	79.60	78.35	80.78
14b	UKF	Range	Fixed Bump	157.6	157.3	157.6	157.3
15b	UKF	Angle and Range	Fixed Bump	192.1	194.1	194.0	195.4
16b	UKF	Angle	Adaptive Bump	163.0	171.0	163.3	172.5
17B	UKF	Range	Adaptive Bump	289.7	278.0	290.6	278.9
18b	UKF	Angle and Range	Adaptive Bump	319.9	303.4	323.6	306.2

Table 5.12: Covariance Trust Ratio (CTR) results for TFCs estimating both observer and RSO state elements.

Test Case	**Estimator**	**Measurement Type(s)**	**Process Noise Covariance Model**	**Full Mean CTR**	**Full Median CTR**	**Framed Mean CTR**	**Framed Median CTR**
19	EKF	Angle	van Loan	0.882	0.850	0.860	0.858
20	EKF	Range	van Loan	0.854	0.766	0.806	0.771
21	EKF	Angle and Range	van Loan	0.973	0.866	0.893	0.868
22	EKF	Angle	Fixed Bump	0.204	0.170	0.175	0.166
23	EKF	Range	Fixed Bump	0.568	0.390	0.581	0.457
24	EKF	Angle and Range	Fixed Bump	0.214	0.188	0.190	0.186
25	EKF	Angle	Adaptive Bump	0.869	0.827	0.846	0.835
26	EKF	Range	Adaptive Bump	0.810	0.731	0.760	0.737
27	EKF	Angle and Range	Adaptive Bump	0.981	0.870	0.901	0.875
28	UKF	Angle	van Loan	0.791	0.786	0.799	0.796
29	UKF	Range	van Loan	0.777	0.739	0.783	0.746
30	UKF	Angle and Range	van Loan	0.888	0.851	0.897	0.861
31	UKF	Angle	Fixed Bump	0.308	0.283	0.309	0.286
32	UKF	Range	Fixed Bump	0.816	0.755	0.823	0.775
33	UKF	Angle and Range	Fixed Bump	0.204	0.196	0.200	0.194
34	UKF	Angle	Adaptive Bump	0.791	0.794	0.799	0.802
35	UKF	Range	Adaptive Bump	0.745	0.709	0.749	0.715
36	UKF	Angle and Range	Adaptive Bump	0.848	0.823	0.854	0.830

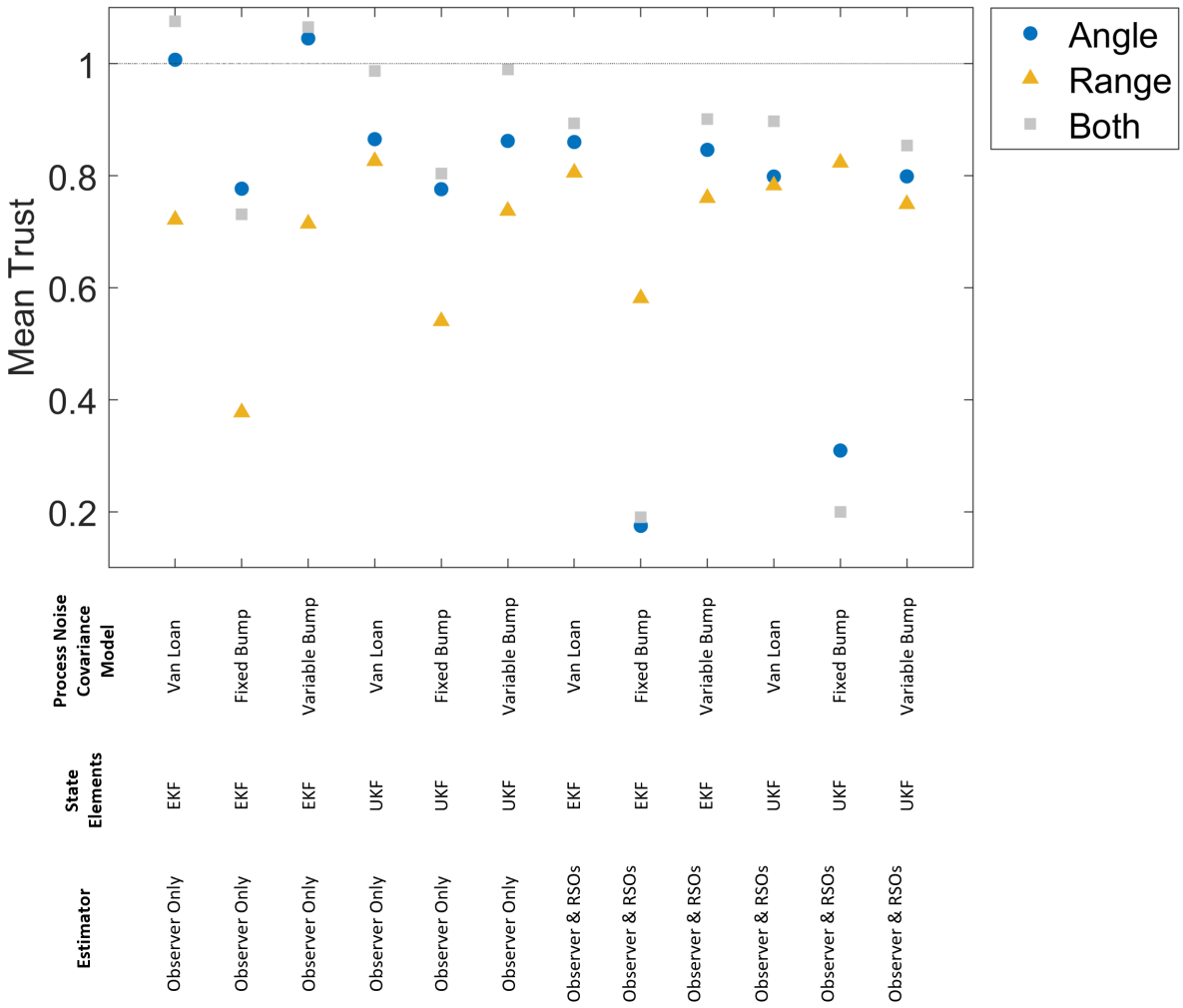

Fig. 5.16: Mean CTRs for each TFC for timesteps 500 to the end of the simulation. TFCs estimating only observer state elements are shown with perfect knowledge of RSO positions.

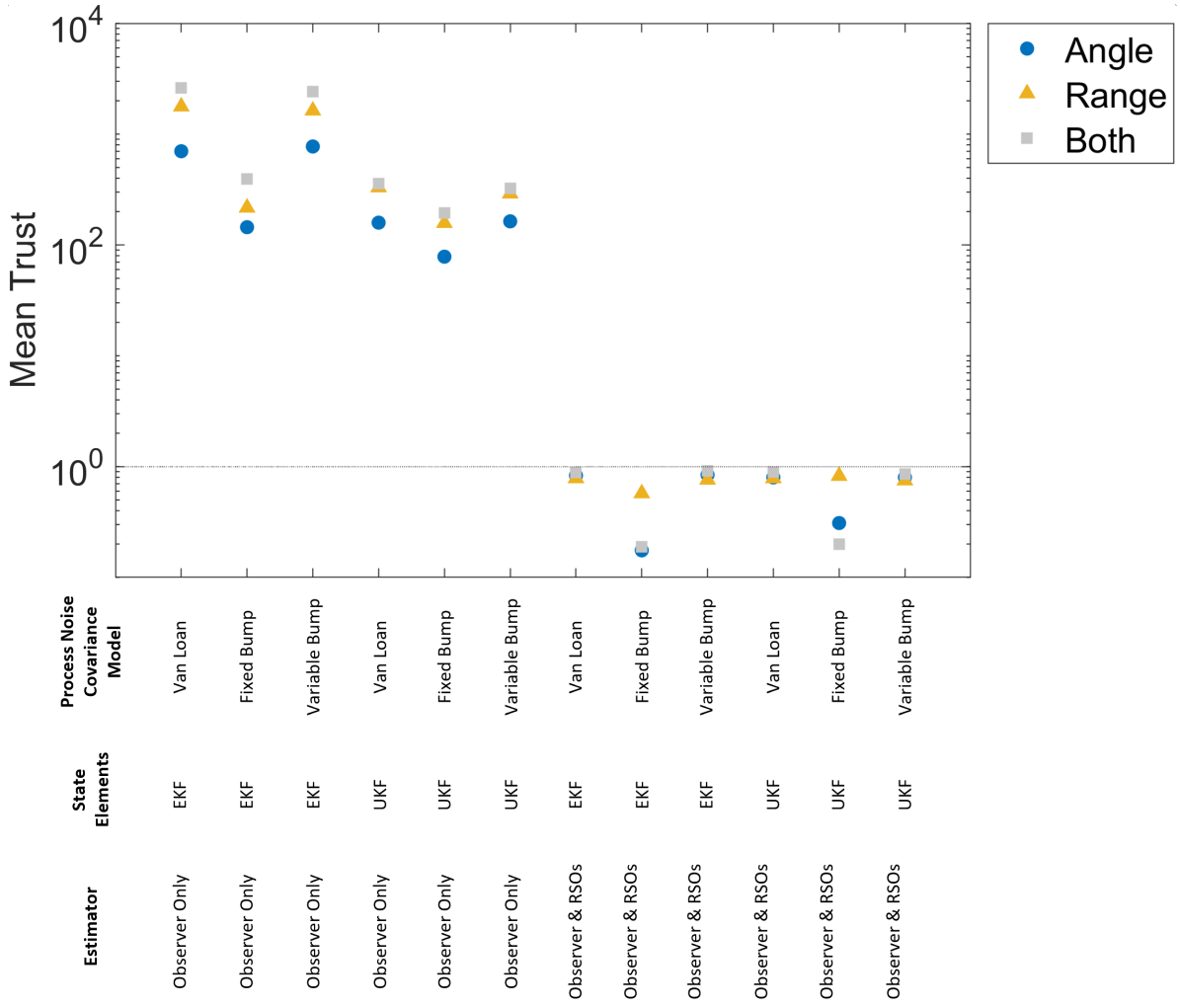

Fig. 5.17: Mean CTRs for each TFC for timesteps 500 to the end of the simulation. TFCs estimating only observer state elements are shown without perfect knowledge of RSO positions.

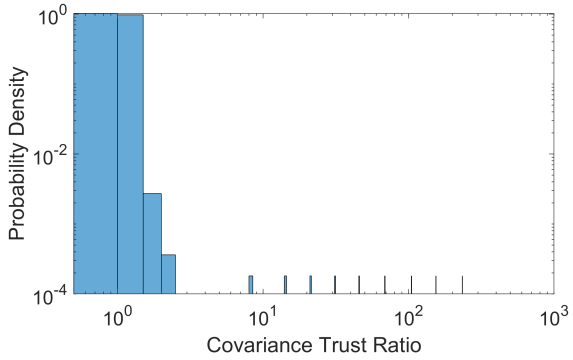

(a) PDF for Test Case 1a av. CTR values

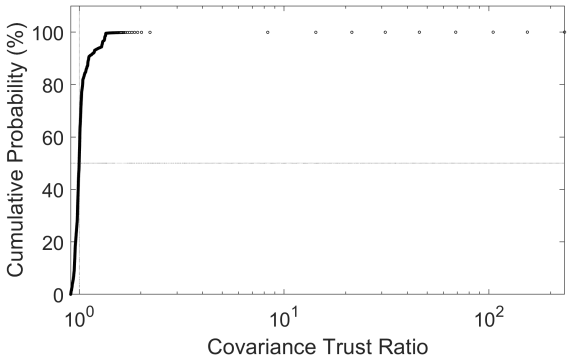

(b) CDF for Test Case 1a av. CTR values

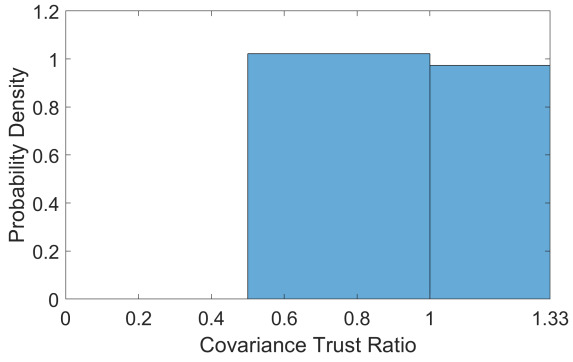

(c) PDF for Test Case 1a av. CTR values, truncated to probabilities below 98%

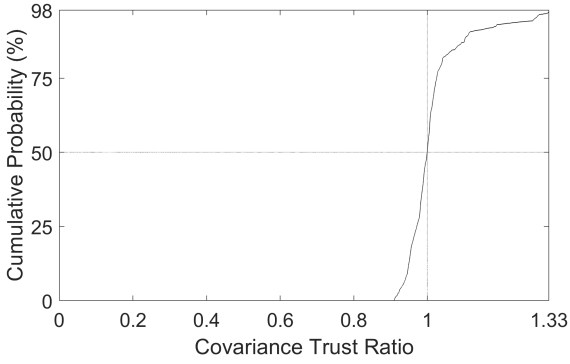

(d) CDF for Test Case 1a av. CTR values, truncated to probabilities below 98%

Fig. 5.18: CDFs and PDFs for TFC Test Case 1a: filters using the EKF to estimate the observer's state using angle measurements and the van Loan process noise covariance model with perfect RSO position knowledge.

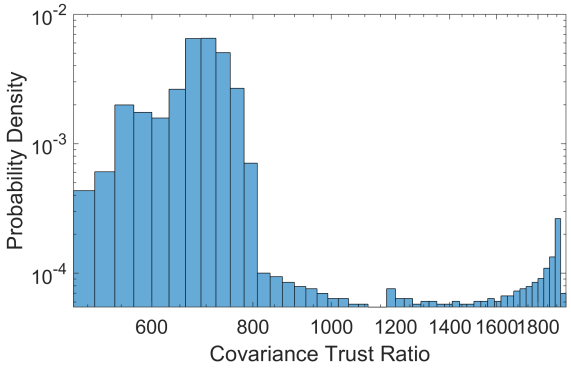

(a) PDF for Test Case 1b av. CTR values

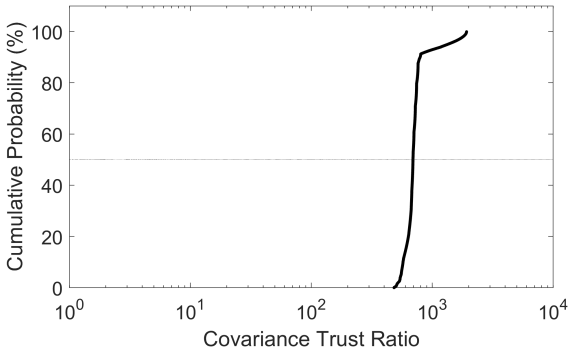

(b) CDF for Test Case 1b av. CTR values

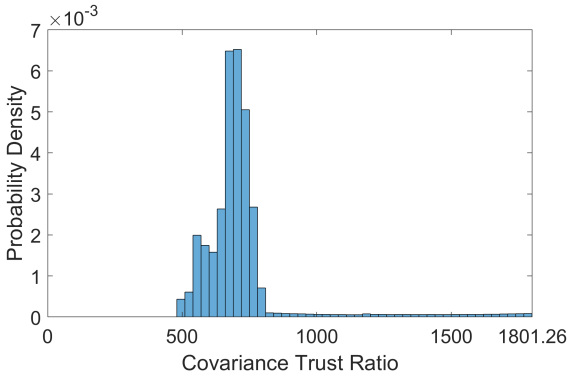

(c) PDF for Test Case 1b av. CTR values, truncated to probabilities below 98%

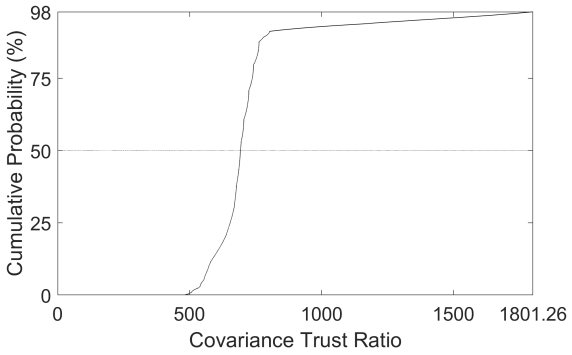

(d) CDF for Test Case 1b av. CTR values, truncated to probabilities below 98%

Fig. 5.19: CDFs and PDFs for TFC Test Case 1b: filters using the EKF to estimate the observer's state using angle measurements and the van Loan process noise covariance model without perfect RSO position knowledge without perfect RSO position knowledge.

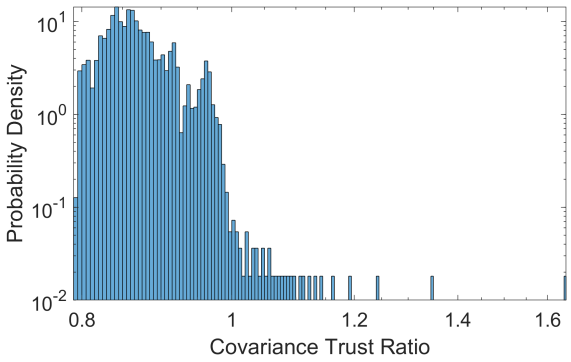

(a) PDF for Test Case 10a av. CTR values

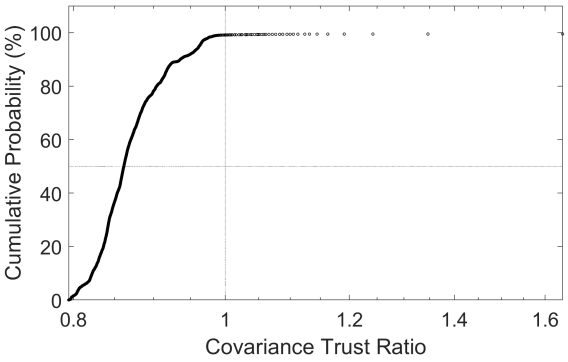

(b) CDF for Test Case 10a av. CTR values

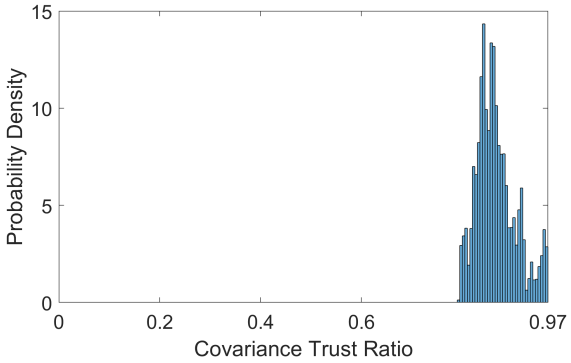

(c) PDF for Test Case 10a av. CTR values, truncated to probabilities below 98%

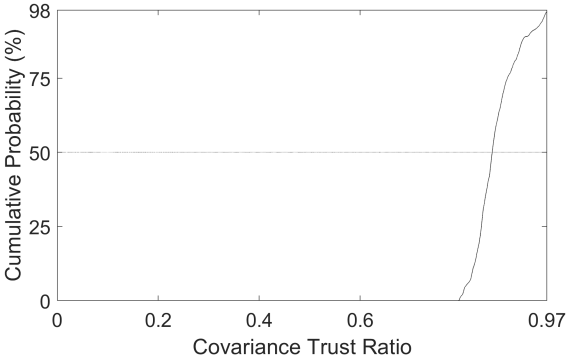

(d) CDF for Test Case 10a av. CTR values, truncated to probabilities below 98%

Fig. 5.20: CDFs and PDFs for TFC Test Case 10a: filters using the UKF to estimate the observer's state using angle measurements and the van Loan process noise covariance model with perfect RSO position knowledge.

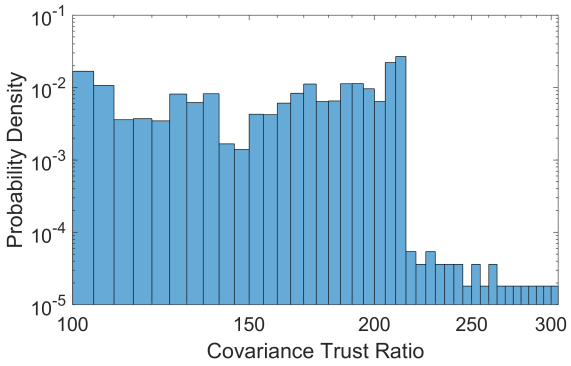

(a) PDF for Test Case 10b av. CTR values

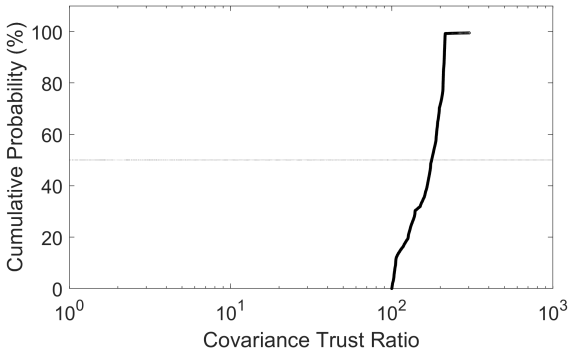

(b) CDF for Test Case 10b av. CTR values

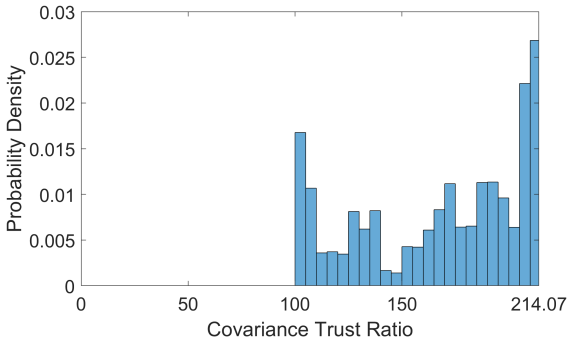

(c) PDF for Test Case 10b av. CTR values, truncated to probabilities below 98%

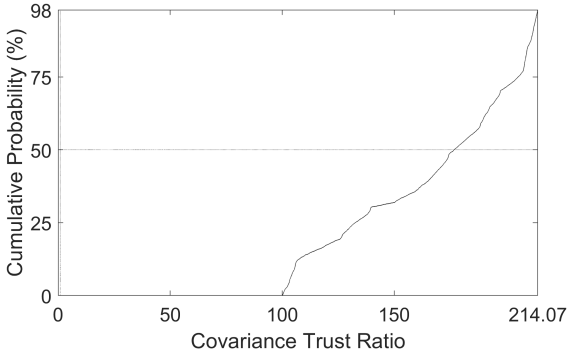

(d) CDF for Test Case 10b av. CTR values, truncated to probabilities below 98%

Fig. 5.21: CDFs and PDFs for TFC Test Case 10b: filters using the UKF to estimate the observer's state using angle measurements and the van Loan process noise covariance model.

Similarly, the NEES analysis results are summarized in Tables 5.13 and 5.14 while Fig. 5.22 and 5.23 show how the NEES values vary for each TFC based on the measurement type selected and whether observer-only TFCs included errors between the assumed and true RSO positions. Figure 5.22 includes the results for TFCs estimating both RSO and observer state elements as well as TFCs estimating only the observer's state elements with perfect RSO position knowledge. Conversely, Fig. 5.23 includes the results for TFCs estimating both RSO and observer state elements as well as TFCs estimating only the observer's state elements without perfect RSO position knowledge.

Table 5.13: NEES results for TFCs estimating only observer state elements, with perfect knowledge of RSO positions.

Test Case	**Estimator**	**Measurement Type(s)**	**Process Noise Covariance Model**	**Full Mean NEES**	**Full Median NEES**	**Framed Mean NEES**	**Framed Median NEES**
1a	EKF	Angle	van Loan	6.919	6.676	6.199	5.950
2a	EKF	Range	van Loan	5.285	5.109	5.166	4.956
3a	EKF	Angle and Range	van Loan	6.207	6.181	6.031	5.999
4a	EKF	Angle	Fixed Bump	3.374	3.326	2.816	2.777
5a	EKF	Range	Fixed Bump	2.037	1.955	1.902	1.813
6a	EKF	Angle and Range	Fixed Bump	2.619	2.624	2.577	2.583
7a	EKF	Angle	Adaptive Bump	7.133	6.784	6.417	6.018
8a	EKF	Range	Adaptive Bump	5.089	4.970	4.950	4.871
9a	EKF	Angle and Range	Adaptive Bump	6.234	6.252	6.039	6.014
10a	UKF	Angle	van Loan	3.994	3.978	3.971	3.950
11a	UKF	Range	van Loan	104.1	8.563	5.572	5.256
12a	UKF	Angle and Range	van Loan	9.129	5.273	5.553	4.632
13a	UKF	Angle	Fixed Bump	2.818	2.797	2.809	2.778
14a	UKF	Range	Fixed Bump	112.1	3.381	2.729	2.471
15a	UKF	Angle and Range	Fixed Bump	3.715	3.070	2.928	2.928
16a	UKF	Angle	Adaptive Bump	3.983	3.936	3.970	3.933
17a	UKF	Range	Adaptive Bump	9.986	8.724	5.607	5.301
18a	UKF	Angle and Range	Adaptive Bump	10.58	5.446	5.770	4.660

Table 5.14: NEES results for TFCs estimating only observer state elements, without perfect knowledge of RSO positions.

Test Case	**Estimator**	**Measurement Type(s)**	**Process Noise Covariance Model**	**Full Mean NEES**	**Full Median NEES**	**Framed Mean NEES**	**Framed Median NEES**
1b	EKF	Angle	van Loan	3.815e+06	2.462e+06	3.521e+06	2.294e+06
2b	EKF	Range	van Loan	7.185e+07	5.470e+07	7.427e+07	5.682e+07
3b	EKF	Angle and Range	van Loan	1.702e+08	9.612e+07	1.777e+08	1.001e+08
4b	EKF	Angle	Fixed Bump	3.321e+05	2.562e+05	2.784e+05	1.879e+05
5b	EKF	Range	Fixed Bump	1.784e+06	1.158e+06	1.792e+06	1.150e+06
6b	EKF	Angle and Range	Fixed Bump	4.150e+06	2.449e+06	4.288e+06	2.540e+06
7b	EKF	Angle	Adaptive Bump	4.657e+06	3.195e+06	4.296e+06	2.883e+06
8b	EKF	Range	Adaptive Bump	8.324e+07	6.068e+07	8.568e+07	6.275e+07
9b	EKF	Angle and Range	Adaptive Bump	1.683e+08	1.196e+08	1.758e+08	1.250e+08
10b	UKF	Angle	van Loan	2.734e+05	1.820e+05	2.608e+05	1.777e+05
11b	UKF	Range	van Loan	2.126e+06	1.505e+06	2.171e+06	1.550e+06
12b	UKF	Angle and Range	van Loan	2.449e+06	1.675e+06	2.534e+06	1.728e+06
13b	UKF	Angle	Fixed Bump	1.660e+05	1.210e+05	1.559e+05	1.048e+05
14b	UKF	Range	Fixed Bump	7.678e+05	5.090e+05	7.776e+05	5.066e+05
15b	UKF	Angle and Range	Fixed Bump	1.494e+06	8.761e+05	1.540e+06	9.090e+05
16b	UKF	Angle	Adaptive Bump	2.420e+05	1.117e+05	2.315e+05	9.884e+04
17B	UKF	Range	Adaptive Bump	5.690e+04	6.489e+04	1.790e+06	1.255e+06
18b	UKF	Angle and Range	Adaptive Bump	2.505e+06	1.680e+06	2.591e+06	1.742e+06

Table 5.15: NEES results for TFCs estimating both observer and RSO state elements.

Test Case	**Estimator**	**Measurement Type(s)**	**Process Noise Covariance Model**	**Full Mean NEES**	**Full Median NEES**	**Framed Mean NEES**	**Framed Median NEES**
19	EKF	Angle	van Loan	21.56	20.62	21.13	20.29
20	EKF	Range	van Loan	20.25	19.98	20.39	20.17
21	EKF	Angle and Range	van Loan	13.72	13.42	13.64	13.34
22	EKF	Angle	Fixed Bump	4.557	4.567	3.981	3.986
23	EKF	Range	Fixed Bump	5.361	5.053	5.100	4.781
24	EKF	Angle and Range	Fixed Bump	3.333	3.327	3.190	3.177
25	EKF	Angle	Adaptive Bump	20.63	20.41	20.14	20.06
26	EKF	Range	Adaptive Bump	20.32	20.01	20.44	20.10
27	EKF	Angle and Range	Adaptive Bump	14.00	13.95	13.96	13.87
28	UKF	Angle	van Loan	19.69	19.53	19.97	19.79
29	UKF	Range	van Loan	20.13	19.67	20.01	19.58
30	UKF	Angle and Range	van Loan	13.54	13.67	13.74	13.82
31	UKF	Angle	Fixed Bump	4.157	4.076	4.220	4.133
32	UKF	Range	Fixed Bump	6.201	5.892	5.759	5.451
33	UKF	Angle and Range	Fixed Bump	3.008	2.999	3.014	3.003
34	UKF	Angle	Adaptive Bump	19.80	19.53	20.09	19.90
35	UKF	Range	Adaptive Bump	20.60	20.35	20.49	20.21
36	UKF	Angle and Range	Adaptive Bump	13.07	13.04	13.23	13.17

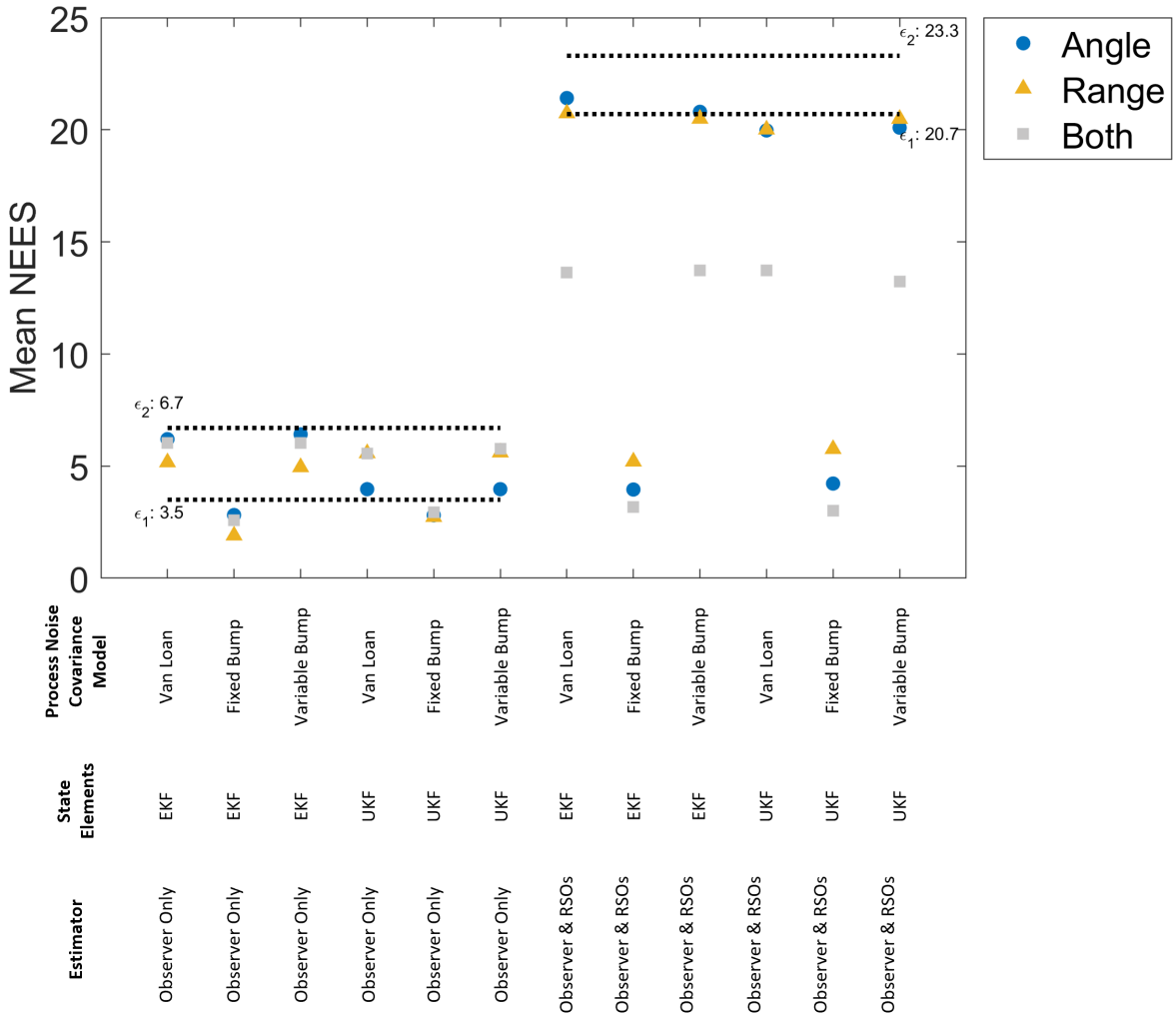

Fig. 5.22: Mean NEES values for each TFC for timesteps 500 to the end of the simulation, along with their expected two sided NEES probability regions ϵ_1 and ϵ_2. TFCs estimating only observer state elements are shown with perfect knowledge of RSO positions.

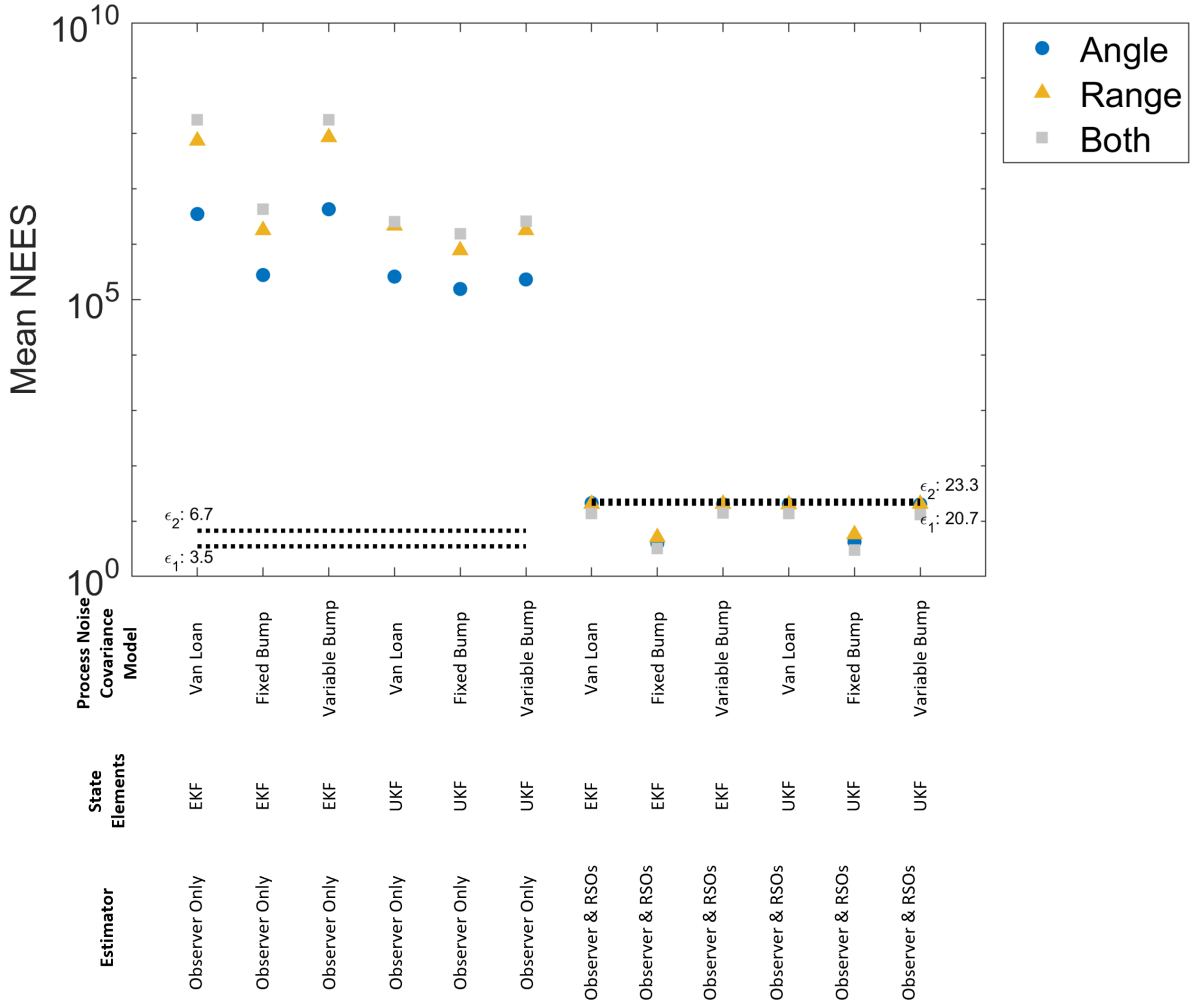

Fig. 5.23: Mean NEES values for each TFC for timesteps 500 to the end of the simulation, along with their expected two sided NEES probability regions ϵ_1 and ϵ_2. TFCs estimating only observer state elements are shown without perfect knowledge of RSO positions.

The NIS analysis results are summarized in Tables 5.16 and 5.17 while Fig. 5.24 and 5.25 show how the NIS values vary for each TFC, based on the measurement type selected and whether observer-only TFCs included errors between the assumed and true RSO positions. Figure 5.24 includes the results for TFCs estimating both RSO and observer state elements as well as TFCs estimating only the observer's state elements with perfect RSO position knowledge. Conversely, Fig. 5.25 includes the results for TFCs estimating both RSO and observer state elements as well as TFCs estimating only the observer's state elements without perfect RSO position knowledge.

Table 5.16: NIS results for TFCs estimating only observer state elements, with perfect knowledge of RSO positions.

Test Case	**Estimator**	**Measurement Type(s)**	**Process Noise Covariance Model**	**Full Mean NIS**	**Full Median NIS**	**Framed Mean NIS**	**Framed Median NIS**
1a	EKF	Angle	van Loan	15.94	15.94	4.206	4.203
2a	EKF	Range	van Loan	11.65	11.65	4.002	4.004
3a	EKF	Angle and Range	van Loan	16.30	16.31	4.153	4.152
4a	EKF	Angle	Fixed Bump	15.83	15.82	4.094	4.093
5a	EKF	Range	Fixed Bump	11.50	11.50	3.896	3.896
6a	EKF	Angle and Range	Fixed Bump	16.16	16.16	4.027	4.023
7a	EKF	Angle	Adaptive Bump	15.94	15.92	4.205	4.202
8a	EKF	Range	Adaptive Bump	11.64	11.63	3.998	3.999
9a	EKF	Angle and Range	Adaptive Bump	16.31	16.31	4.150	4.145
10a	UKF	Angle	van Loan	4.278	4.273	4.167	4.168
11a	UKF	Range	van Loan	5.377	4.653	4.627	4.553
12a	UKF	Angle and Range	van Loan	4.206	4.199	4.179	4.177
13a	UKF	Angle	Fixed Bump	4.106	4.098	3.995	3.998
14a	UKF	Range	Fixed Bump	5.231	4.555	4.470	4.462
15a	UKF	Angle and Range	Fixed Bump	4.055	4.040	4.022	4.022
16a	UKF	Angle	Adaptive Bump	4.286	4.280	4.170	4.165
17a	UKF	Range	Adaptive Bump	4.651	4.654	4.547	4.548
18a	UKF	Angle and Range	Adaptive Bump	4.284	4.196	4.180	4.180

Table 5.17: NIS results for TFCs estimating only observer state elements, without perfect knowledge of RSO positions.

Test Case	**Estimator**	**Measurement Type(s)**	**Process Noise Covariance Model**	**Full Mean NIS**	**Full Median NIS**	**Framed Mean NIS**	**Framed Median NIS**
1b	EKF	Angle	van Loan	2.634e+03	1.335e+03	1.629e+03	909.8
2b	EKF	Range	van Loan	2.569e+05	1.770e+05	2.593e+05	1.708e+05
3b	EKF	Angle and Range	van Loan	4.495e+04	1.644e+04	4.234e+04	1.554e+04
4b	EKF	Angle	Fixed Bump	372.3	261.5	242.8	133.1
5b	EKF	Range	Fixed Bump	3.192e+05	1.964e+05	3.246e+05	1.979e+05
6b	EKF	Angle and Range	Fixed Bump	8.378e+03	4.112e+03	5.698e+03	2.805e+03
7b	EKF	Angle	Adaptive Bump	3.097e+03	1.619e+03	1.875e+03	1.061e+03
8b	EKF	Range	Adaptive Bump	2.733e+05	1.952e+05	2.755e+05	1.943e+05
9b	EKF	Angle and Range	Adaptive Bump	5.129e+04	3.176e+04	4.868e+04	2.950e+04
10b	UKF	Angle	van Loan	329.4	212.7	294.4	177.6
11b	UKF	Range	van Loan	3.863e+04	3.833e+04	2.711e+05	2.150e+05
12b	UKF	Angle and Range	van Loan	4.971e+03	4.203e+03	5.299e+03	2.861e+03
13b	UKF	Angle	Fixed Bump	278.3	132.1	248.6	113.0
14b	UKF	Range	Fixed Bump	4.391e+04	4.490e+04	2.119e+05	1.515e+05
15b	UKF	Angle and Range	Fixed Bump	5.210e+03	3.738e+03	5.963e+03	2.531e+03
16b	UKF	Angle	Adaptive Bump	254.0	160.2	224.7	129.1
17B	UKF	Range	Adaptive Bump	3.901e+04	3.639e+04	2.262e+05	1.754e+05
18b	UKF	Angle and Range	Adaptive Bump	5.033e+03	3.805e+03	5.372e+03	2.569e+03

Table 5.18: NIS results for TFCs estimating both observer and RSO state elements.

Test Case	**Estimator**	**Measurement Type(s)**	**Process Noise Covariance Model**	**Full Mean NIS**	**Full Median NIS**	**Framed Mean NIS**	**Framed Median NIS**
19	EKF	Angle	van Loan	15.92	15.91	4.178	4.179
20	EKF	Range	van Loan	11.65	11.64	3.998	3.998
21	EKF	Angle and Range	van Loan	16.30	16.30	4.145	4.143
22	EKF	Angle	Fixed Bump	15.11	15.11	4.063	4.063
23	EKF	Range	Fixed Bump	11.30	11.30	3.780	3.781
24	EKF	Angle and Range	Fixed Bump	16.04	16.04	3.947	3.947
25	EKF	Angle	Adaptive Bump	15.91	15.92	4.169	4.169
26	EKF	Range	Adaptive Bump	11.65	11.65	4.002	4.002
27	EKF	Angle and Range	Adaptive Bump	16.28	16.28	4.141	4.142
28	UKF	Angle	van Loan	4.300	4.298	4.193	4.192
29	UKF	Range	van Loan	4.120	4.119	4.000	4.002
30	UKF	Angle and Range	van Loan	4.145	4.145	4.143	4.144
31	UKF	Angle	Fixed Bump	4.095	4.097	3.999	3.998
32	UKF	Range	Fixed Bump	3.823	3.826	3.717	3.720
33	UKF	Angle and Range	Fixed Bump	3.886	3.888	3.887	3.887
34	UKF	Angle	Adaptive Bump	4.296	4.292	4.193	4.193
35	UKF	Range	Adaptive Bump	4.120	4.118	3.999	4.001
36	UKF	Angle and Range	Adaptive Bump	4.143	4.144	4.142	4.142

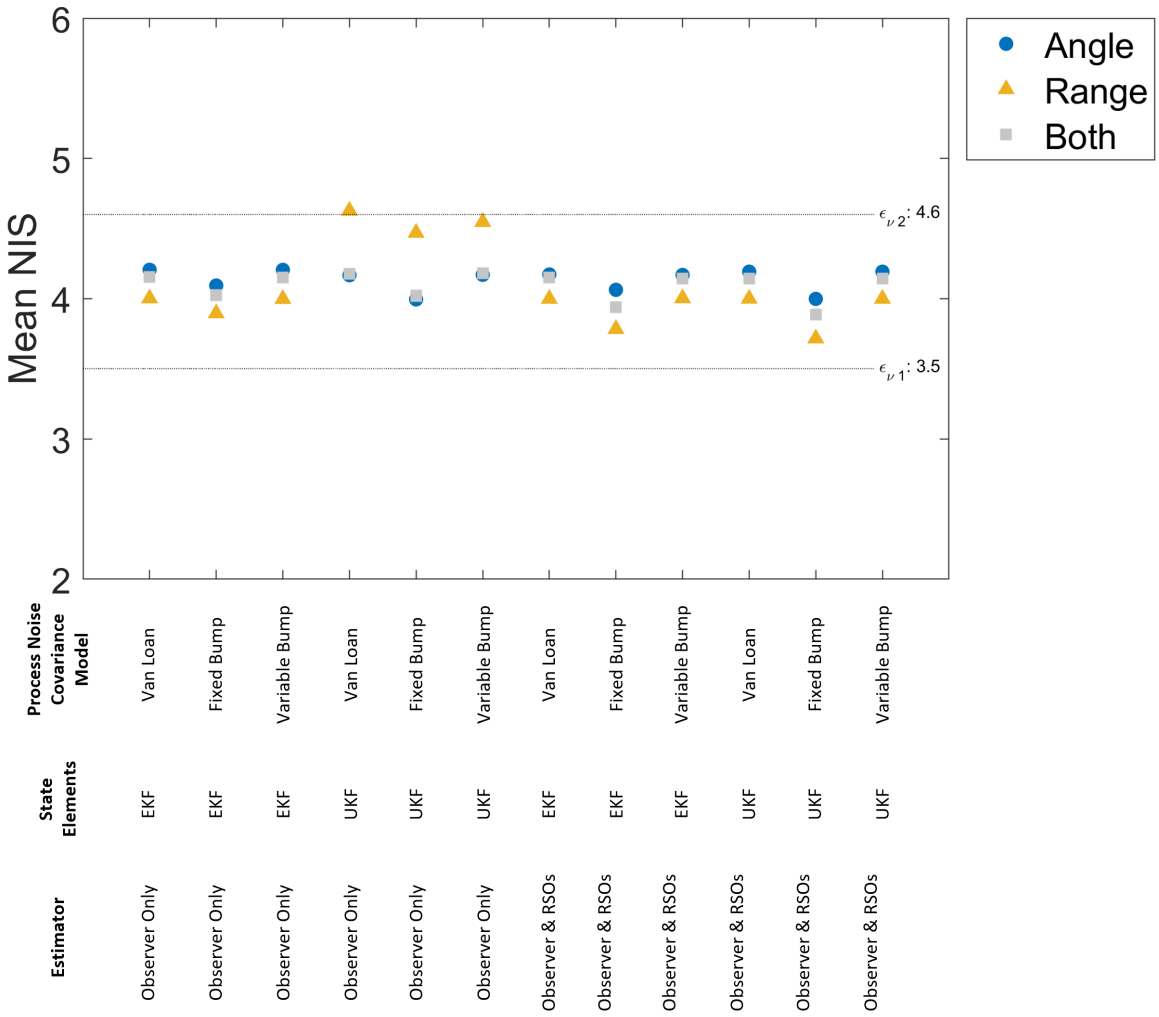

Fig. 5.24: Mean NIS values for each TFC for timesteps 500 to the end of the simulation, along with their expected two sided NIS probability regions $\epsilon_{\nu 1}$ and $\epsilon_{\nu 2}$. TFCs estimating only observer state elements are shown with perfect knowledge of RSO positions. Note that the mean NIS values for the TFCs estimating observers and RSOs, using a UKF, the Adaptive Bump process noise covariance model, and either angle or both angle and range measurements are not shown as these values (1.19E7 and 1.09E7 respectively) greatly exceeded all other values.

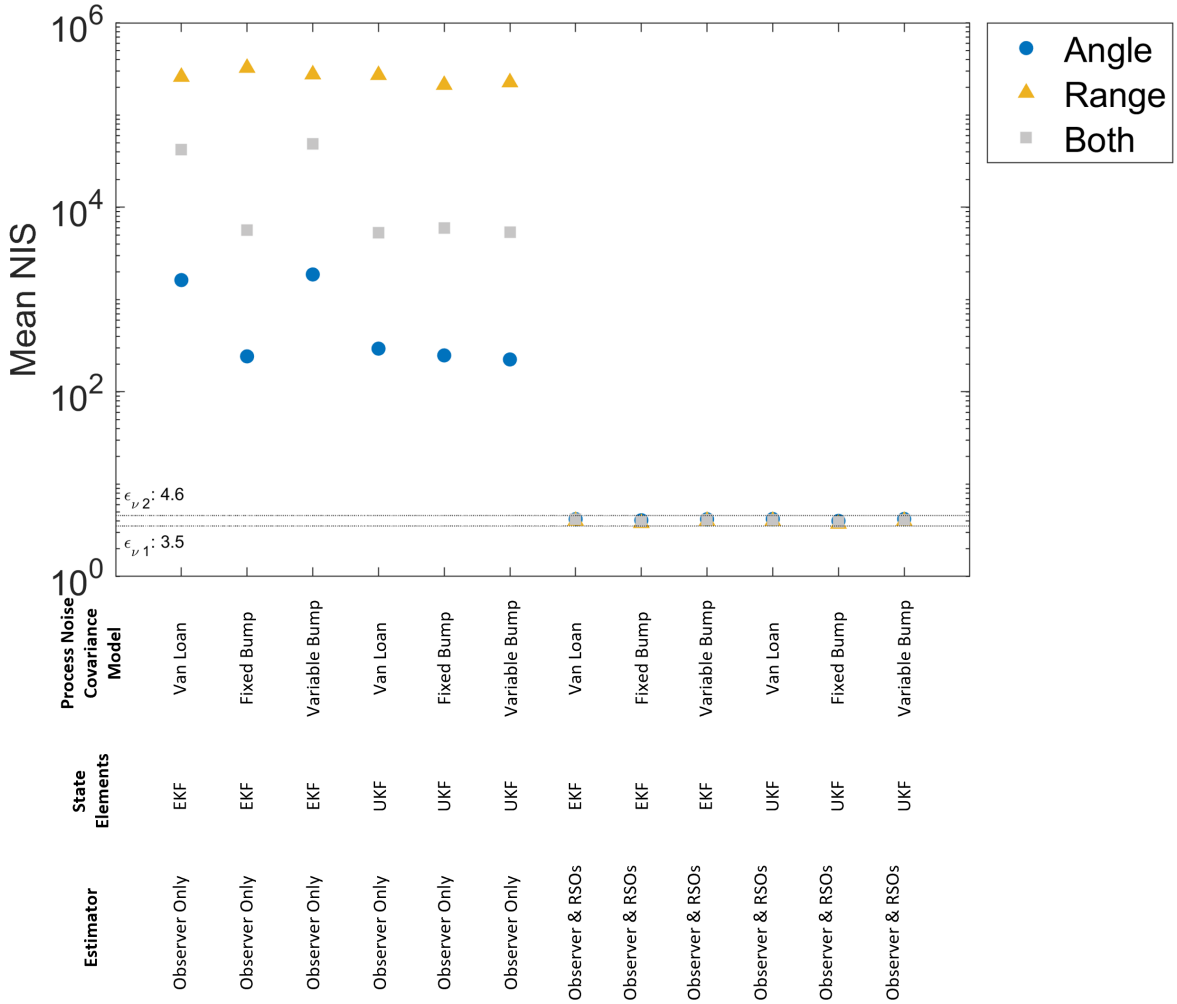

Fig. 5.25: Mean NIS values for each TFC for timesteps 500 to the end of the simulation, along with their expected two sided NIS probability regions $\epsilon_{\nu 1}$ and $\epsilon_{\nu 2}$. TFCs estimating only observer state elements are shown without perfect knowledge of RSO positions.

Reliability Metrics and Non-Positive Definite Covariance Estimates In previous UKF implementations, before using Symmetric Cholesky Factors [149] to calculate the UKF state covariance estimate matrix square roots, I observed that some Monte Carlo runs of the UKF-based TFCs occasionally generated non-PD state covariance estimates. In these previous implementations, I chose to correct non-PD state covariance estimates by adding a small value to the diagonal elements of the affected state covariance estimates. Adding these diagonal elements increased the covariance matrix's eigenvalues so that all eigenvalues were greater than zero and ensured that the matrix was PD, without affecting the values of the matrix square roots. While this is a common solution to non-PD state covariance estimates, [44] recommends other solutions such as covariance factorization, as adding fixed values cannot always ensure that the state covariance estimate has positive eigenvalues [44].

In my previous UKF implementations that used this additive state covariance correction, I observed that some Monte Carlo runs of the UKF-based TFCs experienced occasional spikes in their reliability metrics when non-PD covariance estimates were corrected. Despite correcting the non-PD state covariance estimates, all three reliability metrics were influenced by the non-PD covariances to some extent. NEES values were affected to the greatest extent and increased by 5 orders of magnitude or greater. NIS and the average CTR were also affected, however these metrics remained within one order of magnitude of their previous values. Figure 5.26 shows the NEES, NIS, and average CTR values for one such Monte Carlo run. These spikes corresponded to occasions when the filter's covariance estimates became non-PD and were corrected.

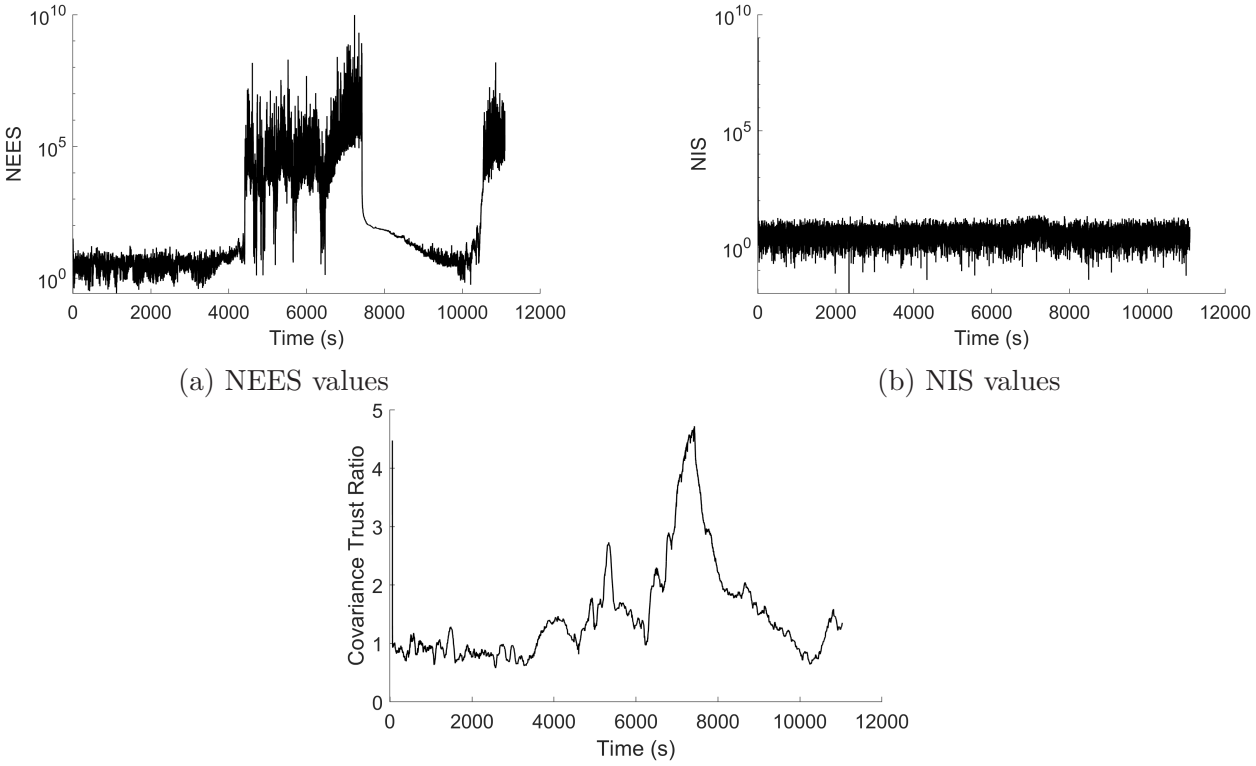

(a) NEES values

(b) NIS values

(c) Average CTR values

Fig. 5.26: NEES, NIS, and average CTR values for Monte Carlo run 30 of a previous iteration of TFC Test Case 10: filters using the UKF to estimate the observer's state using angle measurements and the van Loan process noise covariance model. This Monte Carlo run produced non-PD covariance estimates from 4400 s to 7400 s as well as between 10400 s and the end of the simulation. This previous iteration used a different method of calculating matrix square roots which resulted in non-PD covariance estimates. These non-PD covariance estimates were corrected by adding a small constant to the diagonal elements of the affected covariance estimates.

Implementing Symmetric Cholesky Factors eliminated all non-PD state covariance estimates. However, these non-PD events in this previous UKF implementation provide some insight into the potential utility of each reliability metric. If a filter requires intervention to prevent it from failing due to numerical issues, the filter's trustworthiness should be treated with extreme caution and so NEES' ability to detect such events could be seen as a significant strength. Conversely, if such an intervention is required, it is likely that the monitor is already aware that the intervention has taken place. In these cases the CTR provides a useful tool to evaluate how trustworthy the resulting estimates are.

5.3.3.2 Discussion

This section discusses the simulation results that were presented in the previous section. First, I discuss the convergence results and the observability of the TFCs, followed by a discussion regarding trends that I observed in the CTR, NEES, and NIS metrics. Finally, this section reviews and assesses the hypotheses presented in section 5.3.1.5.

Filter Convergence and Observability Several TFCs failed to converge for all state elements while some completely diverged or had uncertain convergences. Note that, as in Ch. 3, I used Gelb's convergence criteria [8] when assessing the filter's performance. These divergences and uncertain convergences fall under three categories: inappropriately sized fixed process noise covariance bumps, increasing measurement innovation errors, and incomplete observability.

When estimating both the observer and RSO states, TFCs using both the EKF and UKF diverged when using the fixed bump process noise covariance model. This was due to the fixed bump being sized for the EKF when estimating only the observer's state and being inappropriately sized for TFCs estimating both RSO and observer state elements. These divergences highlight the importance of sizing any additive corrections to a filter's process noise covariance appropriately.

The TFCs that estimated only the observer's state fully converged when provided with true RSO positions to use in their measurement models. However, these combinations had likely, but uncertain, convergences when they were not provided with these true RSO positions. In these scenarios, the error between the true and assumed RSO states introduced a small but progressively increasing error into the system which resulted in an increasing measurement innovation error. This innovation error prevented these TFCs from fully converging and, given enough time, will likely cause these TFCs to diverge. These results highlight the importance of accurate filter measurement models.

State observability affected TFC convergences in two ways. The most obvious being the inability of TFCs which used only range measurements to converge on angular position and velocity state elements. However, incomplete observability also affected the convergence of TFCs which estimated both the RSO and observer states.

As expected, the angle and angular velocity state elements did not converge for TFCs that used only range measurements, due to these state elements being unobservable. For a discrete linear time-invariant system to be fully observable, the rank of the following observability matrix $\mathcal{Q}$ must be equal to the number of state elements n [139][5]

$$\mathcal{Q} = \begin{bmatrix} H_k \\ H_k\Phi \\ H_k\Phi^2 \\ \cdots \\ H_k\Phi^{n-1} \end{bmatrix} \tag{5.37}$$

where H_k is the discretized linear observation model and Φ is the discretized linear state transition model. Note that this linear observability criterion requires linear state transition and linear observation models. While this criterion can be used directly with an EKF, the criterion cannot be applied to the nonlinear models used by the UKF. As noted by [139], observability for nonlinear systems is more difficult to quantify. Formally deriving the UKF's observability for the nonlinear observation and state transition models used here is outside the scope of this dissertation. However, the UKF's observability can be inferred from the linearized system observability criterion and the UKF test results.

Applying Eq. 5.37 to the EKF TFCs that used only range measurements to estimate the observer's state yielded a linear observability matrix $\mathcal{Q}$ of rank 4. This observability rank was below the $n = 6$ state elements included in these TFCs and indicated that these TFCs were not fully observable. This confirms that the divergent angular position and rates observed for TFCs using only range measurements were due to poor observability. Conversely, TFCs that used either angle or both range and angle measurements to estimate the observer state had full ranks and, as expected, were able to converge for all state elements.

Similarly, EKF TFCs that used both range and angle measurements to estimate both the observer and RSO states ($n = 22$) had full observability rank and, aside from combinations that used the inappropriately sized fixed process noise covariance bump, were able to converge. However, combinations that used either range or angle measurements to estimate both RSO

[5]pp 41.

and observer state elements did not have full observability. The TFCs that used only range measurements had observability matrix $\mathcal{Q}$ ranks of 12 while those using only angle measurements had ranks of 14. Unlike the TFCs that estimated only the observer's state, these relative measurements were not tied to an external reference outside of the combined RSO-observer system's state. The state dynamics restricted the possible solutions but TFCs that used angle or range measurements had insufficient observability to distinguish errors in the observer's state from those in the RSO's state. This resulted in steady-state estimate errors that appeared to move as random walks rather than converging towards the system's process noise covariance or to cyclical patterns. While these TFCs will likely remain converged to these bounded random walks, this continued behaviour is not guaranteed.

As noted previously, the linear observability matrix $\mathcal{Q}$ rank is not directly applicable to the UKF. However, based on the linear observability analysis as well as the similarities between the UKF and EKF test results, it is likely that the divergences observed for the UKF were also due to insufficient observability.

Additionally, this observability analysis did not consider the effects of RSO-observer geometries on the system's observability. As discussed in Sec. 3.4.2, elements of H_k may approach zero as the relative distance between the observer and an RSO approaches zero in one of the system's Cartesian axes. If this occurs, the system's observability may temporarily drop below the values presented here. However, due to the rapidly changing orbital positions of the RSOs and observer, such events are unlikely to last for more than a handful timesteps. While not explored in this dissertation, intelligently selecting RSO references to avoid scenarios where the relative distance between an RSO and the observing spacecraft approaches zero in any axes would remove these effects.

While observability appeared to have a noticeable effect on filter convergence, incomplete observability had a significantly lesser effect on filter reliability. The following section examines this relationship, as well as other reliability trends between the different TFC results.

Filter Reliability Trends and Observations All of the TFCs that estimated the observer's state with perfect RSO position knowledge and most of the TFCs that estimated both the observer and RSO states (except for Test Case 32, the UKF estimating both RSO and

observer states using range measurements and the fixed bump process noise covariance model) had state covariance estimates that were proportional to the filter's estimate errors. As seen in Fig. 5.16, 5.22, and 5.24, the TFCs which estimated both RSO and observer state elements tended to produce lower average CTR and NEES values and equivalent NIS values when compared to observer-only TFCs with perfect RSO position knowledge. This indicates that filters estimating both RSO and observer state elements tended to over-estimate the state covariance but accurately predicted their expected measurements. These relationships were seen for TFCs with and without full observability. This indicates that, while observability may be an important factor for filter convergence, filters with incomplete observability can still reliably produce state covariances that are reflective of the filter's estimate error and accurately predict expected measurements. Based on these state covariance estimates and expected measurements, a user can assess the trustworthiness of the filter's state estimates.

Conversely, all of the TFCs that estimated the observer's state without perfect RSO position knowledge had state covariance estimates that significantly under-represented the filter's estimate errors. This was caused by the measurement errors introduced into these systems, due to the difference between the true and assumed RSO positions, which were not reflected in these filter's measurement noise covariances. These unmodelled measurement errors are seen in the average CTR, NEES, and NIS values shown in Fig. 5.17, 5.23, and 5.24. Together, these results indicate that, despite having observability ranks that were equal to or proportionally higher than the corresponding TFCs which estimated both RSO and observer state elements, TFCs that estimated only the observer's state elements and included RSO position errors were significantly less trustworthy than TFCs that estimated both RSO and observer state elements. The measurement errors introduced by estimating only observer state elements dramatically worsened the trustworthiness of the observer-only TFCs. These results highlight the importance of adequately modelling a system's measurements and show the benefits of including additional elements in the state to do so.

Comparing the average CTR with the NEES results, the two metrics generally agreed on which of the measurement-types was the most trustworthy. However, NEES values for combinations using both angle and range measurements tended to be lower than combinations that used either angle or range measurements. Conversely, the average CTR values for

combinations using both angle and range measurements tended to be higher than for the other two measurement options. These differences were likely caused by how NEES and the CTR treat the off-diagonal elements of the state covariance estimate (*i.e.* the estimated covariances between different state elements). NEES and NIS both include these inter-state element covariance estimates in their calculations while the CTR only uses the state covariance estimate's diagonal elements (*i.e.* the estimated state variances). TFCs that use both angle and range measurements have stronger correlations between state elements due to their additional measurement sources. These stronger correlations are reflected in the NEES metric but are neglected by the CTR. Similarly, the UKF is able to estimate these inter-state element covariances more accurately than the EKF, as it does not rely on linearized observability models, which is again reflected in the NEES values. Both cases highlight that NEES provides a more holistic evaluation of a filter's state covariance estimate than the average CTR provides, by considering both the state element variances and inter-state element covariances. However, including both state element variances and inter-state element covariances makes NEES more difficult to interpret than the average CTR. While the average CTR and NEES were generally comparable for the converged window, NEES was more heavily influenced by the initial convergence time than the average CTR was, especially for trust factor combinations using the EKF. The average CTR was affected to a much smaller degree (generally within the same order of magnitude as the other values).

Hypothesis Assessments The remainder of this subsection assesses the hypotheses made earlier in this chapter.

Hypothesis 1.2.1: This hypothesis predicted that the UKF would have better (*i.e.* closer to unity) average CTR values than those using the EKF. As shown in Tables 5.10 and 5.11, the results for this hypothesis were mixed. For TFCs estimating only the observer's state with perfect RSO position knowledge, the UKF-based TFCs using angle or range measurements tended to produce average CTR and NEES values that were lower than their EKF-based counterparts. Conversely, the UKF-based TFCs using both angle and range measurements had better CTR and NEES values. When the observer-only TFCs did not have perfect RSO position knowledge, the UKF CTR and NEES values were better, being

Table 5.19: Results from Welch's t-tests to determine if the average CTR values for estimators using the EKF and UKF are equivalent. This analysis was performed using 96 independent simulations for each covariance model and a 5% significance level.

Adaptive Test Case	**van Loan Test Case**	**Equal Means p-value**	**Result**
19	28	0.401	Likely statistically equivalent
20	29	0.270	Likely statistically equivalent
21	30	0.881	Likely statistically equivalent
25	34	0.963	Likely statistically equivalent
26	35	0.645	Likely statistically equivalent
27	36	0.063	Likely statistically equivalent

closer to unity and the NEES ϵ bounds respectively. However, the UKF CTR and NEES were still several orders of magnitude greater than their expected values.

The TFCs that estimated both the observer and RSO states had very similar results when using the EKF or UKF. The EKF may have had slightly better trusts, but a statistical analysis showed that the results were indistinguishable for most instances. This equivalence, summarized in Table 5.19, was determined using Welch's t-test under the null hypothesis that each pair of test cases had equal means for the full time sequence. The alternate hypothesis was that the means are unequal. I used a 5% significance level for these tests.

Based on these results, this hypothesis was incorrect for most TFCs and the UKF has a similar trustworthiness to the EKF. However, for systems with large unmodelled measurement errors, the UKF does have better CTRs.

Hypothesis 1.2.2: This hypothesis predicted that filters estimating both the observer and RSO state elements would have better average CTRs than those estimating only the observer's state. This was correct when the observer-only TFCs did not have perfect knowledge of RSO positions, which is much more representative of a real filter implementation. When the observer-only TFCs had perfect RSO position knowledge, the observer-only combinations had better average CTRs for most cases, which should be expected due to these TFC's better observabilities.

Hypothesis 1.2.3a: This hypothesis predicted that TFCs which used range measure-

ments would have more conservative (*i.e.* lower-valued) position and velocity state element trusts than TFCs that used angle or both angle and range measurements. This hypothesis also predicted that range only TFCs would have divergent (*i.e.* very high-valued) angular position and angular velocity state estimates which would result in these TFCs having non-conservative (*i.e.* high-valued) overall trust.

This hypothesis was true in several aspects. TFCs using range measurements did have lower-valued position and velocity state element trusts and divergent angular position and angular velocity state elements. However, these divergent angular position and angular velocity state elements remained bounded by the filters' state covariance estimates. For TFCs estimating only the observer state using perfect RSO position knowledge and for non-divergent TFCs estimating both RSO and observer states, this resulted in the most conservative, lowest-valued overall trusts compared to combinations using angle or both angle and range measurements. TFCs using range measurements to estimate only the observer's state without perfect RSO position knowledge had better average CTRs when using angle measurements than when using range or angle and range measurements, likely due to the angle measurements being less sensitive to RSO position error than the range measurements were.

The NEES values for non-divergent TFCs using range measurements (when estimating both observer and RSO states and when estimating only the observer's state) were in-between those of the TFCs using only angle measurements and those using both angle and range measurements. This discrepancy between the average CTR and NEES results is likely due to NEES including the off-diagonal elements of the state covariance estimate (*i.e.* the estimated covariances between different state elements) in its calculation. The TFCs that used both range and angle measurements had higher covariances between state elements which resulted in lower NEES values for combinations using both measurement sources than for those using only range measurements.

Hypothesis 1.2.3b: This hypothesis predicted that TFCs using angle measurements would have more conservative (*i.e.* lower-valued) angle and angular velocity trusts, slightly less conservative (*i.e.* higher-valued) position and velocity trusts, and better overall trusts (*i.e* nearer to unity) than the range only TFCs. This hypothesis was correct. Except when

using the EKF to estimate both RSO and observer states using the fixed bump process noise covariance model, all TFCs had better average CTR values and better or equal NEES values when using angle measurements than when using range measurements.

Hypothesis 1.2.3c: This hypothesis predicted that filters using both range and angle measurements would have the best overall trusts (*i.e* closest to unity) compared to angle only and range only filters. The results for this hypothesis were mixed, with some TFCs performing better when using both angle and range measurements and others performing better when using only angle measurements.

For the TFCs estimating both the observer and RSO states that converged, the TFCs that used both range and angle measurements had better average CTR values but worse NEES values than those that used only angle measurements. These results indicate that while filters using both range and angle measurements were able to more closely estimate the diagonal elements of the state covariance (*i.e.* the state element variance) than filters using only angle measurements, these filters over-estimated the off-diagonal elements (*i.e.* the state element covariance). When estimating only the observer state using perfect RSO position knowledge, TFCs using angle measurements had better (but very similar) average CTRs to combinations that used both range and angle measurements.

When estimating only the observer state without perfect RSO position knowledge, the TFCs using both range and angle measurements had the worst average CTR and NEES values. This may have been due to nonlinear interactions between the range and angle measurements caused by their different sensitivities to the measurement innovation errors created by the RSO position estimate errors in these TFCs.

Hypothesis 1.2.4a: This hypothesis predicted that filters using only van Loan's discretized process noise covariance model would slightly under-model the covariance and have the least conservative (*i.e.* highest) trusts. This hypothesis was generally correct, filters using van Loan's discretized process noise covariance model had higher average CTRs than those using the Fixed Bump. However, the average CTRs of filters using van Loan's method and the Adaptive Bump were statistically indistinguishable, with p-values greater than 0.05 for all cases.

This equivalence, summarized in Table 5.20, was determined using Welch's t-test under

Table 5.20: Results from Welch's t-tests to determine if the average CTR values for estimators using the Adaptive and van Loan process noise covariance models are equivalent. This analysis was performed using 96 independent simulations for each covariance model and a 5% significance level.

Adaptive Test Case	**van Loan Test Case**	**Equal Means p-value**	**Result**
1a	7a	0.349	Likely statistically equivalent
2a	8a	0.244	Likely statistically equivalent
3a	9a	0.145	Likely statistically equivalent
10a	16a	0.660	Likely statistically equivalent
11a	17a	0.258	Likely statistically equivalent
12a	18a	0.842	Likely statistically equivalent
1b	7b	0.314	Likely statistically equivalent
2b	8b	0.262	Likely statistically equivalent
3b	9b	0.399	Likely statistically equivalent
10b	16b	0.777	Likely statistically equivalent
11b	17b	0.058	Likely statistically equivalent
12b	18b	0.236	Likely statistically equivalent
19	25	0.577	Likely statistically equivalent
20	26	0.113	Likely statistically equivalent
21	27	0.757	Likely statistically equivalent
28	34	0.825	Likely statistically equivalent
29	35	0.344	Likely statistically equivalent
30	36	0.192	Likely statistically equivalent

the null hypothesis that each pair of test cases had equal means for the full time sequence. The alternate hypothesis was that the means are unequal. I used a 5% significance level for these tests.

Hypothesis 1.2.4c: This hypothesis predicted that filters adding the Adaptive Bump will most accurately model covariance and have the best average CTR values (*i.e.* closest to unity). Hypothesis 1.2.4c was incorrect. As previously discussed, the average CTR values of filters using van Loan's method and those using the Adaptive Bump were mostly statistically equivalent. Including an integration error compensation model in an EKF or UKF's process noise covariance (the basis for the Adaptive Bump) likely had no effect on the filter's average CTR for the TFCs under the conditions that I tested.

Hypothesis 1.2.5a Results: This hypothesis predicted that the UKF estimating both the observer and RSO states, using both range and angle measurements, and using the Adaptive Bump process noise covariance model would have the best average CTR values (*i.e.* closest to unity). Neglecting the TFCs that estimated only the observer's state with perfect RSO position knowledge, due to the unrealistic nature of those TFCs, the best performing TFCs estimated both the observer and RSO states using both angle and range measurements. However, as with Hypothesis 1.2.1, it is hard to say which of these TFC had the best average CTR values due to the similarity of their results. Test Case 27, the EKF using the adaptive bump, had the best CTR value but Test Case 30, the UKF using van Loan's method, was nearly equivalent.

Hypothesis 1.2.5b Results: This hypothesis predicted that the EKF estimating only the observer state, using only range measurements, and using the van Loan process noise covariance model would have the worst (*i.e.* highest valued) trust. Hypothesis 1.2.5b was mostly correct; the worst performing filters were the EKF estimating the observer's state using the van Loan process noise covariance model. However, the TFC using both range and angle measurements had worse average CTR and NEES values than the combination using range measurements.

5.4 Chapter Summary

This chapter has examined several trustworthiness factors that affect filter reliability. These factors included the type of Kalman filter used, whether a filter incorporates elements of the measurement source's state, the type of process noise covariance model used, and the type of measurement sources used. I performed a Monte Carlo study to determine how these trustworthiness factors affected an estimator's trustworthiness and assessed the results using my average CTR method as well as the NEES and NIS metrics.

Based on the results of this study, the UKF and EKF are similarly trustworthy. However, the UKF has better (but still poor) trustworthiness for systems with unmodelled measurement errors. Estimating both the observer and RSO state elements improves a filter's

trustworthiness, however caution should be taken if the expanded state is not fully observable. The van Loan method is the most accurate of the process noise covariance models that I examined. Adding to the van Loan process noise covariance model using the Fixed Bump has the potential to improve –or significantly worsen– a filter's reliability and is highly dependent on the values selected. Conversely, the Adaptive Bump method that I explored had no impact on a filter's reliability. Finally, the measurement model had a significant effect on a filter's trustworthiness. When estimating both observer and RSO states, filters using both angle and range measurements were fully observable and had better average CTRs than filters using either measurement type on their own. Together, these results support my hypothesis that a state estimator's reliability is a function of a set number of quantifiable influencing-factors.

NEES and the average CTR demonstrate that my first research hypothesis was correct. Both metrics can be used to determine and parameterize the reliability of a state estimate. I found that the average CTR and NEES were both able to provide valuable insights into a filter's performance. NEES uses the off-diagonal elements of a filter's state covariance estimate and provides some insight into how well a filter is modelling the covariances between individual state elements. However, NEES is more sensitive to a filter's initial convergence period, as well as to non-PD UKF state covariance estimates, than the CTR. The CTR is not immune to these events, but it is affected to a lesser degree. This allows the CTR to provide insights into a filter's performance as these events occur. NIS provides a quantitative assessment of a filter's measurement model which, as shown in this chapter, can aid in assessing how effects such as unmodelled measurement errors effect a filter's reliability.

Unfortunately, while the CTR and NEES and can be used to reject or adapt state estimates, both metrics require truth data. Neither metric can be used while a system is running unless a highly accurate state data is available from another source. This requirement, along with NEES' reliance on parallel state estimates to build its statistical model, likely limit both methods to use in simulated or laboratory test environments. As NIS does not not require state truth data, NIS can be a useful tool for assessing a system's trustworthiness in the field. However, NIS should not be used on its own, as NIS only assesses the reliability of a filter's measurements as they relate to the filter's measurement model.

Chapter 6

Conclusions and Recommendations

"I am glad you are here with me. Here at the end of all things..."

J.R.R. Tolkien, *The Return of the King*, 1955.

6.1 Research Summary and Conclusions

This research has explored the feasibility of a Resident Space Object (RSO) based optical navigation method to enable Earth-orbiting spacecraft to estimate their orbital positions and attitudes by observing Resident Space Objects (RSOs) orbiting Earth. In the initial stages of the research presented in this dissertation, the following driving hypotheses were made:

Hypothesis 1: Estimator confidence can be determined and parameterized to characterize the reliability of a state estimate and reject or adapt the estimate as needed.

Hypothesis 1.1: A state estimator's reliability is a function of a set number of quantifiable influencing-factors.

Hypothesis 2: A spacecraft's state, including both attitude and position, can be estimated using RSO detections from a commercial star tracker.

VI

The feasibility studies presented in Ch. 3 examined Hypothesis 2, exploring several error sources and physical limitations including numerical precision, Two Line Element (TLE)/propagator accuracy, and RSO Observability. From this analysis, I found that this navigation method is feasible, despite the error sources and physical limitations examined. In this chapter, I also developed two estimators, an Extended Kalman Filter (EKF) and an Unscented Kalman Filter (UKF), to provide observer attitude and position estimates using RSO and star observations. Both estimators were capable of estimating an observing spacecraft's state using a combination of RSO and star measurements. Of these two estimators, the UKF showed superior performance and, unlike the EKF, was able to converge without artificially increasing its process noise covariance. Based on the ≈ 5 km accuracy that the EKF achieved when subjected to the constraints examined in Sec. 3.3, it is difficult to say if either filter can match the accuracy of a propagated TLE for orbital state estimation. As such, more work is needed to determine the accuracy that an RSO-based optical navigation method can achieve. However, this work has proven promising enough to warrant further examination,

To complement Ch. 3's study on the feasibility of optical RSO-based navigation methods, Ch. 4 examined the use of using range sensors for RSO-based navigation. These sensors included laser communication terminals, laser rangefinders, Light Detection and Ranging devices (LIDARs), and synthetic aperture radars (SARs). From this analysis, I determined that LIDAR devices are the most promising sensors to use as range-based sensors for RSO-based navigation. Using parameters from a LIDAR device, I tested the performance of an EKF and a UKF when using range measurements while subjected to a combination of TLE errors and measurement constraints. Both filters were able to determine the observing spacecraft's position and velocity. Based on the work presented in Ch. 4, it may be possible for a spacecraft, using RSO range measurements, to estimate its orbital position and velocity in the near future. However, RSO-based navigation using range measurements will be limited by the maximum detection range of the ranging sensor and the number of RSOs entering this detection range. At present, there are likely not enough conjunction events for an observing sensor to receive sufficient measurements for this navigation method to be viable. However, as the number of RSOs increases over time [100], this method will become more feasible.

As in Ch. 3, I had to artificially increase the range-based EKF's process noise covariance for the filter to converge. Additionally, neither of Ch. 4's filters were able to produce state covariance estimates that reflected their state estimate errors, due to the TLE errors that I included in their measurement models. The effect of this covariance error mismodelling supports Hypothesis 1.1, that a state estimator's reliability is a function of a set number of quantifiable influencing-factors, and that unmodelled measurement errors are one such factor.

While the results of this feasibility study were promising, the space industry is especially cautious of new and untested technologies. To aid in establishing the trustworthiness of the state estimators presented in Ch. 3 and 4, and to investigate Hypothesis 1, Ch. 5 examined the factors that affect reliability and how this reliability can be quantified. These factors included the type of Kalman filter used, whether a filter incorporates elements of the measurement source's state, the type of process noise covariance model used, and the type of measurement sources used. I performed a Monte Carlo study using all permutations of these factors to determine how each variable affected an estimator's trustworthiness. I assessed each trust factor combination's trustworthiness using the CTR, a Kalman filter assessment technique which I developed, as well as two existing methods from the literature: NEES and NIS. Using these metrics, I was able to successfully quantify the reliability of each trust factor combination's state estimate. These results support Hypothesis 1.1 by showing that a state estimator's reliability is a function of a set number of quantifiable influencing-factors.

Unfortunately, both the CTR and NEES require state truth data in order to evaluate an estimator's reliability. As such, neither metric can be used while a system is running unless a highly accurate state data is available from another source. Due to their dependence on truth data, the utility of the CTR and NEES is likely limited to use in simulated or laboratory test environments. However, Ch. 5 also demonstrated the potential utility of the NIS reliability metric. Unlike the CTR and NEES, NIS does not not require state truth data and instead assesses the reliability of a filter's measurements as they relate to the filter's measurement model. Although NIS does not measure the reliability of a filter's covariance estimate, Ch. 5 shows that NIS can be a useful tool as well.

Together, this dissertation has shown that RSO-based optical navigation method is a feasible method for determining an observing spacecraft's state and that range-based

measurements may become another viable method for using RSOs as navigational aids. Additionally, this dissertation examined several factors that affect an estimator's reliability and demonstrated that these factors can be quantitatively assessed to provide confidence in their trustworthiness.

6.2 Recommendations and Future Work

As outlined in the conclusions to Ch. 3, 4, and 5, there are a number of areas in which this research into RSO-based optical navigation can be extended. For the navigation method itself, this includes increasing the fidelity of the model by applying the RSO detection range and TLE/propagator error constraints to the UKF and expanding the simulation to a full six-degree-of-freedom system. These improvements to the simulation's fidelity will no doubt increase the process and measurement noises as well as the sources of error that an estimator must overcome. Additionally, this dissertation did not examine methods for detecting RSOs nor matching detected RSOs to objects in an existing RSO catalogue. While these areas were outside of my research scope, both areas are critical for practically implementing RSO-based navigation techniques. Fortunately, this is an active research area [152, 153].

Based on the results of the reliability study conducted in Ch. 5, this dissertation has several recommendations and considerations for developers when implementing a Kalman filter:

> **Developing Kalman Filters:** When selecting which type of Kalman filter to implement for a system with nonlinear elements, both the EKF and UKF can provide similar trustworthiness if the noise sources are well modelled. However, the UKF can provide some resiliency if unexpected noise sources are encountered.
>
> If multiple measurement sources are available, or if measurement sources can be arranged in multiple forms, developers should select more linear measurement sources if possible. Developers should consider incorporating measurement source state elements into the estimated state where practicable as adding these measurement source state elements can increase an estimator's trustworthiness. However, developers must be mindful of the consideration the additional computational

requirements that this may impose and ensure that the filter remains fully observable.

If a system is well understood, a fixed bump to the process noise covariance can improve the filter's performance. However, care must be taken if a developer chooses to include a fixed bump as an inappropriately sized bump can greatly reduce the filter's trustworthiness and increase its estimate errors. If the filter cannot be tested under similar conditions to what it will be used in, van Loan's method is a reliable method of process noise discretization.

Using Reliability Metrics: Use NEES, NIS, and/or the CTR during development when truth data is available to ensure that the filter is trustworthy before deploying it outside of a development environment. Once development has been deployed to its operational environment, monitor the filter's NIS values. While NIS is not able to provide a direct measure of the filter's state estimate trustworthiness, NIS can monitor the reliability of the filter's measurement innovation and is still a useful reliability monitoring metric for deployed systems.

If high-accuracy data is available from another source on a deployed system, use the CTR to evaluate the deployed filter's performance where possible. *e.g.*, if implementing the RSO-based navigation presented in Ch. 3 as a backup spacecraft state estimator for use in GNSS-denied environments, test the RSO-based navigation filter on orbit when GNSS data is available and use the CTR to evaluate the filter's trustworthiness.

By methodically examining filter parameters to select those with greater reliability and using quantitative metrics to measure the resulting filter's trustworthiness, filter developers can ensure that their estimation methods are reliable. Demonstrating reliability is essential for new estimation methods to become commercially viable, especially in risk-averse fields such as the space industry. As such, the filter parameter analysis and trustworthiness quantification methods presented in this dissertation form an enabling technology that may aid in the more rapid adoption of state estimation techniques.

6.3 Contributions

While conducting this research, I made several key contributions to the areas of spacecraft state estimation, as well as the broader fields of estimation and space systems reliability. The contributions from this research are listed below:

> **Contribution 1)** Developed a covariance trust metric which can quantitatively assess the reliability of a Kalman filter;
>
> **Contribution 2)** Explored and quantified the effect of various factors that affect the performance and reliability of a Kalman filter;
>
> **Contribution 3)** Developed an RSO-based optical navigation method that demonstrates that RSO-based optical navigation is feasible for an Earth-orbiting observing spacecraft detecting RSOs orbiting Earth. This feasibility is demonstrated using the above-mentioned covariance trust metric.

The following three journal articles, based on these contributions, have have been published, in addition to one journal article in preparation and four published conference papers:

Journal Articles

- Driedger, M., Saraygordafshari, S., and Ferguson, P., *Analysis of Factors that Affect the Reliability of Kalman Filters*. In: IEEE Transactions on Aerospace and Electronic Systems, in preparation.

- Driedger, M., Asgari, A., and Ferguson, P., *Feasibility of Gathering Resident Space Object Range Measurements Using In-Orbit Observers*, In: IEEE Journal of Radio Frequency Identification (2022). DOI: 10.1109/JRFID.2022.3160938

- Driedger, M. and Ferguson, P., *Feasibility Study of an Orbital Navigation Filter Using Resident Space Object Observations*, In: Journal of Guidance, Control, and Dynamics, vol. 44, no. 3 (2021), pp. 662-628. DOI: 10.2514/1.G005210

- Driedger, M., Rososhansky, M., and Ferguson, P., *Unscented Kalman filter-based method for spacecraft navigation using resident space objects*, In: Aerospace Systems 3 (2020), pp. 197-205. DOI: https://doi.org/10.1007/s42401-020-00055-w

Conference Papers

- Asgari, A., Driedger, M., and Ferguson, P., *Feasibility Study of Extracting Range Data From Resident Space Objects Using In-Orbit Observers*. In: 2021 IEEE International Conference on Wireless for Space and Extreme Environments (WiSEE). 2021, pp. 54–59. doi: 10.1109/WiSEE50203.2021.9613827.

- Driedger M., Ferguson A., and Ferguson P., *A Safety Monitoring Method for Non-Deterministic Functions in Mission Critical Tasks from the Commercial Drone Industry*, International Astronautical Congress 2019, Washington DC, 2019.

- Driedger, M., Rososhansky, M., and Ferguson, P., *Unscented Kalman Filter Based Method for Spacecraft Navigation Using Resident Space Objects*, ICASSE, Toronto ON, 2019;

- Driedger, M. and Ferguson, P., *Orbital Navigation Using Resident Space Object Observations*, Proceedings of the 2018 Small Satellite Conf., Logan UT, 2018;

References

"All right, you fellows. You can go back to prodding the universe."

Terry Pratchett, *Soul Music*, 1994.

This dissertation used 150 references. For convenience, Fig. 7.1 presents the publication dates for the references used in this dissertation. 54% of these references were published within the past ten years.

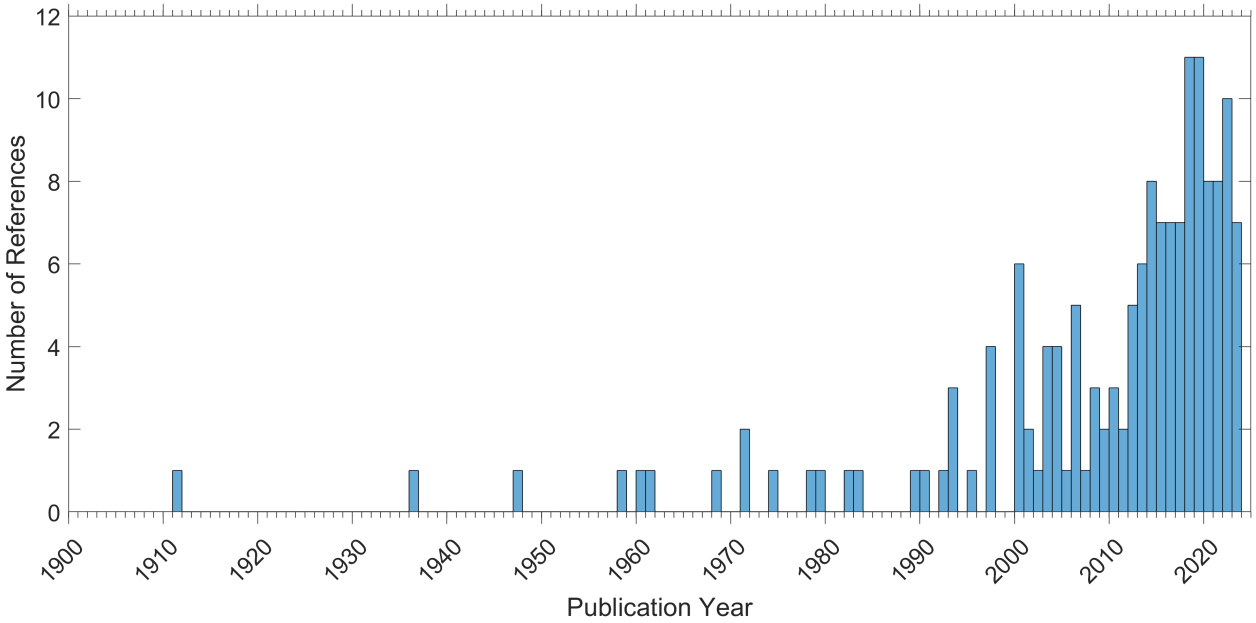

Fig. 7.1: Reference publication dates.

References

[1] NASA, *NASA systems engineering handbook*, NASA SP-2016-6105, 2 ed. Suwanee, GA: NASA, 2016. [Online]. Available: https://www.nasa.gov/wp-content/uploads/2018/09/nasa_systems_engineering_handbook_0.pdf

[2] Forrest Gasdia, "Optical tracking and spectral characterization of cubesats for operational missions," M.S. thesis, Physical Sciences Dept., Embry-Riddle Aeronautical Univ., Daytona Beach, FL, 2016.

[3] John Enright, Doug Sinclair, and Tom Dzamba, "The things you can't ignore: evolving a sub-arc second star tracker," in *AIAA/USU Small Satellite Conference*, Logan, UT, 2012.

[4] Herbert J. Kramer. RCM (RADARSAT Constellation Mission). Visited on 20/07/2021. [Online]. Available: https://directory.eoportal.org/web/eoportal/satellite-missions/r/rcm

[5] Aurélien Fourmault, Claude Grenier, Peter Allan, and G. Richardson, "RCM SAR antenna capabilities," in *14th International Symposium on ANTEM and the AMEREM Conference*, Ottawa, Canada, 2010, pp. 1–4.

[6] Richard L. Lambour, Nandini Rajan, Thomas H. Morgan, Israel Kupiec, and Eugene G. Stansbery, "Assessment of orbital debris size estimation from radar cross-section measurements," *Advances in Space Research*, vol. 34, no. 5, pp. 1013–1020, 2004.

[7] Herwig Zech, Frank Heine, and Matthias Motzigemba, "Laser communication terminals for data relay applications: Todays status and future developments," in *IEEE International Conference on Space Optical Systems and Applications (ICSOS) 2017*, Naha, Japan, 2017.

[8] Arthur Gelb, Joseph F. Kasper, Raymond A. Nash, Charles F. Price, and Arthur A. Sutherland, *Applied optimal estimation*. MIT press, 1974, pp. 182-189.

[9] University of Calgary Department of Physics and Astronomy, "e-POP database," Online, Sep. 2022. [Online]. Available: https://epop-data.phys.ucalgary.ca/2022/09/28/FAI/

[10] ASTM International, "ASTM F3269-17: standard practice for methods to safely bound flight behavior of unmanned aircraft systems containing complex functions," ASTM International, West Conshohocken, PA, Tech. Rep., 2017.

[11] Yanbing Wang, George Gunter, Matthew Nice, Maria Laura Delle Monache, and Daniel B Work, "Online parameter estimation methods for adaptive cruise control systems," *IEEE Transactions on Intelligent Vehicles*, vol. 6, no. 2, pp. 288–298, 2020.

[12] Lin He, Yangyang Wang, Yujiang Wei, Mingwei Wang, Xiaosong Hu, and Qin Shi, "An adaptive central difference Kalman filter approach for state of charge estimation by fractional order model of lithium-ion battery," *Energy*, vol. 244, p. 122627, 2022. [Online]. Available: https://www.sciencedirect.com/science/article/pii/S0360544221028760

[13] John L. Crassidis, Roberto Alonso, and John. L. Junkins, "Optimal attitude and position determination from line-of-sight measurements," *J. Astronaut. Sci.*, vol. 48, no. 2, pp. 391–408, 2000.

[14] Eyke Hüllermeier and Willem Waegeman, "Aleatoric and epistemic uncertainty in machine learning: an introduction to concepts and methods," *Machine Learning*, vol. 110, no. 3, pp. 457–506, Mar 2021. [Online]. Available: https://doi.org/10.1007/s10994-021-05946-3

[15] Nicklaus O. Richardson, Edmond Wong, and Kevin Melcher, "Analytical redundancy using Kalman filters for rocket engine sensor validation," NASA, techreport NASA/TM-20205000446, 2020.

[16] Zhaozhong Chen, Christoffer Heckman, Simon Julier, and Nisar Ahmed, "Weak in the NEES?: Auto-tuning Kalman filters with bayesian optimization," 2018. [Online]. Available: https://arxiv.org/abs/1807.08855

[17] Rao Yarlagadda, Irfan Ali, Naofal Al-Dhahir, and John E. Hershey, "GPS GDOP metric," *IEE Proceedings - Radar, Sonar and Navigation*, vol. 147, pp. 259–264(5), October 2000.

[18] Thomas Griebel, Johannes Müller, Michael Buchholz, and Klaus Dietmayer, "Kalman filter meets subjective logic: A self-assessing Kalman filter using subjective logic," in *2020 IEEE 23rd International Conference on Information Fusion (FUSION)*, 2020, pp. 1–8.

[19] Richard G. Gibbs, "New Kalman filter and smoother consistency tests," *Automatica*, vol. 49, no. 10, pp. 3141–3144, 2013.

[20] Yaakov Bar-Shalom, X.-Rong Li, and Thiagalingam Kirubarajan, *Estimation with Applications to Navigation and Tracking.* New York: John Wiley & Sons, Inc, 2001, pp. 165–168, 234–236.

[21] Rudolf E. Kalman, "A new approach to linear filtering and prediction problems," *Journal of Basic Engineering*, vol. 1, no. 82, pp. 35–45, 1960.

[22] R. E. Kalman and Richard S. Bucy, "New Results in Linear Filtering and Prediction Theory," *Journal of Basic Engineering*, vol. 83, no. 1, pp. 95–108, 03 1961.

[23] Simon J. Julier and Jeffrey K. Uhlmann, "A new extension of the Kalman filter to nonlinear systems," in *The Proceedings of AeroSense: The 11th International Symposium on Aerospace/Defense Sensing, Simulation and Controls*, Orlando, FL, 1997.

[24] Jeffrey Uhlmann and Simon Julier, "Gaussianity and the Kalman filter: A simple yet complicated relationship," *Jou. Cie. Ing.*, vol. 14, no. 1, pp. 21–26, 2022.

[25] Zhaozhong Chen, Nisar Ahmed, Simon Julier, and Christoffer Heckman, "Kalman filter tuning with bayesian optimization," 2019.

[26] Craig Donlon, B. Berruti, A. Buongiorno, M.-H Ferreira, P. Féménias, J. Frerick, P. Goryl, U. Klein, H. Laur, C. Mavrocordatos, J. Nieke, H. Rebhan, B. Seitz, J. Stroede, and R. Sciarra, "The global monitoring for environment and security (GMES) Sentinel-3 mission," *Remote Sensing of Environment*, vol. 120, pp. 37–57, 2012.

[27] Te Wei, Wei Feng, Yunfei Chen, Cheng-Xiang Wang, Ning Ge, and Jianhua Lu, "Hybrid satellite-terrestrial communication networks for the maritime internet of things: Key technologies, opportunities, and challenges," *IEEE Internet of Things Journal*, vol. 8, no. 11, pp. 8910–8934, 2021.

[28] Eric Jurado, Thierry Martin, Elisabet Canalias, Alejandro Blazquez, Romain Garmier, Thierry Ceolin, Philippe Gaudon, Cedric Delmas, Jens Biele, Stephan Ulamec, Emile Remetean, Alex Torres, Julien Laurent-Varin, Benoit Dolives, Alain Herique, Yves Rogez, Wlodek Kofman, Laurent Jorda, Vladimir Zakharov, Jean-François Crifo, Alexander Rodionov, P. Heinish, and Jean-Baptiste Vincent, "Rosetta lander Philae: flight dynamics analyses for landing site," *Acta Astronautica*, vol. 125, pp. 65–79, 2016.

[29] Franz D. Busse, Jonathan P. How, and James Simpson, "Demonstration of adaptive extended Kalman filter for low-earth-orbit formation estimation using CDGPS," *NAVIGATION*, vol. 50, no. 2, pp. 79–93, 2003.

[30] Mark Psiaki and Lejin Huang, "Ground tests of magnetometer-based autonomous navigation (MAGNAV) for low-earth-orbiting spacecraft," *Journal of Guidance, Control, and Dynamics*, vol. 16, no. 1, pp. 206–214, 1993.

[31] A. I. Zakharov, M. E. Prokhorov, M. S. Tuchin, and A. O. Zhukov, "Minimum star tracker specifications required to achieve a given attitude accuracy," *Astrophysical Bulletin*, vol. 68, no. 4, p. 481–493, 2013, https://doi.org/10.1134/S199034131304010X.

[32] Samuel Clemens, "On-orbit resident space object (RSO) detection using commercial grade star trackers," M.S. thesis, York University, Toronto, ON, 2019.

[33] Sonja Gamse, Fereydoun Nobakht-Ersi, and Sharifi Mohammad A., "Statistical process control of a Kalman filter model," *Sensors (Basel)*, vol. 14, no. 10, p. 18053–18074, 2014.

[34] Prasanta Chandra Mahalanobis, "On the generalized distance in statistics," *Proceedings of the National Institute of Science of India*, vol. 2, pp. 49–55, 1936.

[35] Guobin Chang, "Robust Kalman filtering based on mahalanobis distance as outlier judging criterion," *Journal of Geodesy*, vol. 88, no. 4, pp. 391–401, Apr 2014. [Online]. Available: https://doi.org/10.1007/s00190-013-0690-8

[36] Sergi Lopez-Jimenez, Alejandro Pastor, and Diego Escobar, "Improving orbital uncertainty realism through covariance determination," *Acta Astronautica*, vol. 181, pp. 679–693, 2021.

[37] Alejandro Cano, Alejandro Pastor, Diego Escobar, Joaquín Míguez, and Manuel Sanjurjo-Rivo, "Covariance determination for improving uncertainty realism in orbit determination and propagation," *Advances in Space Research*, vol. 72, no. 7, pp. 2759–2777, 2023. [Online]. Available: https://www.sciencedirect.com/science/article/pii/S0273117722007190

[38] Fabian Küppers, Jonas Schneider, and Anselm Haselhoff, "Parametric and multivariate uncertainty calibration for regression and object detection," in *Computer Vision – ECCV 2022 Workshops*, Leonid Karlinsky, Tomer Michaeli, and Ko Nishino, Eds. Cham: Springer Nature Switzerland, 2023, pp. 426–442.

[39] Philip Ferguson, "Making space for everyone: a research program aimed at breaking down barriers to new technology adoption in space," in *CASI ASTRO*, Quebec City, PQ, 2018.

[40] C. Jones, R. E. Bloomfield, P. K. D. Froome, and P. G. Bishop, "Methods for assessing the safety integrity of safety-related software of uncertain pedigree (SOUP)," Adelard, London, UK, Tech. Rep., 2001.

[41] Steven L. Brunton, J. Nathan Kutz, Krithika Manohar, Aleksandr Y. Aravkin, Kristi Morgansen, Jennifer Klemisch, Nicholas Goebel, James Buttrick, Jeffrey Poskin, Adriana W. Blom-Schieber, Thomas Hogan, and Darren McDonald, "Data-driven aerospace engineering: Reframing the industry with machine learning," *AIAA Journal*, vol. 59, no. 8, pp. 2820–2847, 2021.

[42] Stephen Cook, John Angermayer, Andrew Lacher, Andrew Buttner, Kerry Crouse, and Edward Lester, "Dependability of software of unknown pedigree: case studies on unmanned aircraft systems," in *in 2015 IEEE/AIAA 34th Digital Avionics Systems Conference (DASC)*, Prague, CZ, 2015.

[43] Italo Romani de Oliveira, Jose Alexandre T. Guerreiro Fregnani, Glaucia Costa Balvedi, Michael Ulrey, Jeffrey Musiak, Ricardo Alexandre Veiga Gimenes, João Batista Camargo Jr. Camargo, and Jorge Rady Jr. de Almeida, "Safety analysis methods for complex systems in aviation," in *in XV Brazilian Air Transportation Symposium SITRAER,*, São Luis, BR, 2016.

[44] NASA, "NASA-GB-8719.13: NASA software safety guidebook," NASA, Tech. Rep., 2004. [Online]. Available: https://standards.nasa.gov/sites/default/files/standards/NASA/Baseline/0/nasa-gb-871913.pdf

[45] Matthew Driedger, Allison Ferguson, and Philip Ferguson, "A safety monitoring method for non-deterministic functions in mission critical tasks from the commercial drone industry," in *2019 International Astronautical Congress (IAC)*, Washington, USA, 10 2019.

[46] J. E. Riedel, Jr. Owen, W. M., J. A. Stuve, S. M. Synnott, and R. M. Vaughan, "Optical navigation during the Voyager Neptune encounter," in *AIAA Astrodynamics Conf.*, Portland, OR, Aug. 1990, https://doi.org/10.2514/6.1990-2877.

[47] John Enright, Ilija Jovanovic, Laila Kazemi, Harry Zhang, and Tom Dzamba, "Autonomous optical navigation using nanosatellite-class instruments: a Mars approach case study," *Celest. Mech Dyn. Astr.*, vol. 130, no. 13, 2018, https://doi.org/10.1007/s10569-017-9800-x.

[48] Dan Tuckness and Shih-Yih Young, "Autonomous navigation for lunar transfer," *Journal of Spacecraft and Rockets*, vol. 32, no. 2, pp. 279–285, 1995, https://doi.org/10.2514/3.26607.

[49] John A. Christian and E. Glenn Lightsey, "Review of options for autonomous cislunar navigation," *Journal of Spacecraft and Rockets*, vol. 46, no. 5, pp. 1023–1036, 2009, http://dx.doi.org/10.2514/1.42819.

[50] David G. Hoag, "The history of Apollo onboard guidance, navigation, and control," *J. Guid.*, vol. 6, no. 1, pp. 4–13, 1983, https://doi.org/10.2514/3.19795.

[51] Derek S. Nelson, Frederic J. Pelletier, Marc W. Buie, and et al., "Navigation and orbit estimation for New Horizons' Arrokoth flyby: Overview, results and lessons learned," *Space Sci Rev*, vol. 218, no. 11, 2022, https://doi.org/10.1007/s11214-022-00877-4.

[52] Stephen B. Broschart, Nicholas Bradley, and Shyam Bhaskaran, "Kinematic approximation of position accuracy achieved using optical observations of distant asteroids," *Journal of Spacecraft and Rockets*, vol. 56, no. 5, 2019, http://dx.doi.org/10.2514/1.A34354.

[53] K.K. Gunnam, D.C. Hughes, J.L. Junkins, and N. Kehtarnavaz, "A vision-based dsp embedded navigation sensor," *IEEE Sensors Journal*, vol. 2, no. 5, pp. 428–442, 2002.

[54] Roberto Alonso, John L. Crassidis, and John L. Junkins, "Vision-based relative navigation for formation flying of spacecraft," in *AIAA Guidance, Navigation, and Control Conference*, Denver, CO, 2000.

[55] Yunpeng Hu, Xianzong Bai, Lei Chen, and Hongtao Yan, "A new approach of orbit determination for LEO satellites based on optical tracking of GEO satellites," *Aerosp. Sci. Technol.*, vol. 84, pp. 821–829, 2019, https://doi.org/10.1016/j.ast.2018.11.023.

[56] Matthew Driedger and Philip Ferguson, "Orbital navigation using resident space object observations," in *Proceedings of the 2018 Small Satellite Conf.*, Logan, UT, 2018.

[57] Matthew Driedger, Michael Rososhansky, and Philip Ferguson, "Unscented Kalman filter based method for spacecraft navigation using resident space objects," *Aerospace Systems*, vol. 3, pp. 197–205, 2020.

[58] Richard S. Bucy and Peter D. Joseph, *Filtering for Stochastic Processes with Applications to Guidance*. John Wiley & Sons, 1968.

[59] Robert Grover Brown and Patrick Y. C. Hwang, *Introduction to random signals and applied Kalman filtering 3rd ed.* New York: John Wiley & Sons, 1997, pp. 204.

[60] Simo Sarkka, "On unscented Kalman filtering for state estimation of continuous-time nonlinear systems," *IEEE Transactions on Automatic Control*, vol. 52, no. 9, pp. 1631–1641, 2007.

[61] Michael Rososhansky, "Nonlinear attitude and formation estimation spacecraft and multi-agent systems," Ph.D. dissertation, Ryerson University, Toronto, ON, 2017.

[62] Eric A. Wan and Rudolph van der Merwe, "The unscented Kalman filter for nonlinear estimation," in *Proceedings of the IEEE 2000 Adaptive Systems for Signal Processing, Communications, and Control Symp.*, Lake Louise, AB, 2000.

[63] Mark Psiaki, "Global magnetometer-based spacecraft attitude and rate estimation," *Journal of Guidance, Control, and Dynamics*, vol. 27, no. 2, pp. 240–250, 2004.

[64] Bruce D. Yost, "State of the art of small spacecraft technology," NASA, Tech. Rep., 2018.

[65] D. Sinclair, "Second generation star tracker (ST-16RT2)," Sinclair Interplanetary, Tech. Rep., 2017.

[66] New Space Systems, "Sun sensor performance," Online, Feb. 2018, accessed 27 September 2018. [Online]. Available: http://www.newspacesystems.com/wp-content/uploads/2018/02/NewSpace-Sun-Sensor_6a-2.pdf

[67] Yang Yang, Xiaokui Yue, and Andrew Dempster, "GPS-based onboard real-time oribit determination for LEO satellites using consider Kalman filter," *IEEE Transactions in Aerospace and Electronic Systems*, vol. 52, no. 2, pp. 769–777, 2016.

[68] Katarina Radoš, Marta Brkić, and Dinko Begušić, "Recent advances on jamming and spoofing detection in gnss," *Sensors*, vol. 24, no. 13, 2024.

[69] United States Government Accountability Office, "Gps modernization space force should reassess requirements for satellites and handheld devices," United States Government Accountability Office, Tech. Rep. GAO-23-106018, 2023.

[70] John Degnan, "Millimeter accuracy satellite laser ranging: a review," *Contributions of space geodesy to geodynamics: technology*, vol. 25, pp. 133–162, 1993.

[71] Jin Choi, Jung Hyun Jo, Hong-Suh Yim, Eun-Jung. Choi, Sungki Cho, and Jang-Hyun Park, "Optical tracking data validation and orbit estimation for sparse observations of satellites by the OWL-Net," *Sensors*, vol. 18, no. 6, p. 1868, 2018.

[72] Vishnu Anand Muruganandan, Ji Hyun Park, Sangyoon Lee, In-Seuck Jeung, Sangkyun Kim, and Gwanghyeok Ju, "Development of the Arcsecond Pico Star Tracker (APST)," *Transactions of the Japan Society for Aeronautical and Space Sciences*, vol. 60, no. 6, pp. 355–365, 2017.

[73] Malak A. Samaan, Christian Bruccoleri, Daniele Mortari, and John L. Junkins, "novel techniques for creating nearly uniform star catalog," *Advances in the Astronautical Sciences*, vol. 116, pp. 1–13, 2004.

[74] Jacob E. Darling, Nathan Houtz, Carolin Frueh, and Kyle J. DeMars, "Recursive filtering of star tracker data," in *AIAA/AAS Astrodynamics Specialist Conf.*, Long Beach, CA, 2016.

[75] Liyan Luo, Luping Xu, and Hua Zhang, "An autonomous star identification algorithm based on one-dimensional vector pattern for star sensors," *Sensors*, vol. 15, no. 7, pp. 16 412–16 429, 2015.

[76] Samuel Clemens, Regina Lee, Paul Harrison, and Warren Soh, "Feasibility of using commercial star trackers for on-orbit resident space object detection," in *Advanced Maui Optical and Space Surveillance Technologies Conference*, Maui, HI, Sep. 2018.

[77] Robert Lauchie Scott, Brad Wallace, Michael Sale, Martin Levesque, and Stefan Thorsteinson, "Toward microsatellite based space situational awareness," in *in Proceedings of the Advanced Maui Optical and Space Surveillance Technologies Conference*, Wailea, Maui, Sep. 2013.

[78] Karl Bengtsson Bernander, "A method for detecting resident space objects and orbit determination based on star trackers and image analysis," M.S. thesis, Uppsala Universitet, Uppsala, Sweden, 2014.

[79] David A. Cicci, "Spacecraft formation control and estimation via improved relative-motion dynamics," Air Force Research Laboratory Space Vehicles Directorate, Kirtland Airforce Base, NM, Tech. Rep., 2017.

[80] Trevor Bennett and Hanspeter Schaub, "Space-to-space based relative motion estimation using direct relative orbit parameters," in *Proceedings of the Advanced Maui Optical and Space Surveillance Technologies Conference*, Maui, HI, 2015.

[81] Almat Raskaliyev, Sarosh Hosi Patel, Tarek M. Sobh, and Aidos Ibrayev, "GNSS-based attitude determination techniques—a comprehensive literature survey," *IEEE Access*, vol. 8, pp. 24 873–24 886, 2020.

[82] R.J. James, "A history of radar," *IEE Review*, vol. 35, no. 9, pp. 343–349, 1989.

[83] Richard A. Altes, "Target position estimation in radar and sonar, and generalized ambiguity analysis for maximum likelihood parameter estimation," *Proceedings of the IEEE*, vol. 67, no. 6, pp. 920–930, 1979.

[84] Joachim Ender, Ludger Leushacke, Andreas Brenner, and Helmut Wilden, "Radar techniques for space situational awareness," in *2011 12th International Radar Symposium (IRS)*, 2011, pp. 21–26.

[85] Gregory Fonder, Matthew Hughes, Mark Dickson, Melissa Schoenfeld, and Jennifer Gardner, "Space fence radar overview," in *2019 International Applied Computational Electromagnetics Society Symposium (ACES)*, 2019, pp. 1–2.

[86] Matthias Jirousek, Simon Anger, Stephan Dill, and Markus Peichl, "Challenges in very high resolution imaging of satellites and objects in space," in *Radar Sensor Technology XXIII*, Kenneth I. Ranney and Armin Doerry, Eds., vol. 11003, International Society for Optics and Photonics. SPIE, 2019, p. 1100312.

[87] Yu Ning, Xueru Bai, Feng Zhou, and Lei Liu, "A novel method for ISAR imaging of space debris using improved genetic algorithm," in *2016 CIE International Conference on Radar (RADAR)*, 2016, pp. 1–5.

[88] Matthew Driedger, Aref Asgari, and Philip Ferguson, "Feasibility of gathering resident space object range measurements using in-orbit observers," *IEEE Journal of Radio Frequency Identification*, vol. 6, pp. 250–257, 2022.

[89] Alexandre Pollini, Christophe Pache, and Jacques Haesler, "CSEM space LiDARs for imaging and rangefinding," *International Geoscience and Remote Sensing Symposium (IGARSS)*, pp. 1849–1852, 2018.

[90] Michael A. Steindorfer, Georg Kirchner, Franz Koidl, Peiyuan Wang, Beatriz Jilete, and Tim Flohrer, "Daylight space debris laser ranging," *Nature Communications*, vol. 11, no. 1, pp. 1–6, 2020. [Online]. Available: http://dx.doi.org/10.1038/s41467-020-17332-z

[91] Michael V. Nayak, Bogdan Udrea, Brandon Marsella, and Jaclyn R. Beck, "Application of a laser rangefinder for space object imaging and shape reconstruction," *Advances in the Astronautical Sciences*, vol. 148, pp. 3543–3563, 2013.

[92] Bettina Moebius, Martin Pfennigbauer, and Joao Pereira de Carmo, "Imaging lidar technology: development of a 3d-lidar elegant breadboard for rendezvous and docking, test results, and prospect to future sensor application," in *Proceedings Volume 10565, International Conference on Space Optics — ICSO 2010; 105650H*, Rhodes Island, Greece, 2010.

[93] Stephane Gagnon, Bruno Sylvestre, Louis Gagnon, Alexander Koujelev, Daniel Gratton, and Steve Hranilovic, "Recent developments in satellite laser communications: Canadian context," in *Proceedings of 2012 International Conference on Space Optical Systems and Applications*, Ajaccio, France, 2012.

[94] Morio Toyoshima, "Recent trends in space laser communications for small satellites and constellations," *Journal of Lightwave Technology*, vol. 39, no. 3, pp. 693–699, 2021.

[95] Aref Asgari, Matthew Driedger, and Philip Ferguson, "Feasibility study of extracting range data from resident space objects using in-orbit observers," in *2021 IEEE International Conference on Wireless for Space and Extreme Environments (WiSEE)*, 2021, pp. 54–59.

[96] Gabriella Gaias, Simone D'Amico, and Jean-Sebastien Ardaens, "Angles-only navigation to a noncooperative satellite using relative orbital elements," *Journal of Guidance, Control, and Dynamics*, vol. 37, no. 2, pp. 439–451, 2014.

[97] Yousef Saad, *Iterative methods for sparse linear systems 2nd ed.* Society for industrial and applied mathematics, 2003, pp. 41-42.

[98] MathWorks, "eps: Floating-point relative accuracy," Online, retrieved 12 Dec. 2018. [Online]. Available: https://www.mathworks.com/help/matlab/ref/eps.html

[99] Maxim S. Gorbunov, "Design of fault-tolerant microprocessors for space applications," *Acta Astronautica*, vol. 163A, pp. 252–258, 2019, https://doi.org/10.1016/j.actaastro.2019.04.029.

[100] Norman C. Anheier and Cliff S. Chen, "A new approach to space situational awareness using small ground-based telescopes," Pacific Northwest National Laboratory, Richland, WA, Tech. Rep. No. PNNL- 23994, 2014, https://doi.org/10.2172/1171901.

[101] ed. K. Fletcher, "Space debris: the ESA approach," European Space Agency, Tech. Rep., 2017, available at: $http://esamultimedia.esa.int/multimedia/\ publications/BR-336/$.

[102] Rujing Wang, Juanjuan Liu, and Quanxin M. Zhang, "Propagation errors analysis of TLE data," *Advances in Space Research*, vol. 43, no. 7, pp. 1065–1069, 2009, https://doi.org/10.1016/j.asr.2008.11.017.

[103] Timothy Payne, Felix Hoots, Albert Butkus, Zachary Slatton, and Dinh Nguyen, "Improvements to the SGP4 propagator (SGP4-XP)," in *in Proceedings of the Advanced Maui Optical and Space Surveillance Technologies Conference*, Wailea, Maui, Sep. 2022.

[104] Dave Conkey and Mitchell Zielinski, "Assessing performance characteristics of the SGP4-XP propagation algorithm," in *in Proceedings of the Advanced Maui Optical and Space Surveillance Technologies Conference*, Wailea, Maui, Sep. 2023.

[105] Kathleen Riesing and Kerri Cahoy, "Orbit determination from two line element sets of ISS-deployed cubesats," in *29th Annual AIAA/USU Conf. on Small Satellites*, Logan, UT, 2015.

[106] Charles Gow, Susan Eaves, and Matthew D. Hejuk, "The visual magnitude distribution and optical variability of LEO space objects," in *Advanced Maui Optical and Space Surveillance Conference*, Maui, HI, Sep. 2005.

[107] Ball Aerospace, "High accuracy star tracker," Online, accessed: 24-02-2020. [Online]. Available: http://www.ball.com/aerospace/Aerospace/media/Aerospace/Downloads/D1503_HAST_0118.pdf

[108] Uwe Schmidt, Thomas Fiksel, Axel Kwiatkowski, Ingolf Steinbach, Boris Pradarutti, Klaus Michel, and Edoardo Benzi, "Autonomous star sensor ASTRO APS: flight experience on Alphasat," *CEAS Space Journal*, vol. 7, pp. 237–246, 2015.

[109] Blue Canyon Technologies, "Star trackers," Online, accessed: 24-02-2020. [Online]. Available: https://storage.googleapis.com/blue-canyon-tech-news/1/2019/07/BCT_DataSheet_Components_StarTrackers_F2.pdf

[110] Tom Dzamba, John Enright, Doug Sinclair, Kofi Amankwah, Ronny Votel, Ilija Jovanovic, and Geoffrey R. McVittie, "Success by 1000 improvements: flight qualification of the ST-16 star tracker," in *Small Satellite Conference*, Logan, UT, 2014.

[111] Steve B. Howell, *Handbook of CCD Astronomy*, 2nd ed., ser. Cambridge Observing Handbooks for Research Astronomers. Cambridge University Press, 2006.

[112] J. E. Ryon and D. V. Stark, "ACS Instrument Handbook for Cycle 32 v. 23.0," in *ACS Instrument Handbook for Cycle 32 v. 23.0*, 2023, vol. 23.

[113] Micron Technology Inc, "MT9P031 1-2.5-inch 5-Mp digital image sensor," Tech. Rep. MT9P031-5100-PB-2.fm - Rev. B 8/07 EN, 2006. [Online]. Available: https://static.raptorengineering.com/HDCAM/pdf/LimitedDataSheet_MT9P031_5100_PB.book.pdf

[114] B. C. Reed, "Education notes/rubrique pédagogique- stellar magnitudes and photon fluxes," *Journal of the Royal Astronomical Society of Canada*, vol. 87, pp. 123–127, 1993.

[115] Slavek Rucinski, Kieran Carroll, Rainer Kuschnig, Jaymie Matthews, and Peter Stibrany, "MOST (Microvariability & Oscillations of Stars) Canadian astronomical micro-satellite," *Advances in Space Research*, vol. 31, no. 2, p. 371–373, 2003.

[116] Jason F. Rowe, Jaymie M. Matthews, Sara Seager, Rainer Kuschnig, David B. Guenther, Anthony F. J. Moffat, Slavek M. Rucinski, Dimitar Sasselov, Gordon A. H. Walker, and Werner W. Weiss, "An upper limit on the albedo of HD 209458b: Direct imaging photometry with the MOST satellite," *The Astrophysical Journal*, vol. 646, 2006.

[117] Charles F. van Loan, "Computing integrals involving the matrix exponential," *IEEE Trans. Automatic Control*, vol. 23, no. 3, pp. 395–404, 1978.

[118] James J. Harford, *Reconsidering Sputnik Forty Years Since the Soviet Satellite*. Routledge, 2000, ch. Korolev's Triple Play: Sputniks 1, 2, and 3, p. 84.

[119] E. J. Lefferts, F. Landis Markley, and M. D. Shuster, "Kalman filtering for spacecraft attitude estimation," *J. Guid. Control Dynam.*, vol. 5, no. 5, pp. 417–429, 1982, https://doi.org/10.2514/3.56190.

[120] Yee Kit Chan and Voon. Koo, "An introduction to synthetic aperture radar (SAR)," *Progress In Electromagnetics Research B*, vol. 2, pp. 27–60, 2008.

[121] Iain Woodhouse, *Introduction to Microwave Remote Sensing*. Taylor & Francis Group, 2006, pp. 161.

[122] Bernard L. Edwards, Robert Daddato, Klaus-Juergen Schulz, Randall Alliss, Jon Hamkins, Dirk Giggenbach, Bryan Robinson, and Lena Braatz, "An update on the CCSDS optical communications working group interoperability standards," in *2019 IEEE International Conference on Space Optical Systems and Applications (ICSOS))*, Portland, USA, 2019.

[123] J. B. Zirker, F. L. Whipple, and R. J. Davis, "Time Available for the Optical Observation of an Earth Satellite," in *Scientific Uses of Earth Satellites*, James A. van Allen, Ed., Jan. 1958, pp. 23–28.

[124] Yi Han, Huayan Sun, Yingchun Li, and Huichao Guo, "Fast calculation method of complex space targets optical cross section," *Appl. Opt.*, vol. 52, no. 17, pp. 4013–4019, Jun 2013.

[125] Yi Han, Huayan Sun, Yingchun Li, and Huichao Guo, "Fast calculation method of complex space targets optical cross section: erratum," *Appl. Opt.*, vol. 53, no. 6, pp. 1142–1142, Feb 2014.

[126] Doyle Hall and Paul Kervin, "Analysis of faint glints from stabilized GEO satellites," in *Advanced Maui Optical and Space Surveillance Technologies Conference*, Maui, HI, 2013.

[127] Mark R. Ackermann, John T. McGraw, Jeffrey B. Martin, and Peter C. Zimmer, "Blind search for micro satellites in LEO: Optical signatures and search strategies," in *Advanced Maui Optical and Space Surveillance Technologies Conference*, Maui, HI, 2003.

[128] Sanjeev J. Koppal, "Lambertian reflectance. in: Ikeuchi K. (eds) computer vision," *Optical Engineering*, 2014.

[129] Donald Bédard, Gregg A. Wade, and Kira Abercromby, "Laboratory characterization of homogeneous spacecraft materials," *Journal of Spacecraft and Rockets*, vol. 52, no. 4, pp. 1038–1056, 2015.

[130] Jena Optronik, "RVS 3000 datasheet," Tech. Rep., 2022. [Online]. Available: https://www.jena-optronik.de/products/rendezvous-sensors/rvs-3000-3d.html?file=tl_files/pdf/Data%20Sheet%20RVS%203000-3D%202022-03.pdf

[131] Tim Flohrer, Holger Krag, and Heiner Klinkrad, "Assessment and categorization of TLE orbit errors for the US SSN catalogue," in *Proceedings of the Advanced Maui Optical and Space Surveillance Technologies Conference*, Maui, USA, 2008.

[132] Yagiz Kaymak, Roberto Rojas-Cessa, Jianghua Feng, Nirwan Ansari, MengChu. Zhou, and Tairan Zhang, "A survey on acquisition, tracking, and pointing mechanisms for mobile free-space optical communications," *IEEE Communications Surveys & Tutorials*, vol. 20, no. 2, pp. 1104–1123, 2018.

[133] Will Richardson-Little, Chris Patterson, and Graham Peake, "Collision avoidance management for Earth observation constellation missions," in *First Int'l. Orbital Debris Conference*, Sugar Land, TX, Dec. 2019.

[134] Heiner Klinkrad, "One year of conjunction events of ERS-1 and ERS-2 with objects of the USSpacecom catalog," in *Proceedings of the Second European Conference on Space Debris, ESA SP-393*, Darmstadt, Germany, Mar. 1997, pp. 601–611.

[135] Matthew Driedger, Michael Rososhansky, and Philip Ferguson, "Unscented Kalman filter based method for spacecraft navigation using resident space objects," in *2019 International Conference on Aerospace System Science and Engineering (ICASSE)*, Toronto, Canada, 07 2019.

[136] Matthew Driedger and Philip Ferguson, "Feasibility study of an orbital navigation filter using resident space object observations," *Journal of Guidance, Control, and Dynamics*, vol. 44, no. 3, pp. 622–628, 2021.

[137] Colin Ratcliffe and Bridget Ratcliffe, *Doubt-Free Uncertainty In Measurement: An Introduction for Engineers and Students*. New York: Springer International Publishing, 2015, pp. 9.

[138] Robert J. Fitzgerald, "Divergence of the Kalman filter," *IEEE Transactions on Automatic Control*, vol. 16, no. 6, pp. 736–747, 1971.

[139] Dan Simon, *Optimal state estimation: Kalman, H infinity, and nonlinear approaches*. John Wiley and Sons, 2006, ch. 13: nonlinear Kalman filtering, p. 400.

[140] A. Helbig, Wolfgang Marquardt, and Frank Allgöwer, "Nonlinearity measures: definition, computation and applications," *Journal of Process*

Control, vol. 10, no. 2, pp. 113–123, 2000. [Online]. Available: https://www.sciencedirect.com/science/article/pii/S0959152499000335

[141] The MathWorks Inc., "Statistics and machine learning toolbox," Natick, Massachusetts, United States, pp. 10.26–10.33, 2022. [Online]. Available: https://www.mathworks.com/help/stats/index.html

[142] Robert Hermann and Arthur Krener, "Nonlinear controllability and observability," *IEEE Transactions on Automatic Control*, vol. 22, no. 5, pp. 728–740, 1977.

[143] Philip H. Cowell and Andrew C. D. Crommelin, "Investigation of the motion of halley's comet from 1759 to 1910," *Greenwich Observations in Astronomy, Magnetism and Meteorology made at the Royal Observatory*, vol. 71, 1911.

[144] Fredrik Gustafsson and Gustaf Hendeby, "Some relations between Extended and Unscented Kalman filters," *IEEE Transactions on Signal Processing*, vol. 60, no. 2, pp. 545–555, 2012.

[145] C. William Gear, *Numerical initial value problems in ordinary differential equations*, ser. Prentice-Hall series in automatic computation. Englewood Cliffs, N.J: Prentice-Hall, 1971.

[146] William H. Press and Saul A. Teukolsky, "Adaptive stepsize Runge-Kutta integration," *Computers in physics*, vol. 6, no. 2, pp. 188–191, 1992.

[147] Jenoptik, "Diode laser rangefinder (DLEM)," Tech. Rep., 2023. [Online]. Available: https://www.jenoptik.com/-/media/websitedocuments/optics/sensor/dlem_datasheet_20230818.pdf

[148] Renato Zanetti, Kyle J. DeMars, and Robert H. Bishop, "Underweighting nonlinear measurements," *Journal of Guidance, Control, and Dynamics*, vol. 33, no. 5, pp. 1670–1675, 2010. [Online]. Available: https://doi.org/10.2514/1.50596

[149] Mohinder Grewal and Angus Andrews, *KALMAN Filtering Theory and Practice Using MATLAB, 3rd Edition.* Hoboken: John Wiley & Sons, Inc, 2008, 242.

[150] Bernard Lewis Welch, "The generalization of 'Student's' problem when several different population variances are involved," *Biometrika*, vol. 34, no. 1-2, pp. 28–35, 01 1947. [Online]. Available: https://doi.org/10.1093/biomet/34.1-2.28

[151] Morten W. Fagerland, "t-tests, non-parametric tests, and large studies–a paradox of statistical practice?" *BMC medical research methodology*, vol. 12, no. 78, 2012.

[152] Ryan Clark, Yanchun Fu, Siddharth Dave, and Regina S K Lee, "Resident space object (RSO) attitude and optical property estimation from space-based light curves," *Advances in Space Research*, vol. 70, no. 11, pp. 3271–3280, 2022. [Online]. Available: https://www.sciencedirect.com/science/article/pii/S0273117722008043

[153] Siddharth Dave, Ryan Clark, and Regina S. K. Lee, "Rsonet: An image-processing framework for a dual-purpose star tracker as an opportunistic space surveillance sensor," *Sensors*, vol. 22, no. 15, 2022. [Online]. Available: https://www.mdpi.com/1424-8220/22/15/5688

[154] Richard Simard and Pierre L'Ecuyer, "Computing the two-sided Kolmogorov-Smirnov distribution," *Journal of Statistical Software*, vol. 39, no. 11, p. 1–18, 2011. [Online]. Available: https://www.jstatsoft.org/index.php/jss/article/view/v039i11

Appendix A

Applications of Filter Trust

A.1 Discussion of Trust Applications

The contents of this appendix have been presented at the International Astronautical Congress, IAC 2019, Washington, USA, 21 – 25 October 2019 [45].

This appendix introduces an application for my Covariance Trust Ratio (CTR) metric using "ASTM F3269-17: Standard Practice for Methods to Safely Bound Flight Behaviour of Unmanned Aircraft Systems Containing Complex Functions" for spacecraft state estimation [10]. ASTM F3269-17 is a standard for safely using high-risk software in unmanned aircraft by pairing this risky method, known as the complex function, with a safety monitoring watchdog and one or more recovery control functions (RCFs): well understood, reliable software that fills the same role as the complex function, albeit with poorer performance, less accuracy, or some other draw back that makes using the complex function more desirable. The outputs of the safety monitor, complex function, and RCFs are all fed into a Run Time Architecture (RTA) switch. This switch controls which function's output is passed forward to users, based on the output of the safety monitor. A block diagram of this system is shown in Fig. A.1.

To explore how ASTM F3269-17 could be applied to an RSO-based optical navigation method, I applied this standard to the UKF developed in Ch. 3. While this filter was able to converge onto an accurate position and attitude estimate, it lacks the Technology Readiness Level (TRL) for flight use and is a good candidate for software encapsulation. The following subsections introduce the RCF, safety monitor, and RTA switch used in this study and present the simulation results for this safety monitoring method.

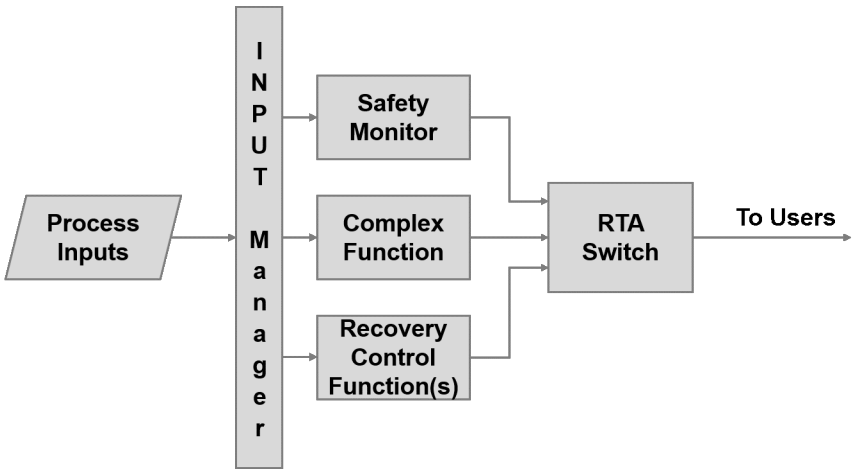

Fig. A.1: Functional components of a system running an ASTM F3269-17 run-time assurance architecture [10]

A.1.1 Encapsulation Code Design

To encapsulate the UKF presented in Ch. 3 and ensure that a reliable state estimate is passed forward, the run-time architecture (RTA) shown in Fig. A.2 was developed. In this architecture, i relative angle measurements of observed RSOs and stars (θ_1 through θ_i) as well as the observing spacecraft's mean motion n and mean anomaly M_0 were fed as inputs to the encapsulating RTA. These inputs are used by the UKF as well as by a TLE propagator which acts as the RCF. In this model, the mean motion and mean anomaly represent components of the observing spacecraft's Two-Line Element (TLE) updates, which would be periodically uplinked to the observing spacecraft.

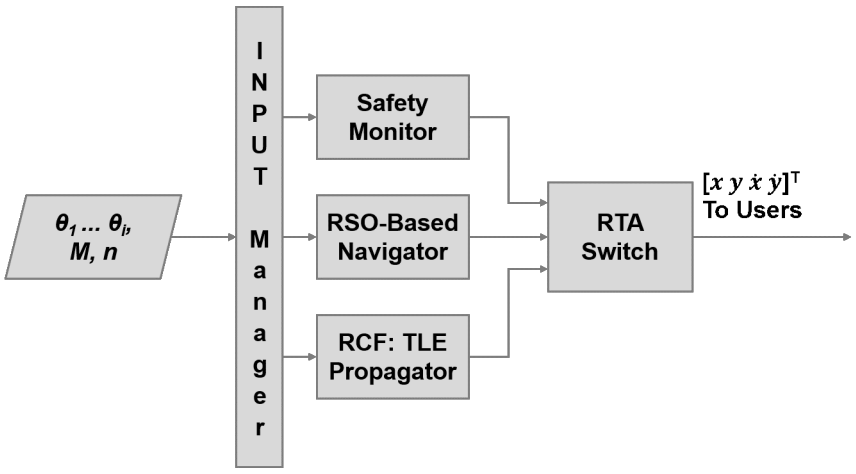

Fig. A.2: Encapsulating RTA for RSO-Based Navigation Method

The TLE components are used by the the TLE propagator, which estimates the spacecraft's state by projecting the spacecraft's expected position using the mean motion n, measured in degrees, and mean anomaly M_0, measured in orbits per day. To do this, the TLE propagator first calculates the spacecraft's orbital period T

$$T = \frac{c_1}{n} \tag{A.1}$$

where c_1 is a conversion factor of 86164.4 seconds per sidereal day. Using T, the observing spacecraft's orbital radius r is then calculated as

$$r = \left(\frac{\mu T^2}{4\pi^2}\right)^{1/3} \tag{A.2}$$

where μ is the Earth's standard gravitational parameter. The spacecraft's true anomaly θ is

$$\tan\left(\frac{\theta}{2}\right) = \sqrt{\frac{1+e}{1-e}}\tan\left(\frac{E}{2}\right) \tag{A.3}$$

where e is eccentricity, and E is the eccentric anomaly. Using these values, the spacecraft's mean anomaly M is calculated as

$$M = E - e\sin E \tag{A.4}$$

Noting that for a circular orbit $e = 0$, θ and E simplify to

$$\theta = E = M \tag{A.5}$$

while the mean anomaly can be related to the mean anomaly at each TLE update epoch as

$$M = M_0 + n(t - t_0) \tag{A.6}$$

where t is the current time and t_0 was the time of the TLE update epoch. Lastly, for a circular orbit, the spacecraft's semilatus rectum p simplifies as follows

$$p = r(1 + e\cos\theta) = r \tag{A.7}$$

The spacecraft's state can then be expressed as

$$X_{TLE}\begin{bmatrix} x_{TLE} \\ y_{TLE} \\ \dot{x}_{TLE} \\ \dot{y}_{TLE} \end{bmatrix} = \begin{bmatrix} r\cos(\theta) \\ r\sin\theta \\ -\frac{\mu}{p}\cos\theta + e \\ \frac{\mu}{p}\sin\theta \end{bmatrix} = \begin{bmatrix} r\cos(M_0 + n(t-t_0)) \\ r\sin(M_0 + n(t-t_0)) \\ -\frac{\mu}{r}\cos(M_0 + n(t-t_0)) \\ \frac{\mu}{r}\sin(M_0 + n(t-t_0)) \end{bmatrix} \tag{A.8}$$

For this simulation, the mean anomaly at the TLE update epoch was calculated as

$$M_0 = \tan\left[\frac{y_{true}}{x_{true}}\right] + \epsilon \tag{A.9}$$

where x_{true} and y_{true} form the observing spacecraft's true position and ϵ is the TLE error. This error was approximated as a Gaussian white noise with a standard deviation of 7.38×10^{-4} radians, equal to a 5 km in-track error at the observing spacecraft's 400 km altitude. The mean anomaly at the TLE update epoch and mean motion were updated once per day, a typical TLE update rate for LEO spacecraft [105].

The safety monitor triggered the RTA switch to send the RCF output to the user when the complex function exceeded one of the following limits:

1) When the complex function's position estimate exceeded the observer's expected orbital radius or orbital velocity by 110%;

2) When the error between the i^{th} state element of complex function X^{CF} and the RCF X^{RCF}, measured as a fraction of the RCF estimate, exceeded a predefined safety threshold ζ_i, as shown in equation A.10;

$$\left|\frac{X_i^{CF} - X_i^{RCF}}{X_i^{RCF}}\right| \leq \zeta_i \tag{A.10}$$

3) When the RCF estimate was not bounded by the complex function estimate plus and minus the square root of the complex function's state covariance estimate P_i^{CF}, as shown in equation A.11.

$$X_i^{CF} - \sqrt{P_i^{CF}} \leq X_i^{RCF} \leq X_i^{CF} + \sqrt{P_i^{CF}} \tag{A.11}$$

Note that the square root of each diagonal element of the UKF's state covariance estimate is equal to the UKF's predicted standard deviation for that element.

A.1.2 Simulation Results

I tested this ASTM F3269-17 implementation by running both the complex function and recovery control function using the same input data set. At each time step, the safety monitor compared the output of both functions using the three previously described heuristics with the safety threshold ζ set to 5%. If the complex function failed one of these heuristics, the RTA switch flaged the event. The results of this test are shown in Fig. A.3.

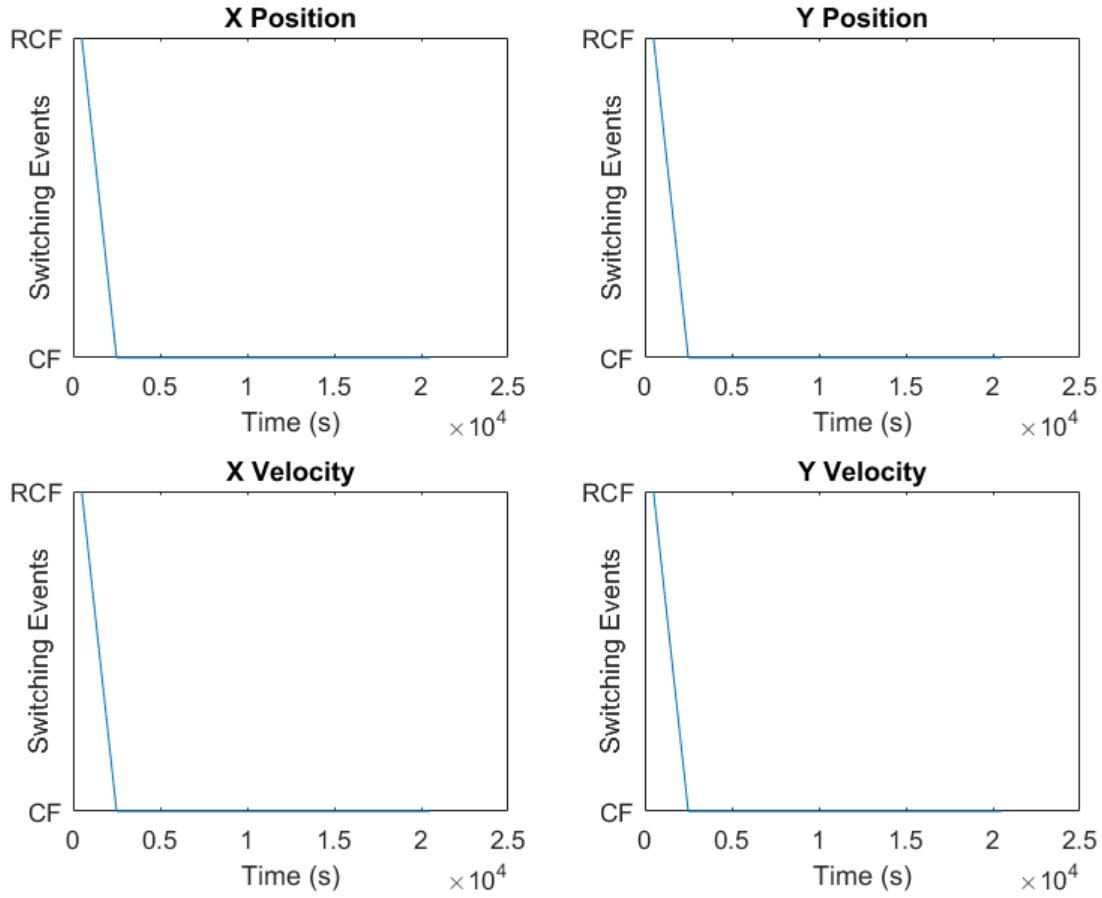

Fig. A.3: Safety Monitor Switching Events when using a 5% safety threshold ζ

A.2 Discussion

During the UKF's initial settling period, the UKF's covariance estimates did not satisfy the safety monitor's heuristics and the safety monitor outputted the propagated TLEs. However, after this settling period the UKF's covariance estimate was within acceptable bounds and the safety monitor outputted the UKF's state estimate. The simulation results show that the trust metric was able to assess the performance of the UKF and pass the UKF's state estimates when the filter had an acceptable level of trustworthiness.

The ASTM F3269-17-based safety monitor was able to detect and prevent non-convergent filter estimates from being passed forward during the filter's initial settling period. Moving forward, one of the primary challenges in implementing this method will be ensuring that the safety monitor's control logic is appropriate to detect and prevent divergent outputs from being passed on without overly constraining the complex function.

Appendix B

Covariance Trust Frame Sizing Optimization

This appendix describes a variable frame sizing analysis that I performed for the Covariance Trust Ratio (CTR) metric [57]. The intent of the variable frame sizing was to allow the covariance trust method to use the largest stationary frame about each sample point when calculating the true standard deviation and true mean error. This would reduce the variability in CTR values due to random fluctuations in individual estimate errors. I found that the increased processing time associated with varying the frame sizes resulted in significantly longer processing times for a marginal (if even statistically significant) improvement in CTR values. Further testing and improved optimization may show that variable frame sizing is worthwhile in some applications, but this was not the case for the scenarios that I examined.

One of the key assumptions in the CTR metric [57] is that the frame on either side of each sampled point is stationary –*i.e.* that the estimate error statistics remain constant over this sampled span–. While estimate errors *should* become stationary, especially if the estimate error approaches some noisy limit as the filter converges, this is certainly not always the case. As such, I developed a method which progressively tests the state errors to either side of the current sampled point (the frame) for stationary, until the sample frame is no longer stationary.

B.1 Method

I developed a simple stationarity test: starting at some minimum number of samples n_{min}, I sampled $n_{min}/2$ samples to the left and right of the current sample k. Next, I used a two-sample Kolmogorov-Smirnov test [154] to check if the left and right half-frames came

from the same distribution. If both half-frames did come from the same distribution, the frame was likely stationary. If the frame passed the Kolmogorov-Smirnov test, I incremented the number of samples n by some amount, and performed another Kolmogorov-Smirnov test. This was repeated until the frame failed the Kolmogorov-Smirnov test.

B.1.1 Method Testing

To assess the performance of this method, I first tested it on a Gaussian random signal, which is stationary by definition. Next, I tested the method on a linearly increasing system with an applied Gaussian white noise which is very non-stationary. Finally, I applied the method to a version of my RSO navigation filter which is of indeterminate stationarity. I hypothesized that the method would work for the Gaussian random signal, that the method would not work for the linear increasing signal, and would work for my RSO navigation filter.

B.1.1.1 Testing on a Random Signal

I first tested the variable frame sizing method on a Gaussian random signal, which is stationary by default. The results of this test on stationary data are shown in Fig. B.1.

During this test, the primary limitation to frame size was the number of samples to the left and right of the current sample point. For test points to the left of the middle timestep, the number of samples further to the left was the primary limitation. Similarly, for test points to the right of the middle timestep, the number of timesteps to the right was the limiting factor. These limitations resulted in the triangular trend seen in Fig. B.1, with the maximum frame size at the middle timestep. Note that some timesteps had frame sizes significantly below this trend, due to short-term non-stationary trends in the random signal.

B.1.1.2 Linear Increasing Signal

To confirm that the method does not give false-positives, I ran the variable frame sizing method on a linearly increasing system with an applied Gaussian white noise. As seen in Fig. B.2, the method did identify some possible stationary points but largely failed to find any stationary points in the signal.

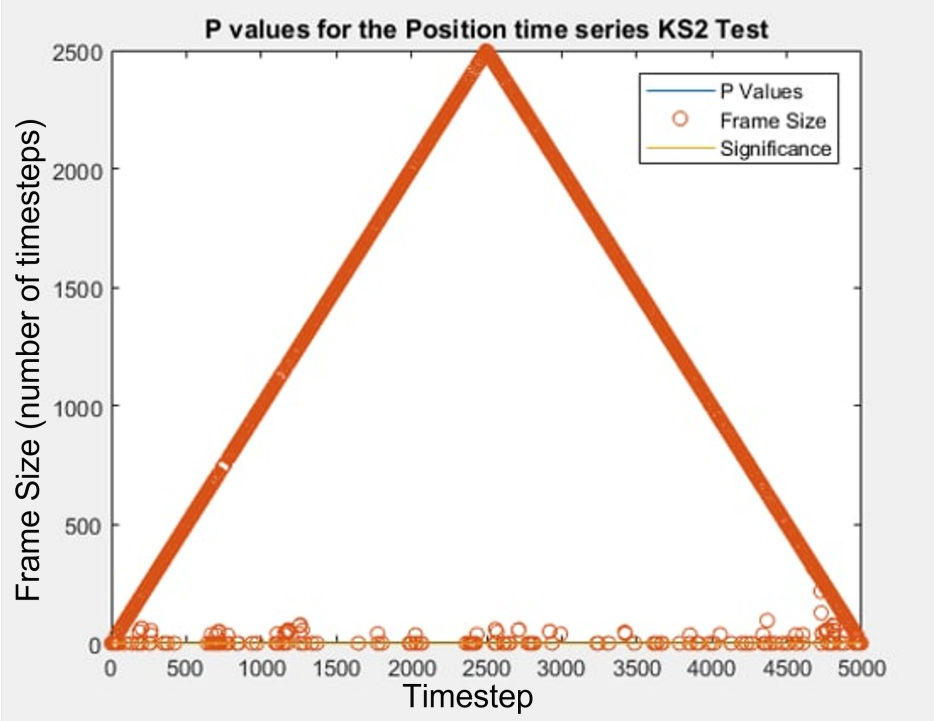

Fig. B.1: Variable Framing Test Results for a Gaussian Random Signal.

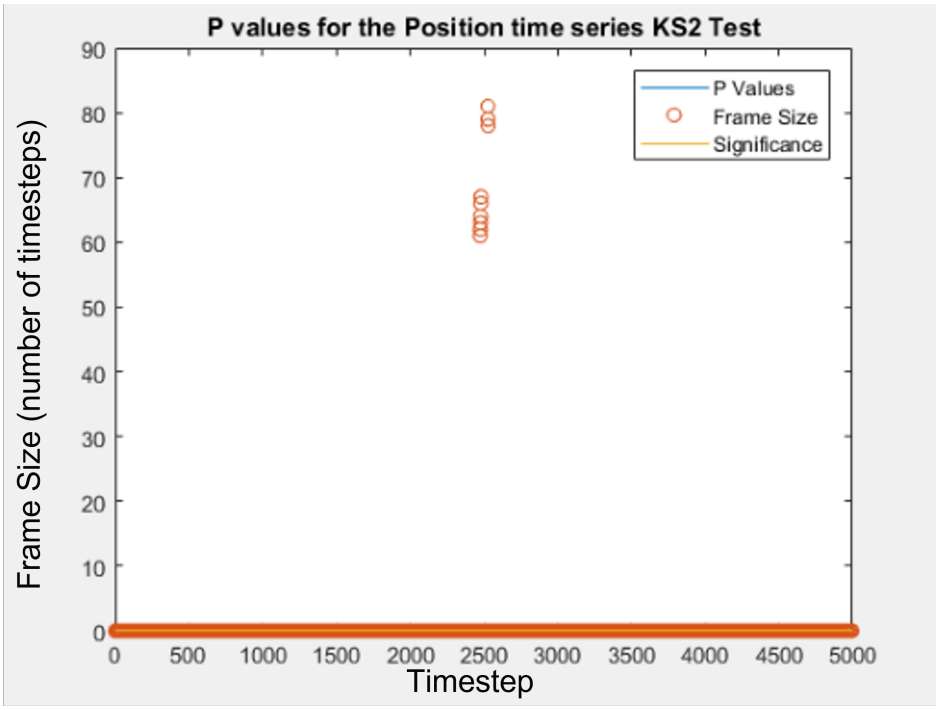

Fig. B.2: Variable Framing Test Results for a linearly increasing system with applied Gaussian white noise.

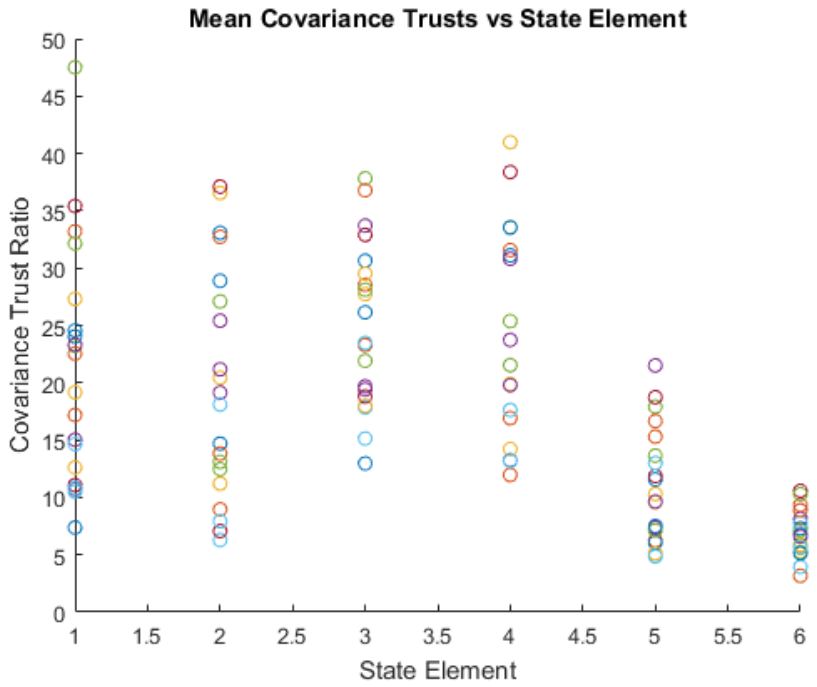

Fig. B.3: Monte Carlo Results for each state element using a variable frame size.

It is possible that these are false-positives but. on examination, it appears that the signal was briefly weakly-stationary. Based on these results, the variable frame sizing method appears to be capable of identifying stationary and non-stationary signals.

B.1.1.3 Navigation Filter Test

Finally, I tested the variable frame size method on my RSO-based Navigation EKF by running two versions of the filter: one with a fixed frame size of 111 timesteps, based on a previous Bayesian Optimization, and one with variable frame sizes. The minimum variable frame size was set to 111 timesteps, the same as the fixed system, and frame increments were set to 10 timesteps. To reduce variability, twenty Monte Carlo simulations were run with each frame type. As seen in Fig. B.3 and B.4, the results for state elements 1-4 (position and velocity) were similar but the variable frame size resulted in significantly larger variability in elements 5 and 6 (angle and angular velocity).

These results were strange at first, as the angle and angular velocity elements showed the greatest degree of stationarity, as seen in Fig. B.5. Conversely, the position and velocity elements showed significantly less stationarity as seen in Fig. B.6.

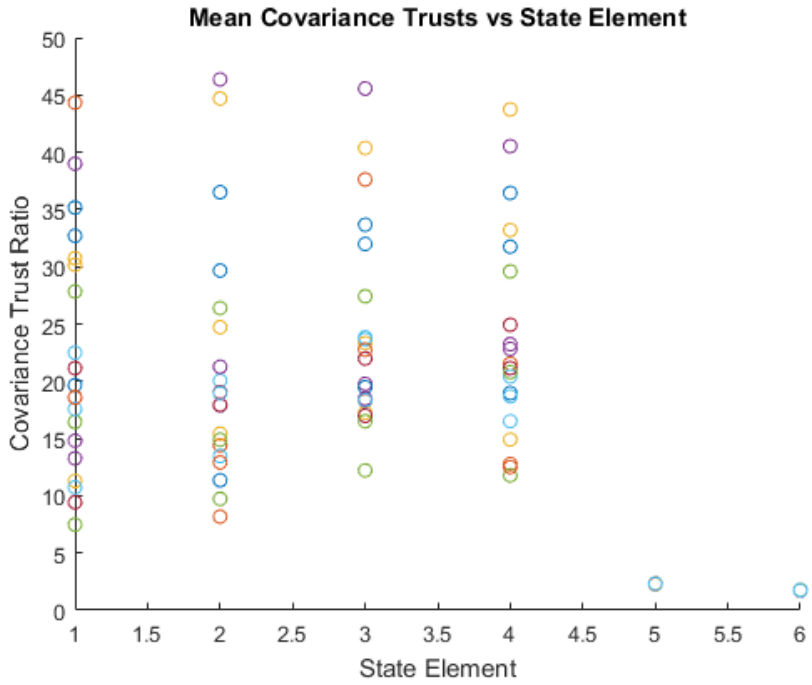

Fig. B.4: Monte Carlo Results for each state element using a fixed frame size.

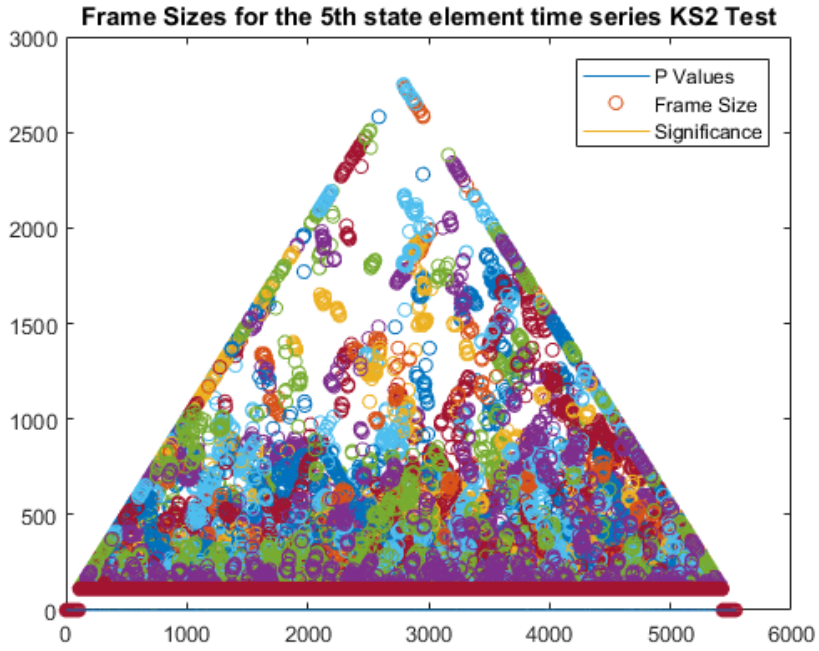

Fig. B.5: Angle frame sizes over the duration of the simulation. Results shown for 20 simulations.

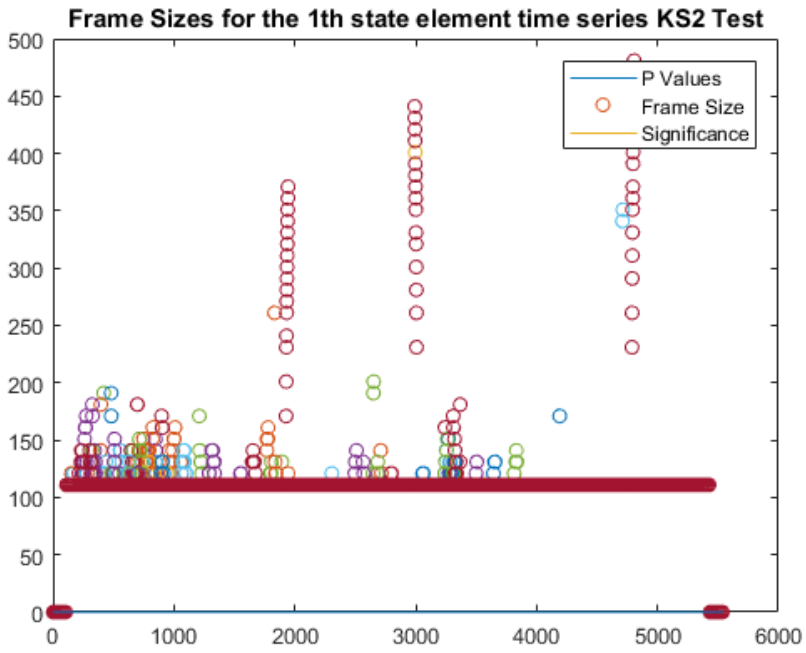

Fig. B.6: x position frame sizes over the duration of the simulation. Results shown for 20 simulations.

These seemingly backwards results were likely due to over-framing for the angle trusts: when the chosen frame size was too large, the trust metric was more susceptible to registering deviations from the mean as untrustworthy. Based on these results, both over and under-sizing of the sample frame must be avoided to have stable, reliable trust metric results.

B.2 Conclusions

This appendix presented a variable frame size calculation method for optimizing the covariance trust metric presented in [57]. The sizing method was validated using stationary and non-stationary signals before being applied to my RSO-Navigation Filter's estimate error. These results were compared with a simulation that used a fixed frame size.

The sizing method was successfully validated but, based on the results from the RSO-Navigation Filter study, did not produce better trust metrics than a version using a fixed frame size. The poor performance of the sizing method, compared to a fixed frame size, was likely due to over-framing which made the trust metric inflexible to minor local variations in

the signal. In the future, I recommend using a fixed frame size which has been tuned either manually or using an optimizer.

Appendix C

Cumulative Distribution Functions and Probability Density Functions for Filter Trustworthiness Test Results

This appendix presents the cumulative distribution functions and probability density functions for each of the 54 trustworthiness factor combinations examined in Charter 5.

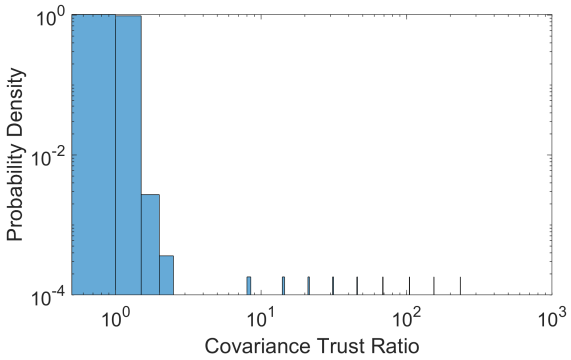

(a) PDF for Test Case 1a average covariance trust ratios

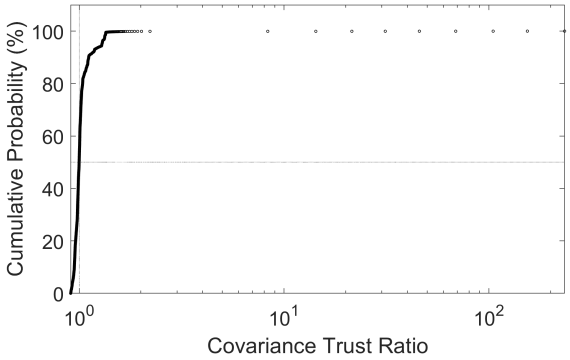

(b) CDF for Test Case 1a average covariance trust ratios

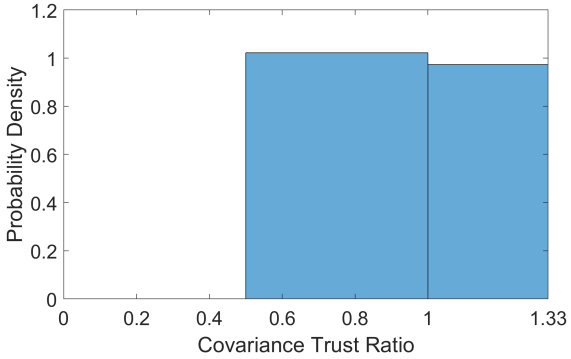

(c) PDF for Test Case 1a average covariance trust ratios, truncated to probabilities below 98%

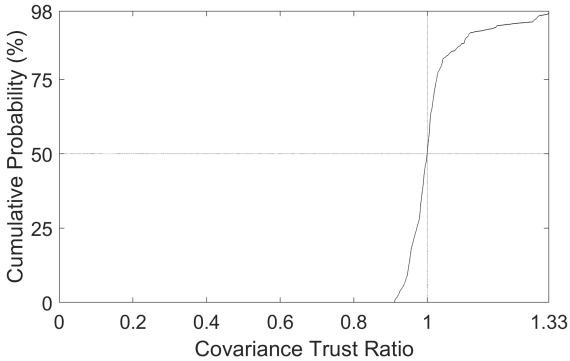

(d) CDF for Test Case 1a average covariance trust ratios, truncated to probabilities below 98%

Fig. C.1: Cumulative distribution functions (CDFs) and probability density functions (PDFs) for trustworthiness factor combination Test Case 1a: filters using the EKF to estimate the observer's state using angle measurements and the van Loan process noise covariance model with with perfect knowledge of RSO positions.

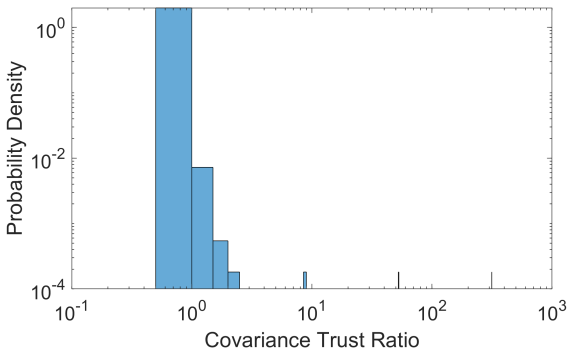

(a) PDF for Test Case 2a average covariance trust ratios

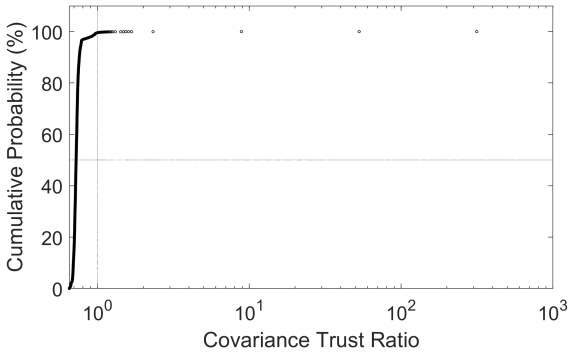

(b) CDF for Test Case 2a average covariance trust ratios

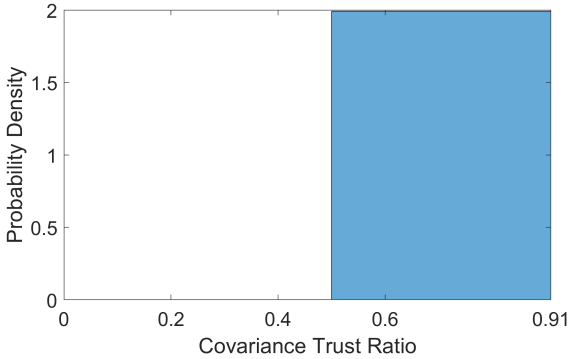

(c) PDF for Test Case 2a average covariance trust ratios, truncated to probabilities below 98%

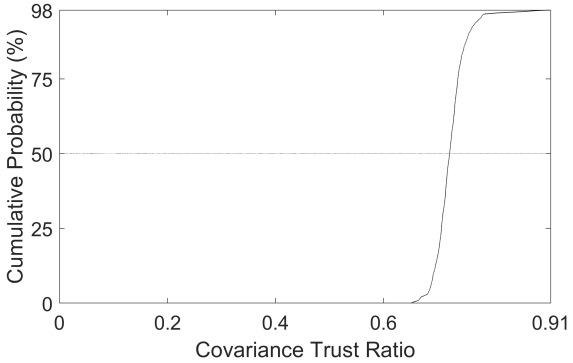

(d) CDF for Test Case 2a average covariance trust ratios, truncated to probabilities below 98%

Fig. C.2: Cumulative distribution functions (CDFs) and probability density functions (PDFs) for trustworthiness factor combination Test Case 2a: filters using the EKF to estimate the observer's state using range measurements and the van Loan process noise covariance model with with perfect knowledge of RSO positions.

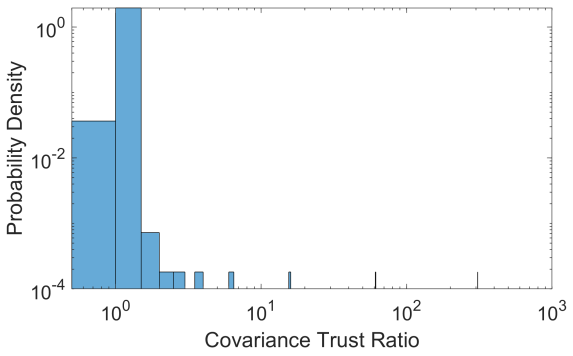

(a) PDF for Test Case 3a average covariance trust ratios

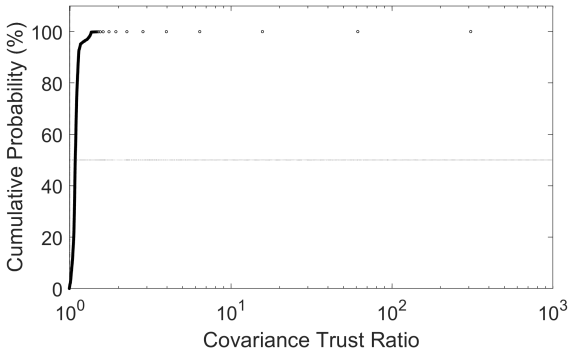

(b) CDF for Test Case 3a average covariance trust ratios

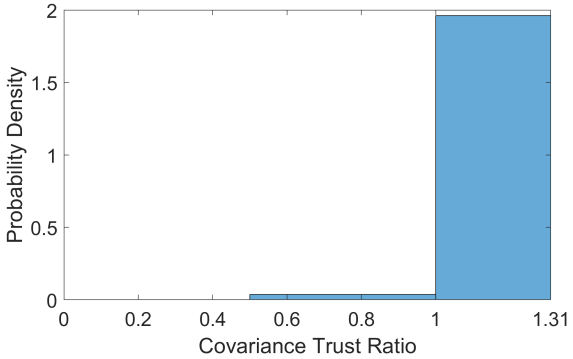

(c) PDF for Test Case 3a average covariance trust ratios, truncated to probabilities below 98%

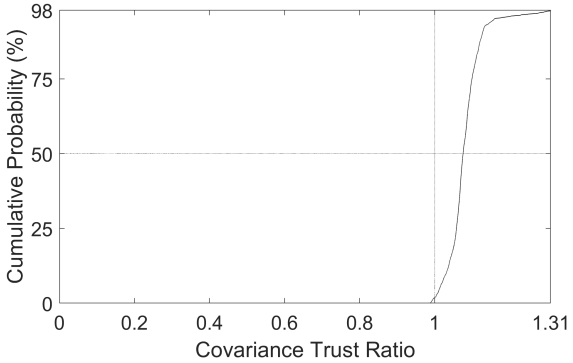

(d) CDF for Test Case 3a average covariance trust ratios, truncated to probabilities below 98%

Fig. C.3: Cumulative distribution functions (CDFs) and probability density functions (PDFs) for trustworthiness factor combination Test Case 3a: filters using the EKF to estimate the observer's state using range and angle measurements and the van Loan process noise covariance model with with perfect knowledge of RSO positions.

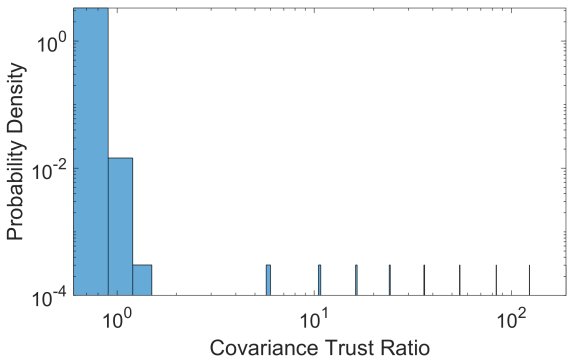

(a) PDF for Test Case 4a average covariance trust ratios

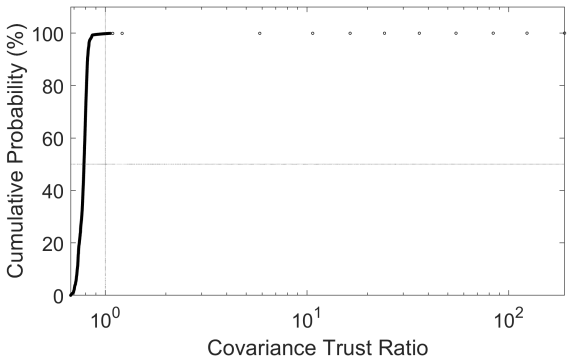

(b) CDF for Test Case 4a average covariance trust ratios

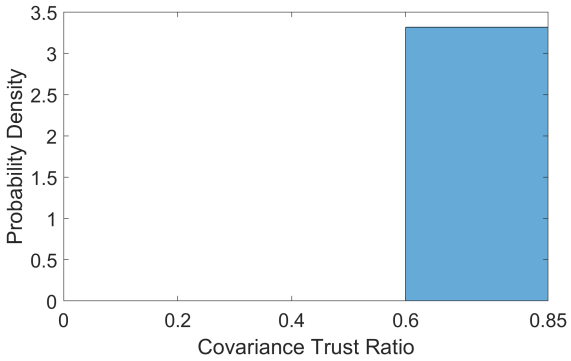

(c) PDF for Test Case 4a average covariance trust ratios, truncated to probabilities below 98%

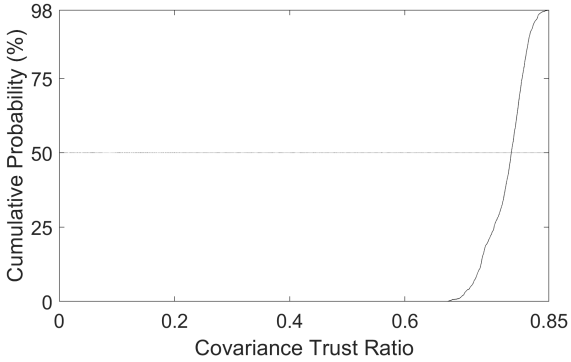

(d) CDF for Test Case 4a average covariance trust ratios, truncated to probabilities below 98%

Fig. C.4: Cumulative distribution functions (CDFs) and probability density functions (PDFs) for trustworthiness factor combination Test Case 4a: filters using the EKF to estimate the observer's state using angle measurements and the fixed bump process noise covariance model with with perfect knowledge of RSO positions.

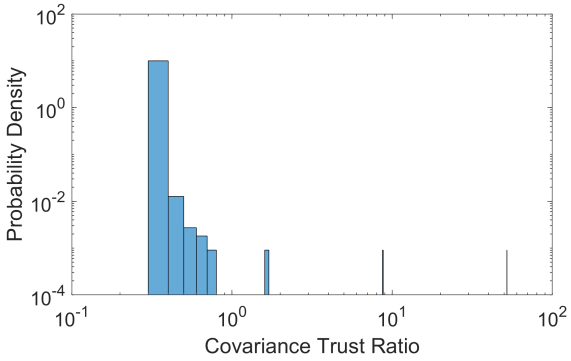

(a) PDF for Test Case 5a average covariance trust ratios

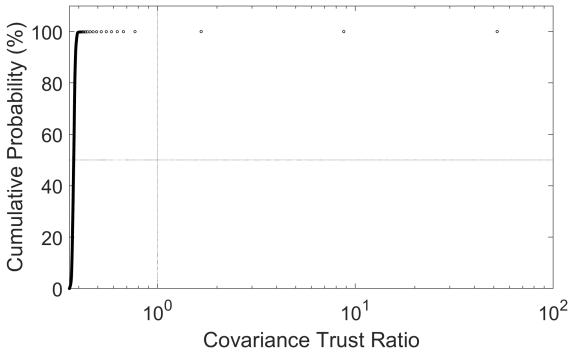

(b) CDF for Test Case 5a average covariance trust ratios

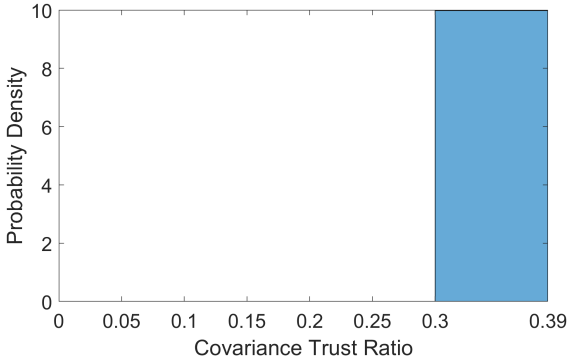

(c) PDF for Test Case 5a average covariance trust ratios, truncated to probabilities below 98%

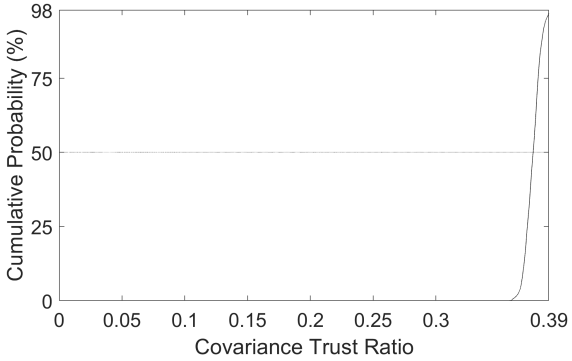

(d) CDF for Test Case 5a average covariance trust ratios, truncated to probabilities below 98%

Fig. C.5: Cumulative distribution functions (CDFs) and probability density functions (PDFs) for trustworthiness factor combination Test Case 5a: filters using the EKF to estimate the observer's state using range measurements and the fixed bump process noise covariance model with with perfect knowledge of RSO positions.

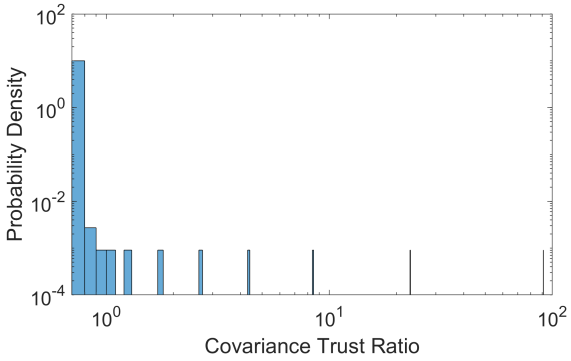

(a) PDF for Test Case 6a average covariance trust ratios

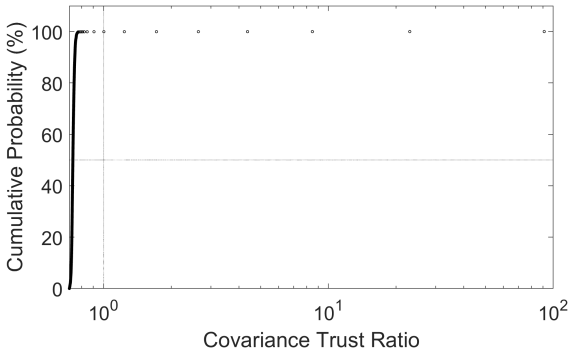

(b) CDF for Test Case 6a average covariance trust ratios

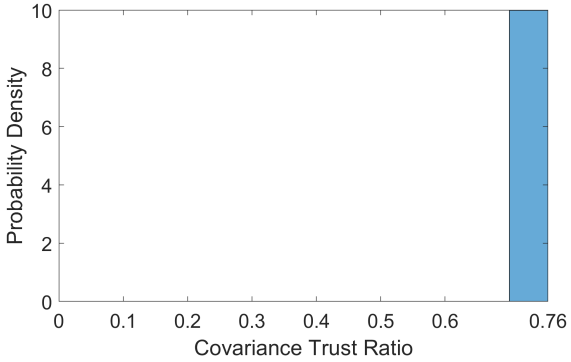

(c) PDF for Test Case 6a average covariance trust ratios, truncated to probabilities below 98%

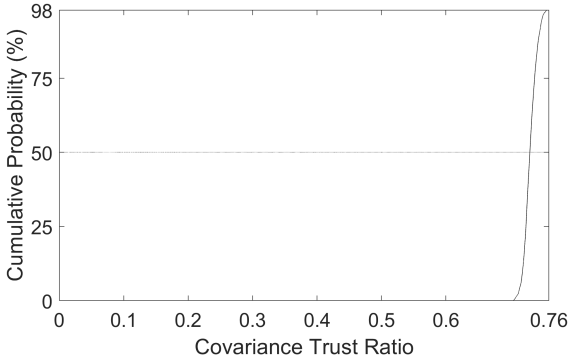

(d) CDF for Test Case 6a average covariance trust ratios, truncated to probabilities below 98%

Fig. C.6: Cumulative distribution functions (CDFs) and probability density functions (PDFs) for trustworthiness factor combination Test Case 6a: filters using the EKF to estimate the observer's state using range and angle measurements and the fixed bump process noise covariance model with with perfect knowledge of RSO positions.

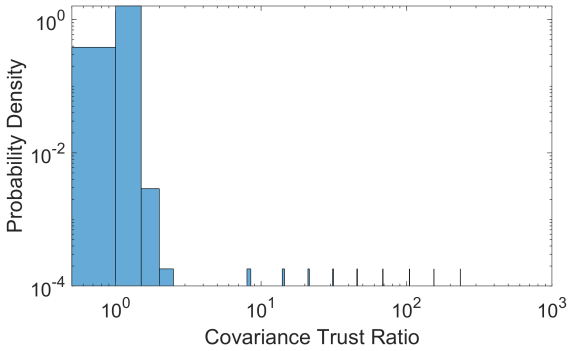

(a) PDF for Test Case 7a average covariance trust ratios

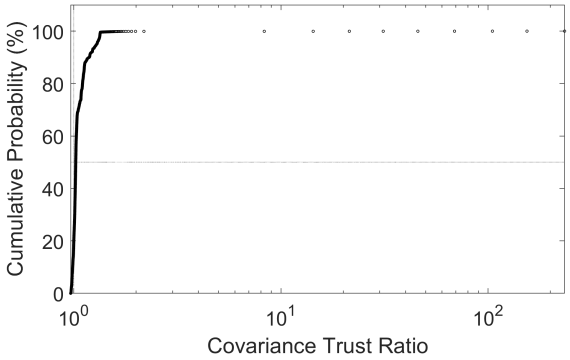

(b) CDF for Test Case 7a average covariance trust ratios

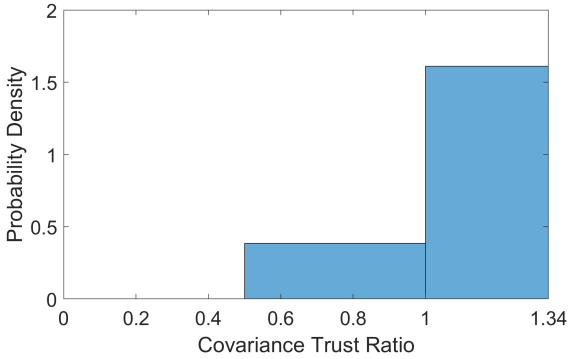

(c) PDF for Test Case 7a average covariance trust ratios, truncated to probabilities below 98%

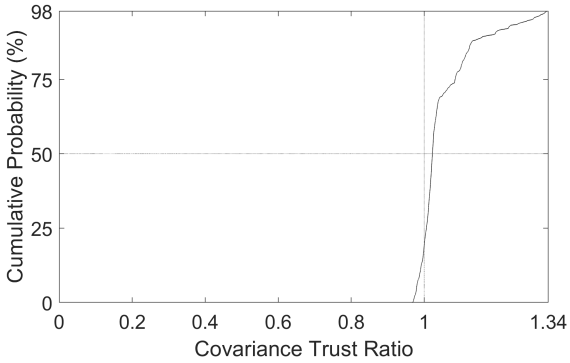

(d) CDF for Test Case 7a average covariance trust ratios, truncated to probabilities below 98%

Fig. C.7: Cumulative distribution functions (CDFs) and probability density functions (PDFs) for trustworthiness factor combination Test Case 7a: filters using the EKF to estimate the observer's state using angle measurements and the variable bump process noise covariance model with with perfect knowledge of RSO positions.

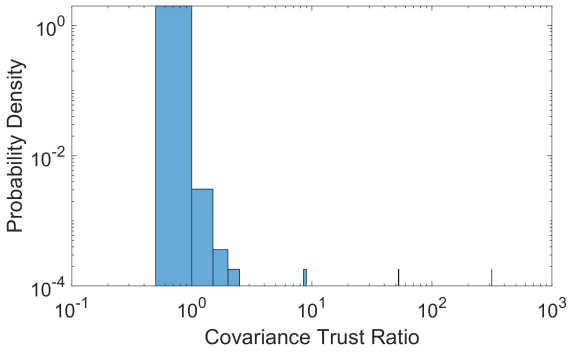

(a) PDF for Test Case 8a average covariance trust ratios

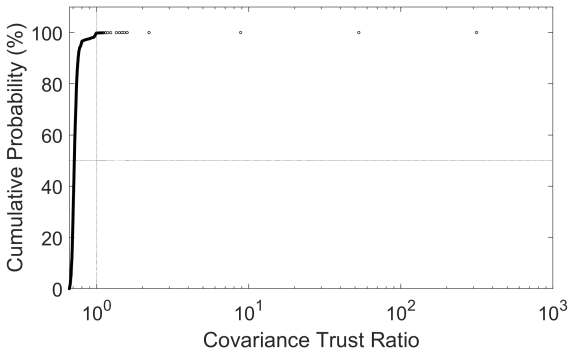

(b) CDF for Test Case 8a average covariance trust ratios

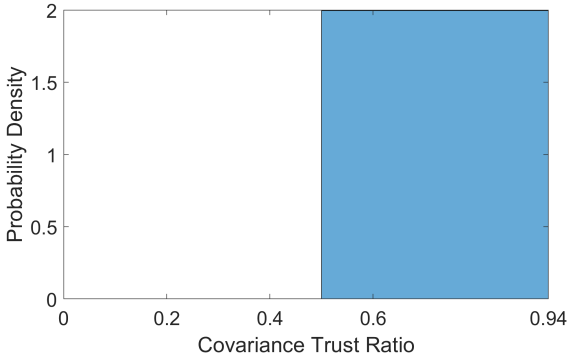

(c) PDF for Test Case 8a average covariance trust ratios, truncated to probabilities below 98%

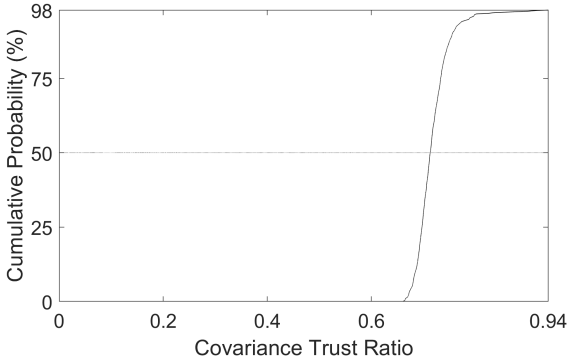

(d) CDF for Test Case 8a average covariance trust ratios, truncated to probabilities below 98%

Fig. C.8: Cumulative distribution functions (CDFs) and probability density functions (PDFs) for trustworthiness factor combination Test Case 8a: filters using the EKF to estimate the observer's state using range measurements and the variable bump process noise covariance model with with perfect knowledge of RSO positions.

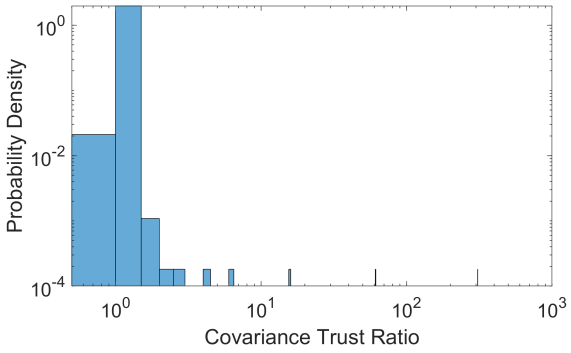

(a) PDF for Test Case 9a average covariance trust ratios

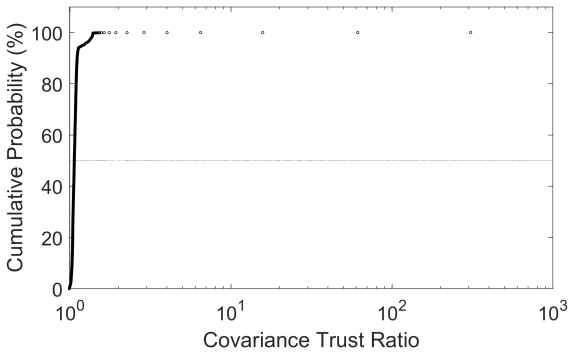

(b) CDF for Test Case 9a average covariance trust ratios

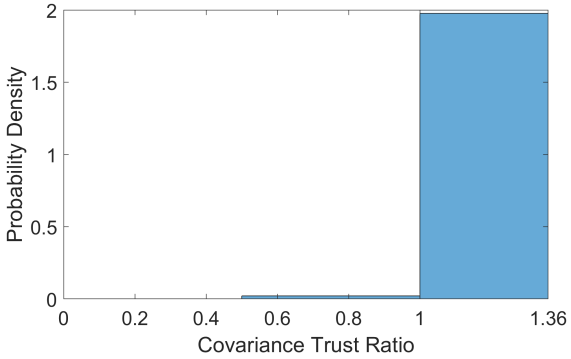

(c) PDF for Test Case 9a average covariance trust ratios, truncated to probabilities below 98%

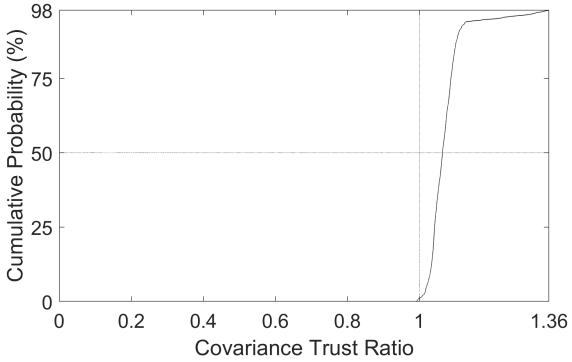

(d) CDF for Test Case 9a average covariance trust ratios, truncated to probabilities below 98%

Fig. C.9: Cumulative distribution functions (CDFs) and probability density functions (PDFs) for trustworthiness factor combination Test Case 9a: filters using the EKF to estimate the observer's state using range and angle measurements and the variable bump process noise covariance model with with perfect knowledge of RSO positions.

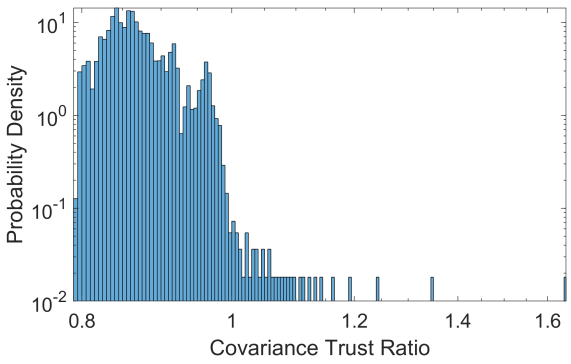

(a) PDF for Test Case 10a average covariance trust ratios

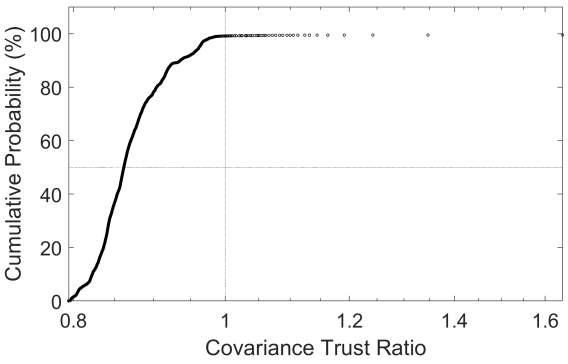

(b) CDF for Test Case 10a average covariance trust ratios

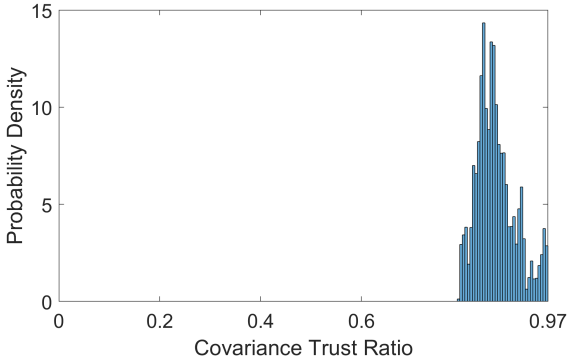

(c) PDF for Test Case 10a average covariance trust ratios, truncated to probabilities below 98%

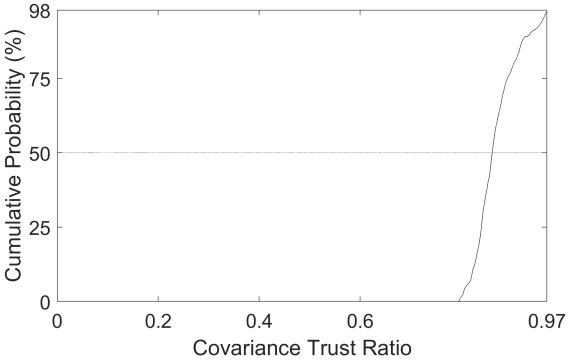

(d) CDF for Test Case 10a average covariance trust ratios, truncated to probabilities below 98%

Fig. C.10: Cumulative distribution functions (CDFs) and probability density functions (PDFs) for trustworthiness factor combination Test Case 10a: filters using the UKF to estimate the observer's state using angle measurements and the van Loan process noise covariance model with with perfect knowledge of RSO positions.

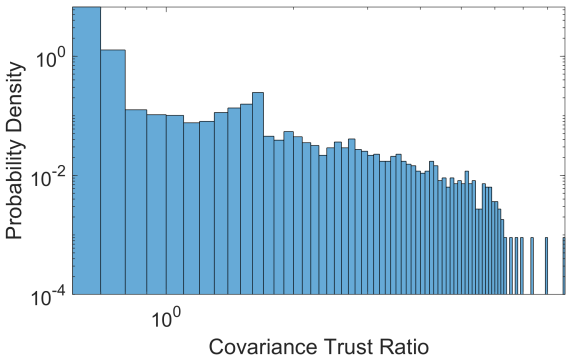

(a) PDF for Test Case 11a average covariance trust ratios

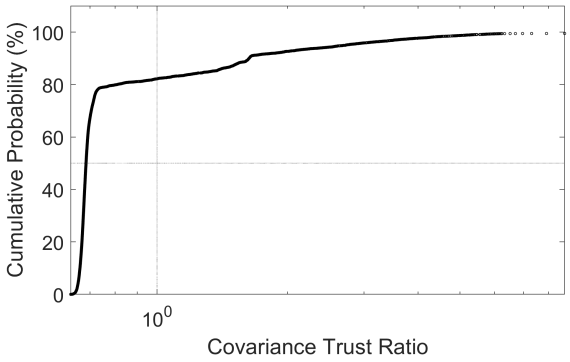

(b) CDF for Test Case 11a average covariance trust ratios

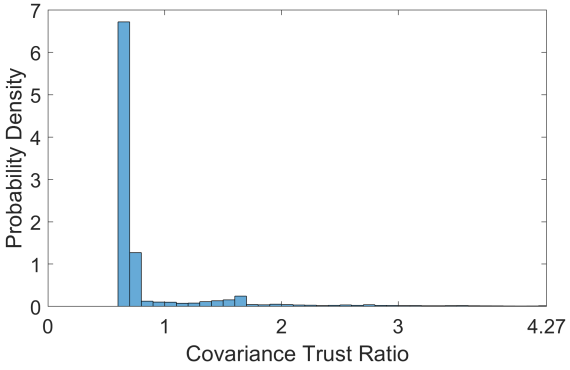

(c) PDF for Test Case 11a average covariance trust ratios, truncated to probabilities below 98%

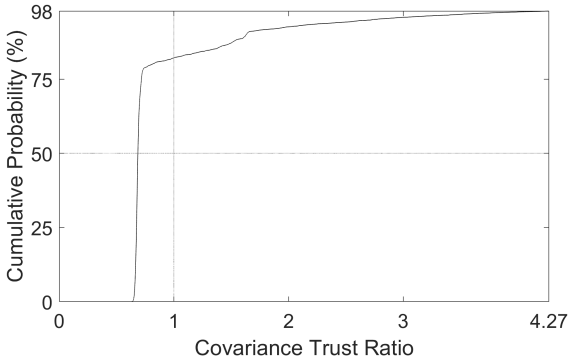

(d) CDF for Test Case 11a average covariance trust ratios, truncated to probabilities below 98%

Fig. C.11: Cumulative distribution functions (CDFs) and probability density functions (PDFs) for trustworthiness factor combination Test Case 11a: filters using the UKF to estimate the observer's state using range measurements and the van Loan process noise covariance model with with perfect knowledge of RSO positions.

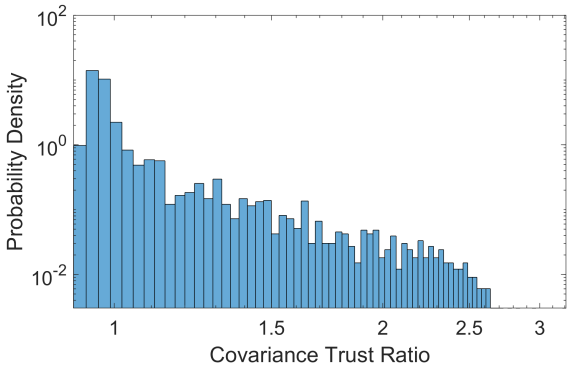

(a) PDF for Test Case 12a average covariance trust ratios

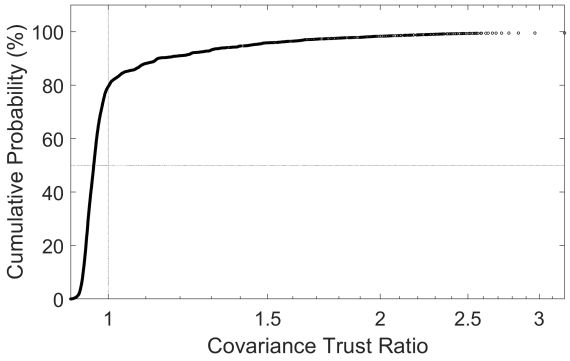

(b) CDF for Test Case 12a average covariance trust ratios

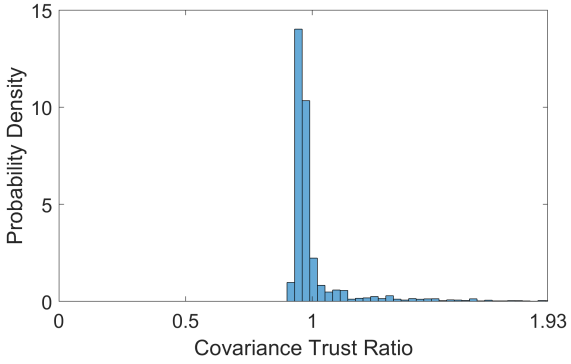

(c) PDF for Test Case 12a average covariance trust ratios, truncated to probabilities below 98%

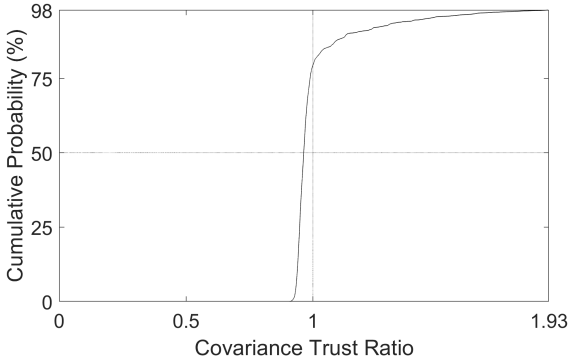

(d) CDF for Test Case 12a average covariance trust ratios, truncated to probabilities below 98%

Fig. C.12: Cumulative distribution functions (CDFs) and probability density functions (PDFs) for trustworthiness factor combination Test Case 12a: filters using the UKF to estimate the observer's state using range and angle measurements and the van Loan process noise covariance model with with perfect knowledge of RSO positions.

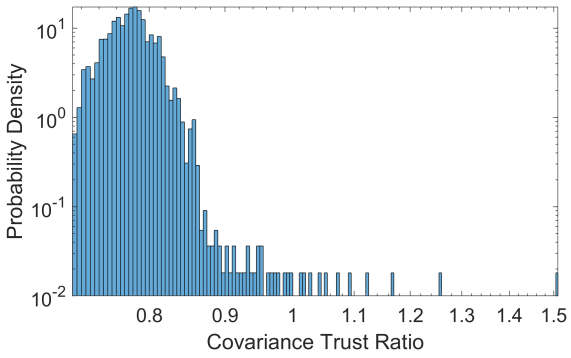

(a) PDF for Test Case 13a average covariance trust ratios

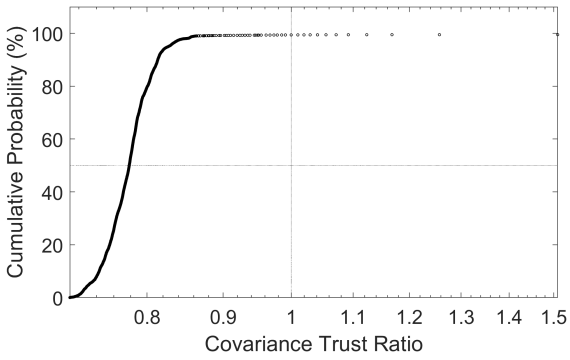

(b) CDF for Test Case 13a average covariance trust ratios

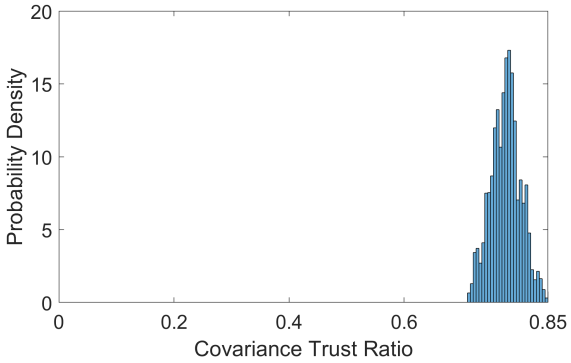

(c) PDF for Test Case 13a average covariance trust ratios, truncated to probabilities below 98%

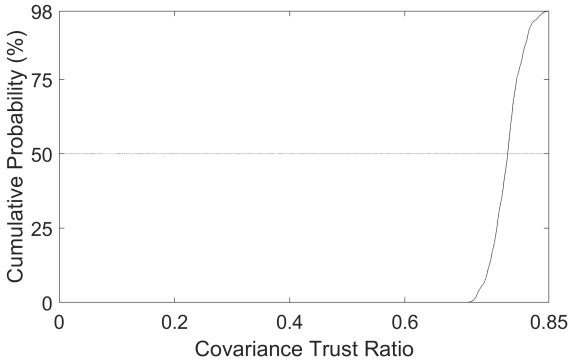

(d) CDF for Test Case 13a average covariance trust ratios, truncated to probabilities below 98%

Fig. C.13: Cumulative distribution functions (CDFs) and probability density functions (PDFs) for trustworthiness factor combination Test Case 13a: filters using the UKF to estimate the observer's state using angle measurements and the fixed bump process noise covariance model with with perfect knowledge of RSO positions.

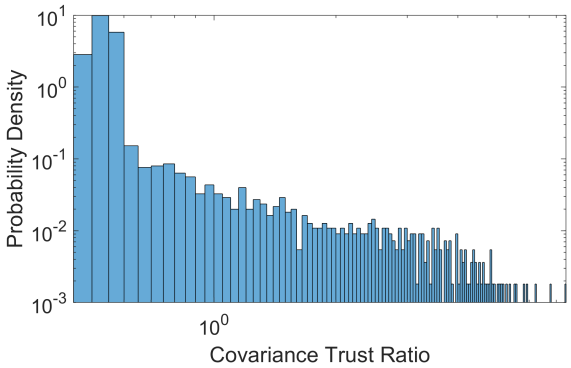

(a) PDF for Test Case 14a average covariance trust ratios

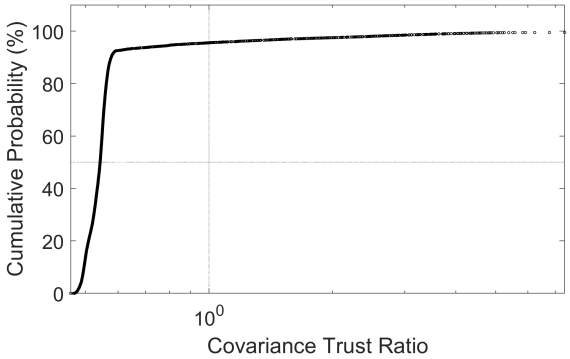

(b) CDF for Test Case 14a average covariance trust ratios

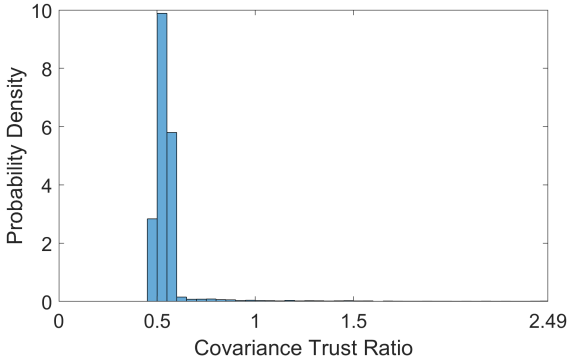

(c) PDF for Test Case 14a average covariance trust ratios, truncated to probabilities below 98%

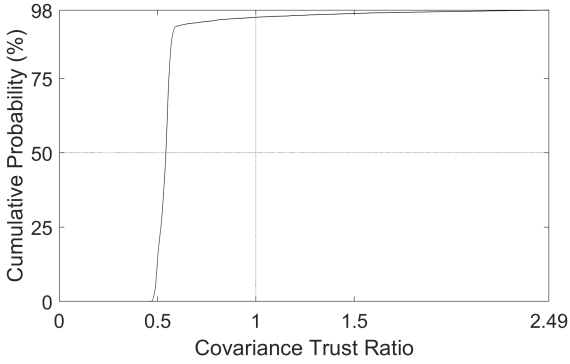

(d) CDF for Test Case 14a average covariance trust ratios, truncated to probabilities below 98%

Fig. C.14: Cumulative distribution functions (CDFs) and probability density functions (PDFs) for trustworthiness factor combination Test Case 14a: filters using the UKF to estimate the observer's state using range measurements and the fixed bump process noise covariance model with with perfect knowledge of RSO positions.

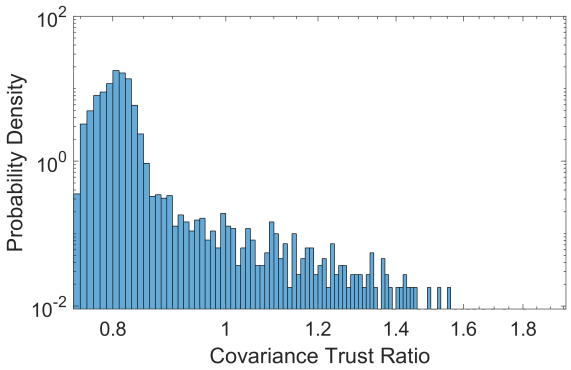

(a) PDF for Test Case 15a average covariance trust ratios

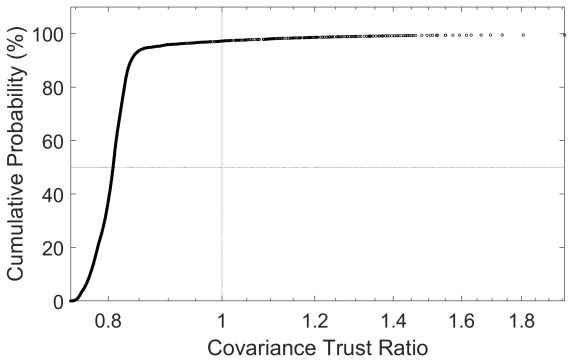

(b) CDF for Test Case 15a average covariance trust ratios

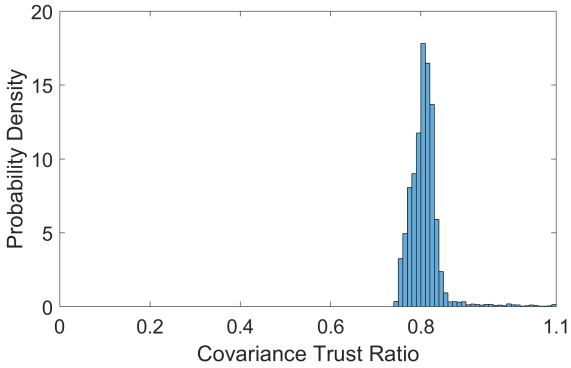

(c) PDF for Test Case 15a average covariance trust ratios, truncated to probabilities below 98%

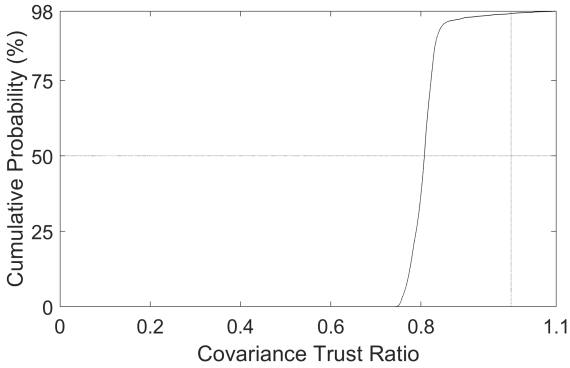

(d) CDF for Test Case 15a average covariance trust ratios, truncated to probabilities below 98%

Fig. C.15: Cumulative distribution functions (CDFs) and probability density functions (PDFs) for trustworthiness factor combination Test Case 15a: filters using the UKF to estimate the observer's state using range and angle measurements and the fixed bump process noise covariance model.

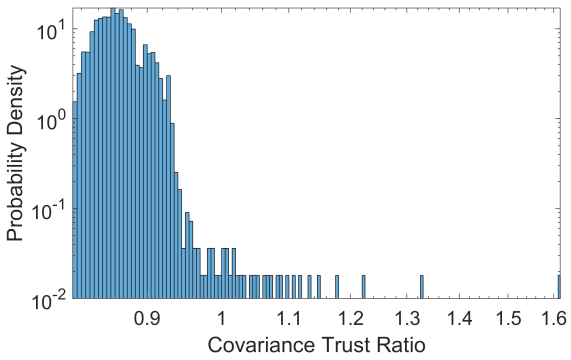

(a) PDF for Test Case 16a average covariance trust ratios

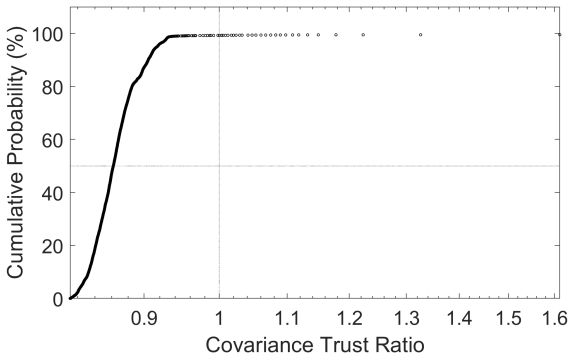

(b) CDF for Test Case 16a average covariance trust ratios

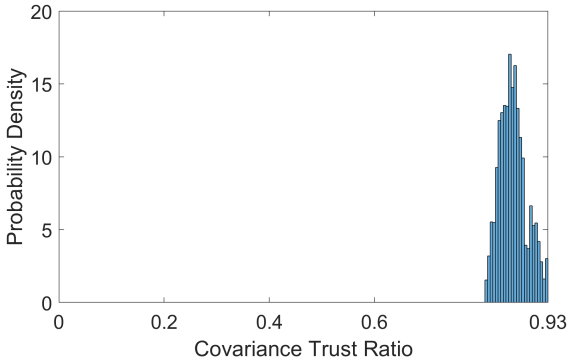

(c) PDF for Test Case 16a average covariance trust ratios, truncated to probabilities below 98%

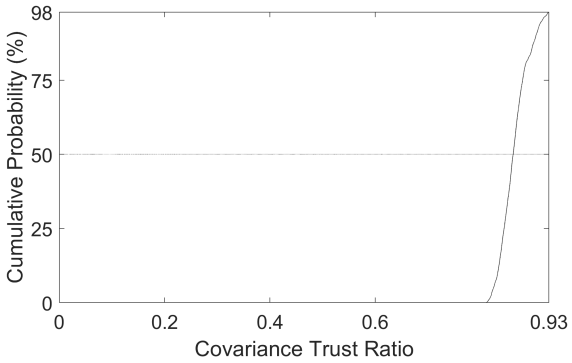

(d) CDF for Test Case 16a average covariance trust ratios, truncated to probabilities below 98%

Fig. C.16: Cumulative distribution functions (CDFs) and probability density functions (PDFs) for trustworthiness factor combination Test Case 16a: filters using the UKF to estimate the observer's state using angle measurements and the variable bump process noise covariance model.

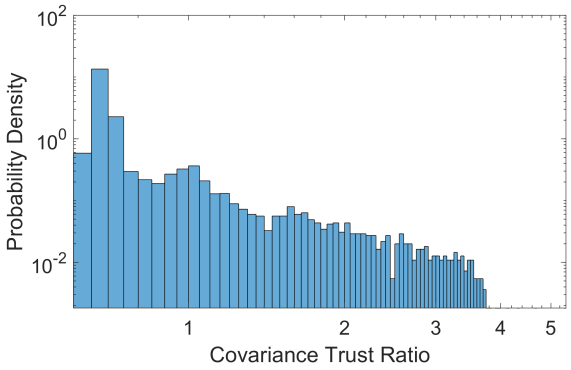

(a) PDF for Test Case 17a average covariance trust ratios

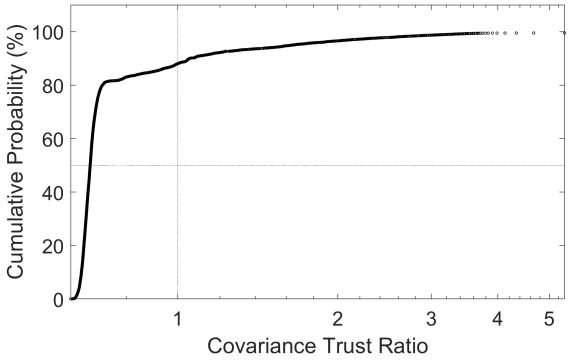

(b) CDF for Test Case 17a average covariance trust ratios

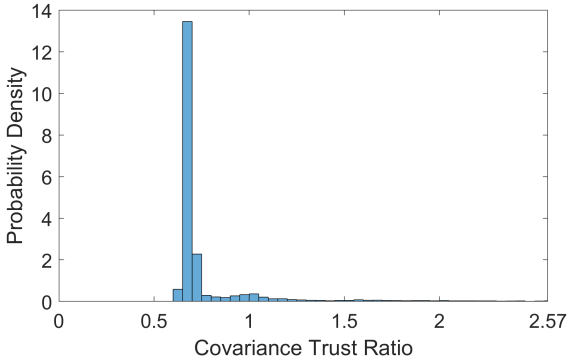

(c) PDF for Test Case 17a average covariance trust ratios, truncated to probabilities below 98%

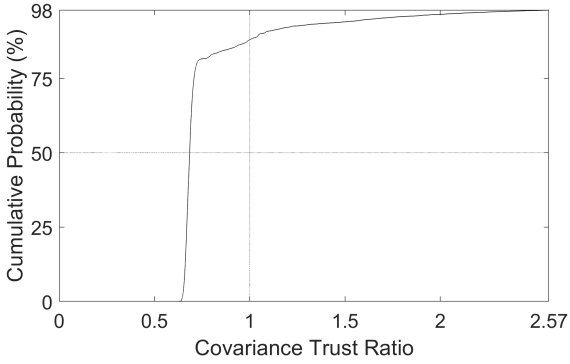

(d) CDF for Test Case 17a average covariance trust ratios, truncated to probabilities below 98%

Fig. C.17: Cumulative distribution functions (CDFs) and probability density functions (PDFs) for trustworthiness factor combination Test Case 17a: filters using the UKF to estimate the observer's state using range measurements and the variable bump process noise covariance model with with perfect knowledge of RSO positions.

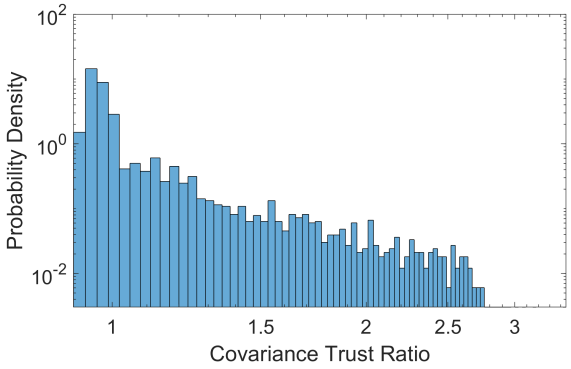

(a) PDF for Test Case 18a average covariance trust ratios

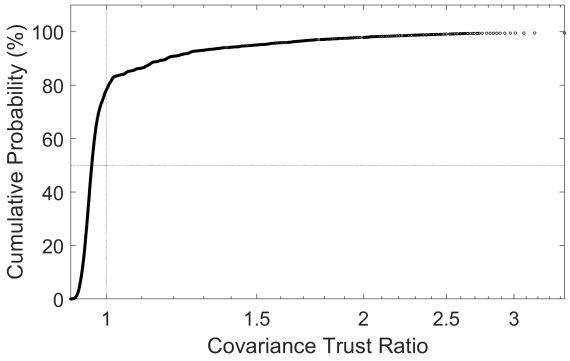

(b) CDF for Test Case 18a average covariance trust ratios

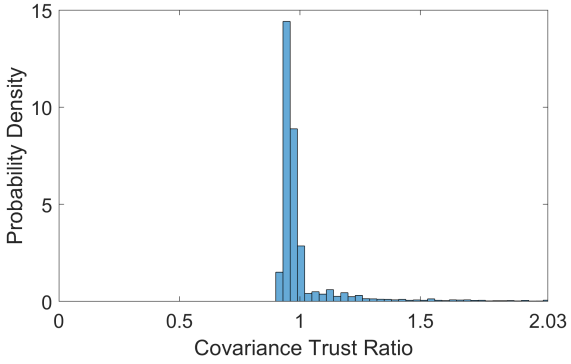

(c) PDF for Test Case 18a average covariance trust ratios, truncated to probabilities below 98%

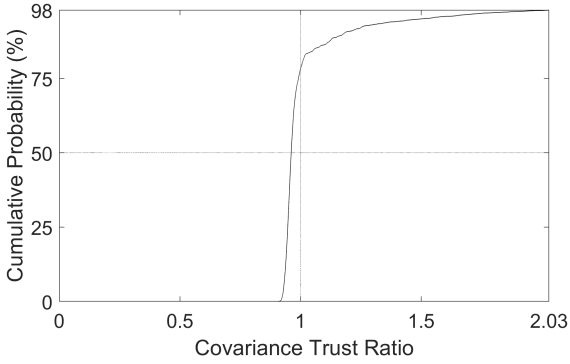

(d) CDF for Test Case 18a average covariance trust ratios, truncated to probabilities below 98%

Fig. C.18: Cumulative distribution functions (CDFs) and probability density functions (PDFs) for trustworthiness factor combination Test Case 18a: filters using the UKF to estimate the observer's state using range and angle measurements and the variable bump process noise covariance model with with perfect knowledge of RSO positions.

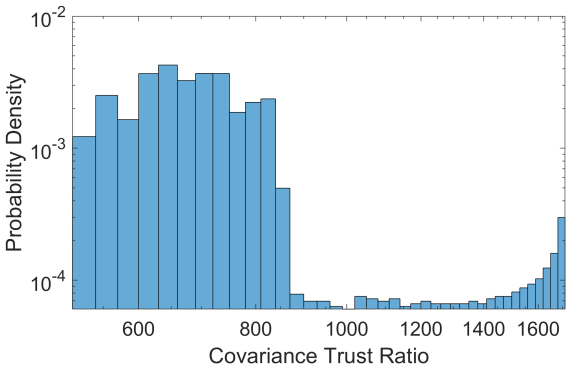

(a) PDF for Test Case 1b average covariance trust ratios

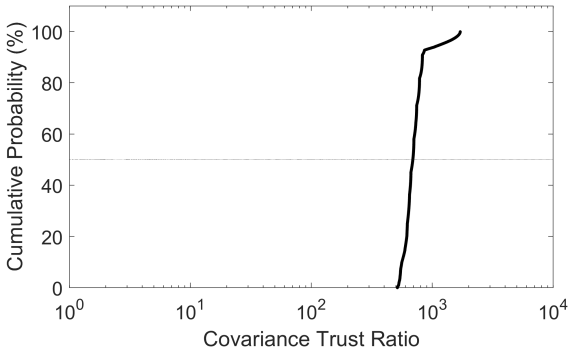

(b) CDF for Test Case 1b average covariance trust ratios

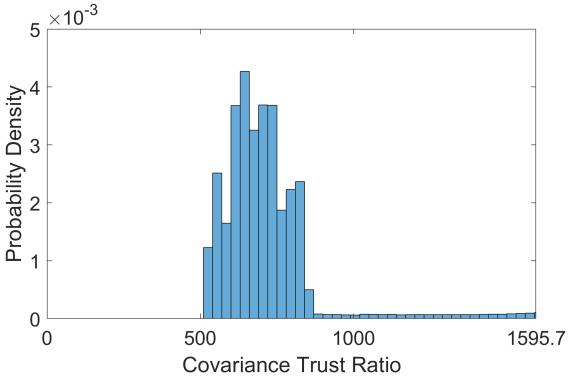

(c) PDF for Test Case 1b average covariance trust ratios, truncated to probabilities below 98%

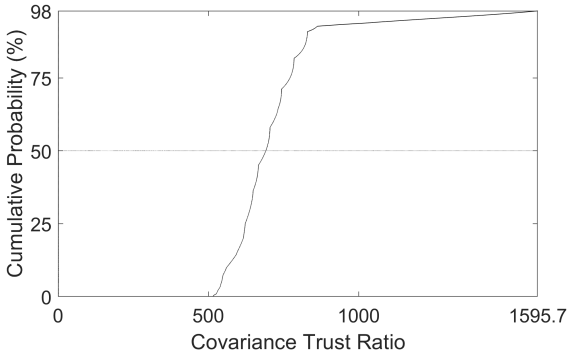

(d) CDF for Test Case 1b average covariance trust ratios, truncated to probabilities below 98%

Fig. C.19: Cumulative distribution functions (CDFs) and probability density functions (PDFs) for trustworthiness factor combination Test Case 1b: filters using the EKF to estimate the observer's state using angle measurements and the van Loan process noise covariance model without with perfect knowledge of RSO positions.

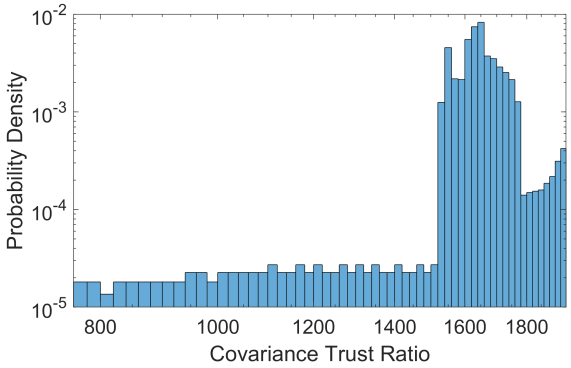

(a) PDF for Test Case 2b average covariance trust ratios

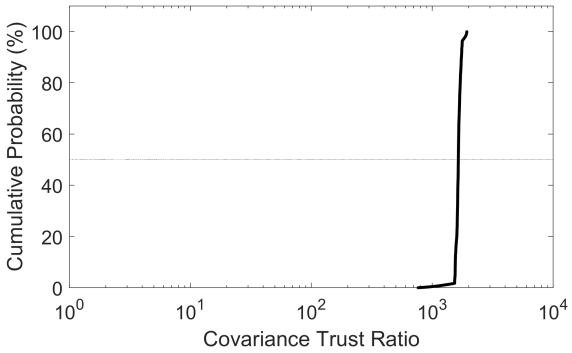

(b) CDF for Test Case 2b average covariance trust ratios

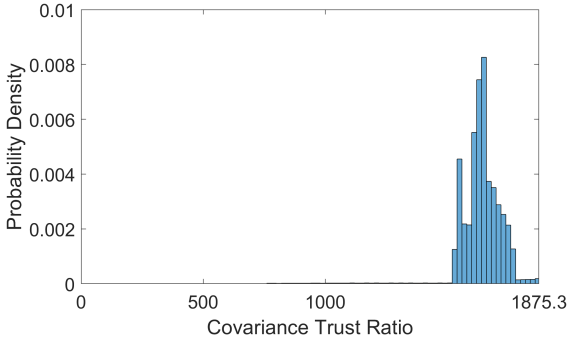

(c) PDF for Test Case 2b average covariance trust ratios, truncated to probabilities below 98%

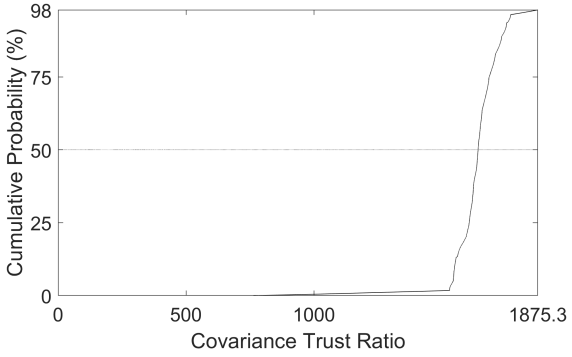

(d) CDF for Test Case 2b average covariance trust ratios, truncated to probabilities below 98%

Fig. C.20: Cumulative distribution functions (CDFs) and probability density functions (PDFs) for trustworthiness factor combination Test Case 2b: filters using the EKF to estimate the observer's state using range measurements and the van Loan process noise covariance model without with perfect knowledge of RSO positions.

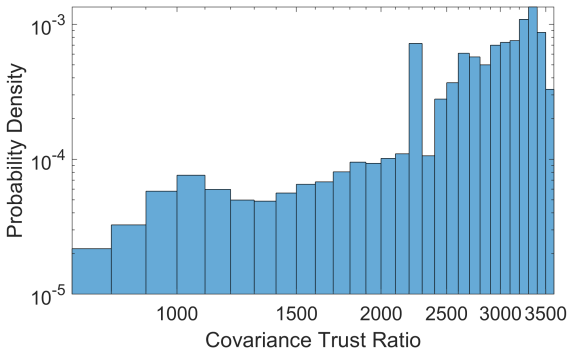

(a) PDF for Test Case 3b average covariance trust ratios

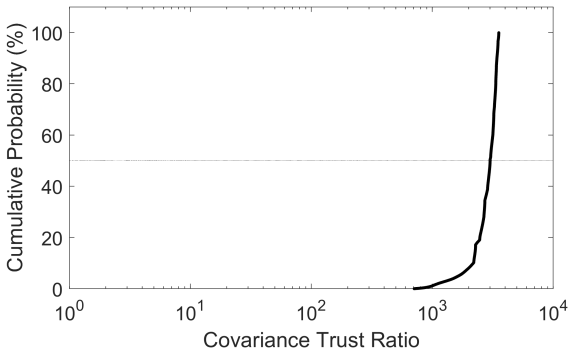

(b) CDF for Test Case 3b average covariance trust ratios

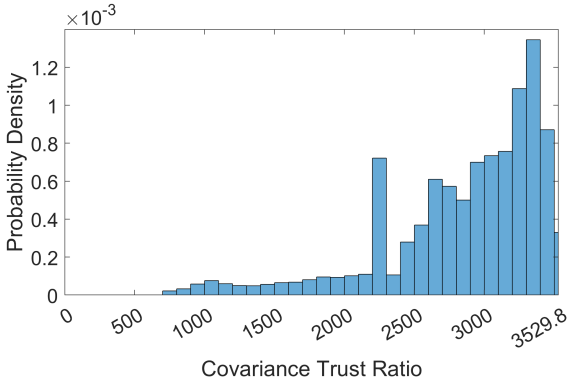

(c) PDF for Test Case 3b average covariance trust ratios, truncated to probabilities below 98%

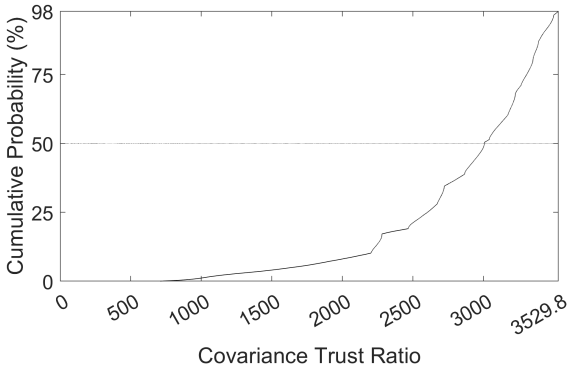

(d) CDF for Test Case 3b average covariance trust ratios, truncated to probabilities below 98%

Fig. C.21: Cumulative distribution functions (CDFs) and probability density functions (PDFs) for trustworthiness factor combination Test Case 3b: filters using the EKF to estimate the observer's state using range and angle measurements and the van Loan process noise covariance model without with perfect knowledge of RSO positions.

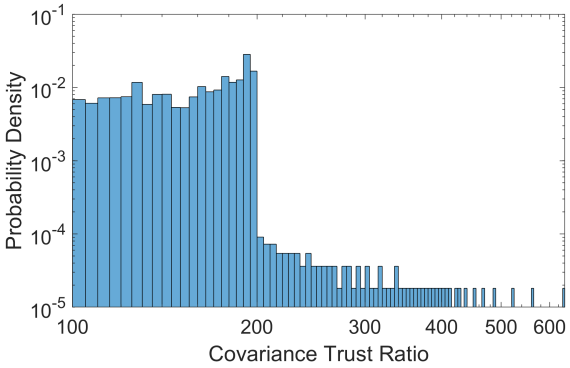

(a) PDF for Test Case 4b average covariance trust ratios

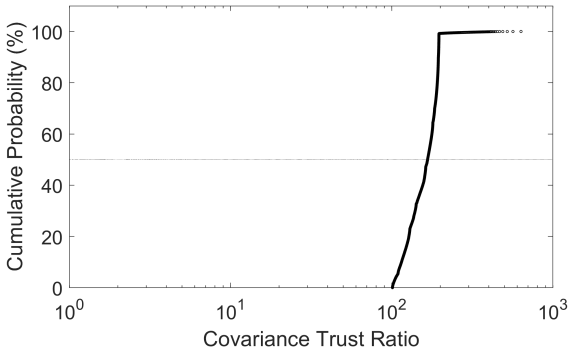

(b) CDF for Test Case 4b average covariance trust ratios

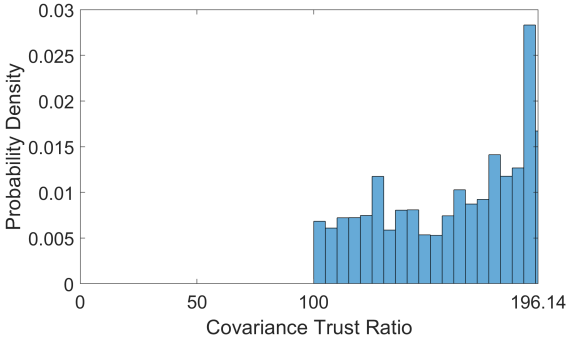

(c) PDF for Test Case 4b average covariance trust ratios, truncated to probabilities below 98%

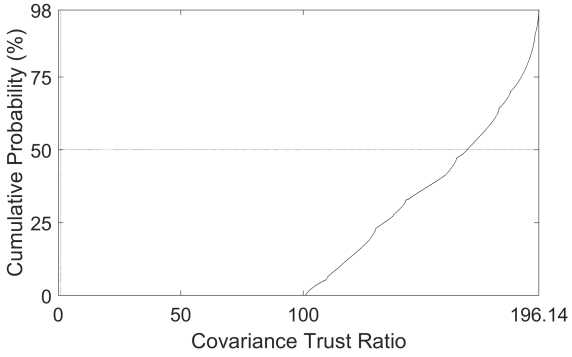

(d) CDF for Test Case 4b average covariance trust ratios, truncated to probabilities below 98%

Fig. C.22: Cumulative distribution functions (CDFs) and probability density functions (PDFs) for trustworthiness factor combination Test Case 4b: filters using the EKF to estimate the observer's state using angle measurements and the fixed bump process noise covariance model without with perfect knowledge of RSO positions.

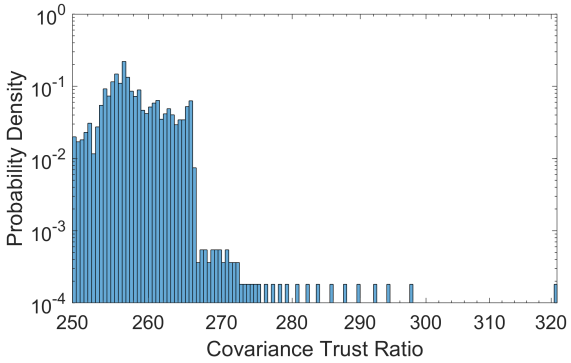

(a) PDF for Test Case 5b average covariance trust ratios

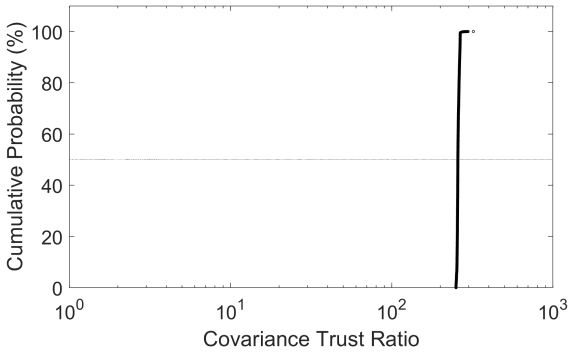

(b) CDF for Test Case 5b average covariance trust ratios

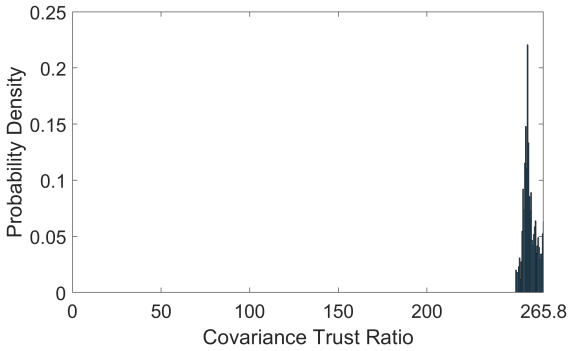

(c) PDF for Test Case 5b average covariance trust ratios, truncated to probabilities below 98%

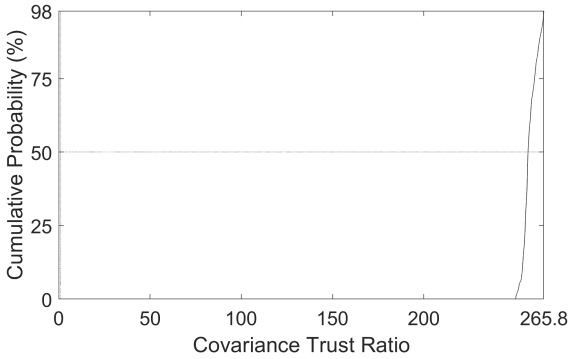

(d) CDF for Test Case 5b average covariance trust ratios, truncated to probabilities below 98%

Fig. C.23: Cumulative distribution functions (CDFs) and probability density functions (PDFs) for trustworthiness factor combination Test Case 5b: filters using the EKF to estimate the observer's state using range measurements and the fixed bump process noise covariance model without with perfect knowledge of RSO positions.

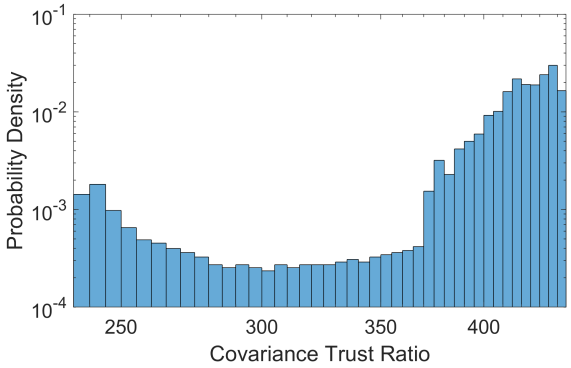

(a) PDF for Test Case 6b average covariance trust ratios

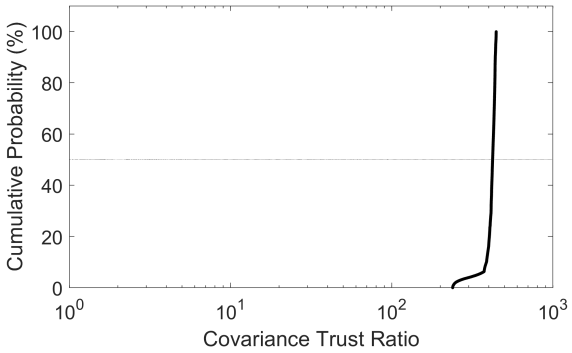

(b) CDF for Test Case 6b average covariance trust ratios

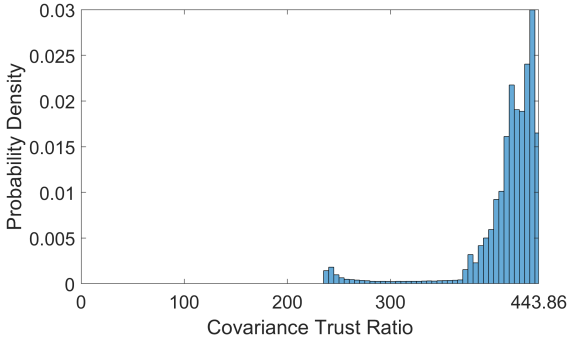

(c) PDF for Test Case 6b average covariance trust ratios, truncated to probabilities below 98%

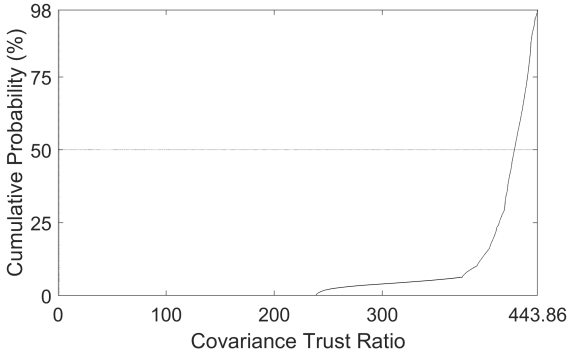

(d) CDF for Test Case 6b average covariance trust ratios, truncated to probabilities below 98%

Fig. C.24: Cumulative distribution functions (CDFs) and probability density functions (PDFs) for trustworthiness factor combination Test Case 6b: filters using the EKF to estimate the observer's state using range and angle measurements and the fixed bump process noise covariance model without with perfect knowledge of RSO positions.

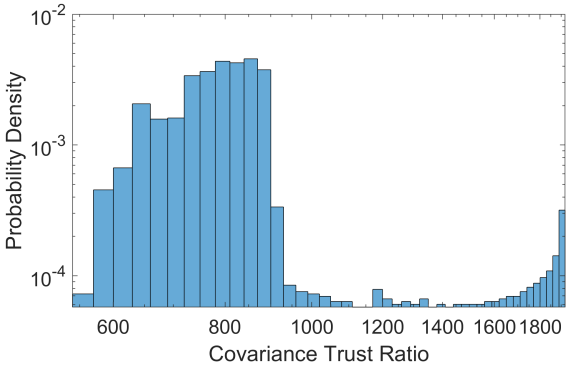

(a) PDF for Test Case 7b average covariance trust ratios

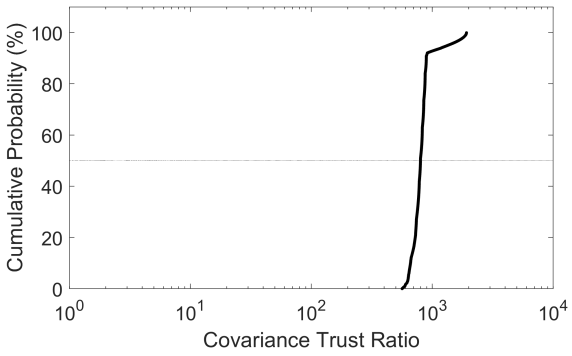

(b) CDF for Test Case 7b average covariance trust ratios

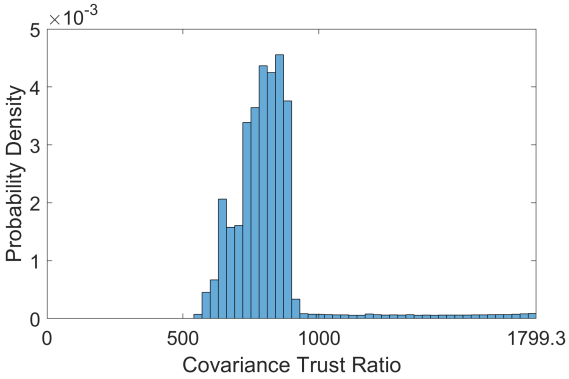

(c) PDF for Test Case 7b average covariance trust ratios, truncated to probabilities below 98%

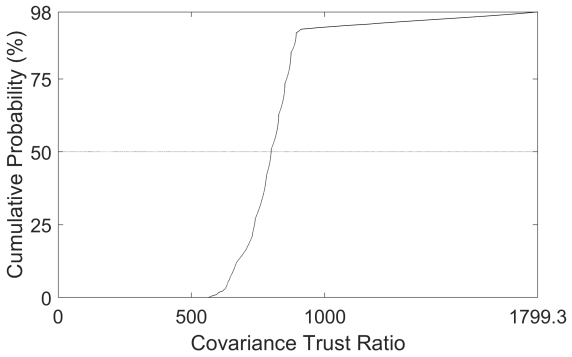

(d) CDF for Test Case 7b average covariance trust ratios, truncated to probabilities below 98%

Fig. C.25: Cumulative distribution functions (CDFs) and probability density functions (PDFs) for trustworthiness factor combination Test Case 7b: filters using the EKF to estimate the observer's state using angle measurements and the variable bump process noise covariance model without with perfect knowledge of RSO positions.

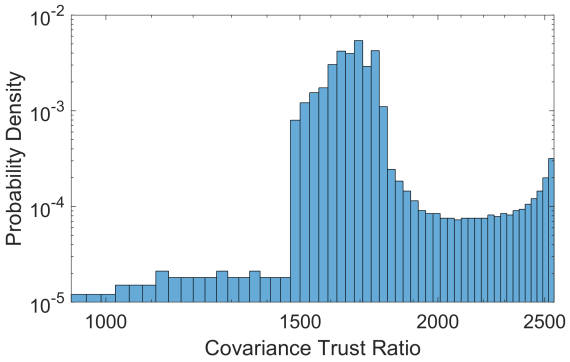

(a) PDF for Test Case 8b average covariance trust ratios

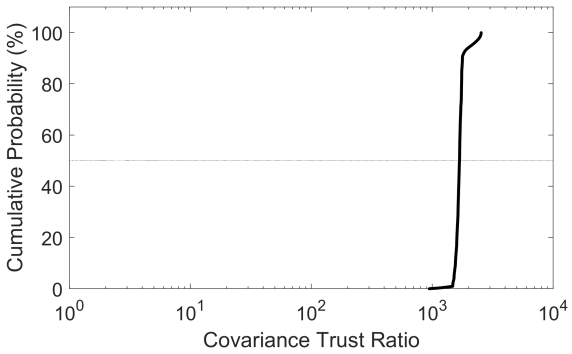

(b) CDF for Test Case 8b average covariance trust ratios

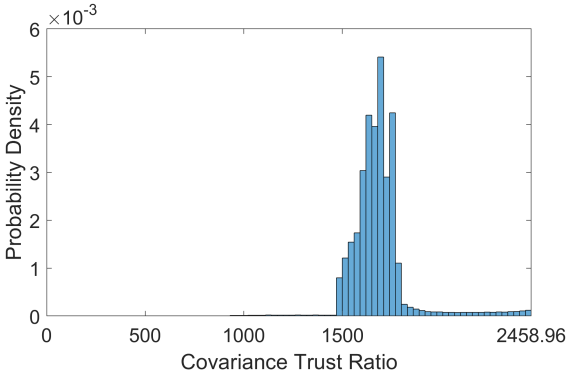

(c) PDF for Test Case 8b average covariance trust ratios, truncated to probabilities below 98%

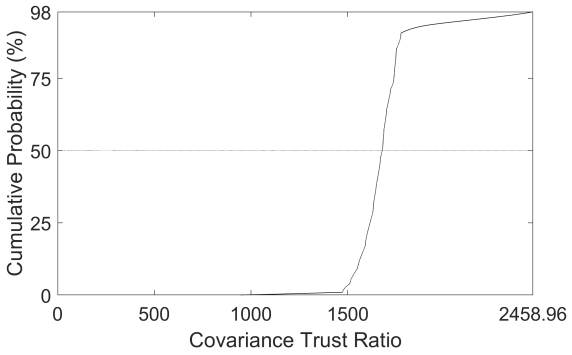

(d) CDF for Test Case 8b average covariance trust ratios, truncated to probabilities below 98%

Fig. C.26: Cumulative distribution functions (CDFs) and probability density functions (PDFs) for trustworthiness factor combination Test Case 8b: filters using the EKF to estimate the observer's state using range measurements and the variable bump process noise covariance model without with perfect knowledge of RSO positions.

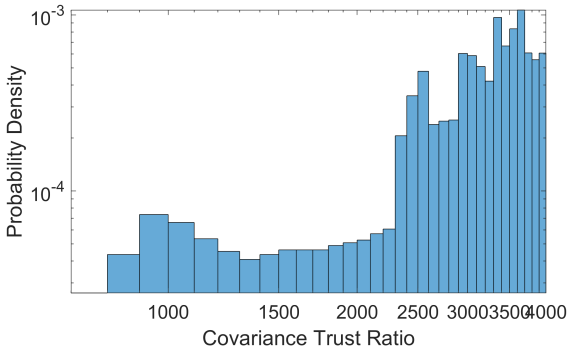

(a) PDF for Test Case 9b average covariance trust ratios

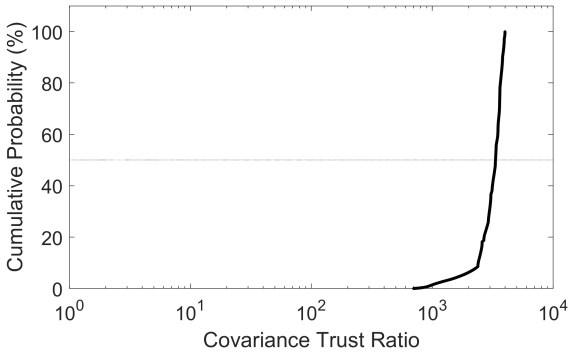

(b) CDF for Test Case 9b average covariance trust ratios

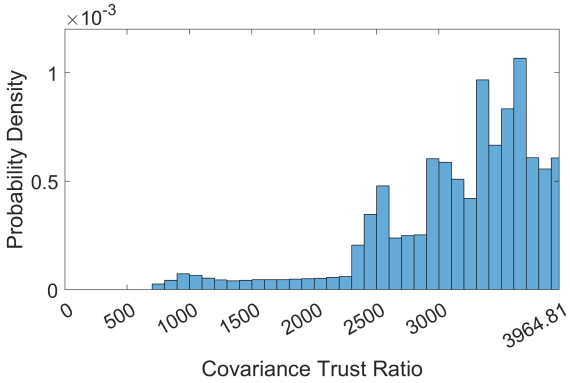

(c) PDF for Test Case 9b average covariance trust ratios, truncated to probabilities below 98%

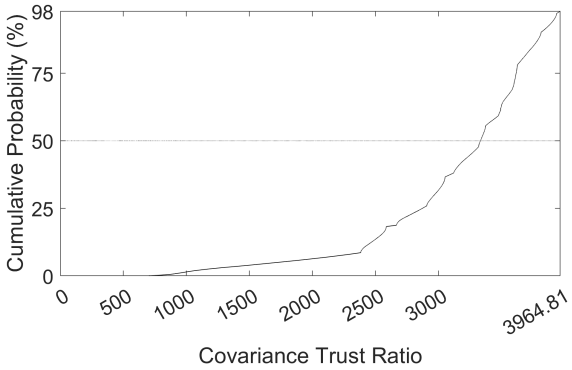

(d) CDF for Test Case 9b average covariance trust ratios, truncated to probabilities below 98%

Fig. C.27: Cumulative distribution functions (CDFs) and probability density functions (PDFs) for trustworthiness factor combination Test Case 9b: filters using the EKF to estimate the observer's state using range and angle measurements and the variable bump process noise covariance model without with perfect knowledge of RSO positions.

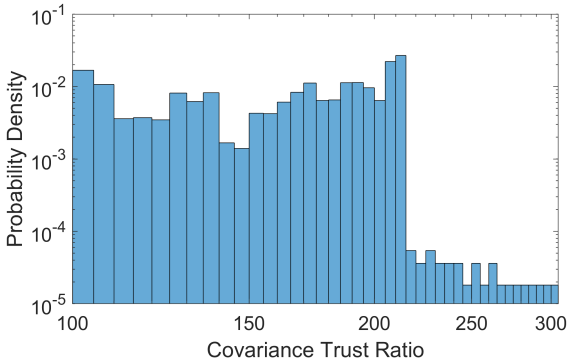

(a) PDF for Test Case 10b average covariance trust ratios

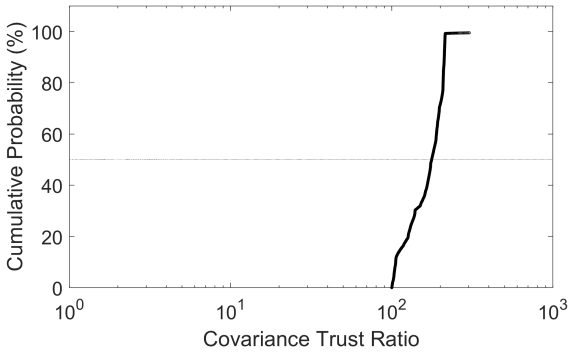

(b) CDF for Test Case 10b average covariance trust ratios

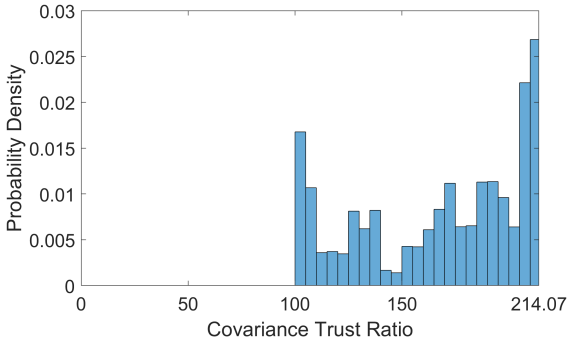

(c) PDF for Test Case 10b average covariance trust ratios, truncated to probabilities below 98%

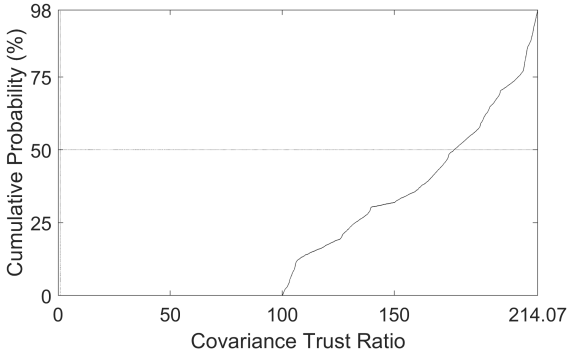

(d) CDF for Test Case 10b average covariance trust ratios, truncated to probabilities below 98%

Fig. C.28: Cumulative distribution functions (CDFs) and probability density functions (PDFs) for trustworthiness factor combination Test Case 10b: filters using the UKF to estimate the observer's state using angle measurements and the van Loan process noise covariance model without with perfect knowledge of RSO positions.

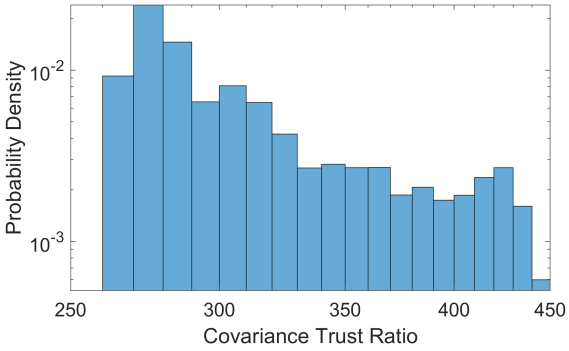

(a) PDF for Test Case 11b average covariance trust ratios

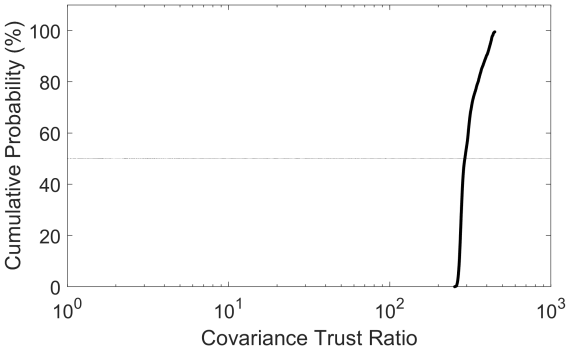

(b) CDF for Test Case 11b average covariance trust ratios

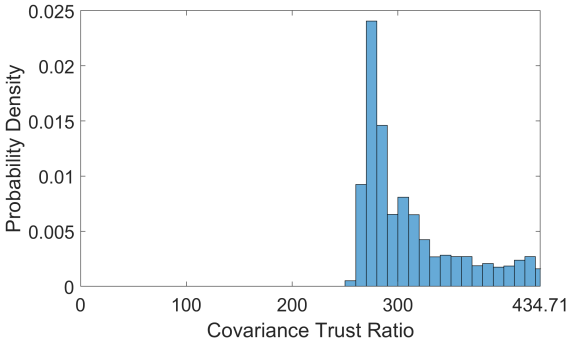

(c) PDF for Test Case 11b average covariance trust ratios, truncated to probabilities below 98%

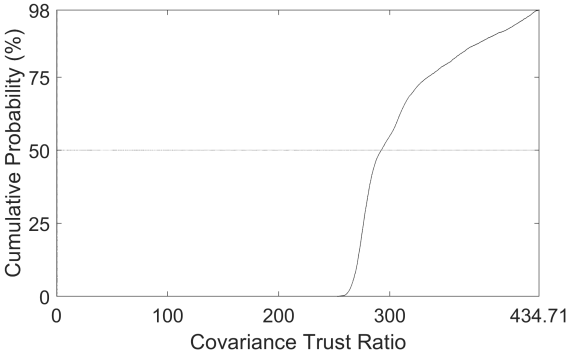

(d) CDF for Test Case 11b average covariance trust ratios, truncated to probabilities below 98%

Fig. C.29: Cumulative distribution functions (CDFs) and probability density functions (PDFs) for trustworthiness factor combination Test Case 11b: filters using the UKF to estimate the observer's state using range measurements and the van Loan process noise covariance model without with perfect knowledge of RSO positions.

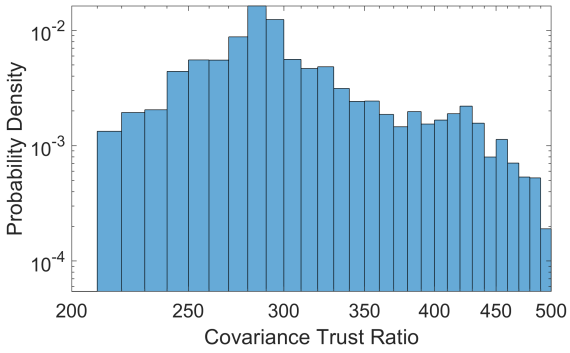

(a) PDF for Test Case 12b average covariance trust ratios

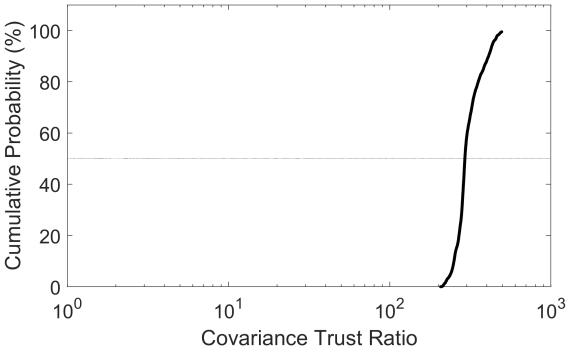

(b) CDF for Test Case 12b average covariance trust ratios

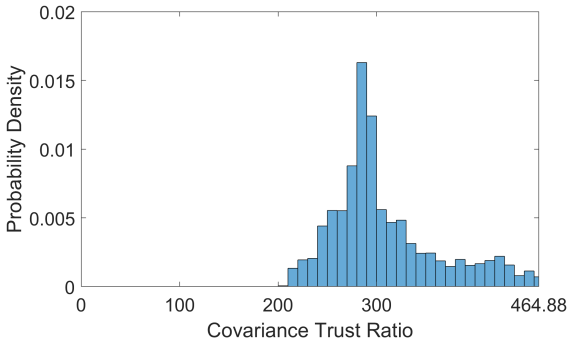

(c) PDF for Test Case 12b average covariance trust ratios, truncated to probabilities below 98%

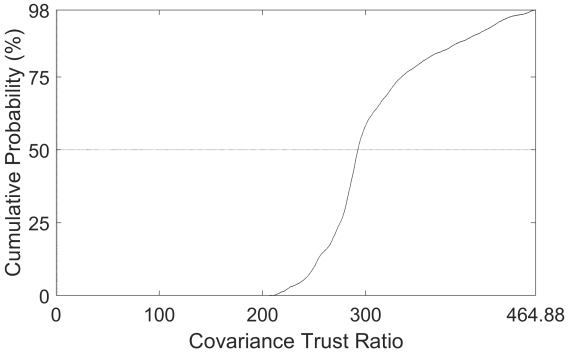

(d) CDF for Test Case 12b average covariance trust ratios, truncated to probabilities below 98%

Fig. C.30: Cumulative distribution functions (CDFs) and probability density functions (PDFs) for trustworthiness factor combination Test Case 12b: filters using the UKF to estimate the observer's state using range and angle measurements and the van Loan process noise covariance model without with perfect knowledge of RSO positions.

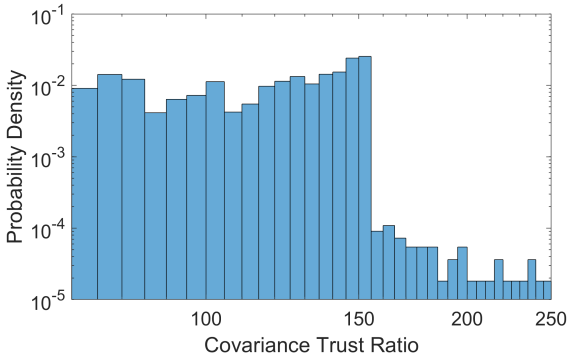

(a) PDF for Test Case 13b average covariance trust ratios

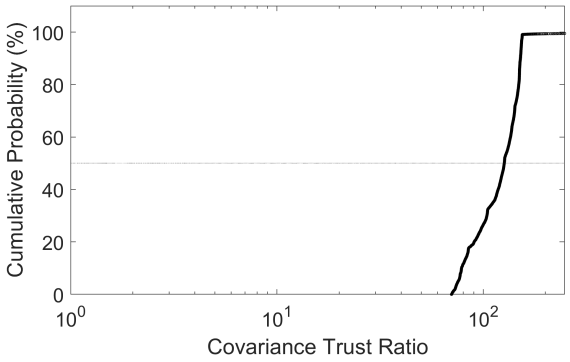

(b) CDF for Test Case 13b average covariance trust ratios

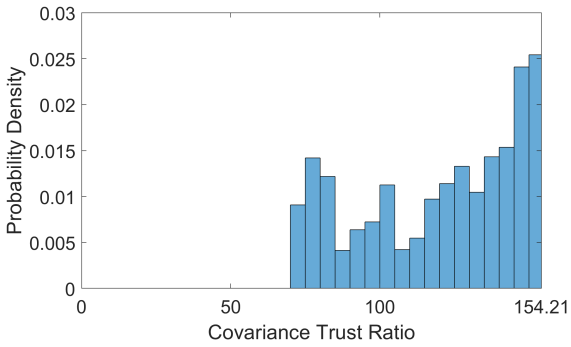

(c) PDF for Test Case 13b average covariance trust ratios, truncated to probabilities below 98%

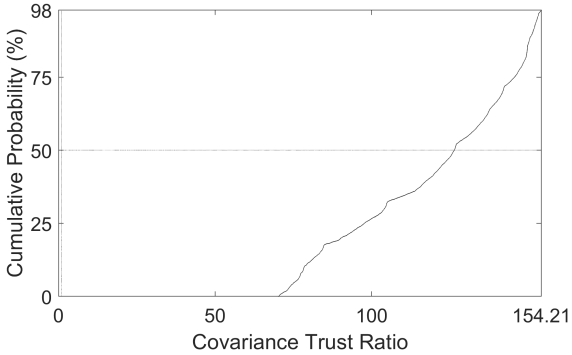

(d) CDF for Test Case 13b average covariance trust ratios, truncated to probabilities below 98%

Fig. C.31: Cumulative distribution functions (CDFs) and probability density functions (PDFs) for trustworthiness factor combination Test Case 13b: filters using the UKF to estimate the observer's state using angle measurements and the fixed bump process noise covariance model without with perfect knowledge of RSO positions.

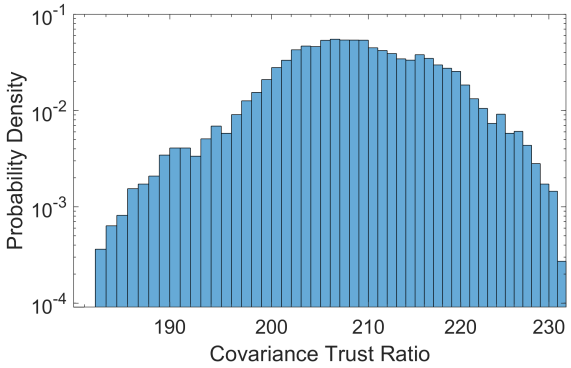

(a) PDF for Test Case 14b average covariance trust ratios

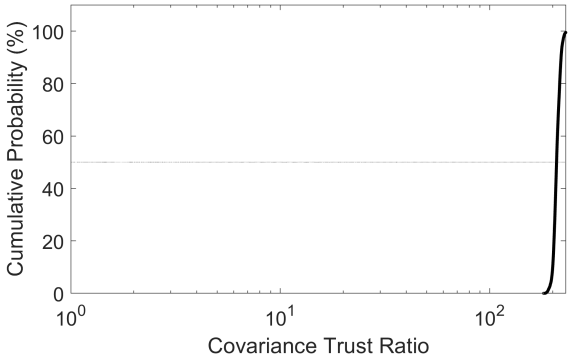

(b) CDF for Test Case 14b average covariance trust ratios

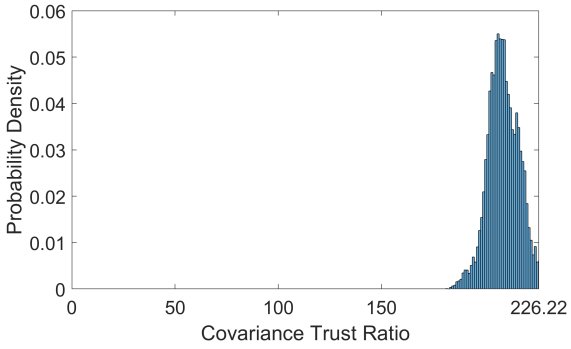

(c) PDF for Test Case 14b average covariance trust ratios, truncated to probabilities below 98%

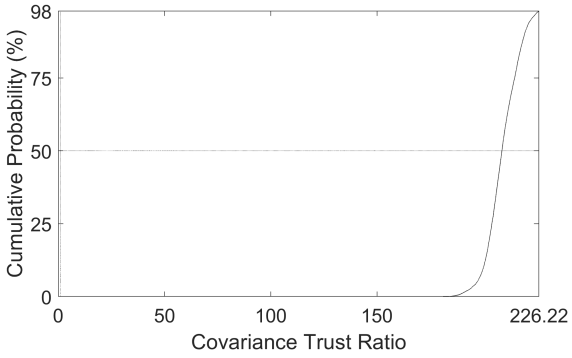

(d) CDF for Test Case 14b average covariance trust ratios, truncated to probabilities below 98%

Fig. C.32: Cumulative distribution functions (CDFs) and probability density functions (PDFs) for trustworthiness factor combination Test Case 14b: filters using the UKF to estimate the observer's state using range measurements and the fixed bump process noise covariance model without with perfect knowledge of RSO positions.

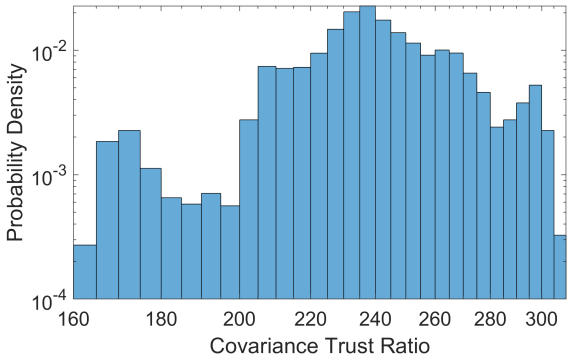

(a) PDF for Test Case 15b average covariance trust ratios

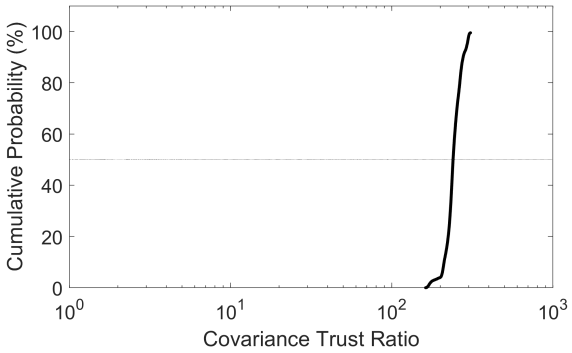

(b) CDF for Test Case 15b average covariance trust ratios

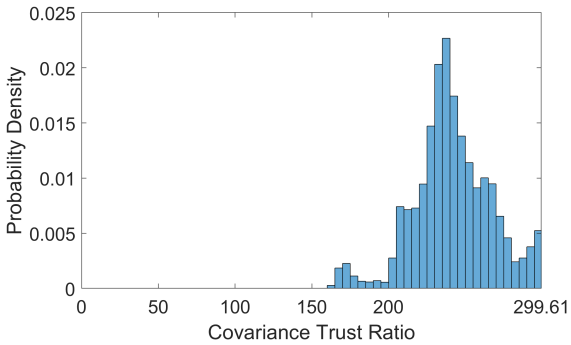

(c) PDF for Test Case 15b average covariance trust ratios, truncated to probabilities below 98%

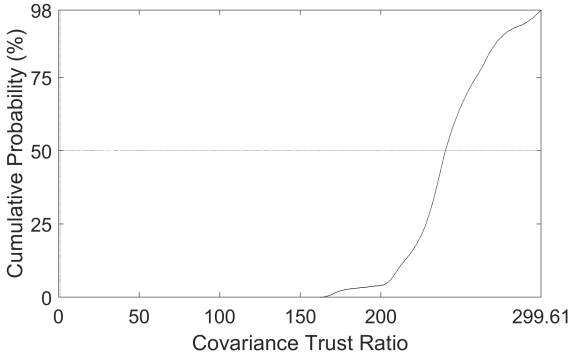

(d) CDF for Test Case 15b average covariance trust ratios, truncated to probabilities below 98%

Fig. C.33: Cumulative distribution functions (CDFs) and probability density functions (PDFs) for trustworthiness factor combination Test Case 15b: filters using the UKF to estimate the observer's state using range and angle measurements and the fixed bump process noise covariance model.

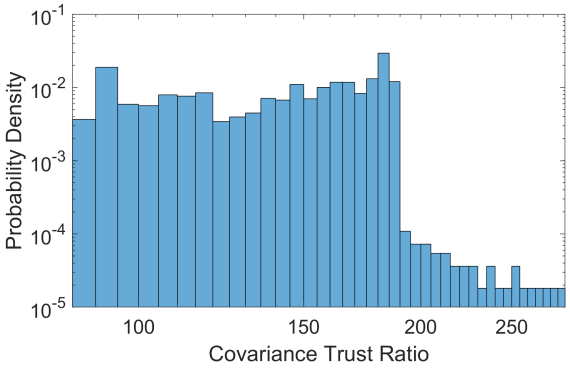

(a) PDF for Test Case 16b average covariance trust ratios

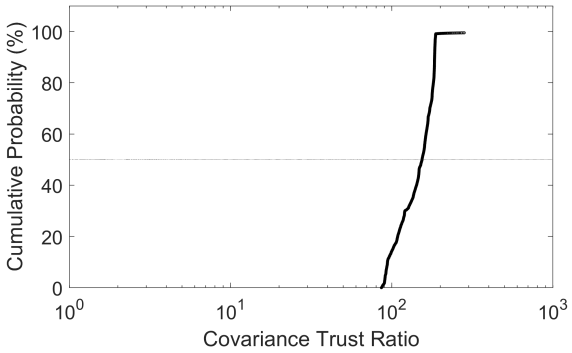

(b) CDF for Test Case 16b average covariance trust ratios

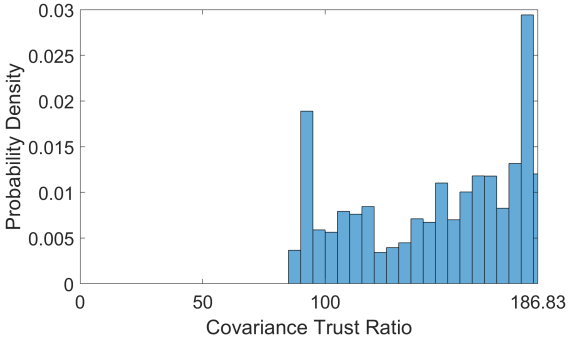

(c) PDF for Test Case 16b average covariance trust ratios, truncated to probabilities below 98%

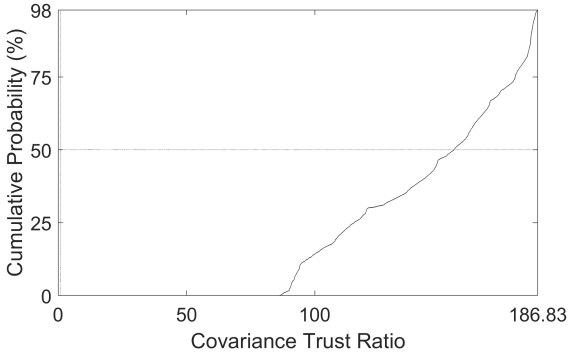

(d) CDF for Test Case 16b average covariance trust ratios, truncated to probabilities below 98%

Fig. C.34: Cumulative distribution functions (CDFs) and probability density functions (PDFs) for trustworthiness factor combination Test Case 16b: filters using the UKF to estimate the observer's state using angle measurements and the variable bump process noise covariance model.

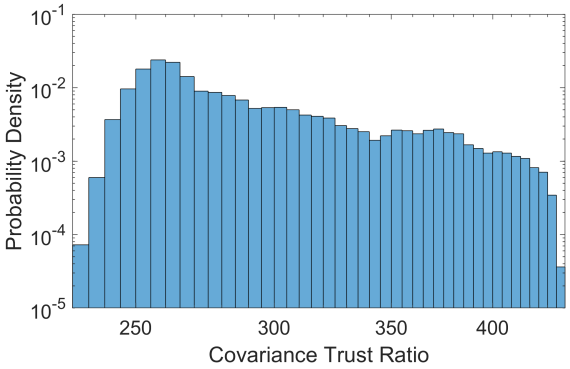

(a) PDF for Test Case 17b average covariance trust ratios

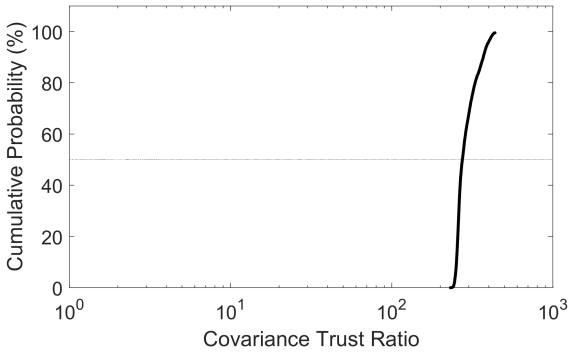

(b) CDF for Test Case 17b average covariance trust ratios

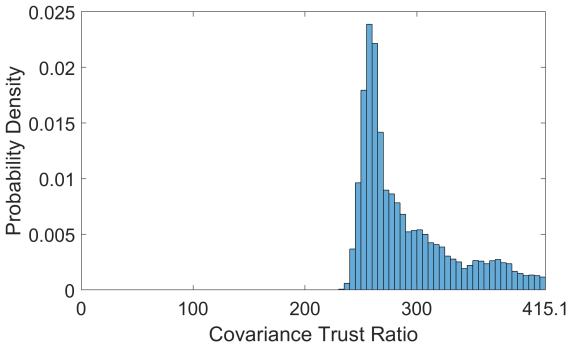

(c) PDF for Test Case 17b average covariance trust ratios, truncated to probabilities below 98%

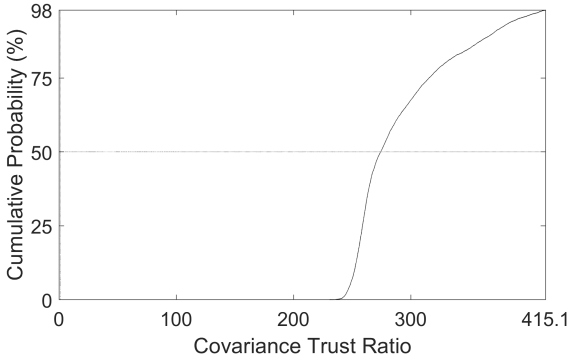

(d) CDF for Test Case 17b average covariance trust ratios, truncated to probabilities below 98%

Fig. C.35: Cumulative distribution functions (CDFs) and probability density functions (PDFs) for trustworthiness factor combination Test Case 17b: filters using the UKF to estimate the observer's state using range measurements and the variable bump process noise covariance model without with perfect knowledge of RSO positions.

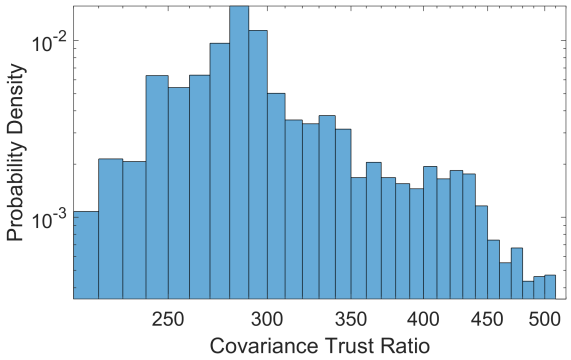

(a) PDF for Test Case 18b average covariance trust ratios

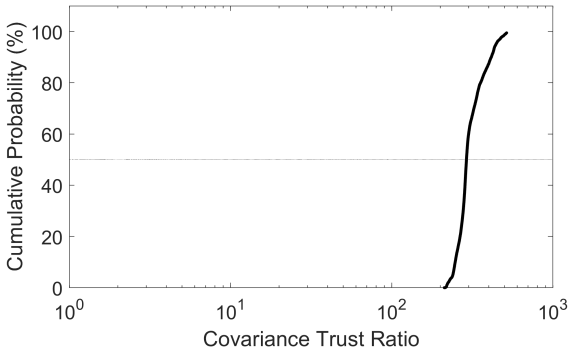

(b) CDF for Test Case 18b average covariance trust ratios

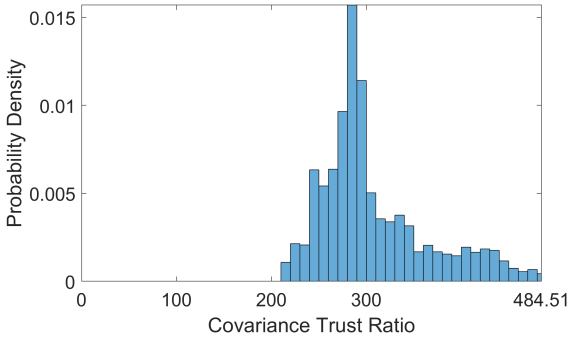

(c) PDF for Test Case 18b average covariance trust ratios, truncated to probabilities below 98%

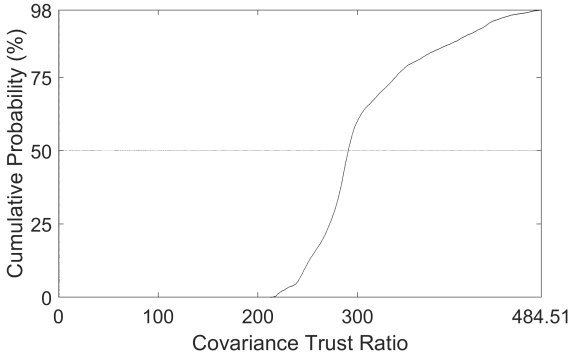

(d) CDF for Test Case 18b average covariance trust ratios, truncated to probabilities below 98%

Fig. C.36: Cumulative distribution functions (CDFs) and probability density functions (PDFs) for trustworthiness factor combination Test Case 18b: filters using the UKF to estimate the observer's state using range and angle measurements and the variable bump process noise covariance model without with perfect knowledge of RSO positions.

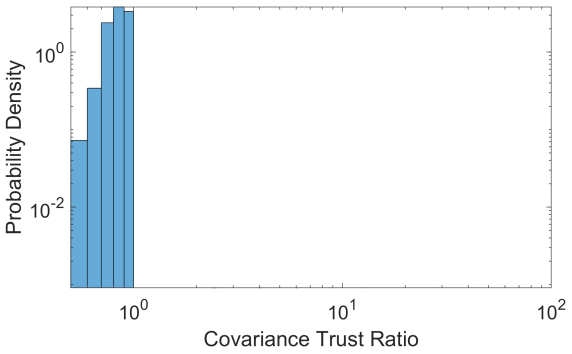

(a) PDF for Test Case 19 average covariance trust ratios

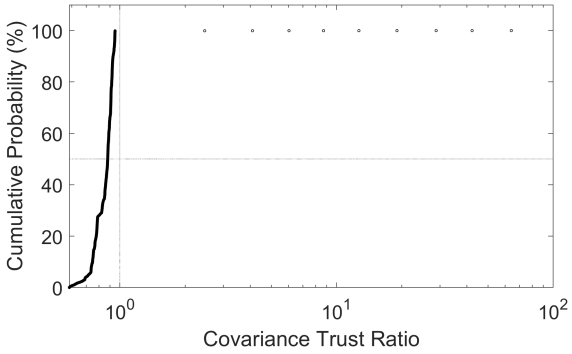

(b) CDF for Test Case 19 average covariance trust ratios

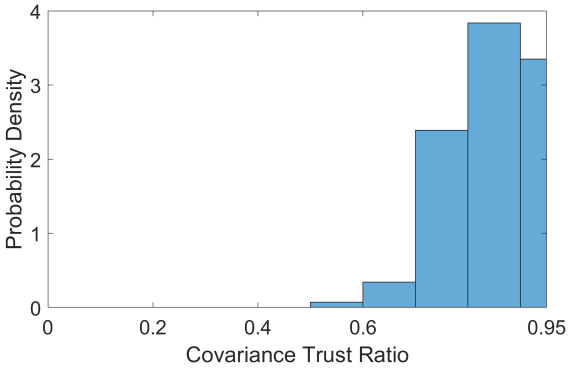

(c) PDF for Test Case 19 average covariance trust ratios, truncated to probabilities below 98%

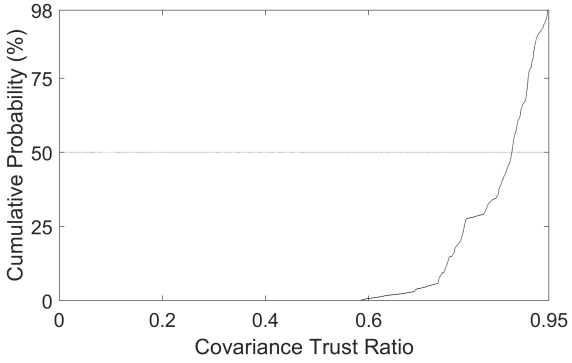

(d) CDF for Test Case 19 average covariance trust ratios, truncated to probabilities below 98%

Fig. C.37: Cumulative distribution functions (CDFs) and probability density functions (PDFs) for trustworthiness factor combination Test Case 19: filters using the EKF to estimate the observer and RSO state using angle measurements and the van Loan process noise covariance model.

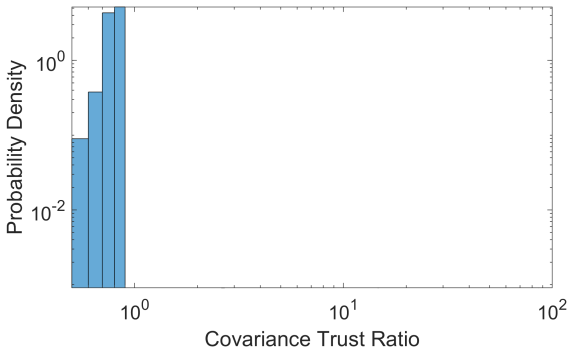

(a) PDF for Test Case 20 average covariance trust ratios

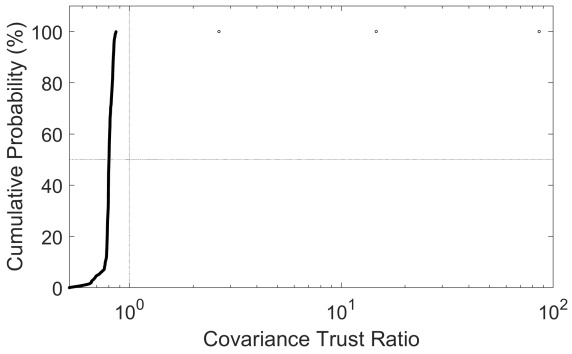

(b) CDF for Test Case 20 average covariance trust ratios

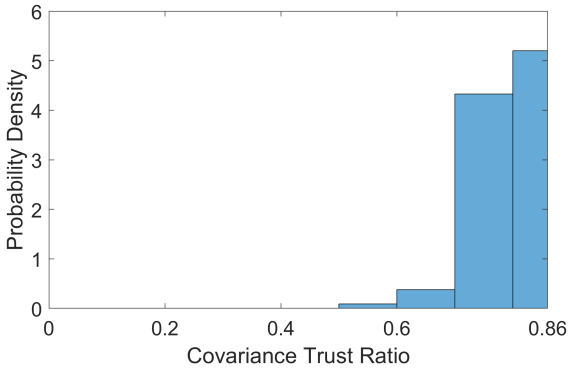

(c) PDF for Test Case 20 average covariance trust ratios, truncated to probabilities below 98%

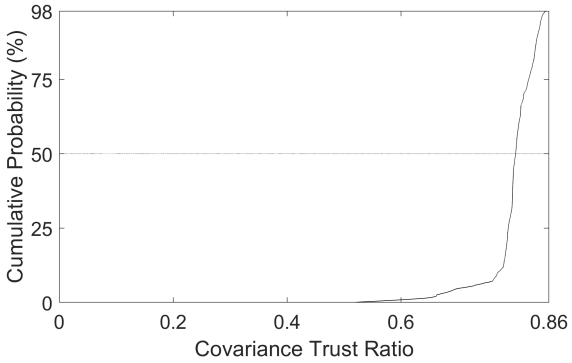

(d) CDF for Test Case 20 average covariance trust ratios, truncated to probabilities below 98%

Fig. C.38: Cumulative distribution functions (CDFs) and probability density functions (PDFs) for trustworthiness factor combination Test Case 20: filters using the EKF to estimate the observer and RSO state using range measurements and the van Loan process noise covariance model.

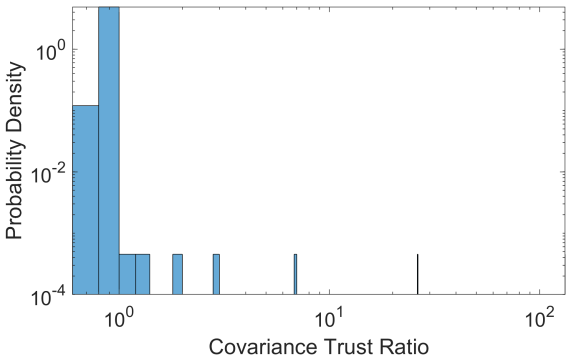

(a) PDF for Test Case 21 average covariance trust ratios

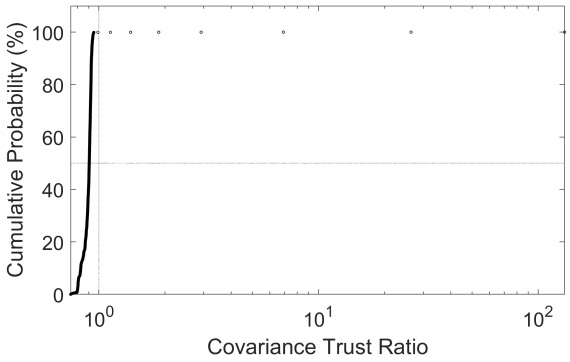

(b) CDF for Test Case 21 average covariance trust ratios

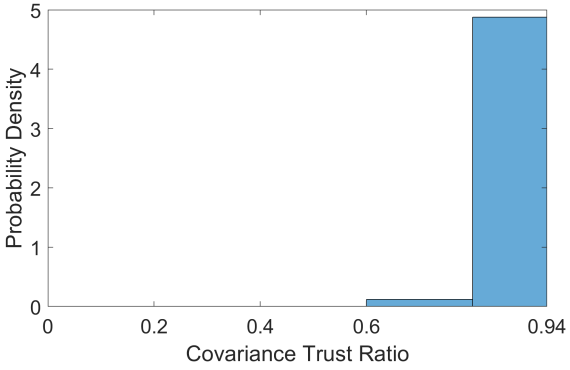

(c) PDF for Test Case 21 average covariance trust ratios, truncated to probabilities below 98%

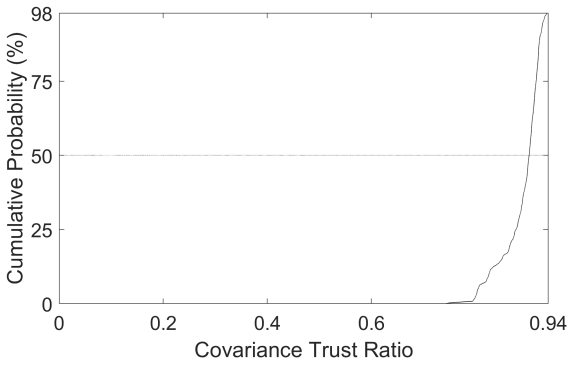

(d) CDF for Test Case 21 average covariance trust ratios, truncated to probabilities below 98%

Fig. C.39: Cumulative distribution functions (CDFs) and probability density functions (PDFs) for trustworthiness factor combination Test Case 21: filters using the EKF to estimate the observer and RSO state using range and angle measurements and the van Loan process noise covariance model.

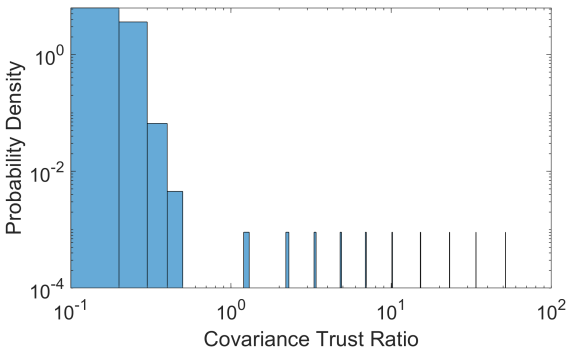

(a) PDF for Test Case 22 average covariance trust ratios

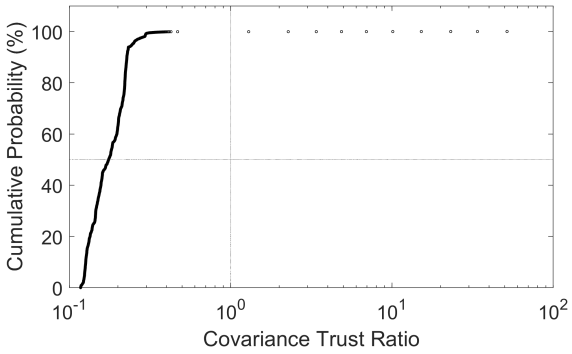

(b) CDF for Test Case 22 average covariance trust ratios

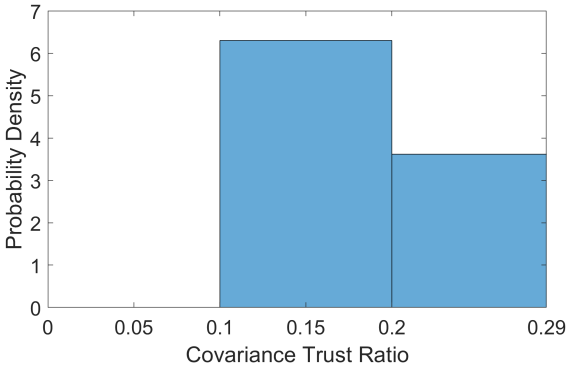

(c) PDF for Test Case 22 average covariance trust ratios, truncated to probabilities below 98%

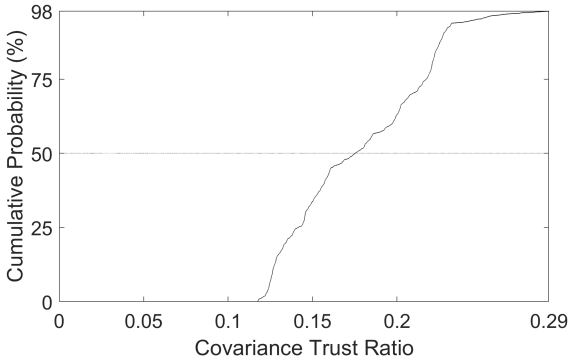

(d) CDF for Test Case 22 average covariance trust ratios, truncated to probabilities below 98%

Fig. C.40: Cumulative distribution functions (CDFs) and probability density functions (PDFs) for trustworthiness factor combination Test Case 22: filters using the EKF to estimate the observer and RSO state using angle measurements and the fixed bump process noise covariance model.

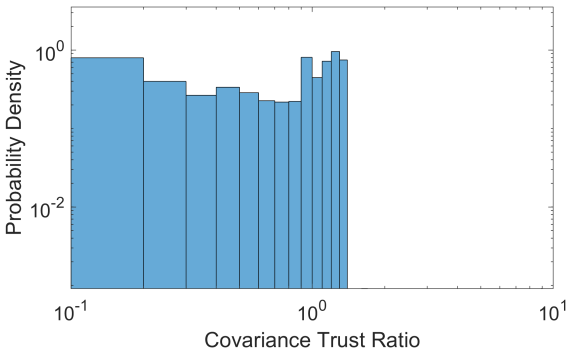

(a) PDF for Test Case 23 average covariance trust ratios

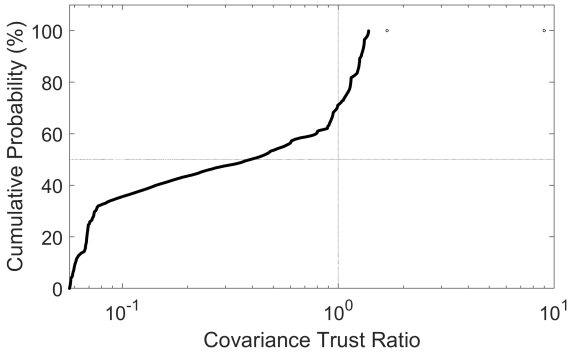

(b) CDF for Test Case 23 average covariance trust ratios

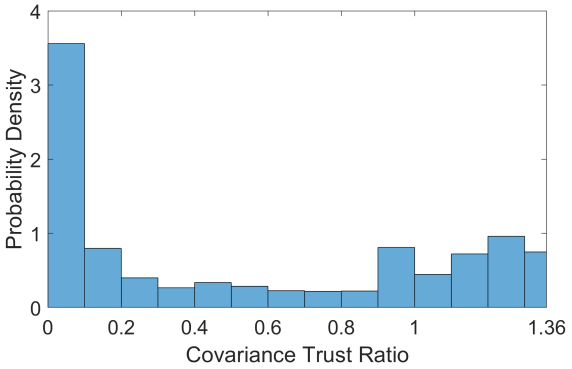

(c) PDF for Test Case 23 average covariance trust ratios, truncated to probabilities below 98%

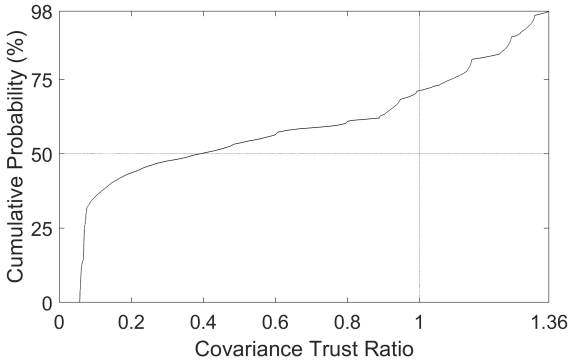

(d) CDF for Test Case 23 average covariance trust ratios, truncated to probabilities below 98%

Fig. C.41: Cumulative distribution functions (CDFs) and probability density functions (PDFs) for trustworthiness factor combination Test Case 23: filters using the EKF to estimate the observer and RSO state using range measurements and the fixed bump process noise covariance model.

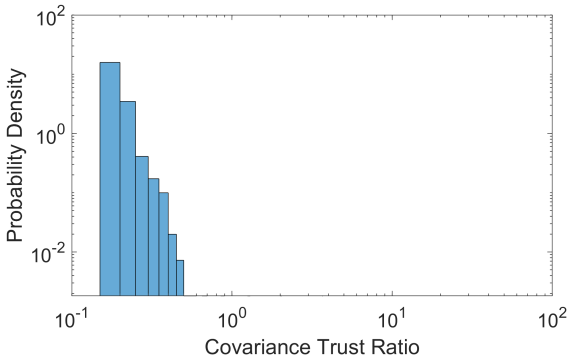

(a) PDF for Test Case 24 average covariance trust ratios

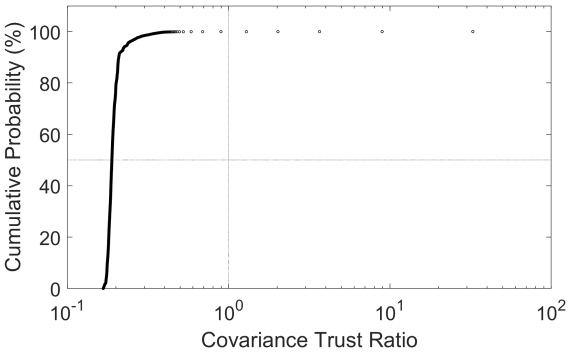

(b) CDF for Test Case 24 average covariance trust ratios

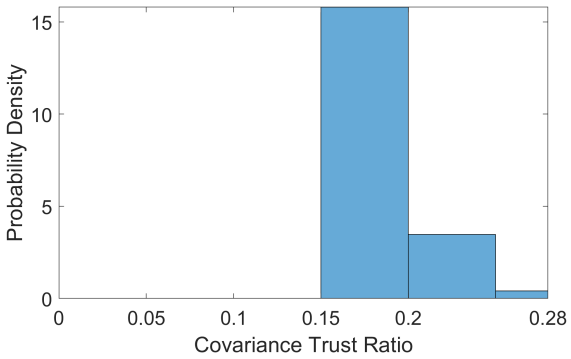

(c) PDF for Test Case 24 average covariance trust ratios, truncated to probabilities below 98%

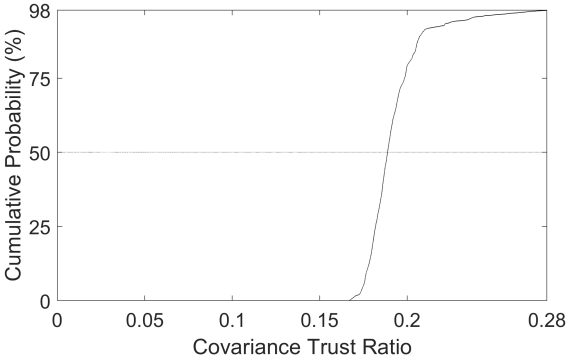

(d) CDF for Test Case 24 average covariance trust ratios, truncated to probabilities below 98%

Fig. C.42: Cumulative distribution functions (CDFs) and probability density functions (PDFs) for trustworthiness factor combination Test Case 24: filters using the EKF to estimate the observer and RSO state using range and angle measurements and the fixed bump process noise covariance model.

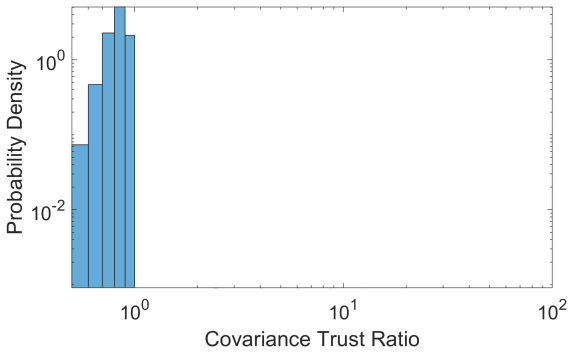

(a) PDF for Test Case 25 average covariance trust ratios

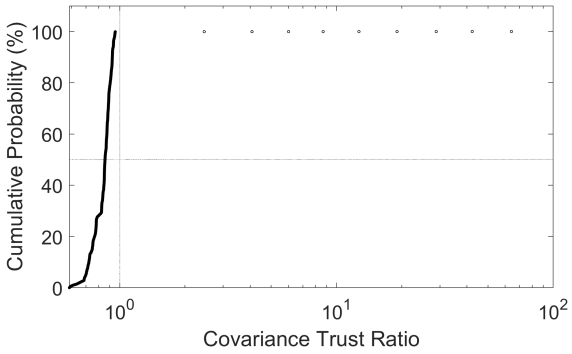

(b) CDF for Test Case 25 average covariance trust ratios

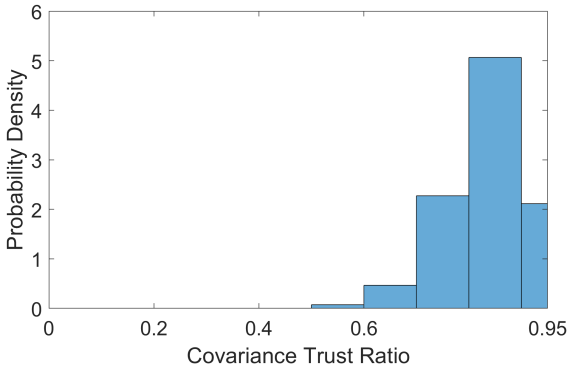

(c) PDF for Test Case 25 average covariance trust ratios, truncated to probabilities below 98%

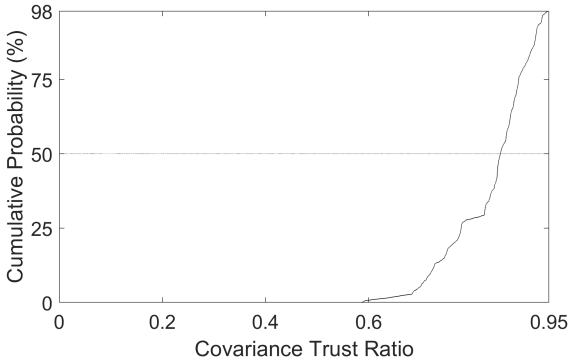

(d) CDF for Test Case 25 average covariance trust ratios, truncated to probabilities below 98%

Fig. C.43: Cumulative distribution functions (CDFs) and probability density functions (PDFs) for trustworthiness factor combination Test Case 25: filters using the EKF to estimate the observer and RSO state using angle measurements and the variable bump process noise covariance model.

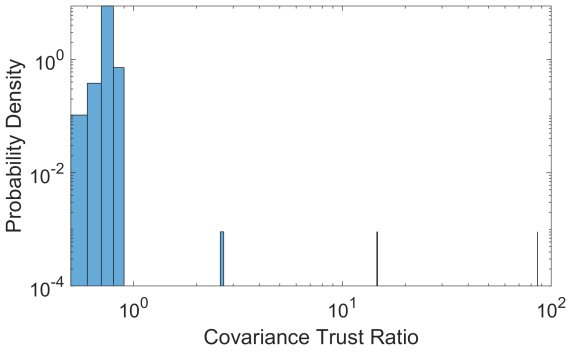

(a) PDF for Test Case 26 average covariance trust ratios

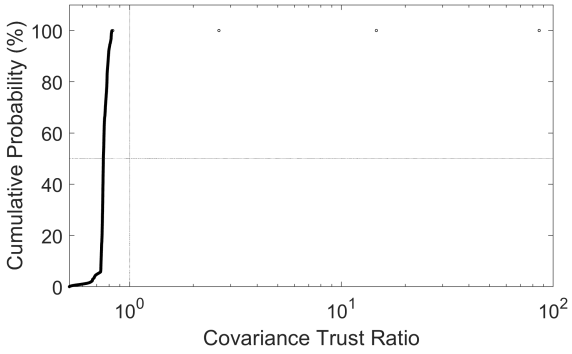

(b) CDF for Test Case 26 average covariance trust ratios

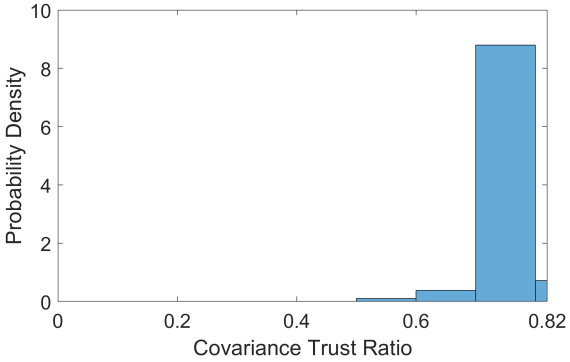

(c) PDF for Test Case 26 average covariance trust ratios, truncated to probabilities below 98%

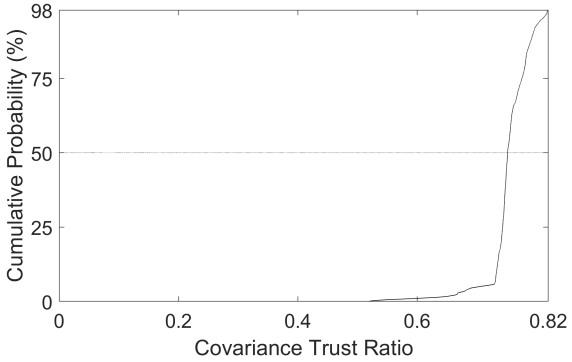

(d) CDF for Test Case 26 average covariance trust ratios, truncated to probabilities below 98%

Fig. C.44: Cumulative distribution functions (CDFs) and probability density functions (PDFs) for trustworthiness factor combination Test Case 26: filters using the EKF to estimate the observer and RSO state using range measurements and the variable bump process noise covariance model.

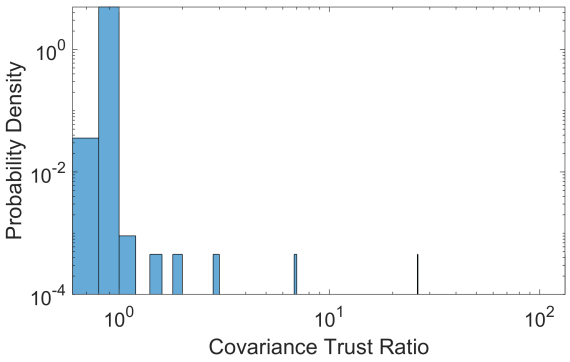

(a) PDF for Test Case 27 average covariance trust ratios

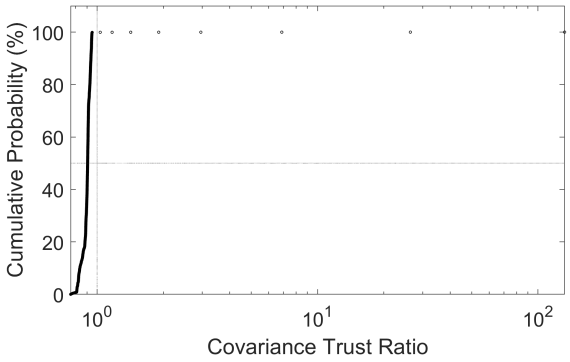

(b) CDF for Test Case 27 average covariance trust ratios

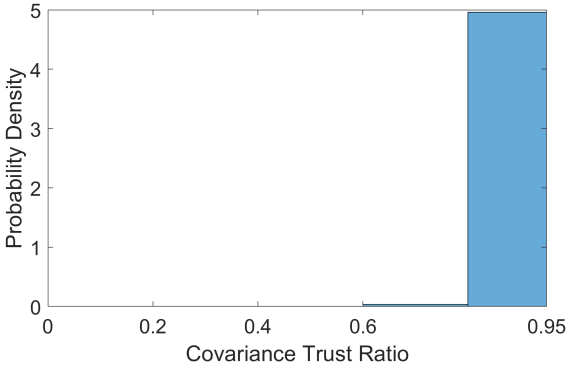

(c) PDF for Test Case 27 average covariance trust ratios, truncated to probabilities below 98%

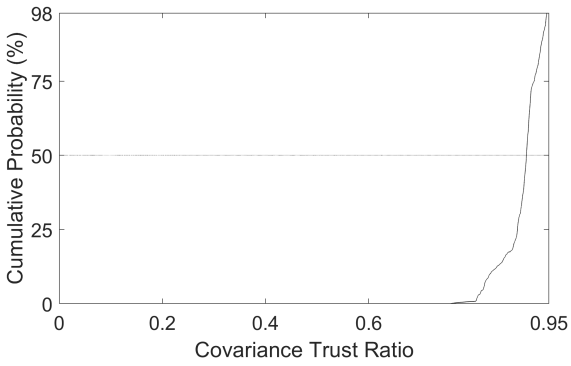

(d) CDF for Test Case 27 average covariance trust ratios, truncated to probabilities below 98%

Fig. C.45: Cumulative distribution functions (CDFs) and probability density functions (PDFs) for trustworthiness factor combination Test Case 27: filters using the EKF to estimate the observer and RSO state using range and angle measurements and the variable bump process noise covariance model.

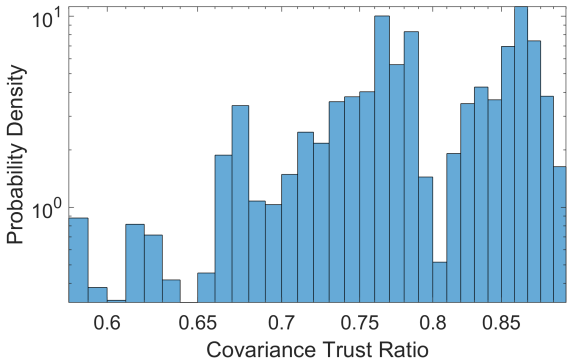

(a) PDF for Test Case 28 average covariance trust ratios

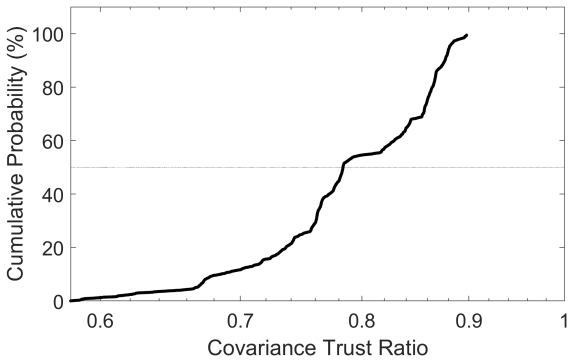

(b) CDF for Test Case 28 average covariance trust ratios

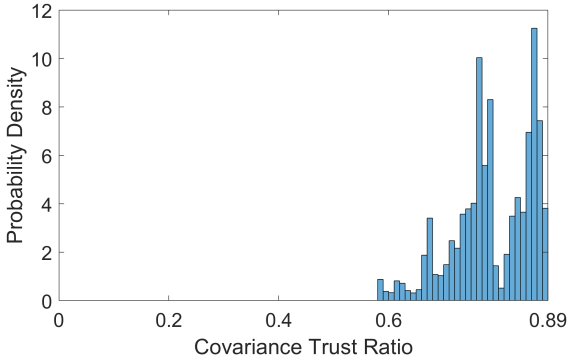

(c) PDF for Test Case 28 average covariance trust ratios, truncated to probabilities below 98%

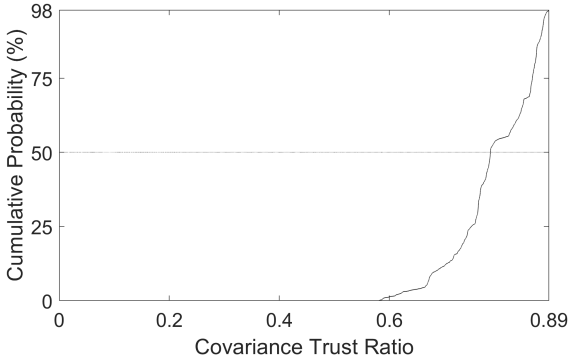

(d) CDF for Test Case 28 average covariance trust ratios, truncated to probabilities below 98%

Fig. C.46: Cumulative distribution functions (CDFs) and probability density functions (PDFs) for trustworthiness factor combination Test Case 28: filters using the UKF to estimate the observer and RSO state using angle measurements and the van Loan process noise covariance model.

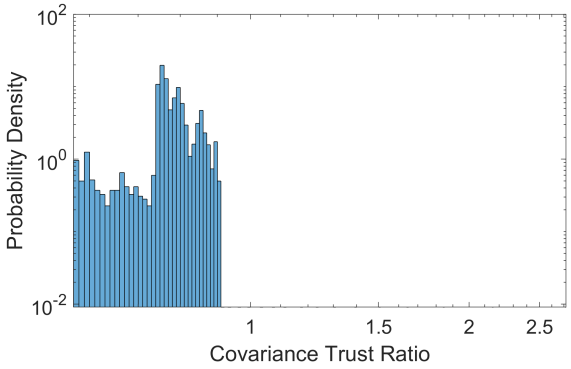

(a) PDF for Test Case 29 average covariance trust ratios

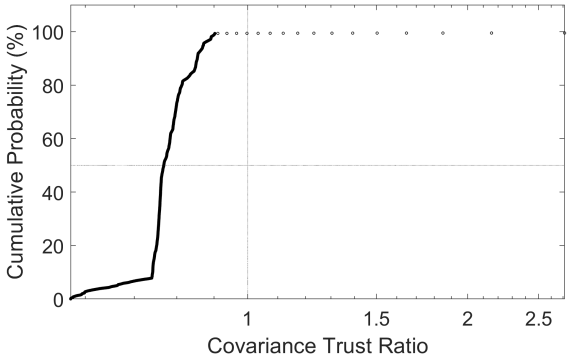

(b) CDF for Test Case 29 average covariance trust ratios

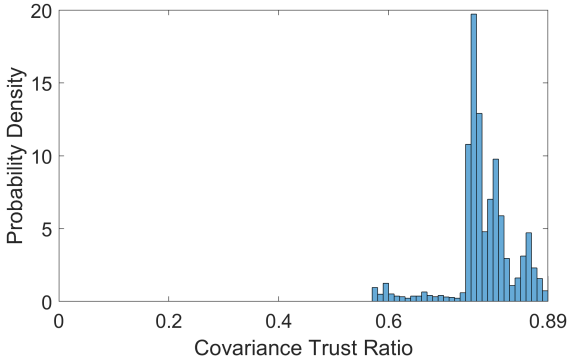

(c) PDF for Test Case 29 average covariance trust ratios, truncated to probabilities below 98%

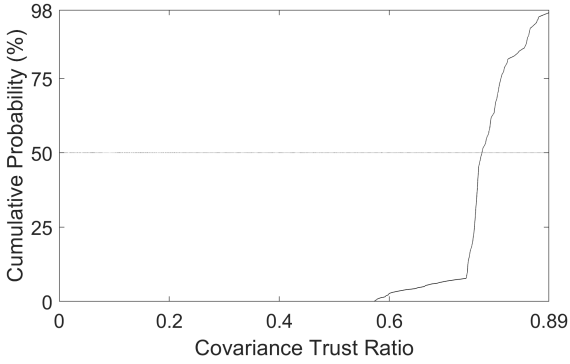

(d) CDF for Test Case 29 average covariance trust ratios, truncated to probabilities below 98%

Fig. C.47: Cumulative distribution functions (CDFs) and probability density functions (PDFs) for trustworthiness factor combination Test Case 29: filters using the UKF to estimate the observer and RSO state using range measurements and the van Loan process noise covariance model.

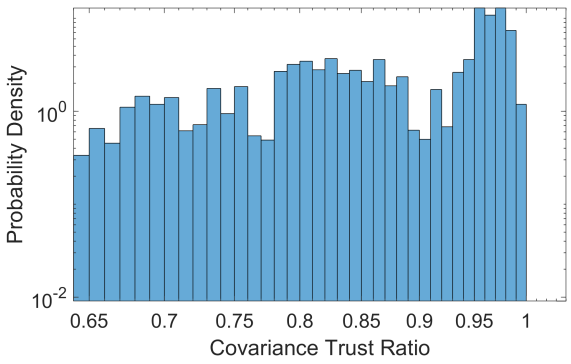

(a) PDF for Test Case 30 average covariance trust ratios

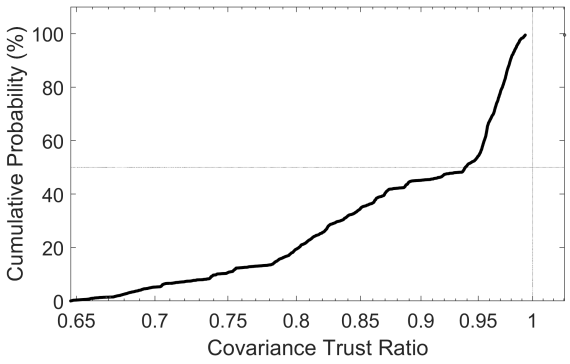

(b) CDF for Test Case 30 average covariance trust ratios

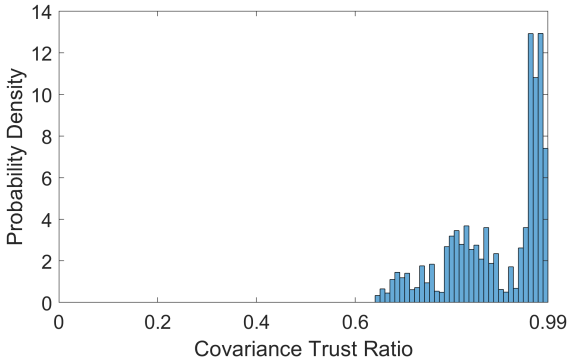

(c) PDF for Test Case 30 average covariance trust ratios, truncated to probabilities below 98%

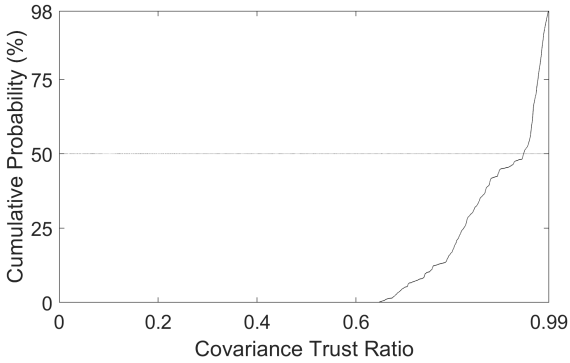

(d) CDF for Test Case 30 average covariance trust ratios, truncated to probabilities below 98%

Fig. C.48: Cumulative distribution functions (CDFs) and probability density functions (PDFs) for trustworthiness factor combination Test Case 30: filters using the UKF to estimate the observer and RSO state using range and angle measurements and the van Loan process noise covariance model.

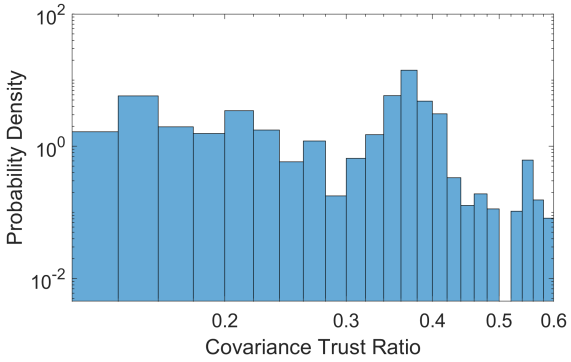

(a) PDF for Test Case 31 average covariance trust ratios

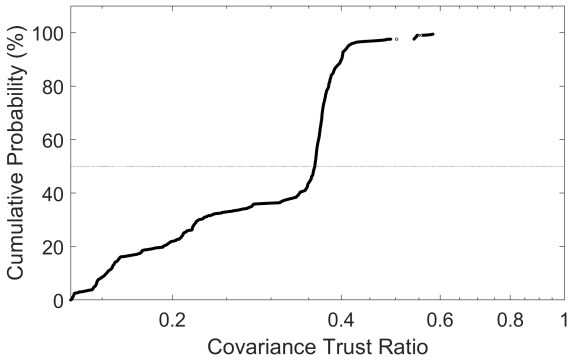

(b) CDF for Test Case 31 average covariance trust ratios

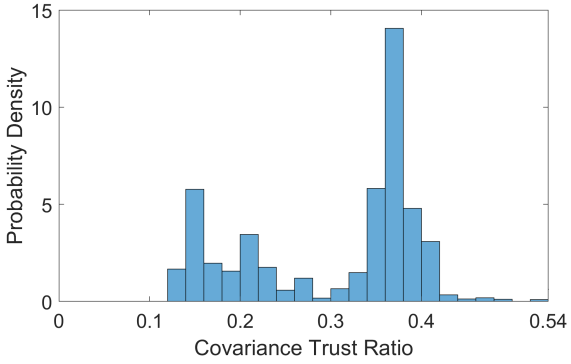

(c) PDF for Test Case 31 average covariance trust ratios, truncated to probabilities below 98%

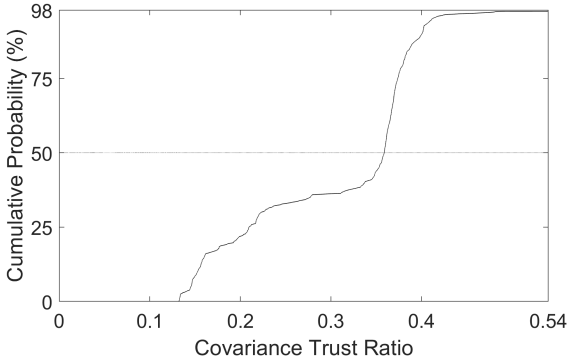

(d) CDF for Test Case 31 average covariance trust ratios, truncated to probabilities below 98%

Fig. C.49: Cumulative distribution functions (CDFs) and probability density functions (PDFs) for trustworthiness factor combination Test Case 31: filters using the UKF to estimate the observer and RSO state using angle measurements and the fixed bump process noise covariance model.

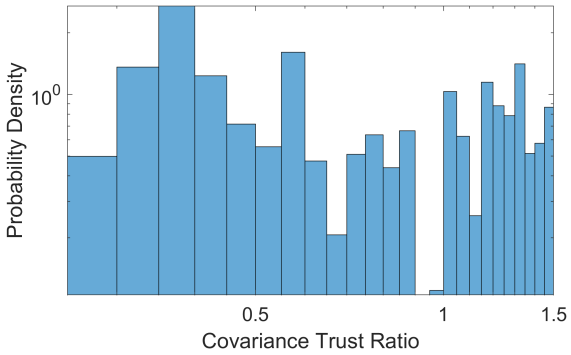

(a) PDF for Test Case 32 average covariance trust ratios

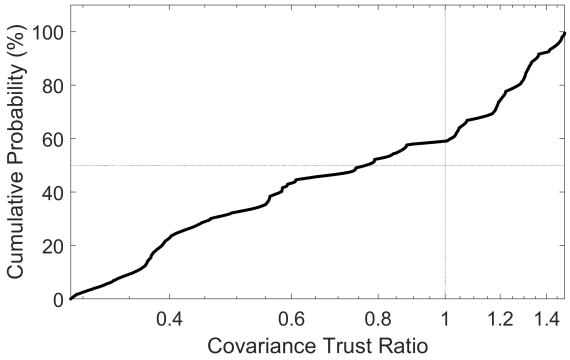

(b) CDF for Test Case 32 average covariance trust ratios

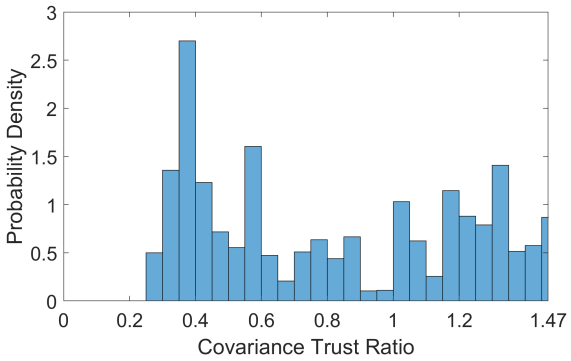

(c) PDF for Test Case 32 average covariance trust ratios, truncated to probabilities below 98%

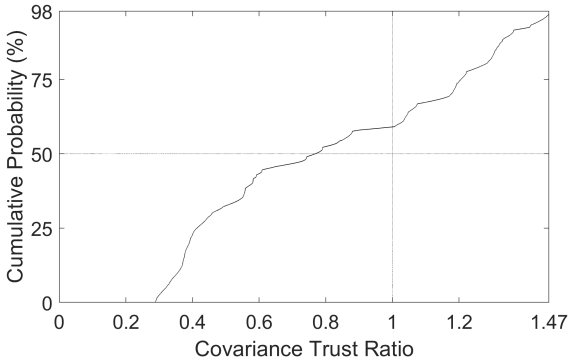

(d) CDF for Test Case 32 average covariance trust ratios, truncated to probabilities below 98%

Fig. C.50: Cumulative distribution functions (CDFs) and probability density functions (PDFs) for trustworthiness factor combination Test Case 32: filters using the UKF to estimate the observer and RSO state using range measurements and the fixed bump process noise covariance model.

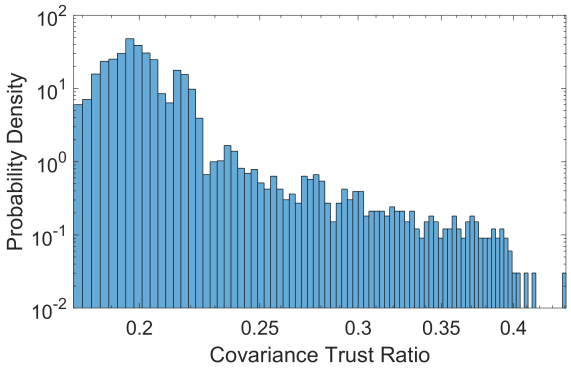

(a) PDF for Test Case 33 average covariance trust ratios

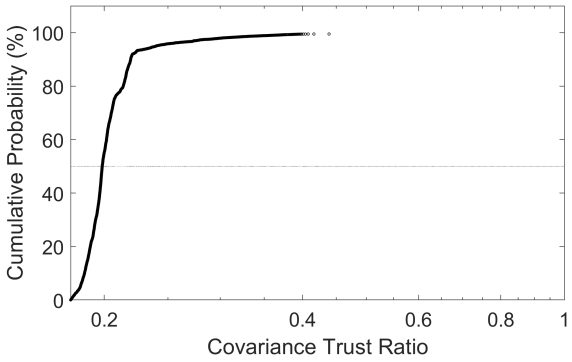

(b) CDF for Test Case 33 average covariance trust ratios

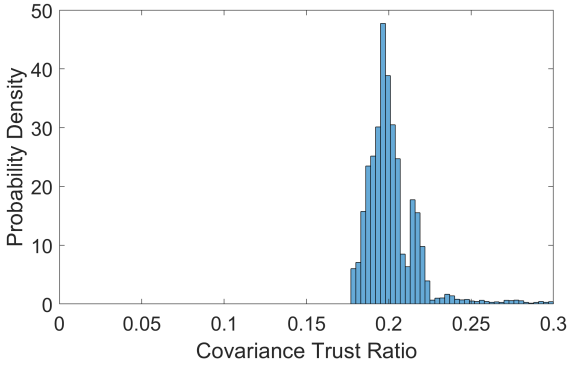

(c) PDF for Test Case 33 average covariance trust ratios, truncated to probabilities below 98%

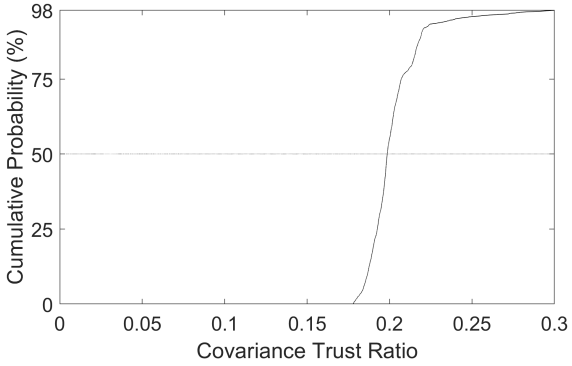

(d) CDF for Test Case 33 average covariance trust ratios, truncated to probabilities below 98%

Fig. C.51: Cumulative distribution functions (CDFs) and probability density functions (PDFs) for trustworthiness factor combination Test Case 33: filters using the UKF to estimate the observer and RSO state using range and angle measurements and the fixed bump process noise covariance model.

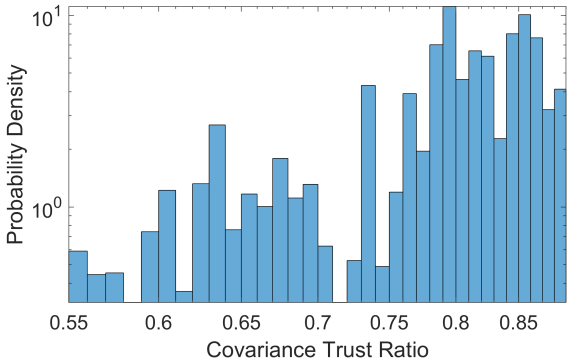

(a) PDF for Test Case 34 average covariance trust ratios

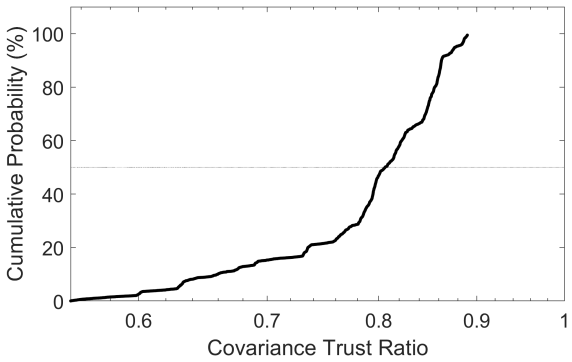

(b) CDF for Test Case 34 average covariance trust ratios

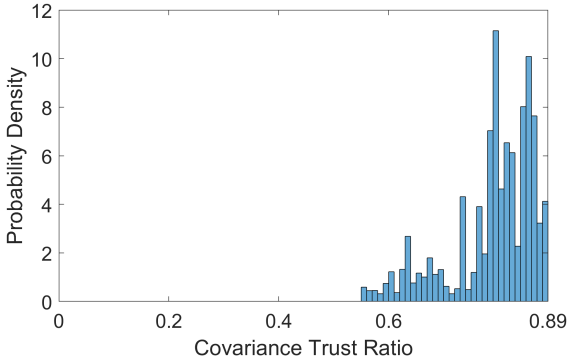

(c) PDF for Test Case 34 average covariance trust ratios, truncated to probabilities below 98%

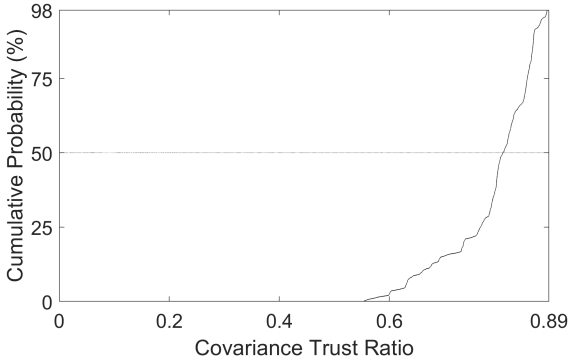

(d) CDF for Test Case 34 average covariance trust ratios, truncated to probabilities below 98%

Fig. C.52: Cumulative distribution functions (CDFs) and probability density functions (PDFs) for trustworthiness factor combination Test Case 34: filters using the UKF to estimate the observer and RSO state using angle measurements and the variable bump process noise covariance model.

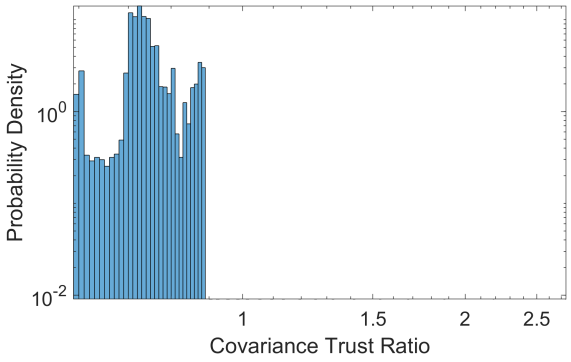

(a) PDF for Test Case 35 average covariance trust ratios

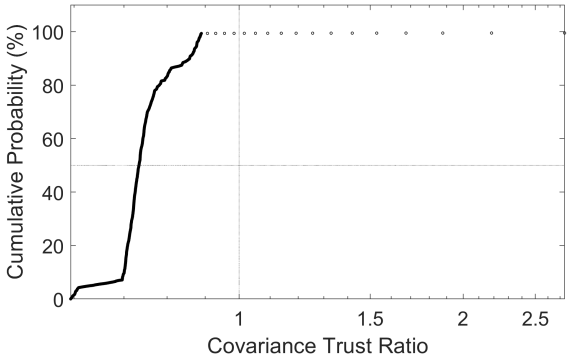

(b) CDF for Test Case 35 average covariance trust ratios

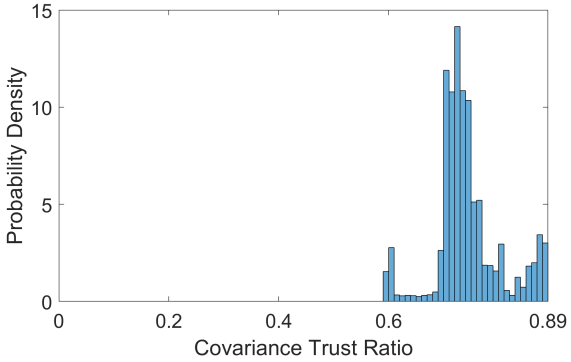

(c) PDF for Test Case 35 average covariance trust ratios, truncated to probabilities below 98%

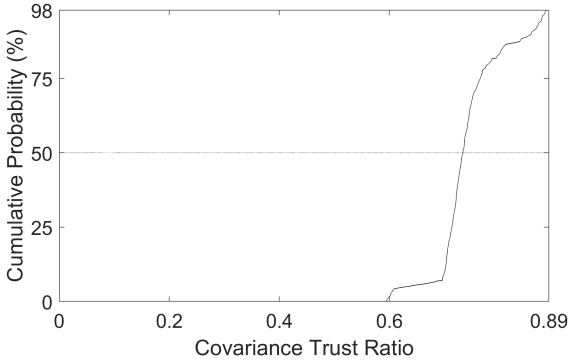

(d) CDF for Test Case 35 average covariance trust ratios, truncated to probabilities below 98%

Fig. C.53: Cumulative distribution functions (CDFs) and probability density functions (PDFs) for trustworthiness factor combination Test Case 35: filters using the UKF to estimate the observer and RSO state using range measurements and the variable bump process noise covariance model.

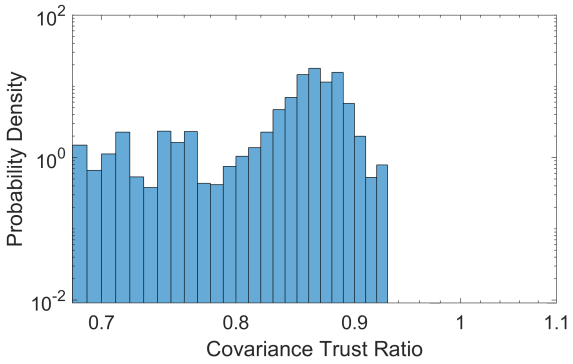

(a) PDF for Test Case 36 average covariance trust ratios

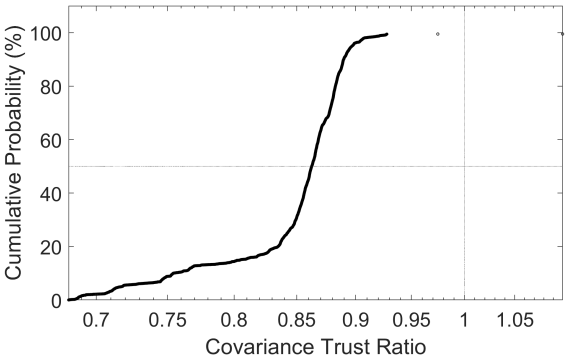

(b) CDF for Test Case 36 average covariance trust ratios

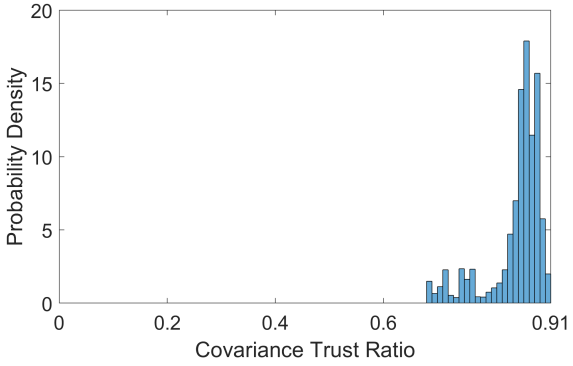

(c) PDF for Test Case 36 average covariance trust ratios, truncated to probabilities below 98%

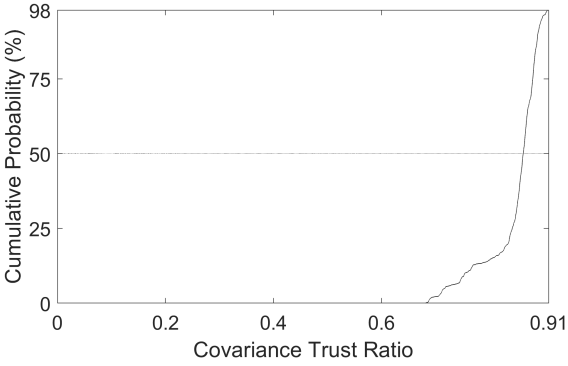

(d) CDF for Test Case 36 average covariance trust ratios, truncated to probabilities below 98%

Fig. C.54: Cumulative distribution functions (CDFs) and probability density functions (PDFs) for trustworthiness factor combination Test Case 36: filters using the UKF to estimate the observer and RSO state using range and angle measurements and the variable bump process noise covariance model.